AUTHOR: **Jonathan Girven**   DEGREE: **Ph.D.**

TITLE: **Stellar and Planetary Remnants in Digitial Sky Surveys**

DATE OF DEPOSIT: ....

    I agree that this thesis shall be available in accordance with the regulations governing the University of Warwick theses.

    I agree that the summary of this thesis may be submitted for publication.

    I **agree** that the thesis may be photocopied (single copies for study purposes only).

    Theses with no restriction on photocopying will also be made available to the British Library for microfilming. The British Library may supply copies to individuals or libraries. subject to a statement from them that the copy is supplied for non-publishing purposes. All copies supplied by the British Library will carry the following statement:

> "Attention is drawn to the fact that the copyright of this thesis rests with its author. This copy of the thesis has been supplied on the condition that anyone who consults it is understood to recognise that its copyright rests with its author and that no quotation from the thesis and no information derived from it may be published without the author's written consent."
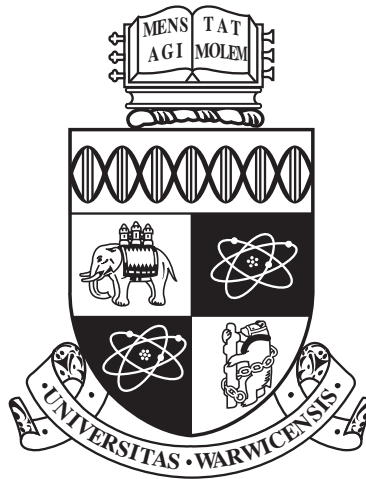
AUTHOR'S SIGNATURE: ....

USER'S DECLARATION

1. I undertake not to quote or make use of any information from this thesis without making acknowledgement to the author.

2. I further undertake to allow no-one else to use this thesis while it is in my care.

DATE   SIGNATURE   ADDRESS

....

....

....

....

....

Stellar and Planetary Remnants in Digitial Sky Surveys

by

Jonathan Girven

Thesis

Submitted to the University of Warwick

for the degree of

Doctor of Philosophy

Astronomy and Astrophysics

June 2012

THE UNIVERSITY OF

WARWICK

Contents

ii

List of Tables

List of Figures

Acknowledgments

I would like to thank my supervisors for all their help and guidance throughout my PhD: Prof. Boris Gänsicke for never accepting anything less than excellence and Dr. Danny Steeghs for being a mediator in the ensuing arguments. Boris for getting excited about the little things and Danny for delving into the field of subdwarfs with me ... amongst a host of other things. I am extremely grateful to Dr. Carolyn Brinkworth for giving me the opportunity to experience California and all it has to offer. Also, to my collaborators, thank you for your hard work and patience.

I would like to thank all of my friends and family for the support they gave me over my eight years at Warwick:

- Those who shared an office with me (Lieke, Joao, Simon, Nicola and Stelios)
- Sandra Greiss for putting up with me and my "sense of humour"
- Everyone else in the Warwick astronomy group
- My various housemates (to name a few: Anisha, Andy, Jonny, Morwenna and Toby)
- My friends from Rootes J-block (Liam, Sean, Peps, Alex, Michael, Kerrie, Rachel, Hannah and many others)
- Barley Blighton (a constant source of entertainment)
- Everyone on my physics undergraduate course (Tom, Jamie, Luke, etc.)
- The Warwick windsurfing club (Ben Jones, Jess Precious, Cousins, Kay Polley, Ben Wood, Matt Matt, Joey, Harriet, Polly, Alice, Max Thurlow ...)
- My parents and my brother, Chris.

A huge thank you to you all. Sorry if I forgot anyone!

Declarations

I declare that this thesis has not been submitted in any previous application for a higher degree. Chapters 1-2 provide information gathered from the literature. Chapter 3 outlines some common methods used through this work. In Chapters 4-8, I present my own work. Finally, in Chapter 9, I summarise the results and draw conclusions.

Chapters 4 and 5 are based on Girven et al. [2011]: Girven, J., Gänsicke, B. T., Steeghs, D., Koester, D., "DA white dwarfs in Sloan Digital Sky Survey Data Release 7 and a search for infrared excess emission", MNRAS, 417, 1210 (2011)

Chapter 6 is based on Girven et al. [2012a]: Girven, J., Brinkworth, C. S., Farihi, J., Gänsicke, B. T., Hoard, D. W., Marsh, T. R., Koester, D., "Constraints on the Lifetimes of Disks Resulting from Tidally Destroyed Rocky Planetary Bodies", ApJ, 749, 154 (2012)

Chapter 7 is based on Girven et al. [2012b]: Girven, J.; Steeghs, D.; Heber, U.; Gnsicke, B. T.; Marsh, T. R.; Breedt, E.; Copperwheat, C. M.; Pyrzas, S.; Longa Peña, P., "The Unseen Population of F to K-type Companions to Hot Subdwarf Stars", MNRAS, accepted for publication (2012)

Chapter 8 is based on Girven et al. [2010]: Girven, J., Gänsicke, B. T., Külebi, B., Steeghs, D., Jordan, S., Marsh, T. R., Koester, D., "PG 1258+593 and its common proper motion magnetic white dwarf counterpart", MNRAS, 404, 159 (2010)

Abstract

Large scale digital sky surveys have produced an unprecedented volume of uniform data covering both vast proportions of the sky and a wide range of wavelength, from the ultraviolet to the near-infrared. The challenge facing astronomers today is how to use this multitude of information to extract trends, outliers and find rare objects. For example, a large sample of single white dwarf stars has the potential to probe the Galaxy through the luminosity function.

The aim of this work was to study stellar and planetary remnants in these surveys. In the last few decades, it has been shown that a handful of white dwarfs have remnants of planetary systems around them, in the form of a dusty disc. These are currently providing the best constraints on the composition of extra-solar planetary systems. Finding significant numbers of dusty discs is only possible in large scale digital sky surveys.

I ultilised the SDSS DR7 and colour-colour diagrams to find DA white dwarfs from optical photometry. This nearly doubled the number of spectroscopically confirmed DA white dwarfs in the SDSS compared with DR4 [Eisenstein et al., 2006], and introduced nearly $10,000$ photometric-only DA white dwarf candidates. I further cross-matched our white dwarf catalogue with UKIDSS LAS DR8 to carry out the currently largest and deepest untargeted search for low-mass companions to, and dust discs around, DA white dwarfs. Simultaneously, I analyzed *Spitzer* observations of 15 white dwarfs with metal-polluted atmospheres, all but one having helium-dominated atmospheres. Three of these stars were found to have an infrared excess consistent with a dusty disc. I used the total sample to estimate a typical disc lifetime of $\log[t_{\mathrm{disc}}(\mathrm{yr})] = 5.6 \pm 1.1$, which is compatible with the relatively large range estimated from different theoretical models.

Subdwarf population synthesis models predicted a vast population of subdwarfs with F to K-type companions, produced in the efficient RLOF formation channel. I used a cross-match of ultraviolet, optical and infrared surveys to search for this unseen population. I select a complementary sample to those found from radial velocity surveys, offering direct tests of binary evolution pathways.

Finally, I present a method to use common proper motion white dwarf pairs to constrain the initial-final mass relation, which is extremely uncertain at low masses. In the example I show, one of the stars is a magnetic white dwarf with $B \simeq 6\,\mathrm{MG}$, making this a rare and intriguing system from a magnetic white dwarf formation point of view.

Chapter 1

White dwarf and subdwarf stars

1.1 The Hertzsprung-Russell diagram

The night sky consists of a many stars, of varying types, from massive stars fusing heavy elements in their cores to degenerate objects, devoid of an energy source, and fading gradually from view. These stars can be divided and identified by use of a Hertsprung Russell diagram, which is traditionally a plot of temperature against luminosity. It can, however, be shown with absolute magnitude instead of luminosity and either spectral type or B-V colour as an alternative to temperature. Objects in different evolutionary states separate from one another across the diagram. In Figure 1.1, we can see that main-sequence stars run diagonally across the diagram from cool, faint, low mass stars in the lower-right, to the most massive, hot, bright stars in the upper-left. A star on the main-sequence has collapsed from a gas cloud and has reached the temperatures and pressures in its core necessarily to burn hydrogen into helium. The most massive stars will only continue in this phase for a few million years, whereas many low mass stars will continue burning hydrogen for the age of the universe and beyond. Our Sun currently lives on the main-sequence and will for a total of approximately 10 billion years.

When a star creates a sufficient amount of hydrogen in its core (assuming the star has a mass of more than approximately $0.26 \, M_\odot$), the temperatures and pressures increase to a point where hydrogen can fuse into carbon (via the triple alpha process). This reaction occurs in a shell around the core. The outer layers begin to expand, cool and shine less brightly. At this stage, the star is known as a red giant. In Figure 1.1, the giant branch is a sequence moving perpendicular to the main-sequence, towards the upper-right corner of the diagram. For the most massive stars, many other shell burning stages can occur, for elements all the way
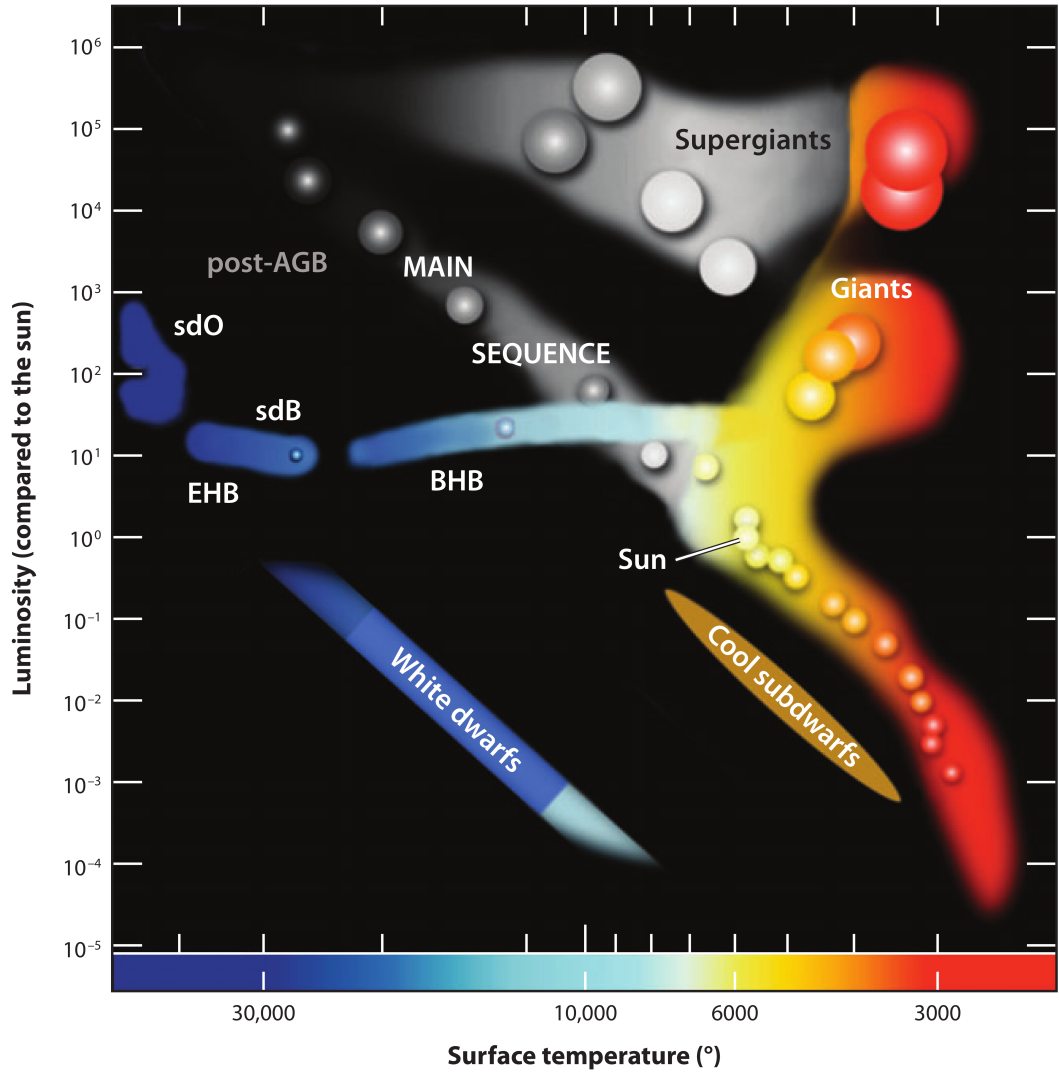
Figure 1.1: A sketch of the Hertzsprung-Russell diagram showing the position of the hot subdwarf (sdO and sdB) and white dwarf stars. Taken from Heber [2009].

up to iron (leading to the blue super giant branch). Solar-like stars, however, will never reach sufficiently high core temperatures for this to happen. Unless external forces intervene (see Section 1.3 on subdwarf stars), the helium core will run out, and the outer layers off the star will drift away, leaving the core exposed. This small, hot, blue object is known as a white dwarf star.

1.2   White dwarfs

White dwarfs are the most common stellar remnants in the Galaxy, having descended from main sequence stars with $0.8M_\odot \lesssim M \lesssim 8M_\odot$ [see D'Antona & Mazzitelli, 1990, Koester & Chanmugam, 1990, Koester, 2002, Hansen, 2004 and Hoard, D. W., 2011 for a review]. Only the most massive of stars do not follow the path to becoming a white dwarf and explode in a core-collapse supernova, leaving behind either a neutron star or black hole. Not only are white dwarfs the end point of our own Sun and allow us to glimpse the distant future of our Solar System, but they provide insight into a multitude of important astrophysical questions. In single star evolution, white dwarfs expose the cores of their main-sequence progenitors, which can not be directly studied while the star is on the main sequence. They also provide a laboratory to test one of the most extreme environments in astrophysics because of their intense gravities, densities and magnetic fields. White dwarfs also have key links to binary star evolution, helping understanding of mass transfer, enrichment of the interstellar medium (via nova explosions) and Supernovae type Ia, the basis for modern cosmology.

White dwarfs no longer undergo nuclear burning in their cores, unlike main-sequence stars. Instead, they are prevented from gravitational collapse by electron degeneracy pressure: the outward pressure from the Pauli Exclusion Principle stopping two electrons from simultaneously being in the same phase space and occupying the same quantum state. This leads to a maximum mass, the Chandrasekhar mass limit [$1.44\,M_\odot$; Chandrasekhar, 1931], beyond which the gravitational potential overwhelms the electron degeneracy pressure and the white dwarf collapses. Accreting white dwarfs which grow to exceed the Chandrasekhar mass limit, or white dwarf mergers, are thought to produce type Ia supernovae, some of the brightest objects in the Universe. Much of the study of cosmology is based upon their use as a standard candle to measure distances across the Universe [e.g. Rowan-Robinson, 1985].

Once the white dwarf has formed, starting its life with a surface temperature of $\sim 100,000\,\mathrm{K}$, it begins to cool and decrease in luminosity following the white dwarf cooling track [Mestel, 1952],

3

$$L(t)/L_\odot = (2.3 \times 10^{-3}) \times M \times t^{-7/5} \tag{1.1}$$

where the mass (M) is given in solar units and the time (t) is given in Gyrs[1]. White dwarfs typically have masses around $0.6\,M_\odot$, but have been found to range from $0.2 - 1.3\,M_\odot$ in some cases. The beauty of Equation 1.1 is that the age of the white dwarf can be deduced from its luminosity, which means white dwarfs can be used as cosmic chronometers [e.g. Oswalt et al., 1996].

1.2.1 Atmospheres

White dwarfs are relatively simple objects, generally being just crystalised (for cool white dwarfs) balls of carbon and oxygen (or helium for the lowest mass white dwarfs and oxygen-neon for the most massive). The cores are highly degenerate, and since degenerate electrons are extremely good conductors, the core is almost isothemal. The core can therefore be thought of as a sphere with a single temperature, containing most of the mass of the white dwarf, upon which a thin [1/100th of the total white dwarf mass for stars with a hydrogen-rich atmosphere; Murdin, 2001] non-degenerate atmosphere layer sits.

Due to the high surface gravities and limited radiative forces, heavy elements sink rapidly within the atmospheres of cool ($T_{\text{eff}} < 25,000\,\text{K}$) white dwarf stars, resulting in the differentiation of the atmosphere [Fontaine & Michaud, 1979; Koester, 2009]. The spectra of white dwarfs therefore consist of essentially pure hydrogen or helium and thus are dominated by pressure broadened Balmer or Helium lines for hydrogen-rich (DA; Figure 1.2) or helium-rich (DB; Figure 1.3) atmospheres, respectively. The downward diffusion of metals occurs over a timescale that is typically only days to years for $\sim 11,000 - 25,000\,\text{K}$ white dwarfs with hydrogen-rich atmospheres.

DA white dwarfs are the largest subset, however helium-rich white dwarfs do make up about 8 per cent [Eisenstein et al., 2006]. The latter have been split into a number of different subclasses: DO-types are the hottest of these with effective temperatures between approximately $100,000$ to $45,000\,\text{K}$ and spectra dominated by singularly ionised helium. At the next step down in temperature ($\sim 30,000$ to $12,000\,\text{K}$), DB white dwarfs are classified as having spectra dominated by neutral helium. Below $12,000\,\text{K}$, DC white dwarfs have featureless spectra (DA white dwarfs

---

[1]More recent works on white dwarf cooling tracks are given in e.g. Hansen [1999] and Chabrier et al. [2000]
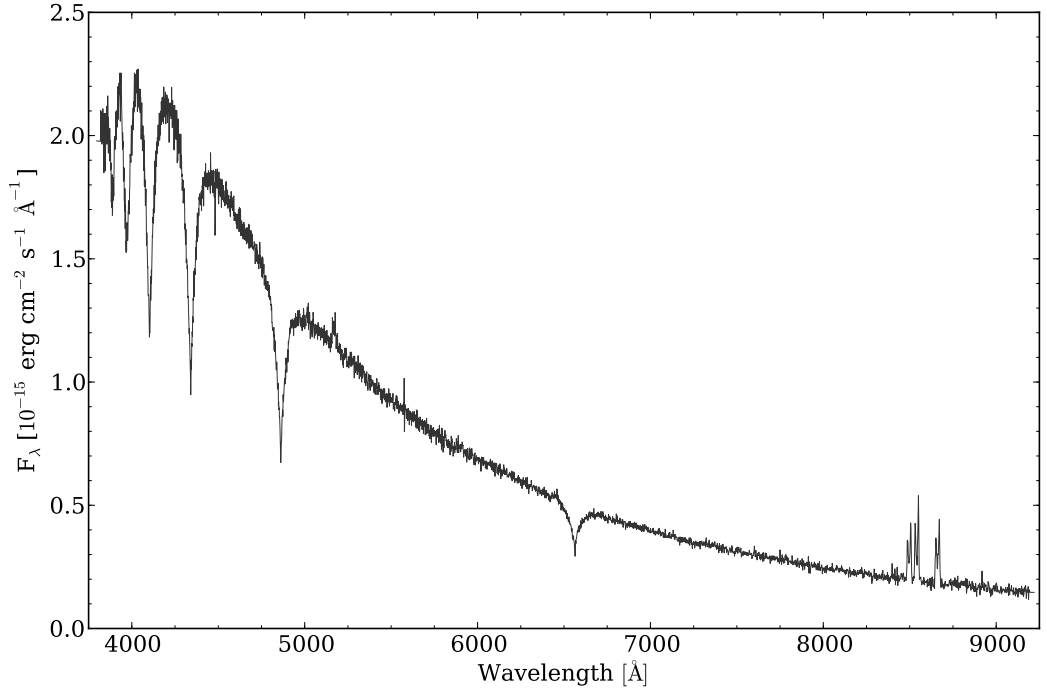
Figure 1.2: An example of an optical (SDSS) spectrum of a white dwarf with a hydrogen-rich atmosphere (here: SDSS J1228+1040). SDSS J1228+1040 also shows Fe II (5020 and 5170 Å) and Ca triplet (8500 − 8660 Å) emission indicative of accretion from a gaeseous disk [Gänsicke et al., 2006b].

below $6,000$ K would also appear as a DC white dwarf). A small fraction (1 per cent) of white dwarfs are found to have carbon-rich atmospheres (DQ), and a couple of very rare white dwarfs have oxygen-rich atmospheres [Gänsicke et al., 2010]. Finally, DZ white dwarfs show absorption features from metals such as calcium, magnesium and iron in the optical spectra of cooler ($\sim 5,000 - 20,000$ K) objects [Zuckerman et al., 2003; Koester et al., 2005b, also see Section 1.2.2.1], and carbon and silicon in the ultraviolet for warmer ($\sim 12,500 - 25,000$ K) objects [Dupuis et al., 2009a,b]. Hybrid classes do also exist, such as DBA, DAB, DAO, DAZ and DBZ, where multiple sets of features are seen. For example, a DBA spectra is primarily dominated by absorption from neutral helium, but does show evidence of hydrogen as well (the dominant element being the second letter).

Not all white dwarfs have atmospheres completely dominated by gravitational settling. On the one hand, above $\sim 25,000$ K, radiative levatation becomes a significant factor [Chayer et al., 1995], supporting significant amounts of metals in the atmosphere. On the other hand, below a surface temperature of $\sim 10,000$ K [for DA white dwarfs; Dufour et al. 2007 - see Figure 14; but much higher for DB white

5
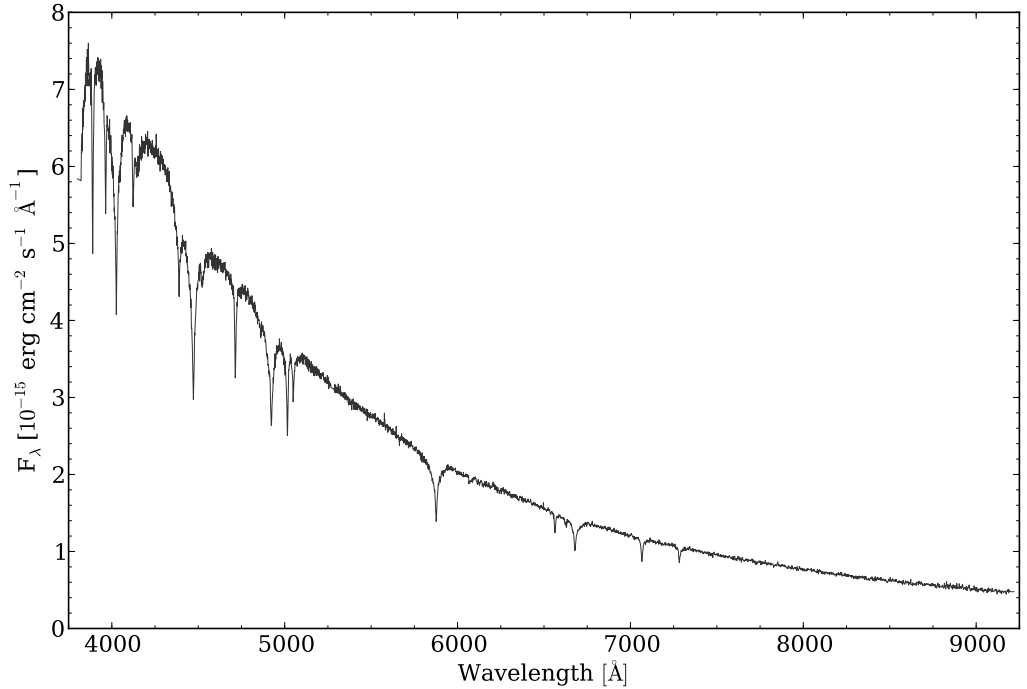
Figure 1.3: An example of an optical (SDSS) spectrum of a white dwarf with a helium-rich atmosphere (here: SDSS J0020+1352).

dwarfs; Bergeron et al. 2011 - see Figure 3], a convective zone develops [associated with the partial ionisation of the dominant atmospheric component; Koester et al., 1982; Fontaine et al., 1984], which also draws metals to the surface.

The relative simplicity of white dwarf atmospheres has allowed state of the art model atmosphere codes to be developed [Koester, 2009, 2010; Tremblay & Bergeron, 2009], which allow spectral fitting to calculate the white dwarfs effective temperature (T_{eff}) and surface gravity ($\log(g)$). Systematic uncertainties often reach as low as tens to hundreds of Kelvin and 0.1 dex for the T_{eff} and $\log(g)$, respectively. This is discussed further in Section 3.4.1.

1.2.2   Tidally destroyed asteroids

Extra-solar planets around main-sequence stars are an exciting, but challenging field, from the perspective of measuring compositions. The bulk density of transiting planets and the atmospheres from transit spectroscopy have been estimated in cases such as Valencia et al. [2010] and Grillmair et al. [2008], respectively. However, over the past decade it has become increasingly clear that planetary systems survive, at least in part, the late evolution of their host stars, and therefore can be studied after

the death of the central star. The observational evidence supporting this conclusion comes from metal pollution observed in white dwarf atmospheres, and the commonly detected circumstellar discs of solid and gaseous debris [e.g. Zuckerman & Becklin, 1987; Kilic et al., 2006a; Gänsicke et al., 2006b, 2007, 2008; Jura et al., 2007a; von Hippel et al., 2007; Brinkworth et al., 2009; Farihi et al., 2010b; Debes et al., 2011; Farihi et al., 2011a; Melis et al., 2011; Brinkworth et al., 2012; Dufour et al., 2012, and a host of other references therein].

1.2.2.1 Metal pollution

Despite the extremely rapid time scale on which metals sink out of a white dwarfs atmosphere, about 25 per cent of DA and 33 per cent of DB white dwarfs exhibit absorption features due to the presence of trace metals [Zuckerman et al., 2003; Koester et al., 2005b; Zuckerman et al., 2010], and these must be the result of external sources and a sign of ongoing accretion [Sion et al., 1990].

Although metal absorption features have been seen in single white dwarf spectra for over a century [van Maanen, 1917; Kuiper, 1941], it is only relatively recently that we have begun to understand the nature of the potentially huge, asteroid-sized, accretion reservoirs [Farihi et al., 2010a] and metal accretion rates of $\langle dM_\mathrm{z}/dt \rangle > 10^8\,\mathrm{g\,s^{-1}}$ [Koester & Wilken, 2006]. Surveys such as the Hamburg Schmidt survey [Heber et al., 1991], Hamburg/ESO survey [Friedrich et al., 2000], and the ESO supernovae Ia progenitor survey (SPY) [Koester et al., 2001, 2005b; Voss et al., 2007] have been instrumental in discovering large numbers of bright ($V \lesssim 16$) metal-polluted white dwarfs. An increasing number of DZ white dwarfs have also been discovered using the SDSS spectroscopic survey [e.g. Dufour et al., 2007; Koester et al., 2011] and other large surveys [Zuckerman et al., 2010; Kawka et al., 2011].

Detailed abundance studies have been limited to a handful of white dwarfs because of the need for high-resolution, high-quality spectroscopy. Zuckerman et al. [2007] detected 15 metals (atomic number, $Z > 2$) in the atmosphere of the dramatically metal polluted white dwarf GD 362, using Keck/High Resolution Echelle Spectrometer (HIRES), a significant advance over previous work that detected only Ca, Mg, and Fe [Gianninas et al., 2004; Kawka & Vennes, 2006]. From the atmospheric abundances of GD 362, the white dwarf has accreted at least the equivalent of a 240 km asteroid. The most polluted DAZ white dwarf currently known, GALEX 1931+0117, accretes approximately solar-like material at a rate of $3 - 4 \times 10^9\,\mathrm{g\,s^{-1}}$ [Vennes et al., 2010; Debes et al., 2011; Melis et al., 2011; Vennes et al., 2011b; Gänsicke et al., 2012]. The chemical abundances of the photospheric

pollutants in these, and all DZ white dwarfs, can be analytically linked to those of the accreted matter [Koester, 2009; Jura et al., 2009b]. Initially, the metals were believed to be accreted from the interstellar medium [ISM; e.g. Dupuis et al., 1992, 1993a,b]. However, the general lack of accreted hydrogen in DBZ-type white dwarfs was a constant problem for the hypothesis [e.g Koester, 1976; Wesemael, 1979; Aannestad et al., 1993]. Alcock et al. [1986] first proposed the idea that cometary impacts could be the source of photospheric metals. In a number of cases, the accreting material has been confirmed to be silicate-rich, and typical of the material associated with planet formation [e.g. zodiacal and cometary dust; Reach et al., 2005; Jura et al., 2009a; Reach et al., 2009]. The detection of O (along with eight others, including the major elements; Mg, Si, and Fe) in the spectra of GD 40 allowed Klein et al. [2010] to confirm that the properties of the accreted material were consistent with the balance of mineral oxides in the bulk Earth.

A number of authors have tentatively claimed to have detected the accretion of differentiated bodies, planetary lithospheres and possible water-worlds [e.g. Jura et al., 2009a; Farihi et al., 2011a; Zuckerman et al., 2011] from the abundances of white dwarf atmospheres. However, this is still in debate. Although water is widespread in the outer solar system [Jewitt et al., 2007; Encrenaz, 2008], and can be more than 50 per cent of the mass of Kuiper Belt objects and comets, Jura & Xu [2012] find that the majority of DZ white dwarfs have accreted objects that are significantly drier than the CI chondrites. Gänsicke et al. [2012, in press] find substantial diversity in the accretion rates among four white dwarfs observed with *Hubble Space Telescope* ultraviolet spectroscopy, at least comparable with the variation in the solar system asteroids.

A diverse group of different exoplanets; Earth-like, refractory-rich and carbon-rich objects, are predicted to exist [Bond et al., 2010]. The atmospheres of gas giant exoplanets around main–sequence stars can be probed by transmission spectroscopy during transit. However, studying planetary systems around white dwarfs unlocks the potential to measure the bulk chemical composition of destroyed, and subsequently accreted, rocky planetary bodies such as asteroids, moons, or possibly major planets [e.g. Dufour et al., 2010; Klein et al., 2010; Vennes et al., 2010; Zuckerman et al., 2010; Farihi et al., 2011a,b; Klein et al., 2011; Zuckerman et al., 2011].

1.2.2.2 Dust discs

Zuckerman & Becklin [1987] discovered that the white dwarf G29−38 had a large infrared excess over the flux expected from a single white dwarf. This was initially interpreted to be the contribution from a brown dwarf companion, however, this was

subsequently ruled out [Graham et al., 1990b; Kleinman et al., 1994; Kuchner et al., 1998]. The $10\,\mu$m flux far exceeds that expected from a brown dwarf companion and is more consistent with a cloud of dust [Graham et al., 1990a; Telesco et al., 1990; Tokunaga et al., 1990]. The dust was confirmed by Reach et al. [2005] using the *Spitzer Space Telescope* [Werner et al., 2004] and evidence of silicate emission, consistent with the dust disc hypothesis, was seen in several cases [Graham et al., 1990a; Tokunaga et al., 1990; Reach et al., 2005]. G29−38 is accreting from this dust disc at a rate of $5 \times 10^{-15}\,\mathrm{M_\odot}$ per year [Koester et al., 1997].

Ground based searches for white dwarfs with discs were successful in a number of cases [Becklin et al., 2005; Kilic et al., 2005, 2006b; Kilic & Redfield, 2007]. However, the launch of the *Spitzer Space Telescope* has lead to an order of magnitude more objects [Jura et al., 2007a,b; von Hippel et al., 2007; Farihi et al., 2007, 2008b, 2009; Jura et al., 2009a; Reach et al., 2009; Farihi et al., 2010b; Chu et al., 2011; Girven et al., 2012a; Xu & Jura, 2012]. Recently, observations from UKIDSS [Girven et al., 2011; Steele et al., 2011] and the *Wide-field Infrared Survey Explorer* [*WISE*; Wright et al., 2010] mission [Debes et al., 2011] have contributed significantly to the number of known white dwarfs with dust discs. It has been shown that $\sim 1 - 3\,$per cent of all single white dwarfs with cooling ages $\lesssim 0.5\,$Gyr ($\mathrm{T_{eff}} \sim 10,000 - 20,000\,$K) have dust discs [Farihi et al., 2009; Girven et al., 2011].

Dust discs are modelled with an optically thick, geometrically thin, flat disc, defined by the temperature of inner and outer edges and the inclination with respect to the observer [Adams et al., 1988; Chiang & Goldreich, 1997; Jura, 2003, 2006; Jura et al., 2007a]. The known discs fall in three catagories: Firstly, $\gtrsim 15\,$per cent of pre-white dwarfs harbour dust with an inner disc temperature of $\sim 100\,$K [Chu et al., 2011], which is believed to form in collisions between Kuiper-belt-like objects [Bonsor & Wyatt, 2010; Dong et al., 2010]. Secondly, two cool ($\mathrm{T_{eff}} \lesssim 10,000\,$K) white dwarfs (G 166−58; Farihi et al. 2008b and PG 1225−079; Farihi et al. 2010b) have been shown to have $\sim 500\,$K dust in a disc with a large inner hole, the origin of which is still unknown. Finally, a significant fraction of DZ white dwarfs are surrounded by a dust disc with an inner disc temperature of $\sim 1,000\,$K. The dust, in this case, originates from tidal disruption of either comets [Alcock et al., 1986; Debes & Sigurdsson, 2002a] or asteroids [Jura, 2003, 2008]. The observed level of accretion, and corresponding numbers of asteroids and comets, can be explained by the post-main sequence evolution of a star and its planetesimal belt [Bonsor et al., 2011]. The maximum disc temperature is constrained by the sublimation temperature of the dust grains ($\sim 1,700\,$K). The minimum grain temperature, or corresponding maximum radius, is associated with the system's tidal disruption

radius for comets and asteroids ($\simeq 1.2R_\odot$; Davidsson 1999), where rocky bodies are shredded and accrete [Debes & Sigurdsson, 2002a; Jura, 2003; Zuckerman et al., 2007; Dufour et al., 2010; Klein et al., 2010].

1.2.2.3 Gas discs

Around the same time as the first *Spitzer* discoveries of the white dwarfs with dusty discs, SDSS J1228+1040 (a $22,000$ K white dwarf with a hydrogen-rich atmosphere) was shown to have double peaked Ca II triplet emission in the SDSS DR4 optical spectrum [see Figure 1.2; Gänsicke et al., 2006b]. This is the hallmark of a gaseous, rotating disc [Young et al., 1981; Horne & Marsh, 1986]. SDSS J1228+1040 also shows strong Mg II absorption (even though it has a diffusion timescale of only a few days), but a lack of helium absorption, indicating that the white dwarf must be orbited by hydrogen and helium deficient, metal-rich material. From modelling of the Calcium triplet emission, the kinematics imply that the white dwarf must be orbited by a thin, flat gaseous disc with an outer radius of $\simeq 1.2R_\odot$. This outer limit corresponds to the Roche limit of large ($d \gtrsim 1$ km) solid bodies and therefore the radius at which they are destroyed by tidal gravitational forces [Davidsson, 1999].

Brinkworth et al. [2009] confirmed the presence of a dusty component to the gaseous disc at SDSS J1228+1040 using *Spitzer*. At the inner edge, the disc has an effective temperature of $\sim 1,700$ K, consistent with the temperature that even the most refractory elements sublimate [Lodders, 2003].

Four more white dwarfs (two DBZ; SDSS J0738+1835: Dufour et al. 2012 and SDSS J0845+2257: Gänsicke et al. 2008, and two DAZ; SDSS J0959−0200: Farihi et al. 2012 and SDSS J1043+0855: Gänsicke et al. 2007) have subsequently been shown to have a gaseous disc. All of which also show metal-pollution and have a dusty component to the disc [Melis et al., 2010; Debes et al., 2011]. The dust disc around SDSS J1043+0855, however, was not confirmed by the analysis of Brinkworth et al. [2012]. Not observing the dust disc may imply that the disc is edge-on or that almost all the dust has accreted and we are seeing the final stages of the accretion event.

1.2.2.4 Remnants of planetary systems

In numerous cases, the origin of the metal pollutants in white dwarf atmospheres (Section 1.2.2.1) has been unambiguously identified as circumstellar dust (Section 1.2.2.2), primarily via *Spitzer* studies [e.g. Reach et al., 2005; Jura et al., 2009a; Brinkworth et al., 2009; Farihi et al., 2009, 2010b; Girven et al., 2012a; Xu & Jura, 2012], and

gas (Section 1.2.2.3). It seems that the three are intimately linked, and if one is present, all must have been present, at some level, and at some time in the past evolution.

The favoured and successful model of a tidally destroyed asteroid [Graham et al., 1990a; Jura, 2003] is consistent with the observed disc properties [Gänsicke et al., 2006b; Farihi et al., 2010a; Melis et al., 2011; Debes et al., 2011], the subsequent photospheric pollution, and the composition of both the orbiting and accreted material [e.g. Klein et al., 2011; Zuckerman et al., 2011]. Such a catastrophic destruction is most readily achieved by a remnant planetary system with at least one major planet [Debes & Sigurdsson, 2002b] that perturbs a belt of smaller objects. Thus, white dwarfs with discs and/or photospheric metals may harbor complex planetary systems.

1.2.2.5 Disk lifetimes

Although metal-pollution, gaseous and dusty discs are all bi-products of a single (or multiple) comet or asteroid disruption, some of the most metal-polluted white dwarfs show no evidence of an infrared excess, consistent with no disc [e.g. Farihi et al., 2009; Klein et al., 2011; Girven et al., 2012a]. Similarly, only a handful of white dwarfs with dusty discs have detectable gas discs (see Section 1.2.2.3), even though gas discs are predicted to be formed from collisions in the disc and sublimation of the inner disc edge. This provides some important information about the relative durations of each of the three channels: metal-pollution, gaseous and dusty discs.

The typical lifetime of dust discs is a significant uncertainty [Jura, 2008; Kilic et al., 2008], yet this is an important indicator of the mass of the parent body (or bodies) that generated the observed debris. There are numerous stars with cooling ages greater than 1 Gyr that exhibit atmospheric metal pollution, such as the prototype system, vMa 2 [van Maanen, 1917; Greenstein, 1956; Weidemann, 1960]. Koester et al. [2011] recently identified 26 white dwarfs with temperatures $5000 - 8000\,\mathrm{K}$ and $10^{20} - 10^{23}\,\mathrm{g}$ of accreted metals in their convection zones. These stars have typical cooling ages of $1 - 6\,\mathrm{Gyr}$ (assuming the canonical surface gravity; $\log g = 8$), but must have accreted material recently, within the past few million years. Interestingly, even though there are many with metal pollution, there is only a single (and anomalous) infrared excess around white dwarfs with cooling ages older than 1 Gyr [G166-58; Farihi et al., 2008b], so this may be viewed as an upper limit for typical disc lifetimes.

From theoretical considerations, Rafikov [2011a] finds that the lifetimes of the compact dust discs around white dwarfs should be of the order $10^6\,\mathrm{yr}$, when

dominated by Poynting-Robertson drag (the spiralling in of dust particles due to interaction with the emission from the host star). However, Poynting-Robertson drag cannot produce the highest (average) accretion rates inferred for the helium atmosphere stars (DB) with metals, which are on the order of $10^{10}-10^{11}\,\mathrm{g\,s^{-1}}$ [Farihi et al., 2010b]. Xu & Jura [2012] extend the estimates of Rafikov [2011a] and find a factor of five higher accretion rates, but this still does not lead to high enough rates. To produce higher accretion rates, gas resulting from sublimated dust, produced at the inner edge of the dust disc [Jura, 2008; Farihi et al., 2009], efficiently transports angular momentum outward and fuels a more rapid in-fall of material. Rafikov [2011b] calculates that the lifetime of a $10^{22}\,\mathrm{g}$ disc is then reduced to several 10^4 yr. A strong coupling between the gas and the dust, such as even a slight eccentricity of the gas disc, would substantially increase the likelyhood of runaway accretion [Metzger et al., 2012].

In Chapter 6, we study the infrared excess that is the trademark of warm dust orbiting within the tidal disruption radius around three white dwarfs; $\mathrm{HE\,0110-5630}$, $\mathrm{GD\,61}$, and $\mathrm{HE\,1349-2305}$, and use these results to produce a statistical estimate of a typical disc lifetime.

1.2.3 Large samples of white dwarf stars

Large samples of white dwarfs are particularly useful in many studies, for example constraining the luminosity function, which in turn can be used to determine the ages of many Galactic populations [e.g. Winget et al., 1987; Oswalt et al., 1996; De Gennaro et al., 2008]. The low luminosity of white dwarfs also makes them ideal targets for searches of low-mass companions, such as pioneered by Probst & O' Connell [1982]. For main-sequence binaries, the companion mass distribution is thought to drop near the low-mass end ($\sim 0.1\mathrm{M_\odot}$), and the fraction of FGK stars with substellar companions estimated from radial velocity surveys is $\lesssim 1\%$ [e.g. Marcy & Butler, 2000; Grether & Lineweaver, 2006], though Metchev & Hillenbrand [2009] suggest that substellar companions are more frequent at larger orbital separations. Because white dwarfs are the progeny of main-sequence stars with masses of up to $8\,\mathrm{M_\odot}$, studies of white dwarf binaries can probe the companion mass function over a wide range of (initial) host star masses. Currently, only four white dwarfs are confirmed to have (non-interacting) substellar companions (Becklin & Zuckerman, 1988; Farihi & Christopher, 2004; Maxted et al., 2006; Steele et al., 2009, but see Luhman et al., 2011 for a very low-mass candidate), and the fraction of white dwarfs with brown dwarf companions appears to be consistent with the low number found around FGK stars [Farihi et al., 2005; Hoard et al., 2007].

Rebassa-Mansergas et al. [2010] used the SDSS spectroscopic database to identify white dwarf plus main-sequence binaries. We use the SDSS photometric data, in Chapter 4, to identify hydrogen-rich white dwarfs, and then determine those with infrared flux excess, consistent with late-M and later-type companions, in the UKIRT Infrared Deep Sky Survey (UKIDSS) in Chapter 5.

1.2.4 Magnetic fields

It has been shown that a significant number, possibly $\sim 10-15\%$, of all white dwarfs may be magnetic with fields $\gtrsim 1 \times 10^6$ G [Liebert et al., 2003; Wickramasinghe & Ferrario, 2005]. The SDSS has been a rich source for finding new magnetic white dwarfs (MWD) (Gänsicke et al., 2002; Schmidt et al., 2003; Vanlandingham et al., 2005, and Külebi et al., 2009), bringing the number of known magnetic white dwarfs to > 200. However, the formation mechanism for magnetic white dwarfs is still under debate, with the two favoured progenitors being either magnetic Ap/Bp (perculiar-A / perculiar-B) stars [Moss, 1989] or close binaries that evolved, and potentially merged, through a common envelope [Tout & Pringle, 1992].

In the Ap/Bp scenario, the magnetic white dwarfs field is a relic of the large-scale magnetic fields of their intermediate mass progenitor stars. These in turn are fossils of the magnetic field in star formation [Moss, 1989]. Assuming flux conservation, the surface fields observed in Ap/Bp stars ($\sim 10^2 - 2 \times 10^4$ G) are sufficient to explain the range of fields found in magnetic white dwarfs. However, population synthesis suggest that only 40% of the known magnetic white dwarfs may have descended from Ap/Bp stars [Wickramasinghe & Ferrario, 2005].

A clue to a possible link between binary evolution and strongly magnetic white dwarfs came from the *absence* of detached magnetic white dwarf plus M-dwarf binaries, i.e. magnetic pre-CVs [Liebert et al., 2005b], which could not be explained within the Ap/Bp scenario. Differential rotation and convection are predicted to be key to a magnetic dynamo [Tout & Pringle, 1992], both of which are prevalent in common envelope (CE) evolution. Tout et al. [2008] recently revisited the CE scenario for the formation of magnetic white dwarfs, and proposed that if a strong field is generated during a CE, the two possible outcomes are either a merger, leading to a single massive, strongly magnetic white dwarf, or a short-period magnetic white dwarf plus low-mass star binary, that rapidly evolve into a mass-transferring CV state.

A key for testing which of the hypotheses is correct would be a set of wide common proper motion (CPM) magnetic white dwarfs. For the magnetic white dwarf in a wide pair to have formed from a merger or close binary, the system

would have to have formed with three stars, an unlikely scenario. Large quantities of wide common proper motion (CPM) magnetic white dwarfs would favour the Ap/Bp scenario. In Chapter 8, we report the discovery of one such system: SDSS J130033.48+590407.0 (henceforth SDSS J1300+5904).

1.3   Subdwarfs

Subluminous blue stars were first discovered by Humason & Zwicky [1947] in a photometric survey of the North Galactic Pole region. Green et al. [1986] found many more hot subdwarfs in the Palomar-Green (PG) survey, to the extent that they were the dominant species among faint ($B \lesssim 16.1$) blue objects. In the PG survey they outnumber white dwarfs, and thus are prevalent enough to account for the ultraviolet upturn in early-type galaxies [Brown et al., 1997].

Hot subdwarf stars are either core helium-burning stars at the end of the horizontal branch (HB; BHB and EHB in Figure 1.1) or have evolved even beyond that stage [see Figure 1.1; Heber et al., 1984; Heber, 1986] [2]. Their high temperatures (blue colours), but relatively low luminosities clearly distinguishes them from main-sequence stars. They represent the degenerate core of a post-main-sequence star, interrupted from its normal evolution, following the asymptotic giant branch (AGB) route, into a white dwarf star.

1.3.1   Subdwarf structure and atmospheres

Subdwarfs are thought to have a relatively well defined mass around a canonical value of $0.46\,M_\odot$ [Saffer et al., 1994; Han et al., 2003; Politano et al., 2008] and radii of a few tenths of a solar radius. They have very thin layers of hydrogen ($M_{env} < 0.01 M_\odot$) on the surface, which are not able to support shell burning after helium-core exhaustion.

Hot subdwarf stars are split into two catagories; B-type and O-type subdwarfs (sdB and sdO, respectively). On the one hand, B-type subdwarfs are core helium-burning stars at the blue end of the horizontal branch. They differ from ordinary horizontal branch stars because their hydrogen envelopes are too thin to sustain hydrogen burning. They therefore evolve directly into white dwarf stars, avoiding the AGB. The spectra of sdB stars show strong hydrogen absorption and

---

[2]Hot subdwarfs have little in common with traditional cool subdwarfs (see Figure 1.1), other than their small radii. Cool subdwarfs are core helium burning stars, just like main-sequence stars (see Section 1.1). Their smaller radii (and therefore lower luminosities) are explained by low metallicities. This decreases the opacity of the atmosphere, which reduces the radiation pressure, resulting in a smaller, hotter star for its mass.
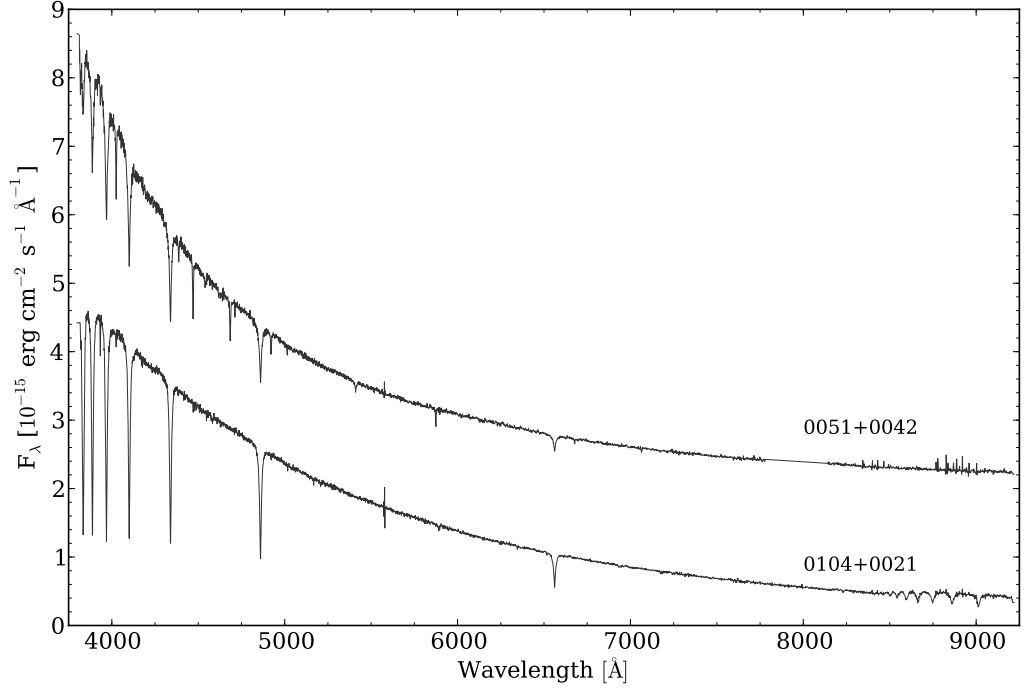
Figure 1.4: Example optical (SDSS) spectra of an sdB and sdO subdwarf star (SDSS J0104+0021 and SDSS J0051+0042, respectively). SDSS J0051+0042 is offset by $+2 \times 10^{-15}$ flux units for clarity (see Chapter 7).

they are generally helium-poor. On the other hand, O-type subdwarfs are a mixture of post red-giant branch, post-HB, and post-AGB stars, often showing helium-rich spectra. Example spectra of both an sdB and sdO star are shown in Figure 1.4. A detailed review on this and the field as a whole is given by Heber [2009].

1.3.2 Subdwarf formation

Formation scenarios of subdwarfs are still significantly uncertain, and invoke either fine-tuned single star evolution or rely on close-binary star interactions. In the *late hot-flasher scenario*, a low-mass ($\sim 0.8 \, M_{\odot}$) star undergoes the He core-flash at the tip of the red-giant branch. However, if sufficient mass is lost on the red giant branch, the star can experience the He core-flash whilst descending the white dwarf cooling track [Castellani & Castellani, 1993]. Such a star would end up close to the He main sequence, at the very hot end of the extreme horizontal branch [D'Cruz et al., 1996]. Alternatively, the formation involves one or two phases of common-envelope evolution and/or stable Roche-lobe overflow (RLOF) within a close binary system [Mengel et al., 1976]. Binary evolution could even take the route of merging

15

two helium white dwarfs followed by He ignition [Webbink, 1984; Iben, 1990; Saio & Jeffery, 2000]. All formation scenarios require substantial mass loss before the start of core He-burning, however the specific physical mechanisms for this are still unclear.

1.3.3 Binarity

Since the first quantitative estimates of the contribution of different binary channels to the population of subdwarf stars [Tutukov & Yungelson, 1990], it has been shown that a large fraction of subdwarfs do reside in binaries. In the PG sample of subdwarfs, a significant fraction show composite colours or spectra (at least 20 per cent; Ferguson et al. 1984, $\sim 54-66$ per cent; Allard et al. 1994). Radial velocity surveys [e.g. Maxted et al., 2001; Morales-Rueda et al., 2003] confirm a fraction of binaries as high as two-thirds. High-resolution optical spectra from the ESO Supernova Ia Progenitor Survey [SPY; Napiwotzki et al., 2001] led to binary star fractions of 30-40 per cent [Napiwotzki et al., 2004; Lisker et al., 2005]. Copperwheat et al. [2011] estimate that the binary fraction in the sdB population is somewhat higher at 46 - 56 per cent. This is only a lower limit since the radial velocity variations that Copperwheat et al. [2011] search for would be difficult to detect in long period systems.

Other searches have used near-infrared photometry [e.g. Thejll et al., 1995; Ulla & Thejll, 1998; Williams et al., 2001] or photometric catalogues such as the Two Micron All Sky Survey [2MASS; Skrutskie et al., 2006] to find subdwarfs with companions [e.g. Stark & Wade, 2003; Green et al., 2006; Vennes et al., 2011a]. Ca II absorption can also be used to infer the presence of a cooler companion star [Jeffery & Pollacco, 1998]. The majority of companions found to date have either been M-type stars or white dwarfs [Heber, 2009]. However, some F, G and K-type companions to subdwarfs have been seen in studies such as Aznar Cuadrado & Jeffery [2001], Reed & Stiening [2004], Lisker et al. [2005], Wade et al. [2006], Stark & Wade [2006], Wade et al. [2009], Moni Bidin & Piotto [2010] and Geier et al. [MUCHFUSS; 2011b]. Depending on the study, and its corresponding selection effects, the companions to subdwarfs have been shown to be mostly main-sequence stars [e.g. Aznar Cuadrado & Jeffery, 2001] and occasional giant or subgiant companions (e.g. Allard et al. 1994 and BD-7°5977; Heber et al. 2002).

1.3.4 Population synthesis

Many of the previous surveys have been biased by selection effects and inhomogeneous data sets. Han et al. [2003] argued that a large number of sdB stars may be missing from existing samples. Early-type main–sequence stars of spectral type A and earlier would outshine a subdwarf at optical wavelengths. F to K-type companions on the other hand, have generally been avoided because the spectral analysis of the composite spectrum becomes difficult [Heber, 2009]. Systems with earlier type companions are actually predicted, in some cases, to be far more common than the M-type companions that have primarily been found so far. In the population synthesis study by Han et al. [2003], subdwarfs with early type companions are produced in the very efficient first stable RLOF channel and are expected to be in systems with subdwarfs as cool as $15,000\,\mathrm{K}$. Clausen et al. [2012], however, do not find the same frequency of F-type companions. Identifying this predicted population, and determining their relative contribution to the total subdwarf population would offer important constraints on the prior binary evolution that led to their formation. In addition, the distribution of orbital periods and subdwarf temperatures of such a sample will provide direct constraints on key parameters that underpin subdwarf population synthesis models [Clausen et al., 2012].

In Chapter 7, we take advantage of recent large-area ultraviolet, optical and infrared photometric surveys (see Chapter 2) to search for new composite systems comprised of subdwarfs plus main–sequence star companions of mid-M-type and earlier. Cuts in colour-colour space (see Section 3.2) are employed to separate these objects from possible contaminants. We also develop a fitting technique to simultaneously determine the subdwarf and companion effective temperatures from the photometric magnitudes (see Section 3.4). This permits the recovery of composite systems with much earlier type companions than seen in previous studies. Furthermore, we are sensitive to a wide range of separations and binary periods in that we only limit ourselves to spatially unresolved systems. Finally, we discuss the distribution of objects in effective temperature and distance to the system.

Chapter 2

Digital sky surveys, imaging and instruments

The last decade of astronomy has been the era of the large scale digital sky survey. These are generally carried out by telescopes specifically commissioned for the purpose of scanning vast regions of the sky in multi-colour, multi-epoch, photometric and/or spectroscopic observations. Each telescope has filters focused on a region in wavelength, anywhere from the ultraviolet to the infrared. Some, such as the Sloan Digital Sky Survey, also have dedicated follow-up spectroscopic instruments incorporated in the survey. A massive amount of data is produced from these surveys in the form of catalogues and 'Data Releases' (DR). Even though many surveys were conceived with a few primary goals in mind, there are inevitably a host of other uses found. Outlined below, and in Table 2.1, are a number of significant surveys that were made use of in this work.

Table 2.1: Properties of the six key surveys used throughout this work. The faint limit is a 5σ point source detection limit for all surveys apart from 2MASS, which quotes a 10σ limit.

Survey	Data Release	Sky Coverage	Number of Sources [10^6]	Filters	Central Wavelength [Å]	Faint Limit
GALEX AIS	6	$25000\,\mathrm{deg}^2$	225	m_{FUV}	1528	$m_{AB} \lesssim 20.5$
				m_{NUV}	2271	$m_{AB} \lesssim 20.5$
CMC	14	Dec $= -30$ to $50°$	96	r_{CMC}	6211	$r_{CMC} \lesssim 17.0$
SDSS	7	$11500\,\mathrm{deg}^2$	357	u	3539	$u \lesssim 22.3$
				g	4741	$g \lesssim 23.3$
				r	6211	$r \lesssim 23.1$
				i	7584	$i \lesssim 22.3$
				z	8925	$z \lesssim 20.8$
2MASS	ASDR	All Sky	472	J	12350	$J \lesssim 15.8$
				H	16620	$H \lesssim 15.1$
				K_s	21590	$K_s \lesssim 14.3$
UKIDSS LAS	8 & 9	$4028\,\mathrm{deg}^2$	83	Y	10310	$Y \lesssim 20.2$
				J	12480	$J \lesssim 19.6$
				H	16130	$H \lesssim 18.8$
				K	22010	$K \lesssim 18.2$
WISE	PDR	$20000\,\mathrm{deg}^2$	257	$W1$	33680	$f_\nu(W1) \gtrsim 0.08\,\mathrm{mJy}$
				$W2$	46180	$f_\nu(W2) \gtrsim 0.10\,\mathrm{mJy}$
				$W3$	120820	$f_\nu(W3) \gtrsim 0.80\,\mathrm{mJy}$
				$W4$	221940	$f_\nu(W4) \gtrsim 5.00\,\mathrm{mJy}$

2.1 Ultraviolet

2.1.1 GALEX

The Galaxy Evolution Explorer (GALEX) telescope was launched on a Pegasus rocket in April 2003. It has an effective area of $20 - 50\,\mathrm{cm}^2$ and a field of view of $1°\!.2$. The primary focus of the telescope was to observe galaxies in the ultraviolet; to answer how galaxies evolve and change over time and to study star formation in these objects. One of the surveys the GALEX telescope performed was an extra-galactic ultraviolet All-sky Imaging Survey [AIS; Martin et al., 2005]. Observations were made in two ultraviolet band passes, $\mathrm{m_{FUV}}$ and $\mathrm{m_{NUV}}$, ranging from $1350 - 1750$ and $1750 - 2750\,\text{Å}$, respectively (see Figure 2.1), down to a limiting magnitude of $\mathrm{m_{AB}} \simeq 20.5$. Data Release 6 of the GALEX AIS was released in 2010, which now covers two thirds of the sky and has significant improvements in the calibration and data reduction over previous versions. Access to the GALEX database is provided by the Multi-Mission archive at the Space Telescope Science Institute (MAST) and via CasJobs, provided by the Sloan Digital Sky Survey Collaboration. Predefined cross-matching tables between the Sloan Digital Sky Survey (discussed in Section 2.2.2) and GALEX are provided in CasJobs [Budavári et al., 2009]. GALEX is particularly suited to search for (hot) white dwarfs and subdwarfs because both are blue and therefore bright in the ultraviolet.

2.2 Optical

2.2.1 CMC

The Carlsberg Meridian Telescope (CMT) has a 2060×2048 CCD camera (pixel size $0''\!.7$) with a Sloan r filter (see Figure 2.3) operating in drift scan mode. The CMT maps the sky from La Palma (Spain) covering the declination range $-30°$ to $+50°$ with a magnitude range of $r_{\mathrm{CMC}} = 9 - 17$. The Carlsberg Meridian Catalogue, Number 14 [Version 1.0: CMC; Copenhagen University Obs. et al., 2006] is an astrometric and photometric catalogue of 95.9 million stars. The photometric catalogue, along with providing a Sloan type r filter, is also cross-matched with the Two Micron All Sky Survey (within $2''$; described in detail in Section 2.3.1) to provide some colour information. More information on both the telescope and the survey can be found in Evans [2001].
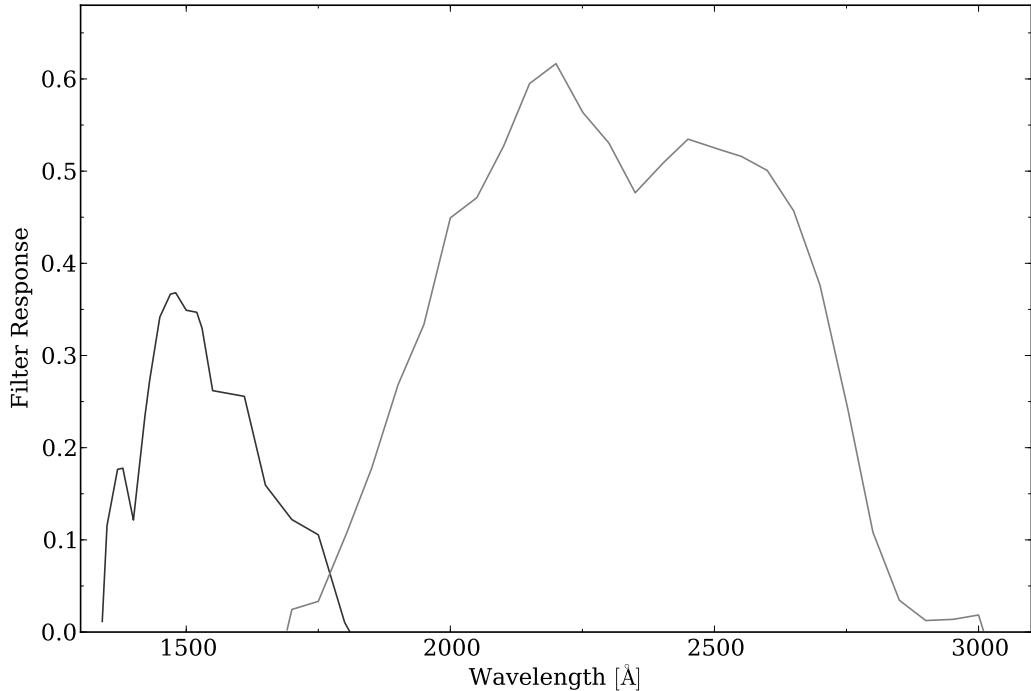
Figure 2.1: Left to right, GALEX m_{FUV} and m_{NUV}-band filter response curves.

2.2.2 SDSS

The Sloan Digital Sky Survey (SDSS) is currently the deepest large-area optical survey that is publicly available. It makes use of a 2.5m wide-field altitude-azimuth telescope at Apache Point Observatory, New Mexico. The telescope has a $3°$ field of view and observations are recorded by a large-format mosaic of 30 2048×2048 Tektronix CCD cameras in five filters (u, g, r, i and z-bands). The total survey is split into two main areas: the northern and southern Galactic cap (shown in Figure 2.2). The northern Galactic cap is centered on $\alpha = 12^h 20^m$, $\delta = +32.5°$, covers $\sim 10,000$ contiguous deg^2 and was chosen to minimise the Galactic extinction. The southern Galactic cap is separated into three stripes, one centered on the celestial equator ($\alpha = 20^h 07^m$, $\delta = 0°$), one north and one south of the equator.

The SDSS is a photometric and spectroscopic survey that is primarily focused on the identification and study of galaxies [e.g. Strauss et al., 2002] and quasars [e.g. Adelman-McCarthy et al., 2006]. The first public release of the SDSS was the Early Data Release in 2001 [EDR; Stoughton et al., 2002], technical details for which can be found in York et al. [2000]. Further Data Releases and the corresponding information can be found in Abazajian et al. [2003, 2004, 2005] and Adelman-McCarthy et al. [2006, 2007, 2008]. Throughout the majority of this work, we have made use
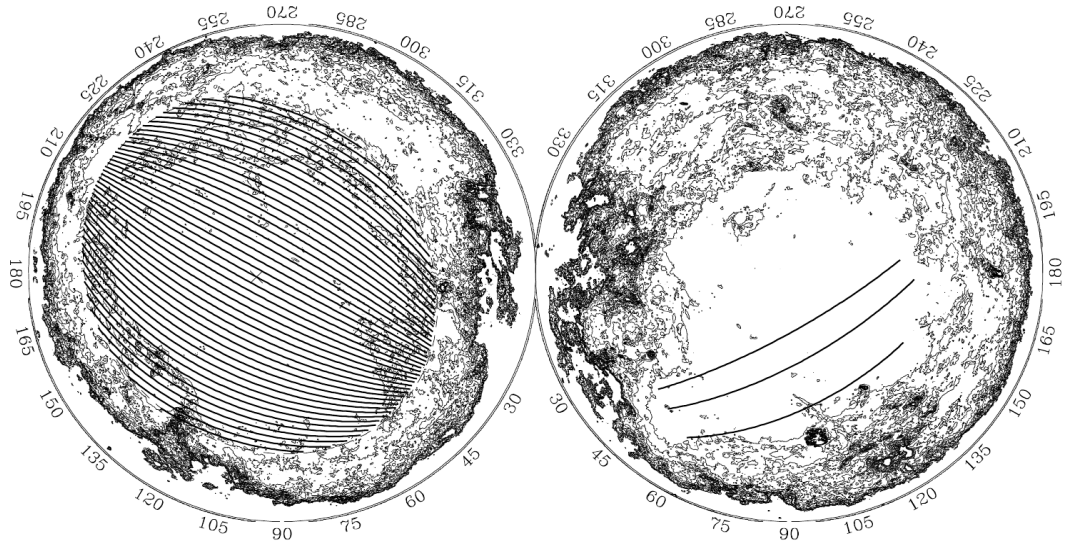
Figure 2.2: Northern and southern Galactic cap areas for the SDSS in Galactic coordinates. The solid black lines represent the SDSS imaging area, whilst the contours map extinction. Taken from York et al. [2000].

of the SDSS Data Release seven (DR7, Abazajian et al. 2009), which represents the final Data Release of the SDSS II project, including the low-latitude Sloan Extension for Galactic Understanding and Exploration [SEGUE; Yanny et al., 2009]. SDSS DR7 provides $ugriz$ photometry for 357 million objects, covering 11500 deg^2, approximately one-quarter of the celestial sphere, as well as follow-up spectroscopy for 1.44 million galaxies, quasars, and stars. The SDSS is an ongoing operation which has been extended greatly since its conception. Following on from the SDSS and SDSS-II discussed herein, SDSS-III has begun to be released, along with the BOSS, SEGUE-2, APOGEE and MARVELS sub-surveys.

The SDSS imaging is obtained in five optical photometric bands: u, g, r, i and z (filter response curves shown in Figure 2.3). The detection limits in $1''$ of seeing are 22.3, 23.3, 23.1, 22.3 and 20.8 mag, respectively, on the AB system, and assuming an airmass of 1.4. The filters have effective wavelengths of 3560, 4680, 6180, 7500 and 8870Å, respectively. The photometric pipeline corrects for: CCD defects, calculated overscan, biases, sky, flat-field values and produces PSF magnitudes for all point sources. Mean errors are 0.03 mag at 20 mag, increasing to about 0.05 at 21 mag and to 0.12 at 22 mag for g, r and i-bands. For the less sensitive u and z-bands, errors increased to 0.05 at 20 mag and 0.12 at 21 mag.

The SDSS also provides a comprehensive follow-up spectroscopic program. Candidates for spectroscopy are chosen based on a series of cuts on their $ugriz$
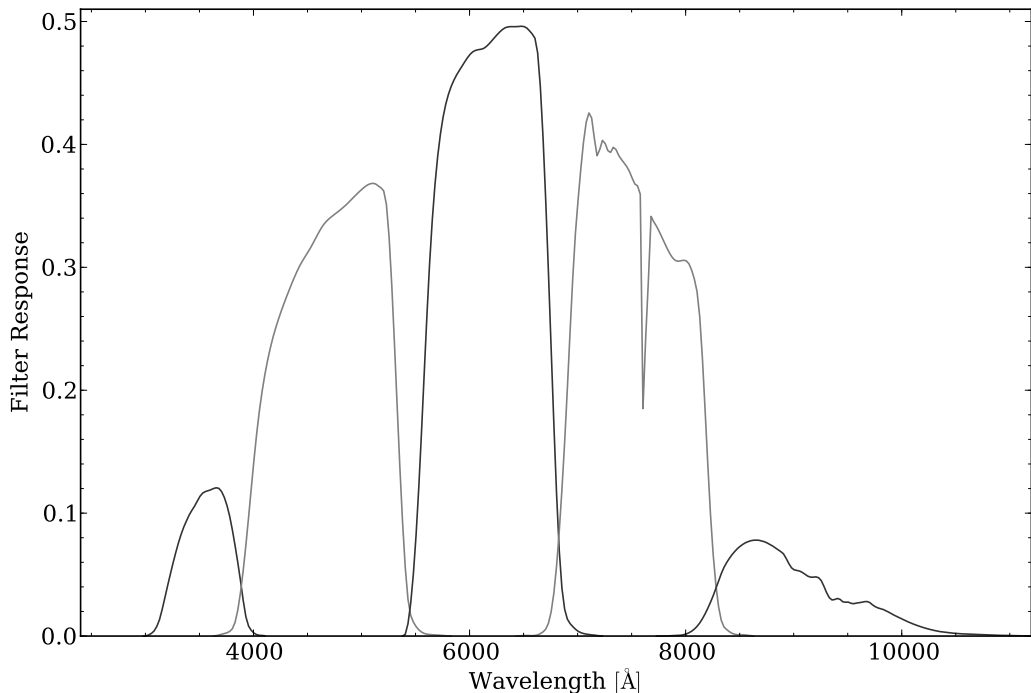
Figure 2.3: Left to right, SDSS u, g, r, i and z-band filter response curves. The curves include the quantum efficiency of the CCD at zero air mass.

colours [see Stoughton et al., 2002]. The focus was primarily on providing spectroscopy and photometry of all the quasars [Richards et al., 2002] and galaxies [Strauss et al., 2002] in the SDSS footprint. The spectrograph covers $3800 - 9200\text{Å}$ at $\lambda/\delta\lambda$ from 1850 to 2200. Each spectroscopic observation was taken using a custom made plate with holes drilled to allow the attachment of 640 fibres covering $\sim 7 \deg^2$. The holes were drilled at the positions of the SDSS photometry and then the spectroscopic fibres were plugged into the plate the day before the observations. A total of nine spectral plates were observed per night. Each spectrum is uniquely identified by their modified Julian date (MJD), spectroscopic plate and the fibre number. The total integration time for each spectra was $45 - 60$ minutes, split into ~ 15 minute exposures. The flux and wavelength-calibrated spectra were provided on a vacuum wavelength scale and corrected to the heliocentric restframe.

Data access to the archive of the SDSS survey is provided in three ways. Firstly, the Catalog Archive Server (CAS) contains the measured parameters for all the objects in the imaging and spectroscopic surveys. The SDSS Query Tool is a stand-alone application for providing queries to the CAS server. Secondly, the Data Archive Server (DAS) makes available all the raw and reduced data (corrected

frames, binned images, colour images, spectra). Finally, the SkyServer provides access to the data through a relational data base server using SQL.

An additional important resource within the SDSS are proper motion measurements. Data Release 7 incorporated substantial improvements in both the astrometric calibration, carried out against the UCAC2 catalogue [Zacharias et al., 2004], as well as an updated table of proper motions computed from the combined SDSS and USNO-B positions [Monet et al., 2003]. Statistical astrometric errors per coordinate for bright stars were reduced to approximately 45 mas, with systematic errors of less than 20 mas.

2.3 Near-infrared

2.3.1 2MASS

The Two Micron All Sky Survey [2MASS; Skrutskie et al., 2006] is a uniform all-sky near-infrared survey designed to, amongst a host of other things, probe the large-scale structure of the Milky Way and the local Universe and to search for rare, extremely red objects, such as brown dwarfs. 2MASS used two automated 1.3 m telescopes, one at Mt. Hopkins, AZ and one at CTIO, Chile. Both were equipped with a three channel camera, each channel consisting of a 256×256 array of HgCdTe detectors, capable of observing the sky simultaneously at J, H and K_s (1.25, 1.65 and 2.17 μm, respectively; see Figure 2.4), with a spatial resolution of about $4''$. Each filter was observed for 7.8 s such that a 1 mJy source would have a signal-to-noise ratio greater than 10 in each band. This corresponds to a 10σ point-source detection level of better than 15.8, 15.1 and 14.3 mag in the J, H and K_s-bands respectively. The 2MASS All-Sky Data Release (ASDR) includes 471 million sources in a Point Source Catalogue, and 1.6 million objects identified as being extended objects in the Extended Source Catalogue.

2.3.2 UKIDSS

The Wide Field Camera (WFCAM), mounted on the United Kingdom Infrared Telescope (UKIRT) in Hawaii, has four 2048×2048 Rockwell devices imaging an exposed solid angle of $0.21 \deg^2$, which leads to a pixel scale of $0.4''$. With this instrument, a set of five near-infrared surveys is being undertaken, collectively known as the UKIRT Infrared Deep Sky Survey [UKIDSS; Hewett et al., 2006; Lawrence et al., 2007]. UKIDSS began in May 2005 and will eventually survey 7500 $\deg^2$ of the Northern sky, entending over both high and low Galactic latitudes. It aims
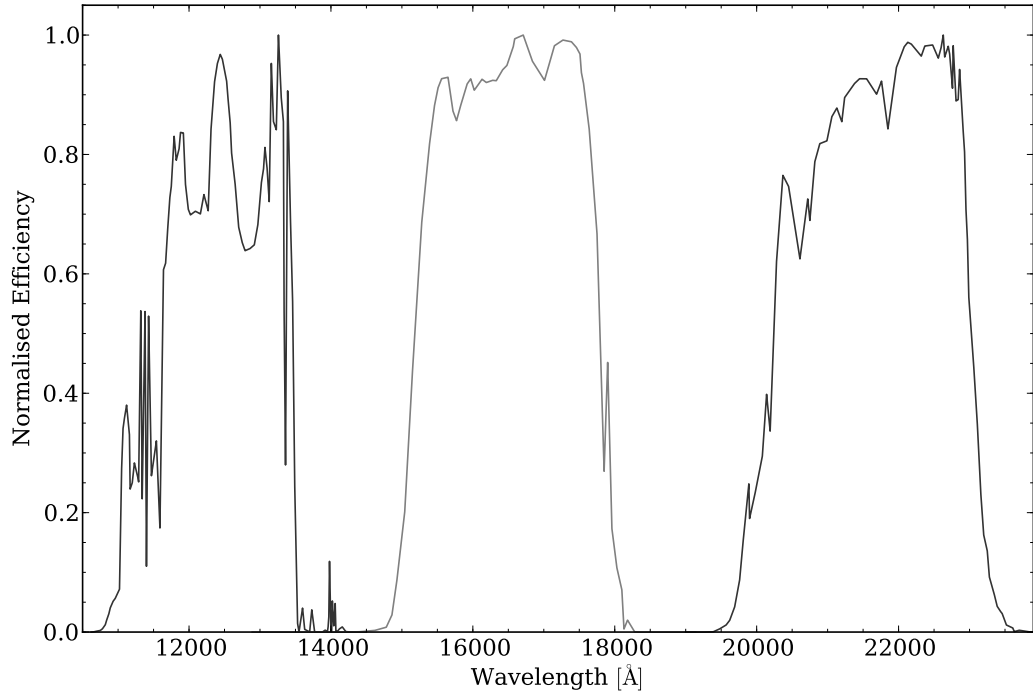
Figure 2.4: Left to right, 2MASS J, H and K_s-band filter response curves. The curves are normalised.

to become the successor to 2MASS, extending three magnitudes deeper in K, in the region it surveys. This project was designed to focus on the search for the coolest and nearest brown dwarfs, high-redshift dusty starburst galaxies, elliptical galaxies and galaxy clusters at redshifts $1 < z < 2$, and the highest-redshift quasars, at z=7. The Early Data Release was made public in 2006 [Dye et al., 2006] and subsequent releases continue to be made on six month or one year separations [e.g. Warren et al., 2007b,a]. The data are made available via the WFCAM science archive [Hambly et al., 2008]. One of the five sub-surveys, the Large Area Survey (LAS), aims to be the infrared counterpart to the SDSS. The UKIDSS LAS will eventually provide imaging over $4028 \, \text{degree}^2$ in four broad band colours, Y, J, H, and K (see Figure 2.5), with limiting (Vega) magnitudes of 20.2, 19.6, 18.8 and 18.2, respectively. This adds a significant increase in depth over 2MASS (Section 2.3.1).
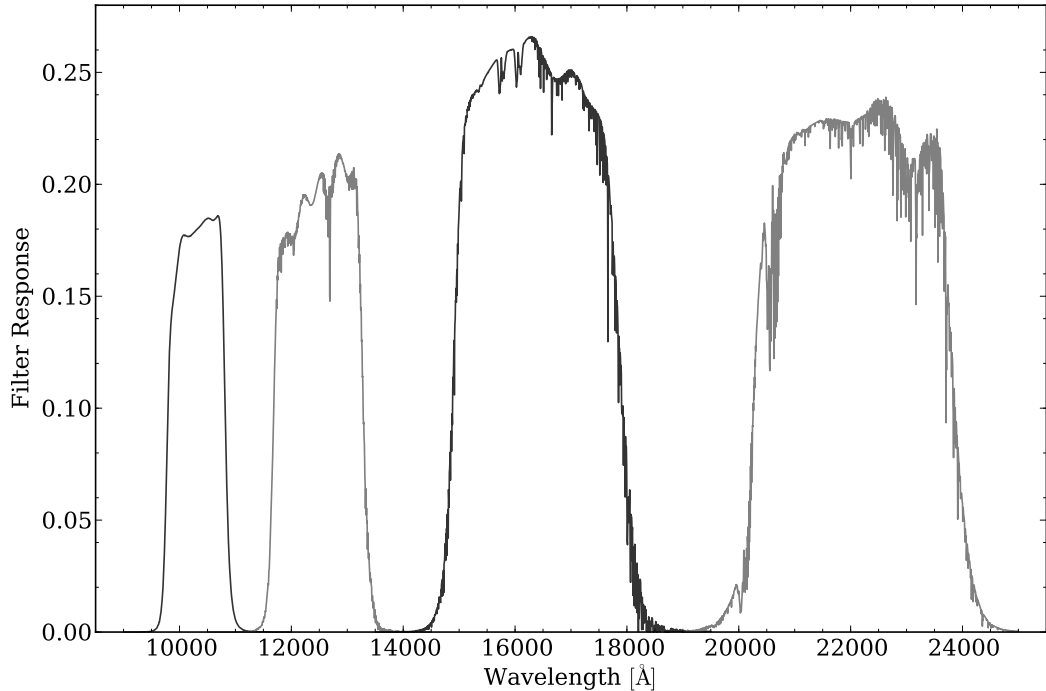
Figure 2.5: Left to right, UKIDSS Y, J, H and K_s-band filter response curves.

2.4 Far-infrared

2.4.1 WISE

The Wide-field Infrared Survey Explorer (WISE) is a NASA Medium-class Explorer mission designed to survey the entire sky in four infrared wavelengths, 3.4, 4.6, 12, and 22μm [see Figure 2.6; Wright et al., 2010]. WISE consists of a 40 cm telescope that images all four bands simultaneously every 11 s. It covers nearly every part of the sky a minimum of eight times, ensuring high source reliability, with more coverage at the ecliptic poles. Astrometric errors are less than 0.5 arcsec with respect to 2MASS. The preliminary estimated S/N = 5 point source sensitivity on the ecliptic is 0.08, 0.1, 0.8, and 5 mJy in the four bands [assuming eight exposures per band; Wright et al., 2010]. Sensitivity improves away from the ecliptic due to denser coverage and lower zodiacal background. Here we use the preliminary data release (PDR), covering half the sky and containing approximately 257 million objects.
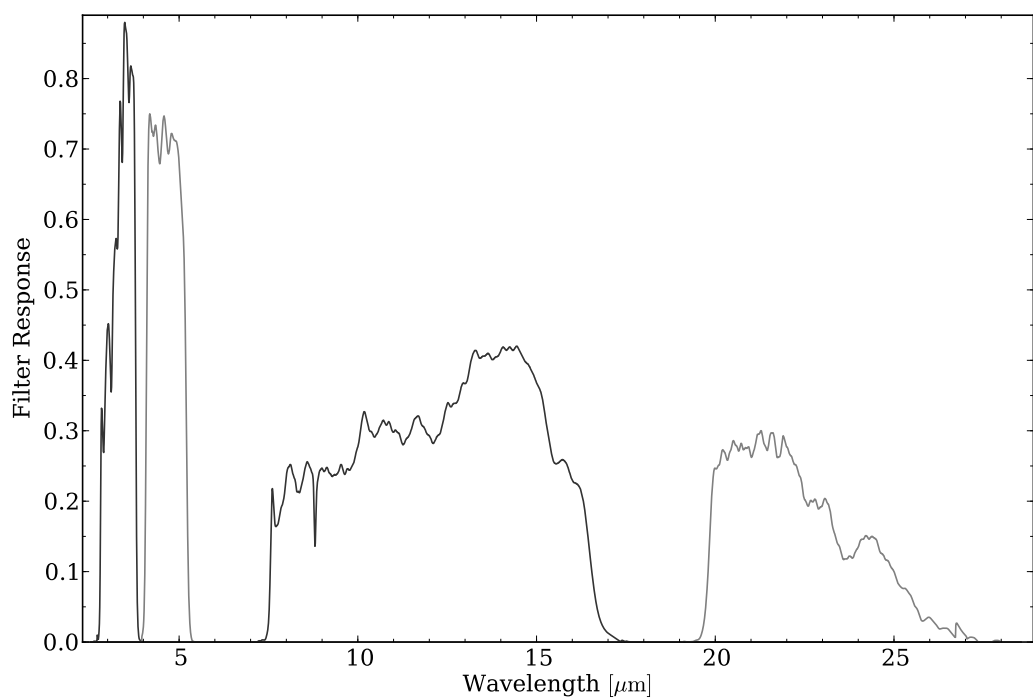
Figure 2.6: Left to right, WISE 3.4, 4.6, 12, and 22μm filter response curves.

Chapter 3

Methods

3.1 Cross-matching

Each survey in Chapter 2 has the potential to unlock extremely interesting science in its own right, however, when combined, the broad range of wavelength coverage is unrivaled for studying the full Spectral Energy Distribution (SED; flux density as a function of wavelength, e.g. Figure 1.2 and 3.4) of objects. The combination of two or more surveys is especially efficient at identifying and decomposing composite objects, as will be shown throughout this work.

The first stage in combining two surveys is to cross-match common objects by position matching. This is done by calculating the distance (r) between each object in spherical coordinates, according to:

$$r = \arccos(\ \cos(\pi/2 - \delta_1) * \cos(\pi/2 - \delta_2)$$
$$+ \sin(\pi/2 - \delta_1) * \sin(\pi/2 - \delta_2) * \cos(\alpha_1 - \alpha_2) \ ), \tag{3.1}$$

where both sets of Right Ascension (R.A.; α_1 and α_2) and declination (δ_1 and δ_2, where the subscripts 1 and 2 refer to the first and second survey, respectively), along with the resulting distance are given in radians. For each object in the first survey, a distance to each object in the second survey is calculated. If an object falls within a pre-defined search radius (r_{max}), this is considered a match, and the two sets of information can be combined. If multiple objects match within r_{max}, the closest object is usually chosen. There is a chance for false matches, however, this is relatively small because we generally look out of the Galactic plane (for example see Section 5.1). Using surveys focussed on the Galactic plane, false matches would be a significant problem.

This method can be relatively computationally intensive when millions of objects in the first survey are being compared to millions in the second survey. For large datasets, we pre-ordered the tables in declination. For an object at α_1 and δ_1, we therefore only needed to calculate the distance to objects with declinations within $\delta_1 - r_{max} \leq \delta_2 \leq \delta_1 + r_{max}$. Finding the first and last position in a ordered list which meets a requirement such as this is a relatively quick task, and the number of objects for which Equation 3.1 needs to be calculated is greatly reduced. The TOPCAT package is a commonly used utility for cross-matching [Taylor, 2005], however, we implemented our own routine using python.

3.2 Colour-colour diagrams

The large scale surveys described in Chapter 2 or a cross-match of multiple surveys (performed using Section 3.1) will each have detailed information for millions to hundreds of million of objects. How to select the few thousand objects we are interested in from the full survey is a challenging problem. In this work, we often take advantage of a diagnostic known as "colour-colour" diagrams to select a specific species of object.

A colour is defined as the difference between two photometric magnitudes and therefore measures the gradient of the SED of the object over a particular wavelength range. Colours are usually defined as the shorter wavelength minus the longer wavelength magnitude. For example, in the case of the SDSS (Section 2.2.2), the colours commonly defined are $(u - g)$, $(g - r)$, $(r - i)$ and $(i - z)$. Blue, hot objects will have negative colour and red, cool objects will be positive. Composite objects, containing two objects of different temperatures will show sharp changes between two colours.

The Hertzsprung-Russell diagram (e.g. Figure 1.1; showing luminosity vs effective temperature) is analogous to a colour-magnitude diagram (e.g. Figure 3.1). These commonly used diagrams show clear separations between different species of objects, however, even more information can be gained from colour-colour diagrams. A colour-colour diagram is a two dimensional plot with a colour index on both axes. An example set of colour-colour diagrams for the SDSS colours is shown in Figure 3.2. Objects with distinctly different SEDs seperate out in certain colour-colour diagrams and can therefore be selected using cuts in colour-colour space. Throughout this work, we use optimised colour-colour cuts to select interesting objects from contaminants (everything else).
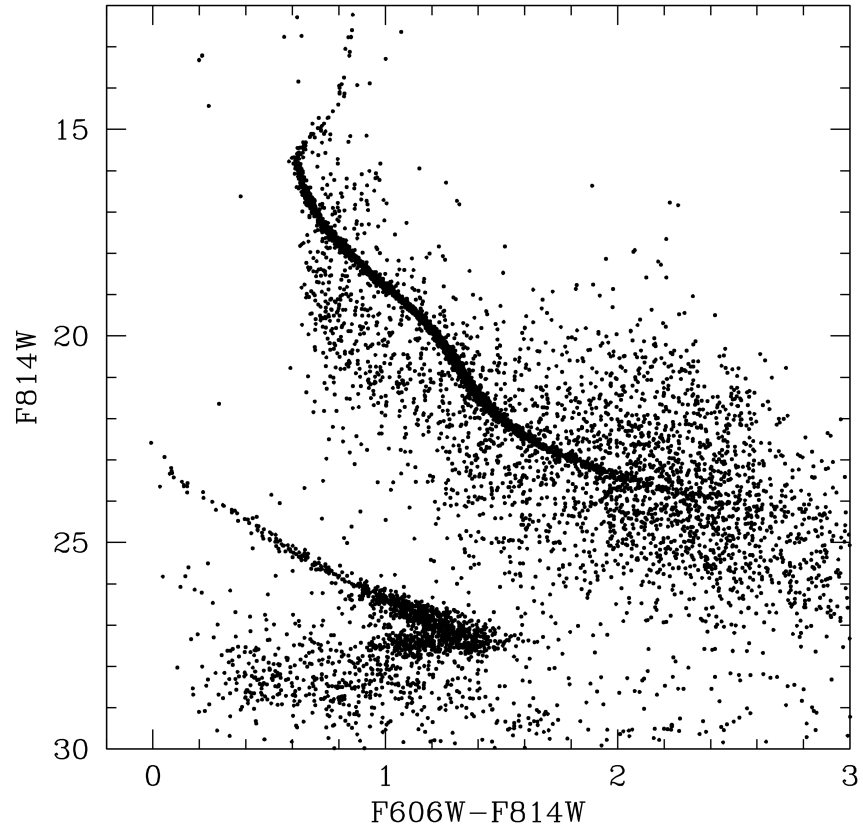
Figure 3.1: An example of colour-magnitude diagram for the globular cluster, NGC 6397, using the F606W and F814W, *HST* bands, taken from [Hansen et al., 2007]. Prominent features include a cluster main sequence, a clear main-sequence turnoff, and a clear white dwarf cooling sequence.
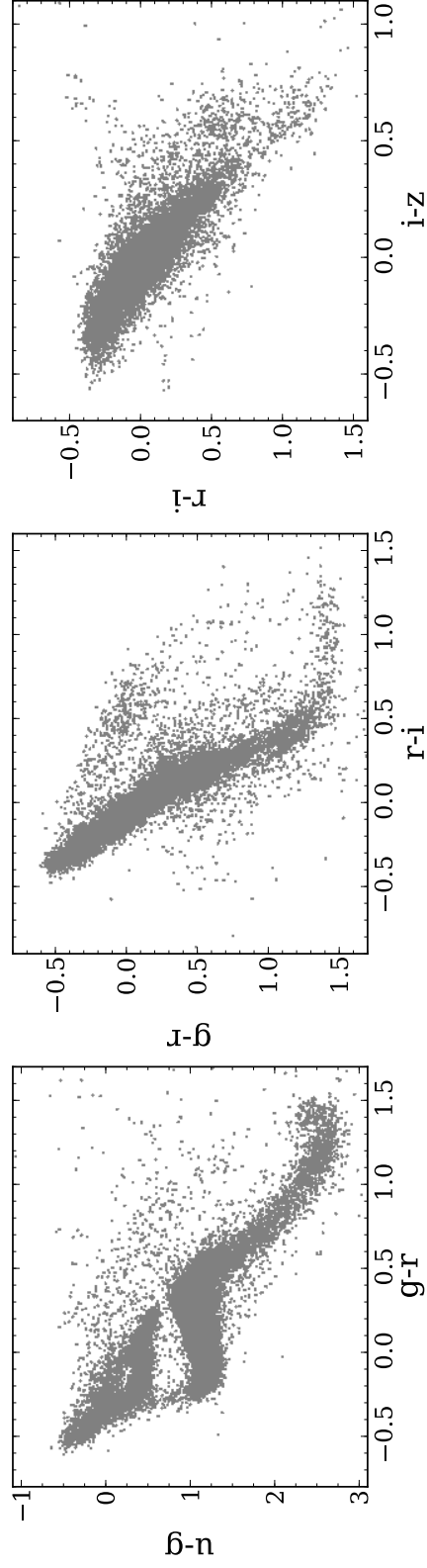
Figure 3.2: An example set of colour-colour diagrams for the *ugriz* SDSS colours. The objects plotted in gray are a random selection of stellar-like objects from the SDSS. The lower group in $(u - g, g - r)$ is populated by main-sequence stars, and the upper triangle is mostly white dwarfs along with other hot stars.

3.3 Completeness and efficiency

Given a set of cuts in colour-colour space, used to select a sample of objects, we aim to quantify the quality of the selection through two parameters; *completeness* and *efficiency*. To define completeness, we require a relatively unbiased sample of the target object. For example, in Chapter 4, we use Eisenstein et al.'s sample of DA white dwarfs. Although subject to the biases of the SDSS spectroscopic selection criteria, Eisenstein et al. [2006] analysed all the spectra in the colour-colour region we target, and therefore should be an otherwise unbiased sample of DA white dwarfs above $T_{eff} = 8,000\,K$ and complete within SDSS down to $g < 19$. Given an unbiased sample, completeness is then defined as the fraction of the sample recovered by our constraints. The efficiency of the selection is simply defined at the ratio of target objects to contaminants. In Chapter 4, we make use of the SDSS spectroscopic follow-up for classifying targets and contaminants. Using these two parameters, one can optimise the selection criteria for the purpose, whether it be maximum completeness, efficiency or a compromise between the two.

3.4 SED modelling and fitting

To predict the location of a group of objects on a colour-colour diagram, we use synthetic stellar models to calculate a set of model fluxes, magnitudes and colours. We can also predict the location of composite objects by summing multiple model components. This is key when designing colour cuts to select a specific group of objects. After the group has been selected, the models can also be used to estimate stellar parameters by χ^2 fitting (discussed further in Section 3.4.5). In the following sections, we introduce the various stellar model grids used throughout this work.

3.4.1 White dwarf models

A grid of synthetic DA white dwarf spectra were calculated with the model atmosphere code described by Koester [2010] and using the latest line profiles of Tremblay & Bergeron [2009]. These cover effective temperature, $T_{eff} = 6,000 - 100,000K$ in 131 steps nearly equidistant in $\log(T_{eff})$, and surface gravity, $\log(g) = 5.0 - 9.5$ in steps of $0.25\,dex$. The white dwarf models cover the range $1,150 - 25,000\,\text{Å}$ in wavelength.
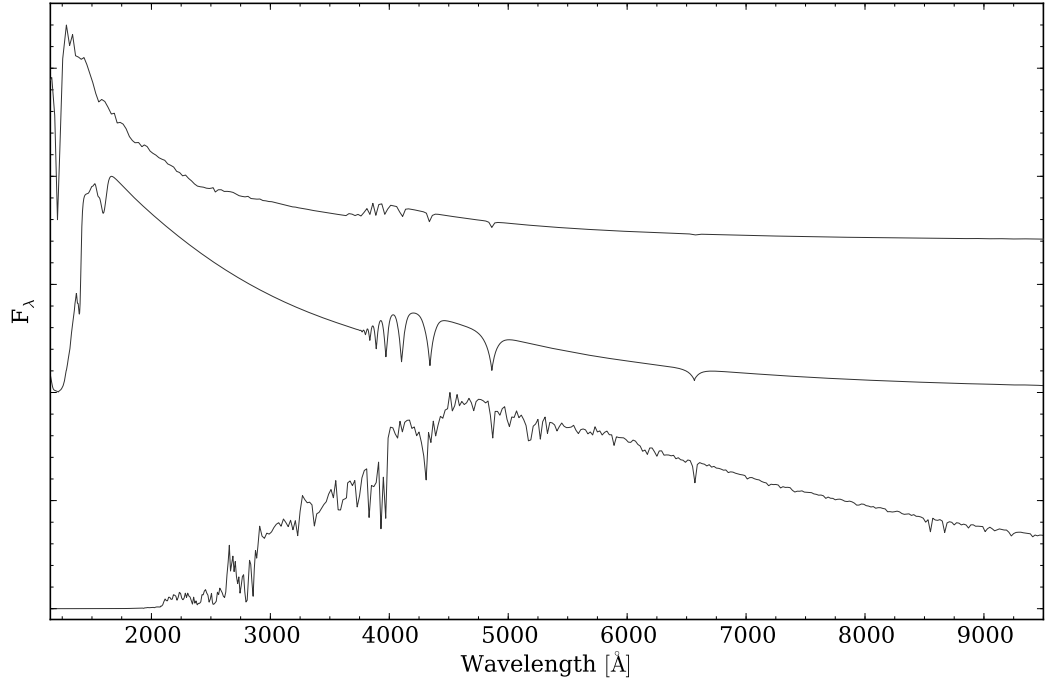
Figure 3.3: Example model SEDs of a $15,000\,\mathrm{K}$ sdB (top), $12,000\,\mathrm{K}$ DA white dwarf (middle) and $6,000\,\mathrm{K}$ main sequence star (bottom) from Sections 3.4.2, 3.4.1 and 3.4.3, respectively. The fluxes are scaled and offset arbitrarily for clarity.

3.4.2 Subdwarf models

The sdB spectra were calculated using the model atmosphere code described by Heber et al. [2000], covering $200 - 200,000\,\text{Å}$ in wavelength and $T_{\mathrm{eff}} = 11,000 - 40,000\,\mathrm{K}$ in steps of $1,000\,\mathrm{K}$. The corresponding surface gravities were chosen to ensure that our temperature sequence tracks the (extreme) horizontal-branch stars [Dorman et al., 1993]. This translates into $\log(g) = 4.0$ for $T_{\mathrm{eff}} = 11,000 - 13,000\,\mathrm{K}$ objects, $\log(g) = 4.5$ for $T_{\mathrm{eff}} = 14,000 - 16,000\,\mathrm{K}$, $\log(g) = 5.0$ covering $T_{\mathrm{eff}} = 17,000 - 20,000\,\mathrm{K}$, $\log(g) = 5.5$ for $T_{\mathrm{eff}} = 21,000 - 28,000\,\mathrm{K}$ and $\log(g) = 6.0$ for $T_{\mathrm{eff}} = 29,000 - 40,000\,\mathrm{K}$. Surface gravity does not significantly affect spectral slope, but primarily affects the width of line profiles, which is a negligible feature when fitting photometry as we do here. It does, however, correspond to a significant change in the size of the subdwarf and therefore the relative brightness of the subdwarf to a companion (see Section 7.3.2).
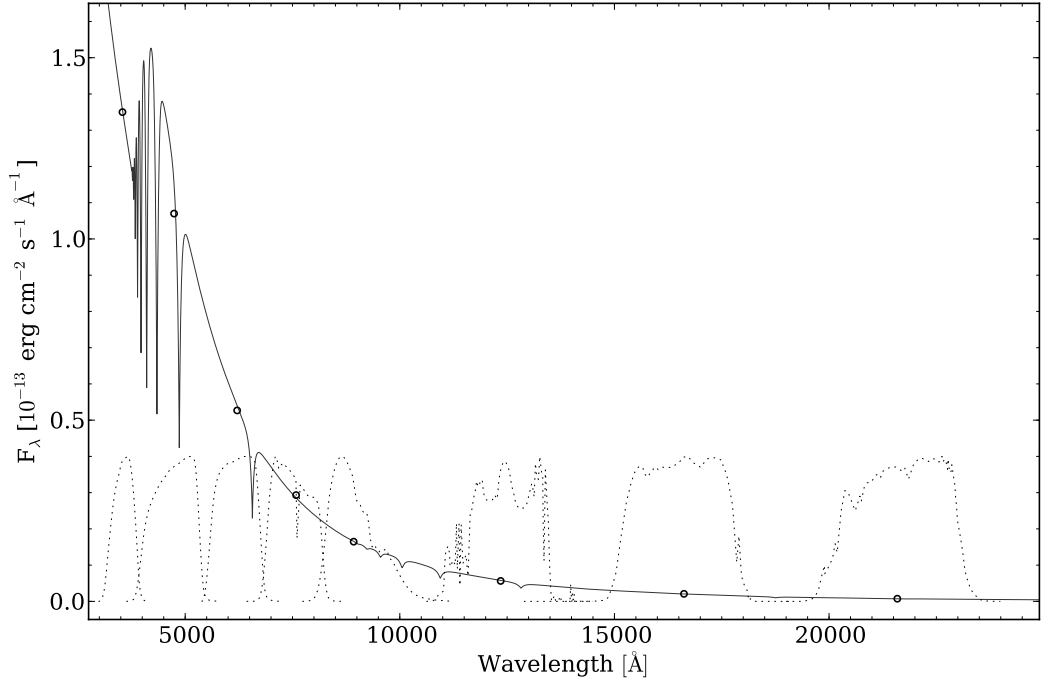
Figure 3.4: An example SED, from the near-ultraviolet to the near-infrared, of a $T_{\rm eff} = 12,000\,\rm K$, $\log(g) = 8.0$ model DA white dwarf star (solid black line). Shown as black dashed lines are the SDSS and 2MASS filter curves as discussed in Section 2.2.2 and 2.3.1, respectively. Folding the white dwarf SED through the filter curves using the method described in Section 3.4.4 results in the magnitudes shown as open black circles.

3.4.3 Main-sequence star models

A range of solar metalicity main sequence star templates of effective temperatures from $4,250\,\rm K$ to $25,000\,\rm K$ in 48 steps were taken from the Castelli & Kurucz [2003] ATLAS9 model atmosphere library. For models below $4,250\,\rm K$, Pickles [1998] stellar spectral library models are substituted because of the problems with Castelli & Kurucz [2003] model colours in this region [Bertone et al., 2004]. A Pickles [1998] M0V star is used as a proxy for a $4,000\,\rm K$ model. Similarly, M1V, M2V, M3V and M5V replace $3,750\,\rm K$, $3,500\,\rm K$, $3,250\,\rm K$ and $3,000\,\rm K$, respectively. We restrict the models to unevolved main sequence stars because we do not expect sub-giant and giant companions to contribute significantly to our samples. The main sequence star spectra cover $1,150 - 25,000$Å in wavelength. To normalise the Castelli & Kurucz [2003] main sequence star models to a flux at $10\,\rm pc$, we rescale the models to match the luminosities from the (zero age main sequence) isochrones of Girardi et al. [2000].

3.4.4   Model magnitudes

The grids of synthetic spectra discussed above were folded through all relevant filter transmission curves to calculate absolute magnitudes. To do this, we use a variation on the method described in Bradt & Padmanabhan [2005, Section 8.2]. First, each filter transmission curve ($\epsilon(\lambda)$) and photon spectral flux density ($S_p(\lambda)$) are spline interpolated onto a common wavelength grid. To account for the higher energy of the bluer photons, the photon spectral flux density must be weighted by the photon energy,

$$S_p'(\lambda) = S_p(\lambda)/(hc/\lambda), \tag{3.2}$$

where h, c and λ are the Planck constant, the speed of light and the wavelength grid of the spectra, respectively. The zero point of the filter (z) must also be multiplied by this factor,

$$z' = z/(hc/\lambda), \tag{3.3}$$

where λ becomes the effective wavelength of the filter. The filter zero points can be found in the relevant literature, or if the magnitude is on the AB scale, the zero point is defined such that a zero magnitude object corresponds to a flux density of 3631 Jy. Finally the magnitude (m) is calculated as:

$$m = -2.5 \times (\ \log_{10}(\ \Sigma(S_p'(\lambda) \times \lambda)\ ) - \log_{10}(\ \Sigma(\epsilon(\lambda) \times \lambda)\ ) - \log_{10}(z')\ ). \tag{3.4}$$

The second $\log_{10}$ accounts for the integral of filter transmission curve and the third $\log_{10}$ rescales the magnitude to the required magnitude scale defined by its zero point. We were therefore able to produce grids of absolute magnitudes for each white dwarf, subdwarf and main-sequence star model described in Sections 3.4.1 - 3.4.3.

3.4.5 χ^2 fitting

To quantify the likely composition of single or composite object, we use the models described in Sections 3.4.1 - 3.4.3 and perform a χ^2 fitting technique to estimate the system parameters of the object. We seperate this method into the two different

cases of analysing either spectra or photometry:

3.4.5.1 Spectroscopic fitting

Fitting of spectra was only performed on DA-type white dwarf stars. The method used was to isolate and fit optical line profiles following that described in Rebassa-Mansergas et al. [2007]. Because of the uncertainties in the flux calibration of the SDSS spectra, we fit normalised Hα to Hϵ absorption lines. Higher order Balmer lines have increased sensitivity to surface gravity, however, we don't include lines higher than Hϵ because of reduced S/N. A χ^2 minimisation is used to find a best fit from our grid of DA white dwarf model spectra, providing $\log(g)$ and T$_{\rm eff}$. The χ^2 surface is interpolated onto a fine grid to calculate a more accurate $\log(g)$ and T$_{\rm eff}$, and the 1σ parameter errors are taken from projecting the minimum $\chi^2 + 1$ contour onto the T$_{\rm eff}$ and $\log(g)$ axis (also discussed in Rebassa-Mansergas et al. 2007).

At around $13,000\,\rm K$ (the exact value being dependent on $\log(g)$; Rebassa-Mansergas et al. 2007), the equivalent width of the Balmer lines goes through a maximum. This leads to a maximum in the χ^2 surface (see Figure 3.5) and therefore a degeneracy in the χ^2 fitting procedure. For each object, a "hot" and a "cold" best fit solution is found from the χ^2 surface. We use the best fitting effective temperature calculated from the photometry (see Section 3.4.5.2) to choose between the "hot" and "cold" solutions, based on the minimum separation in T$_{\rm eff}$.

Using the cooling models of Holberg & Bergeron [2006], we are also able to calculate the mass of the white dwarf (M$_{\rm wd}$), radius of the white dwarf (R$_{\rm wd}$) and the distance (d) to each object.

3.4.5.2 Photometric fitting

When analysing photometry, we pursued SED fitting exploiting the broad wavelength range of the photometric data that is available. When we assume only a single component in the system, such as when fitting the photometric-only DA white dwarf candidates in Section 4.2.2, we simply take a grid of synthetic model magnitudes, and calculate a χ^2 compared to the real magnitudes for each. The best fit is defined by the minimum χ^2 (χ^2_{min}). One sigma errors are defined by a contour in the reduced χ^2 (χ^2 divided by the number of degrees of freedom; usually given as the number of data points minus the number of fitted parameters minus one) surface around the best solution at $\chi^2_{min} + 1$.

When fitting white dwarfs or subdwarfs photometrically, the photometry does not provide sufficient constraints to accurately determine the surface gravity.
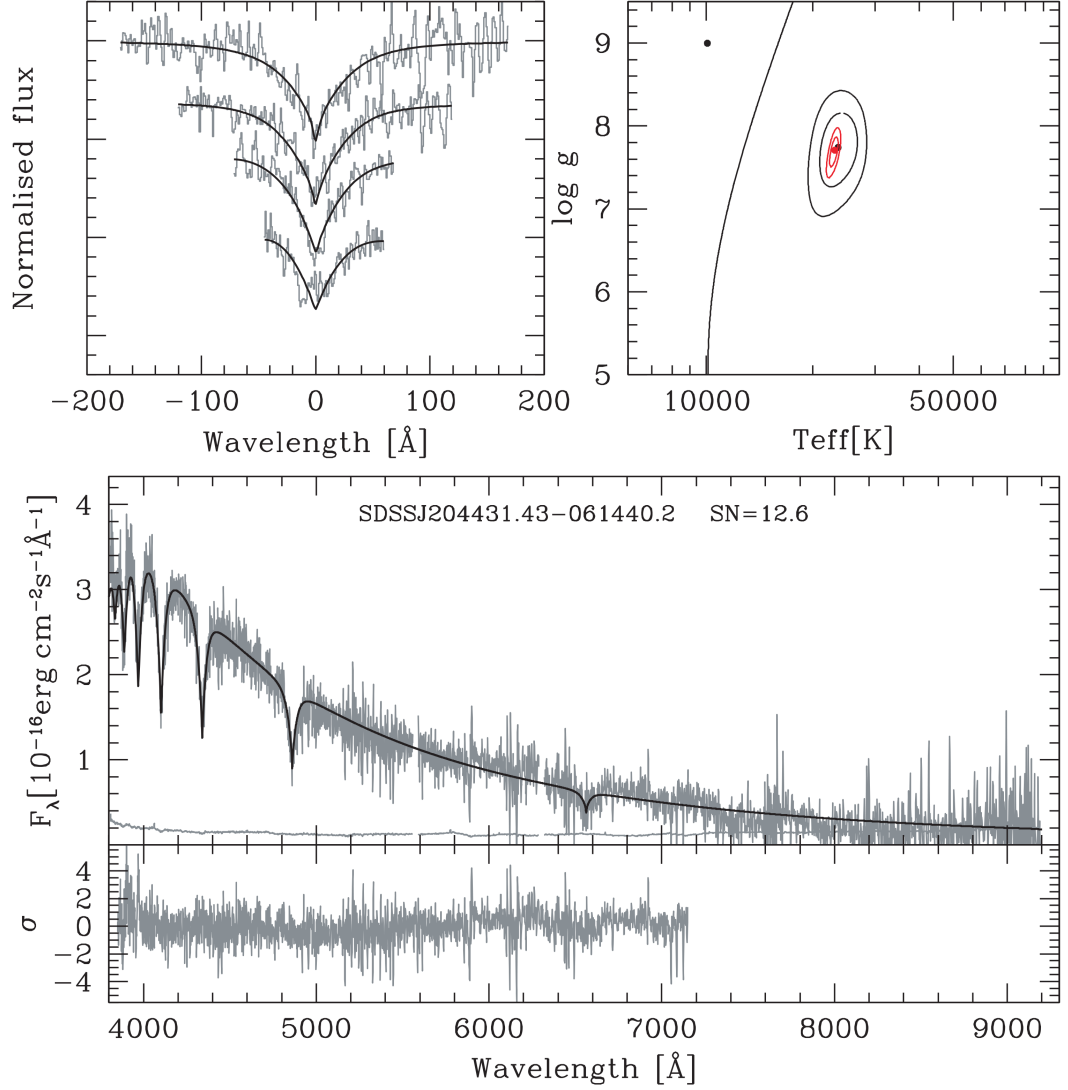
Figure 3.5: An example of fitting the Balmer-line profiles of a DA white dwarf star, taken from Rebassa-Mansergas et al. [2007]. Top left-hand panels: best fit (black lines) to the normalized Hβ to Hϵ (grey lines, top to bottom) line profiles. Top right-hand panels: 3, 5 and 10σ χ^2 contour plots in the $T_{\mathrm{eff}} - \log(g)$ plane. The black contours refer to the best line profile fit, the red contours to the fit of the whole spectrum. The solid line indicates the occurrence of maximum Hβ equivalent width. The best "hot" and "cold" line profile solutions are indicated by black dots, the best fit to the whole spectrum is indicated by a red dot. Bottom panels: the residual white dwarf spectra resulting from the spectral decomposition and their flux errors (grey lines) along with the best-fitting white dwarf model (black line) to the $3850 - 7150$ Å wavelength range (top) and the residuals of the fit (grey line, bottom).

For white dwarfs with effective temperatures outside of the range $9000 - 20000K$, the spectral line widths are narrow and therefore do not significantly affect the SED, we adopted a canonical value of $\log(g) = 8.0$. Between $9000 - 20000K$, the Balmer lines are sufficient broad to provide some constraint on the surface gravity from photometric fitting. As discussed in Section 3.4.2, we limit the subdwarf's surface gravity such that the models track the (extreme) horizontal-branch stars temperature sequence.

In the case where we assume two components in the system, the hotter body dominates the short wavelength flux while the cooler companion dominates at longer wavelengths. This permits the decomposition of the SED into two components at a common distance. To model both components of the system, we merge two synthetic model grids into a single, composite system grid[1]. The observed magnitudes were then fitted with the grid by minimising a weighted χ^2 whilst varying the distance and other common properties, such as the effective temperatures of both components. Uncertainties were again taken from the one sigma contours in the χ^2 surface.

Reddening from interstellar dust can potentially have a significant effect on the shape of the hotter components SED, especially at short wavelengths. It would therefore primarily affect the inferred effective temperature of the white dwarf or subdwarf. The slope will be flattened and thus a systematically lower effective temperature would be found. With prior knowledge of the reddening to the system, this can corrected for, however, this is not always the case, as will be shown in Section 7.5.

---

[1]In the case of the subdwarf plus main-sequence star systems used for Chapter 7, the grid also includes the option for the subdwarf not to have a companion.

Chapter 4

DA white dwarf catalogue

4.1 Selecting DA white dwarfs

Since the first comprehensive list of white dwarfs produced by Eggen & Greenstein [1965], the number of known white dwarfs has increased substantially. The multiple versions of the McCook & Sion catalogue have been instrumental in developing the understanding of white dwarfs, both in bulk properties and finding rare objects. Before the project undertaken here, the most recent catalogue of spectroscopically identified white dwarfs was based on SDSS DR4 [Eisenstein et al., 2006], which comprised 4783 square degrees, roughly half of the sky coverage of DR7. Here, we exploited the much larger footprint of SDSS DR7 (Section 2.2.2), and also extend the white dwarf sample to photometric objects without follow-up spectroscopy. We restricted our ambitions to DA white dwarfs for a number of reasons. Firstly, the vast majority of all known white dwarfs belong to the DA class [McCook & Sion, 1999]. Secondly, determining the atmospheric parameters of DA white dwarfs, T_{eff} and $\log(g)$, from fitting atmosphere models to either spectroscopy [Bergeron et al., 1992] or photometry [Koester et al., 1979] is a well-established and robust procedure. This is essential for the purpose of identifying white dwarfs with infrared excess, as we need to accurately extrapolate the white dwarf flux to the J, H, and K bands (performed in Chapter 5). Thirdly, optical spectra of DA white dwarfs are characterised by strong Balmer absorption lines on a blue continuum, and the strong dependence on the Balmer line equivalent widths results in DA white dwarfs occupying a distinct region in colour space.

We have developed a two-pronged approach to identify as many DA white dwarfs with spectroscopy within DR7, and subsequently to select white dwarf candidates which have *ugriz* photometry but were not spectroscopically followed-up by

SDSS.

As a start, we retrieved the DR7 spectra and $ugriz$ photometry for all white dwarfs with $g \leq 19$ and classified by Eisenstein et al. [2006] as DA or DA_auto, corresponding to visually confirmed and automatically classified hydrogen-dominated white dwarfs, respectively. This totals 2889 unique objects, 938 being classified as DA and 1951 DA_auto. All spectra were visually inspected to corroborate their DA classification, and we found 99.4% agreement with the classification for white dwarfs by Eisenstein et al. [2006]. The 0.6% disagreement primarily comes about from non-DA white dwarfs that were classified as DA_auto by Eisenstein et al.'s classification routine. The sample of spectroscopically confirmed DA white dwarfs was then used to trace the locus of DA white dwarfs in the $(u-g, g-r)$, $(g-r, r-i)$, and $(r-i, i-z)$ colour-colour planes (see Section 3.2). The population of DA white dwarfs follow a boomerang-shape in $(u-g, g-r)$ colours, which is clearly separated from the main sequence, but intersects the quasar population (Fig. 4.1).
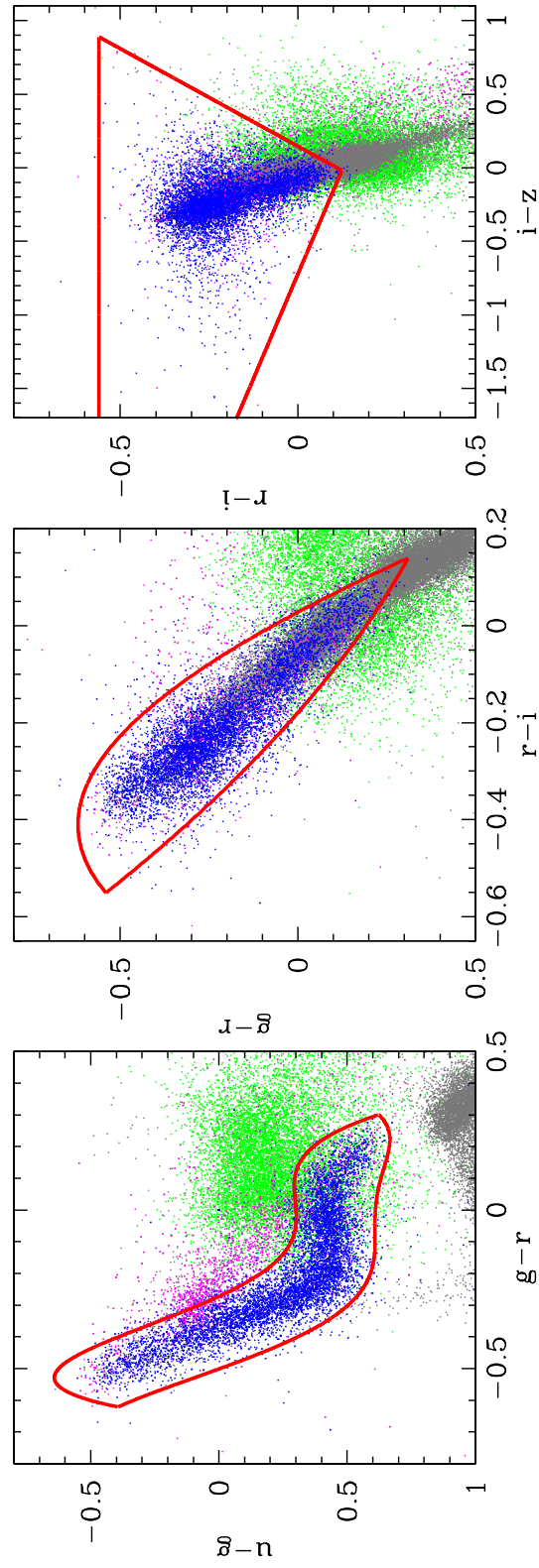
Figure 4.1: Colour-colour plots illustrating the location of the SDSS spectroscopic objects. DA white dwarfs, quasars and main-sequence stars are shown as blue, magenta, green and grey dots respectively. The polynomial colour cuts from Table 4.1 are overlaid as red lines.

Table 4.1: Colour selection for finding DA white dwarfs in $ugriz$ space. Objects were selected to be primary objects and point sources. Flags are shown in Hexagesimal notation. These are the standard SDSS "good photometry" flags, as documented on SDSS CASJOBS [Li & Thakar, 2008], and were chosen so that the object was detected in BINNED1, and did not have any of the following: EDGE, NOPROFILE, PEAKCENTER, NOTCHECKED, PSF_FLUX_INTERP, SATURATED, or BAD_COUNTS_ERROR.

Constraints		
$(u - g)$	$\geq$	$-20.653 \times (g - r)^5 + 10.816 \times (g - r)^4 + 15.718 \times (g - r)^3$ $-1.294 \times (g - r)^2 - 0.084 \times (g - r) + 0.300$
$(u - g)$	$\leq$	$-24.384 \times (g - r)^5 - 19.000 \times (g - r)^4 + 3.497 \times (g - r)^3$ $+1.193 \times (g - r)^2 + 0.083 \times (g - r) + 0.610$
$(g - r)$	$\leq$	$-0.693 \times (r - i)^2 + 0.947 \times (r - i) + 0.192$
$(g - r)$	$\geq$	$-1.320 \times (r - i)^3 + 2.173 \times (r - i)^2 + 2.452 \times (r - i) - 0.070$
$(r - i)$	$\geq$	-0.560
$(r - i)$	$\leq$	$0.176 \times (i - z) + 0.127$
$(r - i)$	$\leq$	$-0.754 \times (i - z) + 0.110$
g	$\leq$	19
0	$!=$	flags & 0x10000000
0	$=$	flags & 0x8100000c00ac

This relatively complex shape was approximated by the intersection of two 5th-order polynomials (Table 4.1). In $(g - r, i - r)$ the DA white dwarfs lie along a relatively narrow band, overlapping with the blue end of the main sequence and, to some extent with quasars, which we approximated by the combination of a 2nd and 3rd order polynomial. Finally, in $(r - i, i - z)$, the DA white dwarfs are again located at the blue end of the main sequence, but display a relatively large spread in $i - z$. Visual inspection of the SDSS spectra of the outliers confirms them as DA white dwarfs, though the majority of them are near the faint end of the Eisenstein et al. sample. We decided to include those outliers in our colour-cut, and hence approximated the DA locus by the intersection of three linear relations in $(r - i, i - z)$.

Finally, we applied a set of recommended data quality flags to the SDSS photometry to minimise contamination by instrumental artifacts and blended stars. Applying the constraint set summarised in Table 4.1 to DR7 resulted in the selection of 7444 unique spectroscopic objects, which were then visually classified as DA white dwarfs, other (non-DA) white dwarfs, quasars, narrow line hot stars (see below), and other objects (Table 4.2).

4.1.1 Narrow line hot stars

The optical spectra of ultra-low mass white dwarfs [e.g Kilic et al., 2007b] and very cool DAs, particularly those at low signal-to-noise ratio, can look rather similar to early type main sequence stars, subdwarfs, extreme horizontal branch stars or very metal-poor halo stars, which we all lump together as contaminants with the designation "narrow line hot stars" (NLHS). These are particularly dominant at the blue end of the white dwarf "banana" ($g \leq 16$, see Table 4.2). While there is noticeable interest in ultra-low mass white dwarfs [e.g. Liebert et al., 2004; Kilic et al., 2007a; Marsh et al., 2011], they represent a tiny fraction of all DAs. Given that our aim is to study the bulk population of DA white dwarfs, we make no attempt to accurately classify ultra-low mass white dwarfs. In addition, our colour selection is only complete to effective temperatures above ~ 8000K. Attempting to include much cooler white dwarfs would result in significant contamination from NLHS.

4.1.2 Overall completeness and efficiency

Completeness and efficiency were the key parameters in designing our selection algorithm (Table 4.1), where completeness and efficiency are defined in Section 3.3. *Completeness* is set as the fraction of Eisenstein et al.'s DA white dwarfs recovered by our constraints, and *efficiency* as the ratio of spectroscopically confirmed DA white dwarfs to all objects in our colour-magnitude selection. In the case of the spectroscopic DA sample, one may argue that completeness is more important than efficiency because contaminants can be removed through visual spectral classification of all candidate objects. On the other hand, the photometric-only DA sample requires a high level of efficiency to minimise the number of contaminants. We optimised the colour boundaries to maximise both completeness and efficiency, and the constraint set in Table 4.1 results in a completeness of 95.4% and an efficiency of 62.3% (Table 4.2). From SDSS DR7, a total 4636 unique spectroscopic DA white dwarfs are contained within the colour-magnitude cuts. This represents a 70 per cent increase in spectroscopic DA white dwarfs with $g \leq 19$ over the Eisenstein et al. [2006] sample. Similarly, the photometric-only DA white dwarf candidates sample contains 9341 objects. Assuming 62.3% efficiency of the selection, ~ 6000 additional photometric white dwarfs are contained within the sample and therefore the total increase over Eisenstein et al. [2006] is approximately a factor of three. The efficiency is, however, only a lower limit for the photometric sample because the SDSS spectroscopic was designed to focus on QSOs. Therefore, QSOs are only a minor

contaminant in the photometric-only sample.

The spectral classification and completeness are given as a function of g-magnitude in Table 4.2. The completeness drops slightly towards larger apparent magnitude because of the larger scatter in the colour-colour diagrams. The fraction of NLHS contaminants is largest at the bright end of our sample, which is a natural consequence of the much larger intrinsic brightness of subdwarfs and early-type main-sequence stars, and the fraction of quasar contaminants increases towards larger apparent magnitudes. It is possible to eliminate a fair fraction of the contaminants in the photometric-only sample by using additional information such as proper motions and infrared colours (see Sect. 5.2.3.4).

Table 4.2: Efficiency and completeness of the polynomial colour-colour cuts (Table 4.1) as a function of SDSS g magnitude. The total number of spectroscopic objects that matched our selection and were visually classified was 7444. The classification "Other white dwarfs" contains white dwarfs of type DAB, DAO, DB, DC, DQ, DZ, magnetic white dwarfs and white dwarf+MS binaries. The classification "Other" includes CVs, galaxies, peculiar objects and unidentified spectra. The final two right hand columns show the number of photometric-only objects in each g magnitude bin (N_{Tot}) and the number of predicted DA white dwarfs, calculated by multiplying this by the efficiency (N_{DA}). The bottom line of the table gives the total number of DA white dwarfs with ($g \leq 19$) in Eisenstein et al. [2006], and the number of them included in our colour cut.

g	All WD Candidates	DA WD N	%	NLHS N	%	QSO N	%	Other WD N	%	Other N	%	Efficiency	Completeness	Photometric-only N_{Tot}	N_{DA}
≤ 16	258	79	30.6	161	62.4	0	0.0	13	5.0	5	1.9	30.6%	95.8%	893	273
16-17	581	326	56.1	185	31.8	22	3.8	44	7.6	4	0.7	56.1%	96.7%	980	550
17-18	1719	1092	63.5	225	13.1	230	13.4	165	9.6	7	0.4	63.5%	96.5%	2278	1447
18-19	4886	3139	64.2	269	5.5	1028	21.0	439	9.0	11	0.2	64.2%	95.0%	5190	3332
Total	7444	4636	62.3	840	11.3	1280	17.2	661	8.9	27	0.4	62.3%	95.5%	9341	5819

	Total DA WD	Photometrically selected DAs	Completeness
Eisenstein	2889	2757	95.4%

4.1.3 Completeness of SDSS spectroscopy for DA white dwarfs

The sample produced here provides an excellent opportunity to investigate the spectroscopic completeness of SDSS for DA white dwarfs. We used the cuts in Table 4.1 to select both the spectroscopic and photometric objects within DR7. From these two sets of data, we then calculate the spectroscopic completeness within the $(u - g, g - r)$ colour-colour plane (Fig. 4.2). The upper middle and right panels display the density of spectroscopically confirmed DA white dwarfs (middle) and contaminants (such as NLHS and quasars, right hand side panel). For comparison, the upper left hand panel shows the DA white dwarf cooling tracks from Holberg & Bergeron [2006][1]. The efficiency of our colour cuts is obtained for each bin within the $(u - g, g - r)$ plane as the ratio of the number of the DA white dwarfs to the total number of objects in the bin (lower centre panel). This clearly displays a reduced efficiency of selecting both the hottest and coldest white dwarf because of the increased numbers of contaminants. Our selection method, however, has an extremely high efficiency when selecting white dwarfs with temperatures between $\sim 10,000 - 20,000$K. The number of DA white dwarfs without SDSS spectroscopy is predicted by scaling the number of photometric-only objects with the efficiency (resulting in the lower left panel). Finally, the DA white dwarf spectroscopic completeness was calculated as the ratio of spectroscopically confirmed DA white dwarfs to the total number of DA white dwarfs, with and without spectroscopy (lower right panel). The overall spectroscopic completeness is 44.3% down to $g = 19$. As mentioned in Sect. 4.1.1, this analysis is limited to white dwarfs with $T_{\text{eff}} \gtrsim 8000$K. The preference of SDSS spectroscopy to target quasars is clearly seen in the lower right corner of the spectroscopic completeness colour-colour diagram, where the vast majority of quasars lie. This corresponds to a very high spectroscopic completeness for cooler DA white dwarfs. In contrast, the spectroscopic completeness for white dwarfs with $T_{\text{eff}} \gtrsim 12000$K is significantly lower.

4.2 Modelling SDSS data

4.2.1 Fitting the SDSS spectroscopy

We fitted the SDSS spectra of all DA white dwarfs found within our colour cuts (Table 4.1) using the models described in Section 3.4.1 and following the method described in Section 3.4.5.1 and Rebassa-Mansergas et al. [2007]. For each white dwarf, we fitted the effective temperature, surface gravity and distance to the white

---

[1]See http://www.astro.umontreal.ca/~bergeron/CoolingModels for an updated grid.
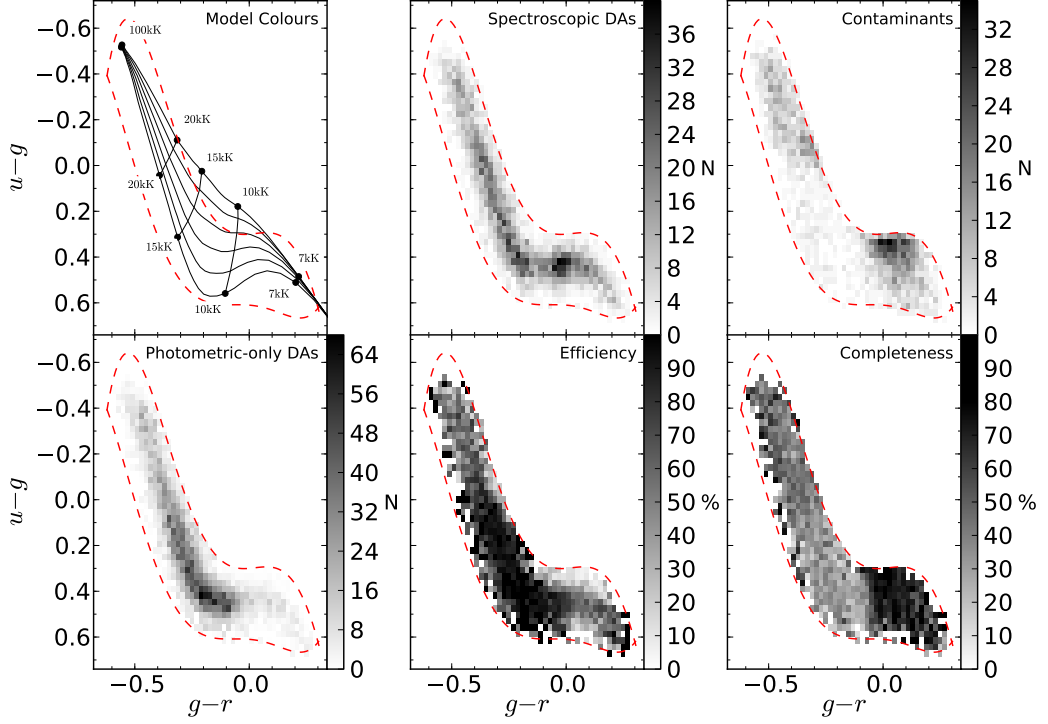
Figure 4.2: The spectroscopic completeness of DA white dwarfs in SDSS DR7 within the $(u-g, g-r)$ colour-colour plane. In the top left panel, the colour selection from Table 4.1 is shown as a red dashed line, overlaid with the DA white dwarf cooling tracks of Holberg & Bergeron [2006]. From the bottom up, these curves represent $\log(g) = 7.0 - 9.5$ in steps of 0.5. The number of spectroscopically confirmed DA white dwarfs and contaminants within our colour selection are shown in the upper middle and right panels, respectively. Two distinct regions of high contamination are visible, with NLHS and quasars being concentrated at the bluest and reddest colours of the DA "banana", respectively. The number of DA white dwarfs without SDSS spectroscopy is shown in the bottom-left panel, calculated as the number of photometric-only objects weighted by the colour-dependent efficiency of our selection algorithm (lower middle panel). Finally, the spectroscopic completeness of SDSS for DA white dwarfs, i.e. the ratio of spectroscopic DAs to the total number of DAs, is shown in the bottom right panel. White dwarfs with $T_{\mathrm{eff}} \lesssim 12000\mathrm{K}$ have a very high completeness thanks to their colour-proximity to ultraviolet-excess quasars, which were intensively targeted by SDSS.

dwarf, and then calculated the white dwarf mass and radius. An example of such a fit is shown in Figure 3.5.

If an object has an excess in the z-band or later, such as those discussed in Chapter 5, it does not significantly affect the spectroscopic fitting method because we fit line profiles, and do not use the continuum flux. This method is most sensitive at shorter wavelengths, where any companion does not significant contribute.

4.2.2 Fitting the SDSS photometry

We also fitted (according to the method described in Section 3.4.5.2) *all* photometric objects found with our colour cuts, including all objects that do have SDSS spectroscopy. We intentionally included objects known *not* to be DA white dwarfs, to allow us to investigate the properties of the contaminants among the photometric-only DA candidates.

Photometric objects were fitted by comparing the SDSS u, g, r and i magnitudes to the white dwarf model grid (Section 3.4.1). Magnitudes redder than i were not included because we chose to allow for composite systems. This ensures we can recognise objects with an excess already showing in z, such as white dwarf plus M-dwarf binaries. The fitting returns an effective temperature, surface gravity and distance to the white dwarf, however, as discussed in Section 3.4.5.2, the surface gravity (and therefore distance) are barely constrained by the fitting. This, fortunately, does not significantly effect the extrapolation into the infrared. An example of a photometrically fitted white dwarf is shown in Figure 4.3.

The temperatures measured from the SDSS photometry were found to be systematically lower than those from the fitting of line profiles (e.g. Table A.3; objects with SDSS spectroscopy, but fitted with the photometric method). Our sample of SDSS white dwarfs overlaps with the Palomar Green (PG) sample, and Fig. 4.4 shows a comparison between our spectroscopic and photometric temperatures with those of Liebert et al. [2005a], which were determined from independent data, spectral models, and fitting routines. We find good agreement between the results of Liebert et al. [2005a] and our spectroscopic method. However, our photometric temperatures are systematically too low, a trend that is strongly correlated with either white dwarf temperature or distance. At 200pc (500pc), the photometric temperatures are on average 5% (10%) below our and Liebert's spectroscopic values. This could suggest that interstellar reddening is, at least in part, the culprit for reduced temperatures. While reddening would not significantly effect the shape of the line profiles, it could noticeably change the slope of the continuum (see also Holberg et al. 2008). No clear correlation is, however, seen when comparing the mismatch
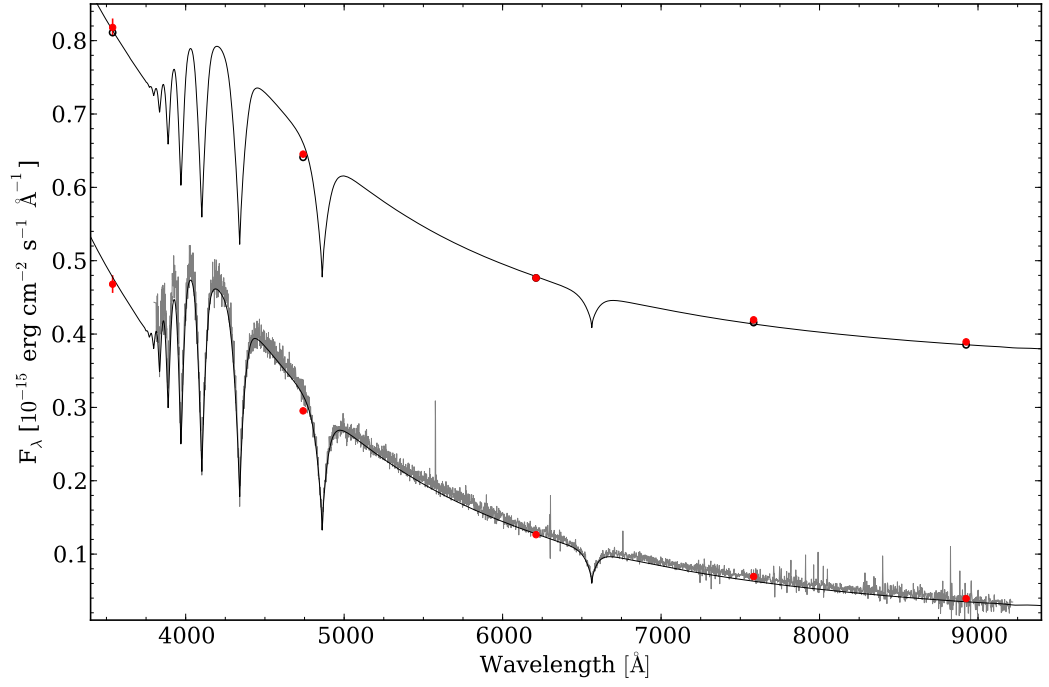
Figure 4.3: An example of a fit to the SDSS spectrum and *ugri* photometry of a DA white dwarf (SDSS J1314+0057). The lower SED shows the SDSS spectrum (gray), photometry (red) and the best fitting white dwarf model based upon fitting of the line profiles (black). The fit is a $T_{\rm eff} = 17707 \pm 163$K, $\log(g) = 7.80 \pm 0.04$ model at a distance of 312 ± 8 pc. The upper SED (offset by 0.35 flux units) shows the best fit to the photometry with a white dwarf of $T_{\rm eff} = 17000\pm^{1050}_{510}$K, $\log(g) = 8.25\pm^{1.21}_{0.60}$. The model white dwarf photometry is plotted as open black circles.

in temperatures to the Schlegel et al. [1998] values of $E(B-V)$ at the positions of the white dwarfs. The Schlegel et al. maps probe interstellar reddening through the entire Galaxy, whereas the white dwarfs in our sample lie at a few hundred parsecs at most. Typical (total Schlegel) reddening along the lines-of-sight towards our white dwarfs is $E(B-V) \sim 0.05$. De-reddening the SDSS photometry with that total $E(B-V)$, and re-fitting the photometric white dwarf sample indeed leads, as expected, to a large over-correction of the white dwarf temperatures. Analysing the sample of spectroscopic DAs, we estimate that the typical reddening in front of the white dwarfs is $E(B-V) \sim 0.01 - 0.02$. However, we can not systematically correct for the effect of reddening for the sample of photometric-only DA candidates. We note that for hot white dwarfs, $T_{eff} \gtrsim 45000$K, non-LTE effects become important, which may also lead to some systematic differences in the fit parameter for the hottest stars in our sample. Therefore, the temperatures calculated from the photometry alone have an additional systematic uncertainty, on top of the statistical uncertainty from the fit, and the true temperatures are likely to be a few thousand Kelvin higher. In the context of our search for infrared flux excess (Sect. 5.2.1 below), changing the white dwarf temperature by a few thousand Kelvin does not have a significant impact on the level of excess detected (see Sect. 5.3 for examples).
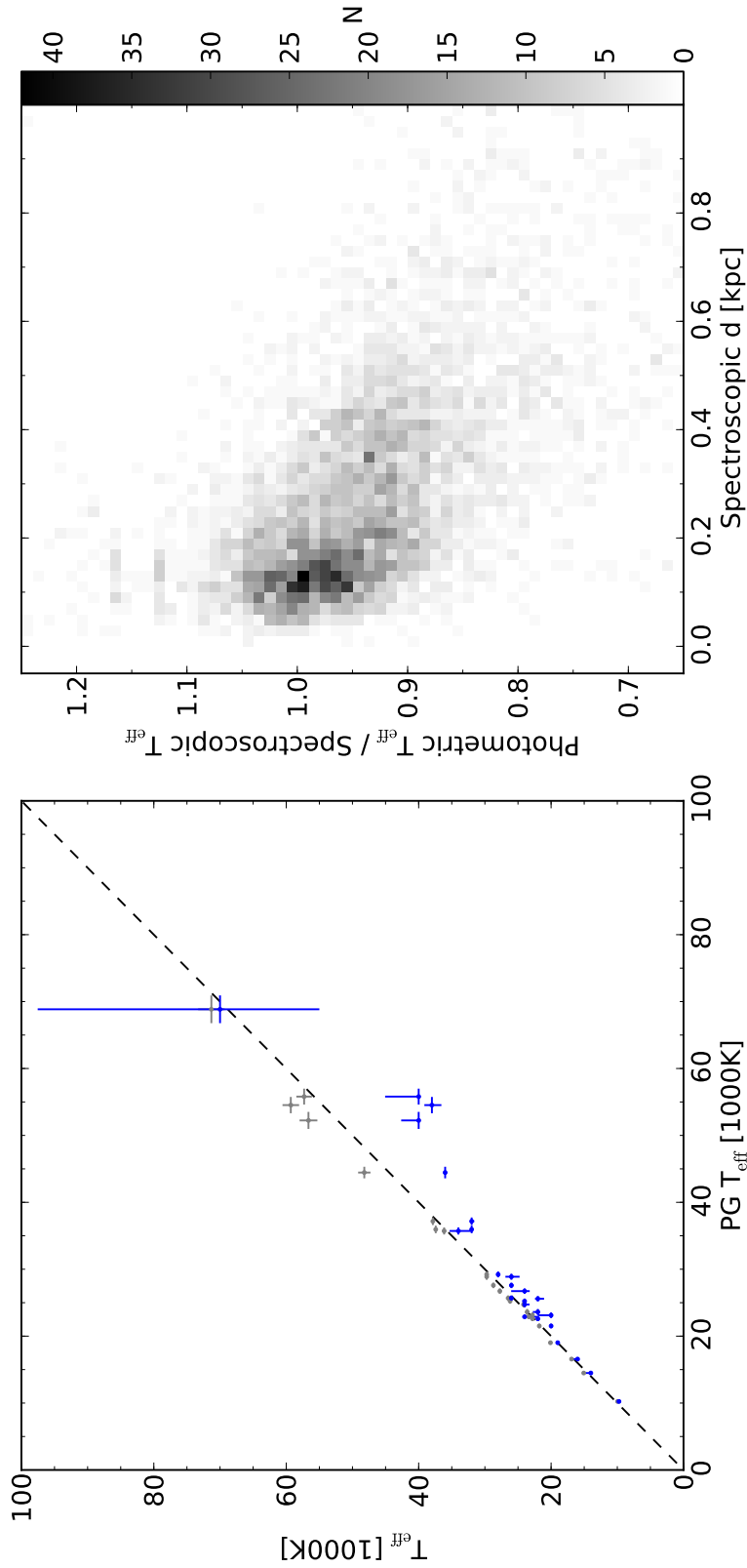
Figure 4.4: A demonstration of the systematically lower measured photometric effective temperatures. The left hand panel shows the Liebert et al. [2005a] PG survey white dwarfs with corresponding stars in our sample (25 objects). This figure compares the effective temperature calculated by Liebert et al. [2005a] with that from our spectroscopic (grey) and photometric (blue) fitting techniques. When using the photometric method, we significantly underestimate the temperature of hot white dwarfs. The hottest white dwarf at 70,000K has a large error on the photometric fit because the continuum slope of the white dwarf at these temperatures is effectively Rayleigh-Jeans and therefore contains no temperature information. In the right hand panel we show the ratio of the effective temperatures calculated using the photometric and spectroscopic fitting methods for each of the objects in the spectroscopic DA white dwarf sample, as a function of distance. Again, we underestimate the effective temperature of white dwarfs at large distances.

The full catalogue of spectroscopic and photometric-only (candidate) white dwarfs is available via VizieR[2].

4.3 Summary

We have developed dedicated colour-colour cuts to select DA white dwarfs only from their optical photometry (Table 4.1, Fig. 4.1). This method can easily be optimised to prioritise for completeness, efficiency or a compromise of both. We have demonstrated that a high completeness (95.4%) can be obtained with a reasonable efficiency (62.3%) based on the *ugriz* data from SDSS DR7. The strengths of this approach, is that it provides substantially larger and statistically better characterised white dwarf samples (Sect. 5.2.3) when compared to spectroscopic catalogues such as McCook & Sion [1999] and Eisenstein et al. [2006]. We have also investigated methods to account for the contamination of the DA white dwarf candidate sample by quasars and NLHS. This method can be adapted to obtain large uniform samples of white dwarfs from other multicolour optical photometric surveys, such as e.g. SkyMapper [Keller et al., 2007].

_____

[2]http://cdsarc.u-strasbg.fr/viz-bin/Cat?J/MNRAS/417/1210

Chapter 5

White dwarf stars with infrared excess in UKIDSS

Circumstellar discs are seen in all stages of stellar evolution. Examples where this is the case include pre-main-sequence stars as they accrete the remnants of the molecular cloud from which they formed, planets forming in discs around young stars and disrupted comets and/or asteroids accreting onto mature main-sequence stars. Furthermore, white dwarfs exist that are accreting a dust disc, presumed to be the disrupted remnants of ancient planetary systems. Identifying the latter of these provides invaluable insight into the future of our Sun and the solar system (see Section 1.2.2.2). Dust discs around white dwarf stars have, in numerous cases, been associated with gas discs [e.g. Brinkworth et al., 2009] and atmospheric metal pollution [e.g. Girven et al., 2012a, see Chapter 6]. Measuring abundances of the accreted material is currently the only feasible way of investigating the composition of planetary systems other than the Solar system. A method to select white dwarfs with dust discs is therefore key to advancing our understanding of extra-solar planets, asteroids and comets.

In this Chapter, we develop a method to select white dwarfs with a near-infrared excess, consistent with a disc or low-mass companion, from large scale digital sky surveys. We used a combination of two surveys; the SDSS and UKIDSS (Section 2.2.2 and 2.3.2, respectively) to systematically search a large area of the sky. However, the method developed is also applicable to the host of other sky surveys coming online now.
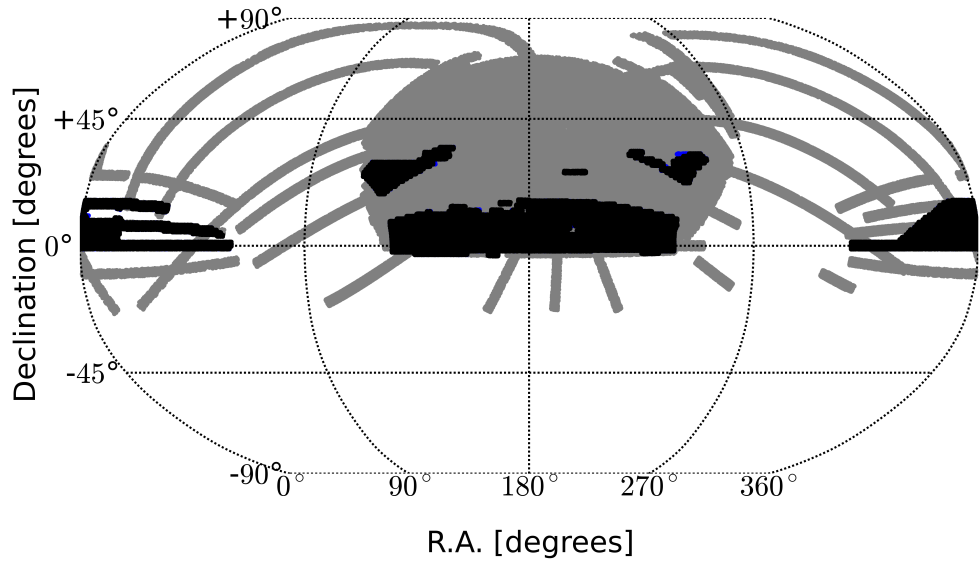
Figure 5.1: Coverage of the SDSS DR7 (grey) and UKIDSS DR8 LAS (black) in equatorial coordinates.

5.1 Cross-matching SDSS and UKIDSS

We cross-matched (Section 3.1) the SDSS DA white dwarf catalogue described in Chapter 4 with the UKIDSS LAS DR8. Previous studies [e.g. Hoard et al., 2007] have used 2MASS, however, since a large majority of the SDSS white dwarfs are too faint in the infrared for 2MASS to pick up, UKIDSS was preferred. The overlap between SDSS DR7 and UKIDSS/LAS DR8 is illustrated in Fig. 5.1, and amounts to ~ 2700 square degrees.

All (spectroscopic and photometric-only) objects from the DA selection in SDSS DR7 were matched with the UKIDSS database using the CrossID function[1]. To decide upon a matching radius, a sample of 5000 randomly selected spectroscopically confirmed DA white dwarfs were matched to the UKIDSS database with a $60''$ search radius r. The distribution of the distance between the SDSS objects and the UKIDSS matches is shown in Fig. 5.2. The number of all possible matches within $60''$ (black histogram) grows approximately as r^2, as would be expected for chance coincidence, whereas true matches are primarily within $r < 3''$. Selecting only the closest match (blue histogram), the majority of these random mismatches are removed. The blue and black distributions agree well at small distances ($r \lesssim 2.5''$), indicating that crowding is not a major problem. $2.5''$ is much larger than the

---

[1]http://surveys.roe.ac.uk:8080/wsa/crossID_form.jsp

54

Table 5.1: The number of all SDSS DR7 objects satisfying our constraint set (Table 4.1), and of various subsets with different UKIDSS bands.

Detections in band	Spectroscopic Objects	Photometric Objects
Total SDSS	7444	9341
Any UKIDSS	1990	1771
Y	1815	1614
J	1787	1549
H	1503	1281
K	1108	840
H & K	1075	809
J, H & K	979	720

quoted astrometric accuracies of both SDSS and UKIDSS (of order a few tenths of an arc second), but the large proper motions of the white dwarfs and the potentially large ($\sim$few years) time interval between both surveys can lead to positional shifts of up to a few arc seconds. We adopt $r = 2.5''$ for the final cross-matching of our spectroscopic and photometric-only SDSS DA samples with UKIDSS, which limits the number of spurious matches, and will exclude only a handful of (halo) objects with extremely high proper motions. Any remaining positional mismatches are flagged in the manual examination of the SDSS and UKIDSS images carried out later. We restrict our analysis to unresolved systems, as the physical association of spatially resolved companions to white dwarfs will be difficult to demonstrate with the available data. Consequently, objects that are flagged as partially resolved in the UKIDSS images are removed from the sample.

A total of 1990 of the SDSS objects with spectra were found to have at least one measured magnitude in the UKIDSS database. 1275 of these are spectroscopically confirmed DA white dwarfs. Similarly, 1771 of the photometric-only objects had at least one match in the UKIDSS database (Table 5.1).

5.2 Identifying infrared excess objects

5.2.1 IR excess detection

In both the spectroscopic and photometric fitting methods (Section 4.2), the best fit model extends into the infrared and all objects with UKIDSS data were examined for an excess by comparing the infrared white dwarf model flux with the observed $YJHK_s$ magnitudes. Objects with a 3σ excess in any band over the white dwarf model were defined as a robust excess candidate ("DAire" and "DA:ire" for the
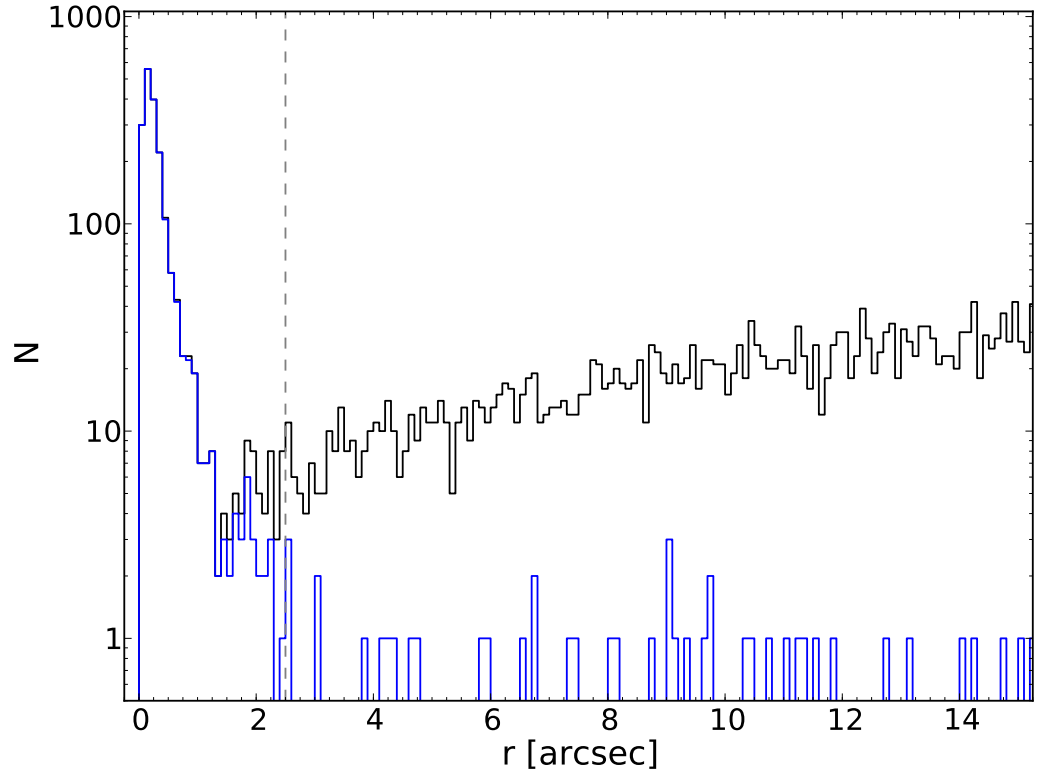
Figure 5.2: Spatial offsets of the SDSS and UKIDSS positions for a sample of 5000 spectroscopically confirmed DA white dwarfs randomly selected from our constraint set (Table 4.2). The blue histogram shows the distance to the closest neighbour in UKIDSS, the black histogram plots the distances to all possible matches. The bins have a width of $0.1''$.

spectroscopically confirmed DAs and the photometric-only DA candidates, see Tables A.1, A.2 and A.3). In addition to these, objects that appeared to have a best fit model which over-estimated the flux in Y, J and H, but showed only a $\sim 2\sigma$ excess in K were also flagged as tentative excess candidates ("DAire:" and "DA:ire:", as above, Tables A.1, A.2 and A.3), see Fig. 5.3 for an example. Further infrared data is definitely needed to confirm these marginal infrared excess candidates. Similarly, spectroscopically confirmed DAs (photometric DA candidates) with close to 3σ excess that by eye require further data to confirm the excess were also marked as "DAire:" ("DA:ire:"). For the photometric-only objects the uncertainty on the model parameters is generally larger compared to the spectroscopically confirmed DAs. This was accounted for by not flagging objects with a marginal infrared excess *and* a large ($\gtrsim 5,000\,\mathrm{K}$) uncertainty on effective temperature as excess candidates.

Spurious excesses were often caused by spatially close background or foreground objects to the white dwarf and bad SDSS or UKIDSS images. We visually inspected all flagged sources and discounted resolved and partially resolved systems because the physical association of the two objects could not be demonstrated based on the available data.

A total of 42 white dwarfs were found to have an excess from the spectroscopic fitting method, and 105 infrared excess candidates were found from the photometric fitting method (Table 5.2). The excesses have a variety of spectral shapes, generally consistent with various companion spectral types. Tables A.1 and A.2 list all the spectroscopic and photometric infrared excess candidates, respectively.

5.2.2 IR excess modelling

The $YJHK$ magnitudes of objects that were found to exhibit an infrared excess were fitted with a composite model consisting of the best-fit white dwarf plus a set of low-mass companions with spectral types M0 through to L8. We used the 2MASS JHK_s magnitudes of Hoard et al. [2007], which we converted into the UKIDSS filter system adopting the equations given in Dye et al. [2006]. Hoard et al.'s absolute magnitudes of the low-mass companions were scaled to apparent magnitudes using the distance modulus calculated from the white dwarf fit. For photometrically fitted objects, the white dwarf distance modulus was calculated as an average of the difference between the best-fit absolute magnitudes and the SDSS apparent magnitudes in each of the u, g, r and i bands. Finally, the model magnitudes of the composite system were computed from the combined white dwarf and companion star fluxes. The best composite fit to the JHK infrared photometry was calculated using a least χ^2 search and subsequently confirmed by visual inspection. Fig 5.4 shows reduced
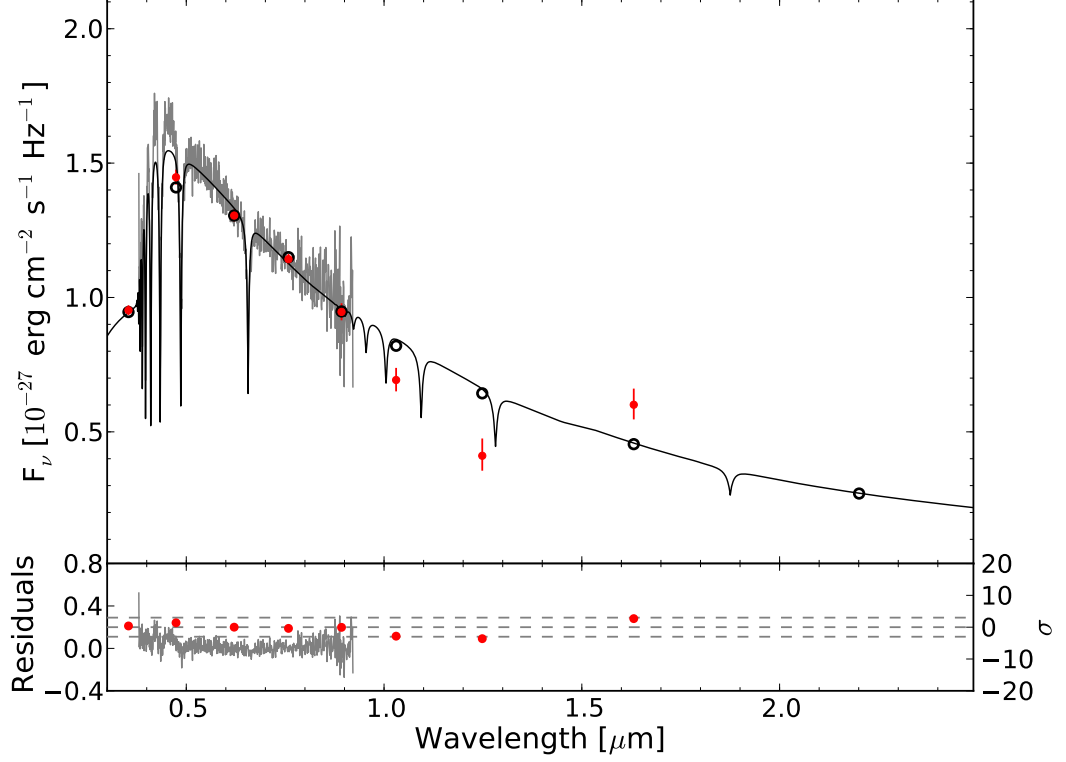
Figure 5.3: The SED of SDSS J1218+0042, an example of a spectroscopically confirmed DA white dwarf with a possible IR flux excess (classified as DAire: in Table A.1), SDSS J1218+0042. The SDSS spectrum is plotted as a grey line. The best-fit model to the *ugri* photometry (red points) is shown (T_{eff} = 10000K, $\log(g)$ = 7.75; black line), which results in an *H*-band excess just below 3σ. The magnitudes calculated from folding the white dwarf model through the SDSS and UKIDSS filters are shown as black, open circles. Adopting the slightly higher temperature (T_{eff} = 11173K) from the analysis of the SDSS spectrum boosts the excess to just above 3σ, flagging the object as an IR excess candidate. However, given that *Y* and *J*-band magnitudes fall significantly below the model, further IR data are necessary to confirm or refute the IR excess of this white dwarf.

χ^2 as a function of companion type for three white dwarfs with well constrained companions using the photometric method as an example. A white dwarf with a good fit to the companion has a reduced $\chi^2 \lesssim 10$, an example of a corresponding SED is shown in Fig. 5.16. Composite fits with $\chi^2 \sim 10 - 100$ were flagged as "bad fits" and flagged as DAire: or DA:ire in Table A.1 and A.2, respectively, as the nature of the infrared excess remains somewhat unclear (see Fig. 5.5 and Sect. 5.2.3.1). Finally, QSOs stand out because of their very high χ^2, $\sim 100 - 1000$ (e.g. Fig. 5.6). A summary of companion types for each method is given in Table 5.2.
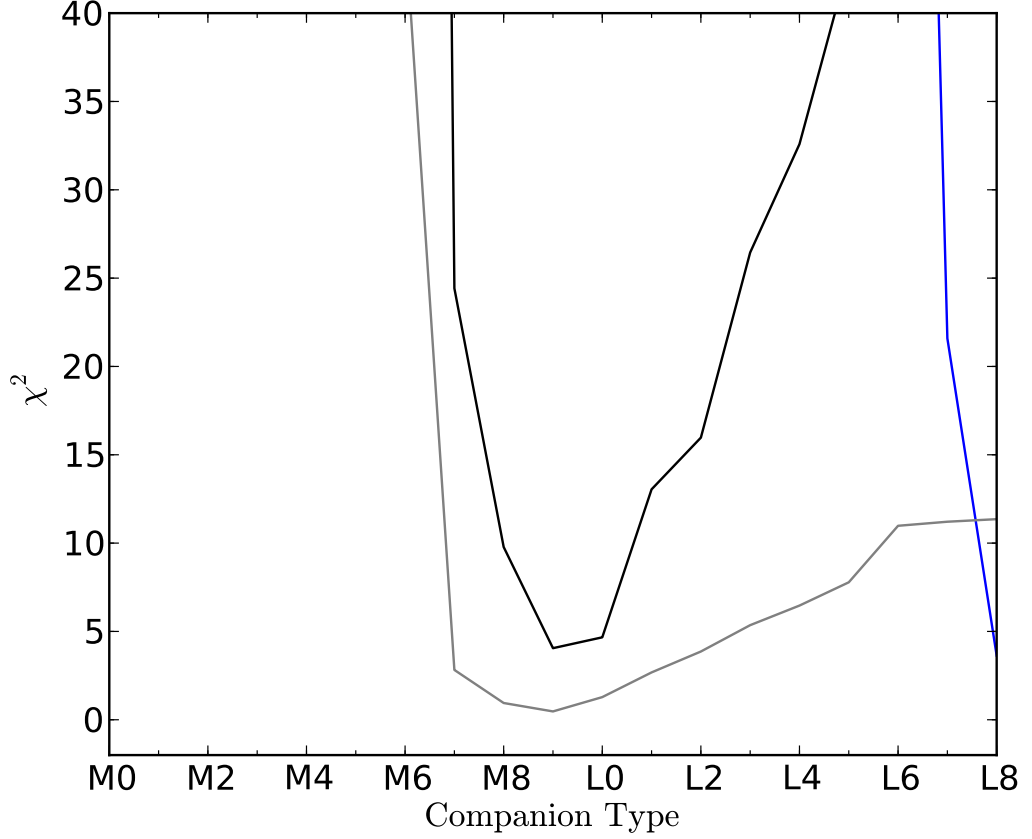
Figure 5.4: Reduced χ^2 as a function of companion type for three white dwarfs with well constrained companions using the photometric method. χ^2 is calculated from comparing the UKIDSS JHK magnitudes with those of the low-mass companions of Hoard et al. [2007]. SDSS J0135+1145, SDSS J0842+0004 and SDSS J0925-0140 are plotted as blue, grey and black, respectively. We find that a good fit (DAire or DA:ire) has a reduced $\chi^2 \lesssim 10$, a bad fit (DAire: or DA:ire: in Tables A.1 and A.2) has $\chi^2 \sim 10 - 100$ and a QSO has $\chi^2 \sim 100 - 1000$. SDSS J0135+1145 (blue) only has an excess in the K-band, which cannot be reproduced by any M-type, and most L-type companions. It is, however, consistent with a later-type brown dwarf or dust disc.
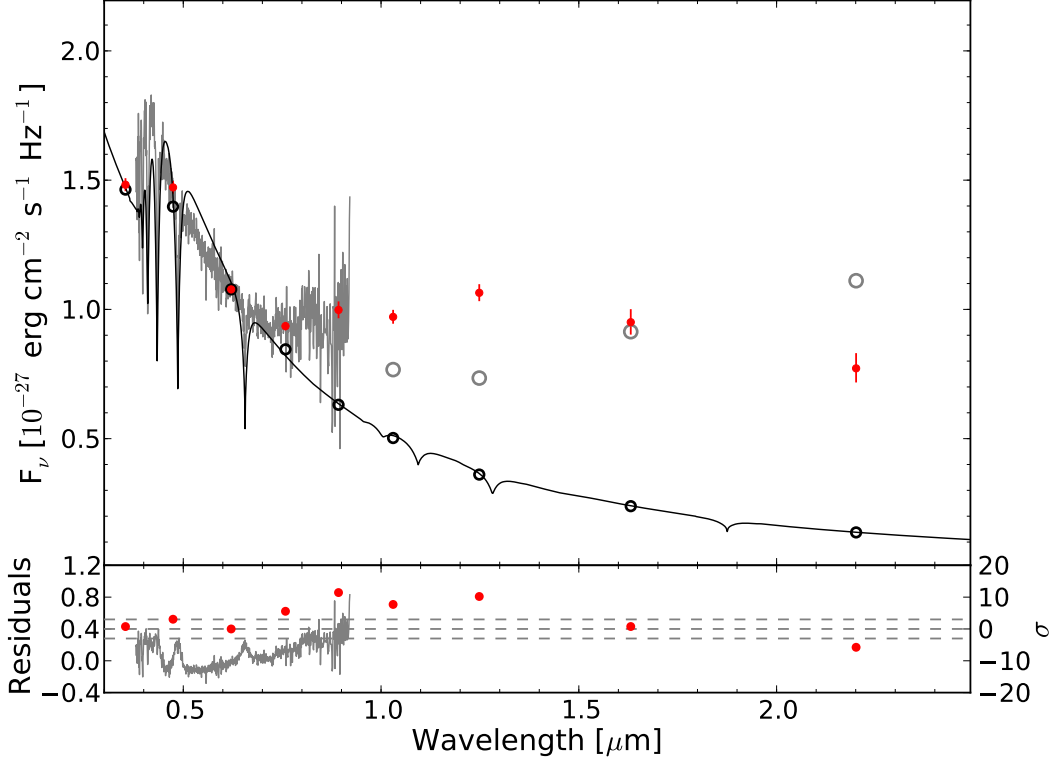
Figure 5.5: The SED of SDSS J1619+2533, an example of a spectroscopically confirmed DA white dwarf where the photometric method substantially underestimates the white dwarf temperature. The best fit to the spectrum is a $T_{eff} = 25595K$ and $\log(g) = 7.21$ DA white dwarf model ($M_{wd} = 0.33 \pm 0.04\,M_\odot$), whereas the photometric fitting method finds the best solution at $T_{eff} = 18000K$ and $\log(g) = 9.5$, the latter is plotted here in black. Within the photometric method, the lower temperature (and higher gravity) leads to the distance being substantially underestimated, and therefore the flux of the companion being overestimated. Fitting the SED with the two-component model described in Sect. 5.2.2 compensates for the low distance by choosing a companion with a larger absolute magnitude, i.e. a later spectral type. For SDSS J1619+2533, the spectroscopic method results in a M4 type companion, the photometric method in an L6 companion. Because the optical-IR SED can not be well fitted with any companion type at the photometric distance, this object is flagged as "bad fit" in Table A.3.

Table 5.2: Objects with an infrared excess split by estimated low-mass companion type. The first column shows the infrared excess candidates among the spectroscopically confirmed DAs (Table A.1) and the final column contains the information on the photometric-only sample (Table A.2), where there is no SDSS spectrum available for classification. The section in the middle shows all objects with SDSS spectroscopy for which fitting their $ugri$ photometry resulted in an infrared flux excess (Table A.3), split by their spectroscopic classification. This set of objects is useful to gauge the contamination of photometric-only infrared excess DA candidates by other types of objects. It also allows the like-for-like comparison of the infrared excess detection/modelling for genuine DA white dwarfs. To aid this comparison of the two methods, the column "DA (w SIRE)" lists the spectroscopically confirmed DA white dwarfs that exhibit an infrared flux excess when fitted with both the spectroscopic and photometric method, and the column "DA (wo SIRE)" lists 6 spectroscopically confirmed DA white dwarfs that are found to have an infrared excess only when analysed with the photometric method. A "-" mark denotes that the corresponding entry is not possible. "No Phot IR Excess" means that no photometric excess was found, even though a spectroscopic excess is seen.

Primary Type ⇒ Companion Type ⇓	Spectroscopic	Spectroscopic using Photometric Method							Photometric
	DA	DA w SIRE	DA wo SIRE	NLHS	WDMS	DAH	QSO	Total	-
M-type	16	9	1	10	2	0	0	22	15
L-type	19	11	0	12	1	0	0	24	19
$\geq L7$ or disc	7	6	2	0	0	0	0	8	4
QSO	-	0	0	0	0	0	323	323	40
Bad fit	0	4	3	9	1	3	0	20	27
No Phot IR Excess	-	12	-	-	-	-	-	12	-
Σ	42	42	6	31	4	3	323	409	105

5.2.3 Comparison of the spectroscopic and photometric methods

The results from using either the spectroscopic or purely photometric methods to find infrared excess can be directly compared because *all* the objects with SDSS spectra also have SDSS photometry. We discuss in the following sub-sections how well the spectroscopic and photometric method compares for genuine DA white dwarfs (Sect. 5.2.3.1), what can be learned from the spectroscopic contaminants that show an infrared excess when fitted with the photometric method (Sect. 5.2.3.2, 5.2.3.3), and how additional information such as infrared colours and proper motion could be used to suppress contaminants in the photometric-only sample (Sect. 5.2.3.2).

5.2.3.1 DA white dwarfs

Of the 42 spectroscopic DA white dwarf infrared excess candidates, 30 ($\sim 71\%$) are recovered by the photometric fitting method as well (column "DA w SIRE" in Table 5.2, 9 M-type, 11 L-type, $6 \geq L7$-type companions/debris discs and 4 "bad fits", which are marked as "DAire:" in Table A.2), and 12 do not show an excess when using the photometric method. These 12 objects are close to the $\sim 3\sigma$ limit in the spectroscopic method and were not recovered by the photometric method because of the larger uncertainty on effective temperature leading to the excesses being within the combined model and flux errors. 6 objects with DA white dwarf SDSS spectra are found to have an infrared excess in the photometric method, but do not exhibit an infrared excess when using the spectroscopic method (column "DA wo SIRE" in Table 5.2). Three of these have excesses which are accentuated by a slightly hotter photometric fit compared to the spectroscopic one. They fall just outside the criteria (Section 5.2.1) for having an excess in the spectroscopic method. For the other three objects the SDSS spectra are too poor to obtain reliable T_{eff} and $\log(g)$ measurements from fitting their Balmer lines. Therefore an excess was not recognised in the spectroscopic method. However, the photometric data were good enough and thus these three objects are classified as photometric infrared excess candidates. We may therefore expect $\sim 9 - 17\%$ (3/36–6/36) spurious infrared excess candidates from the photometric method. All objects that display an infrared excess either in the spectroscopic, or the photometric method, and have an SDSS spectrum are listed in Table A.3.

Table 5.2 also lists the infrared excess candidates split by modelled companion type. Among the 30 objects which are defined as infrared excess candidates in both methods, the distribution of companion type has a similar form. $\sim 80\%$ of the companions have M or early L spectral types (split evenly between the two classes),

and the remaining $\sim 20\%$ have companions $\geq L7$, i.e. we consider these brown dwarf or debris disc candidates.

As briefly outlined in Sect. 4.2.2, the temperatures resulting from the photometric fits are systematically too low, and this will introduce a bias in the spectral type of the companion. The flatter SED of a cooler white dwarf will reduce/distort the infrared flux excess relative to the white dwarf, and therefore a later type companion will provide sufficient flux to account for the excess. An additional effect is that a cooler white dwarf will suggest a lower distance when fitting the *ugri* magnitudes. Underestimating the distance to the system will lead to an underestimate of the absolute flux of the companion. To compensate for this, the fit to the companion will resort to a companion with a larger absolute magnitude, i.e. lead to a companion spectral type that is too late. A moderately extreme example of these effects is shown in Fig. 5.5 (SDSS J1619+2533, see Table A.3). Assuming that the spectroscopic fit parameters are correct, the white dwarf temperature is underestimated by ~ 8000K, which leads to an L6 companion in the photometric method, as opposed to an M6 companion resulting from the spectroscopic analysis. This object is marked in the notes column as having a bad fit to the companion in the photometric method, where a "bad fit" is defined as an object having an excess which is inconsistent with any companion type (at the photometric white dwarf distance).

5.2.3.2 Quasar elimination

As can be seen in Table 5.2, a significant fraction (323) of the infrared excess candidates from the photometric method with spectra are quasars. This is almost the entire population of spectroscopically confirmed quasars in the DA white dwarf sample with UKIDSS magnitudes. The remaining 5 quasars do not have sufficient infrared data to show their quasar nature, but equally are not flagged as infrared excess candidates. This is caused by the flat SED exhibited by QSOs [Covey et al., 2007]. When modelled with a DA white dwarf, they generally have an effective temperature of ~ 8000K and have an infrared excess that is much higher than physically possible for an M-dwarf or brown dwarf companion at the distance of the (photometric) DA fit (e.g. Fig. 5.6). Because of the (apparent) low effective temperatures, the quasars also generally have low (apparent) distances. These properties, however, overlap with those of genuine cool nearby white dwarfs and cannot be used to straightforwardly distinguish between white dwarfs and quasar. Another common sign of QSOs are large jumps in brightness between adjacent magnitudes (caused by emission lines) that are not seen in any of the genuine DA white dwarfs with infrared excess. Given that we correctly classified, on the base of their optical-IR
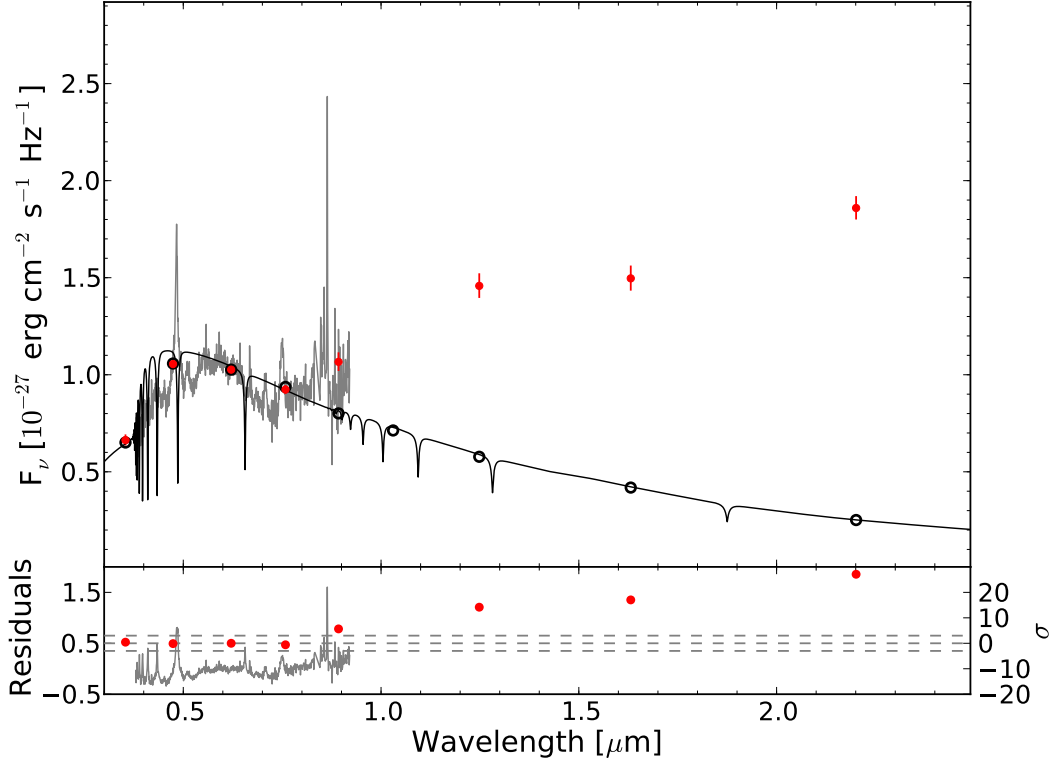
Figure 5.6: The SED of SDSS J0046−0044, an example of a quasar, that was selected as a candidate DA white dwarf (based on its colours, Table 4.1) with possible infrared excess ("DA:ire:") by the photometric method. The best-fit to the *ugri* photometry is found for $T_{eff} = 9000K$ and $\log(g) = 7.0$ at a distance of 37pc and shown as black line. The excess over the model keeps rising steeply into the mid-IR and can not be modelled by any companion type at the distance of the (photometric) DA fit, identifying this object as a quasar contaminant.

SED, 99% of (spectroscopic) quasars contaminants that were found as DA:ire by the photometric method, we are confident that we can identify the vast majority of quasars among the photometric-only sample.

Among the photometric-only sample of infrared excess candidates, we find 38 objects whose SEDs are very similar to those of our 323-strong spectroscopically confirmed quasar sample and which we therefore believe to be quasars as well. Optical spectroscopy is needed to confirm their nature. These have been removed from Table A.2 and can be found in Table A.4.

5.2.3.3 Contamination by NLHS and non-DA white dwarfs

Contaminant NLHS and non-DA white dwarfs are more difficult to identify and remove from the photometric-only DA candidate sample, as their overall SEDs are all rather similar. Closer inspection of the SDSS spectroscopy of the NLHS and cross-checking them in Simbad suggests that a large fraction of them are sdB stars (discussed in more detail in Section 1.3 and Chapter 7). The bulk of subdwarfs are believed to have formed in binary interactions [Han et al., 2003; Heber, 2009] and therefore it is expected that a large majority will still have companions. Such companions would cause an infrared flux excess over the Rayleigh-Jeans tail of the subdwarf, and it is hence likely that our photometric-only sample of candidate DA white dwarfs with infrared excess contains a significant contamination from sdB plus low-mass companion binaries.

Given that we fit all photometric objects with DA model spectra, we may expect some imperfections in the fits to the photometric NLHS objects. Nevertheless, the detection of a near-IR flux excess over the Rayleigh-Jeans tail of the model is likely to be correct for many of the NLHS objects among the photometric sample. However, a DA fit to the photometry of a physically much larger NLHS object will dramatically underestimate its radius, and hence its distance. Consequently, fitting the companion with the composite model (Sect. 5.2.2) will result in a spectral type of the companion that is much too late.

From the spectroscopic sample, we find that the frequency of NLHS inside the DA colour selection (Table 4.1, Fig. 4.1) is 14.6% (Table 4.2), however, the level of contamination is strongly magnitude-dependent. Figure 5.7 (left) shows the distribution of NLHS and DA white dwarfs as a function of g-band magnitude. The ratio of these two, and thus the expected level of contamination of the photometric-only sample, is shown in the middle panel (this assumes that the majority of quasars have been removed because of the characteristic shape of their SED). The contamination of the photometric-only DA candidate sample by NLHS drops significantly towards fainter g magnitudes. Subdwarfs are ~ 100 times brighter than white dwarfs and therefore apparent magnitudes of $g \sim 18 - 19$ sample distances of many kpc. This is several times the exponential scale height of the Galactic thick-disc population, and hence the number of sdBs at such large distances is relatively small (see Chapter 7 for a more detailed discussion on the scale height of subdwarf stars). Figure 5.7 (right panel) shows the photometric-only infrared excess candidates as a function of g magnitude, where we can assume that most objects with $g \lesssim 16$ are likely to be NLHS. We explicitly search for subdwarfs with companions in Chapter 7.

An additional clue on the NLHS vs DA classification of the photometric-only

objects comes from their location in the $(u-g, g-r)$ colour-colour diagram (Fig. 5.8, bottom right panel), where the majority of the spectroscopically confirmed NLHS objects are concentrated at the blue end of the "DA" banana. We can therefore assume that NLHS are the primary contaminants of the photometric sample in this region as well (Fig. 5.8, top right panel).

Assuming that the distribution of NLHS contaminants is similar between the spectroscopic and photometric-only sample, we expect ~ 259 of the 1771 photometric objects to be NLHS. When fitting the photometric sample, 31 (12%) spectroscopically confirmed NLHS were found to have an infrared excess (red dots in the bottom right panel of Fig. 5.8). Again, assuming that the contamination among the spectroscopic and photometric samples is similar, we would expect that ~ 37 (12% of 259) of our photometric DA candidates with infrared excess (DA:ire and DA:ire:) are in reality NLHS, primarily sdB stars with main sequence companions. These are still interesting in their own right (e.g. Sect. 5.3.3.2), but not the primary focus of the infrared excess search (a detailed investigation of subdwarfs with main-sequence star companions is given in Chapter 7).

In contrast to the above discussion on NLHS, fitting non-DA white dwarfs with DA white dwarf models is likely to provide a reasonably good estimate of all system parameters, including the companion type – the downside being that on the base of photometry only, it is nearly impossible to differentiate between DA and non-DA white dwarfs. However, based on the statistics of the Eisenstein et al. [2006], we only expect a small level of contamination (~ 9 per cent) by non-DA white dwarfs (Table 4.2).
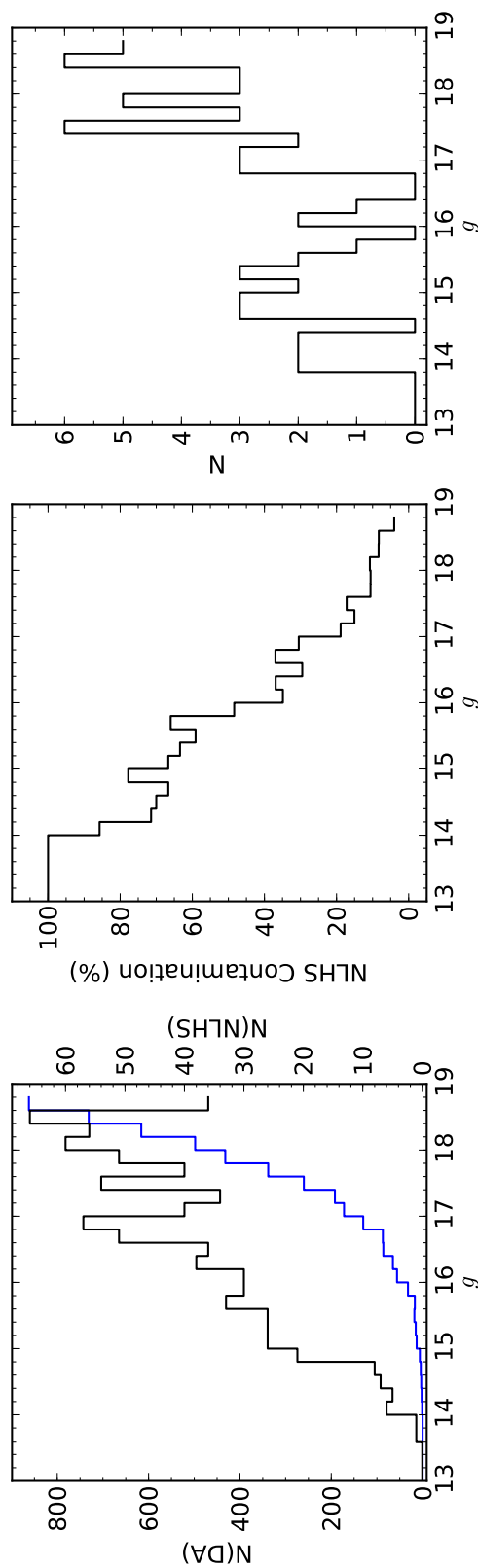
Figure 5.7: Left panel: The distribution of DA white dwarfs (blue, left hand scale) and NLHS (black, right hand scale) as a function of g-band magnitude. Middle panel: the fraction of NLHS as a function of g-band magnitude. The probability of contamination by NLHS clearly drops with increasing g-band magnitude. Right panel: distribution of the photometric-only infrared excess candidates, the brightest of these group are most likely NLHS rather than DA white dwarfs.
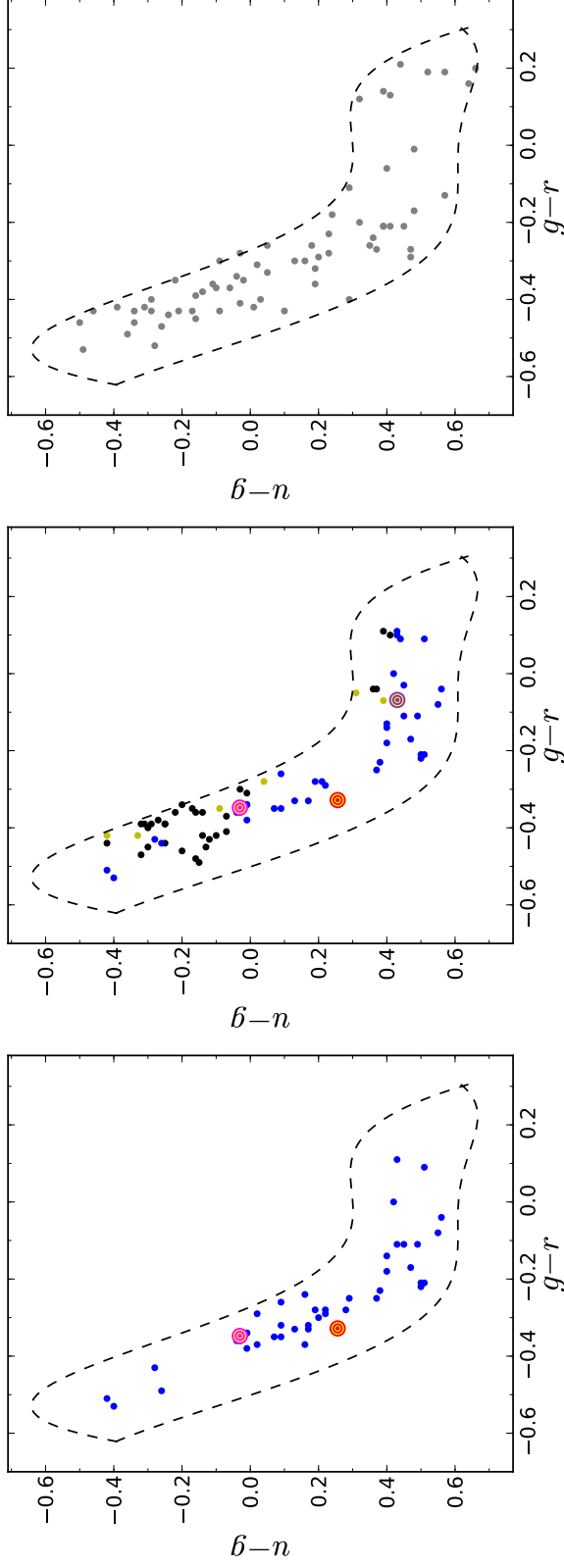
Figure 5.8: Left hand panel: the distribution of the 42 spectroscopically confirmed DA white dwarfs with infrared excess (Table A.1) in the $(u-g, g-r)$ colour-colour space. The black dashed line outlines the $(u-g, g-r)$ DA colour selection (Table 4.1, Fig. 4.1). Middle panel: the distribution of the 74 infrared excess objects found by the photometric method (excluding quasars and quasar candidates), with DA white dwarfs, non-DA white dwarfs and NLHS shown in blue, yellow, and black, respectively. SDSS J1228+1040 and SDSS J1043+0855, two DA white dwarfs known to have debris discs, are indicated by pink and red bulls-eye symbol, respectively (Left hand and middle panels, see Sect. 5.3.1.1, 5.3.1.2). SDSS J1212+0136, a known magnetic white dwarf with a brown dwarf companion is shown as purple bulls-eye symbol (middle panel only, see Sect. 5.3.1.3). Right hand panel: the distribution of the 67 photometric-only infrared excess candidates.

5.2.3.4 Independent checks: infrared colours and proper motions

Our method of identifying infrared excess candidates follows Tremblay & Bergeron [2007], i.e. fitting model spectra to SDSS spectroscopy and photometry. In this section, we carry out an independent investigation of our sample using colour-colour diagrams, such as previously explored by e.g. Wachter et al. [2003] and Hoard et al. [2007], and test our classification of the photometric-only systems by making use of proper motions.

Figure 5.10 shows the distribution of the spectroscopic SDSS/UKIDSS sample in the $(z - H, H - K)$ colour-colour space (left panel). Using model white dwarf colours, it can be seen that the DA cooling sequence runs from top left to bottom right through the white dwarf group. The NLHS and DA white dwarfs are clearly separated from the quasars, which can be understood as stars are on the Rayleigh-Jeans tail in the infrared, whereas quasar follow a flatter power law [Covey et al., 2007]. Therefore, as an additional test of how reliable our classification of the photometric-only quasar candidates works, we inspected the infrared colours of the photometric-only sample. Choosing an empirical cut of $H - K > 0.627$ selects 89.6% of the quasar contaminants in the spectroscopic sample. Adopting the same $H - K$ cut for the photometric-only sample flags 38 objects as quasar candidates. This includes 31 of the 38 photometric-only objects already identified as quasar candidates on the base of their SED (Sect. 5.2.3.2; see Table A.4; of which only 37 have both H and K measurements). In addition, two of the $H - K$ selected QSO candidates correspond to the two "weak" photometric-only quasar candidates listed in Table A.2.
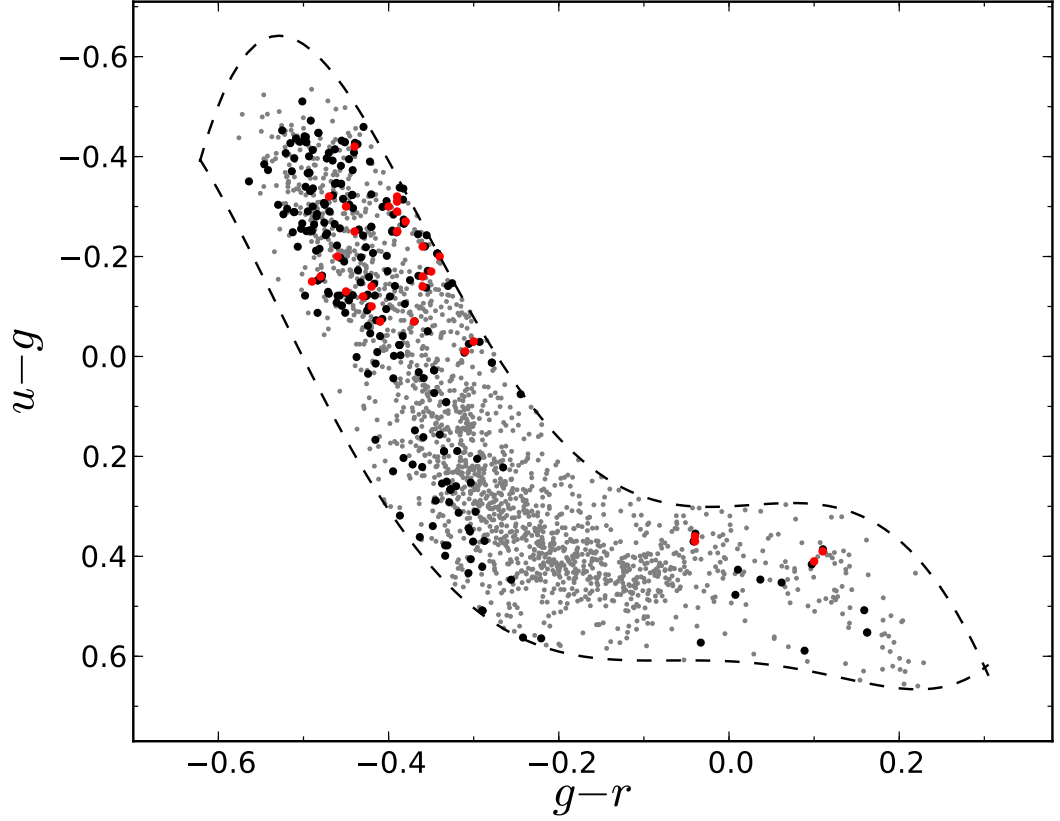
Figure 5.9: All photometric-only objects satisfying our DA constraint set from Table 4.1 (1771 objects, gray dots), spectroscopically classified NLHS (209 objects, black), and spectroscopically classified NLHS with an infrared excess (31 objects, red). The figure follows the same format as Figure 5.8. Based on the analysis of the spectroscopic sample (Sect. 5.2.3.3), we estimate that $\sim 12\%$ of the photometric-only objects are NLHS, with a strong concentration towards the (blue) top-end of the DA "banana".
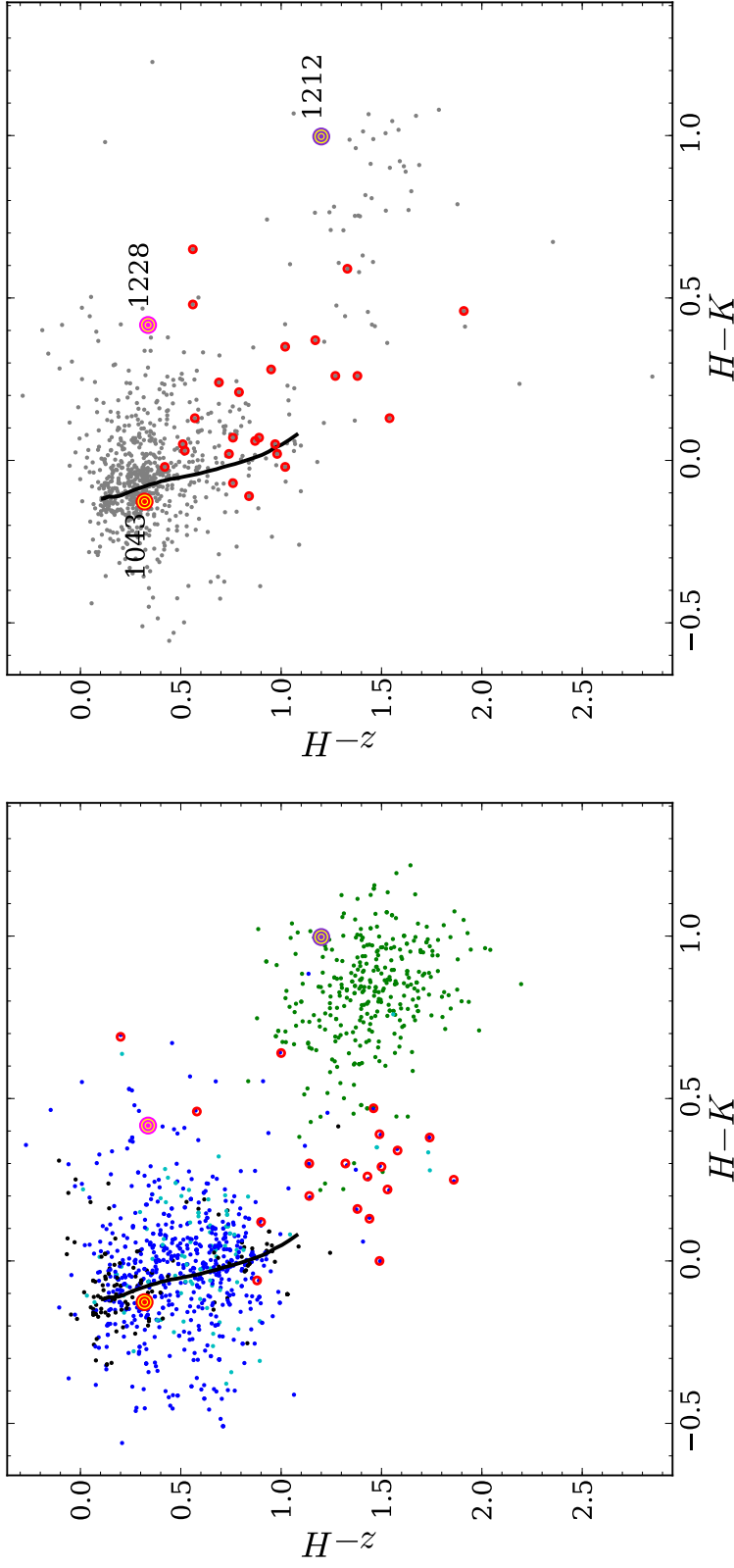
Figure 5.10: Location of the SDSS/UKIDSS sample in $(z - H, H - K)$ colour space. The left panel shows the objects with SDSS spectra, DA white dwarfs, NLHS, other white dwarfs and quasars in blue, black, cyan and green, respectively. The 23 robust "DAire" infrared excess objects from Table A.1 are shown as red open circles. The positions of SDSS J1228+1040, SDSS J1043+0855 and SDSS J1212+0136, two white dwarfs in the sample known to have a debris disc and a DAH white dwarf plus brown dwarf binary (see Sect 5.3.1.1, 5.3.1.2 and 5.3.1.3), are indicated by pink, red and purple bulls-eye symbols, respectively. A track of model DA white dwarf colours for 6000K $\leq$ T$_{\text{eff}}$ $\leq$ 100000 K and $\log(g) = 8.0$ is plotted as a solid black line. High temperature white dwarfs are found at the top left end of the line. The scatter about this line cannot be explained by a spread in $\log(g)$ alone, but by uncertainties on the magnitudes (primarily those from UKIDSS) and background contamination. The photometric-only objects are shown in the right hand panel, with the 29 robust "DA:ire" infrared excess candidates (Table A.2) again highlighted in red.

A third concentration of objects can be seen in Fig. 5.10 in the region between the DA white dwarfs and the quasars, a significant fraction of which are DA infrared excess candidates. The presence of an infrared excess over the stellar flux distribution results in a flatter spectral slope, and hence moves these objects closer to the quasar locus. On closer inspection, some white dwarfs in this region are found to be blended sources or suffer from background contamination from a nearby galaxy and therefore were not included as infrared excess candidates.

In summary, adopting $H - K > 0.627$ would efficiently remove the bulk of contaminating quasars from the photometric-only sample, however, such a cut would also remove a handful of genuine white dwarfs with the largest infrared excess emission (such as e.g. SDSS J1228+1040, see Sect. 5.3.1.1).

Given that white dwarfs are nearby low-luminosity objects, they are expected to exhibit larger proper motions than the more luminous NLHS, and quasars are not expected to show any significant proper motion at all. Thus, proper motions can be used to distinguish between white dwarfs and quasars in the region with $H - K > 0.627$. We have retrieved proper motions from DR7 for all objects in the SDSS/UKIDSS sample. Figure 5.12 (left panel) shows a cumulative proper motion distribution for the white dwarfs, quasars and NLHSs. Based upon this, we chose a cut in proper motion of p.m. $\leq 10 \, \mathrm{mas/yr}$ to define low proper motion objects such as quasars. In the spectroscopic sample, this cut selects 7%, 74% and 97% of the DA white dwarfs, NLHS and quasar, respectively, efficiently eliminating the majority of the quasars without removing too many white dwarfs.

Figure 5.12 (middle panel) plots the magnitude of the proper motion as a function of $H - K$. The statistical significance of the proper motion is encoded in the size of the points, where larger points denote more significant proper motions. As expected, the spectroscopically objects classified as NLHS stars and quasars show very small proper motions, which are in most cases consistent with zero. The right hand side panel of Fig. 5.12 shows the location of 35 photometric-only objects classified as quasar because of the characteristic shape of their SEDs (see Table A.4) that have both $H - K$ colours and proper motions. The vast majority of these objects are contained within $H - K > 0.627$ and p.m. $\leq 10 \, \mathrm{mas/yr}$, corroborating our SED-based classification.

A small number of objects with $H - K > 0.627$, i.e. within the "quasar" region, display large and statistically significant proper motions (Fig. 5.12, middle panel). These are listed in Table 5.3. Among those objects are three spectroscopically confirmed DA white dwarfs. At closer inspection, the UKIDSS magnitudes of SDSS J1244+0402 may be contaminated by a nearby background ob-

ject, which would lead to a spurious $H - K$ colour. The other two spectroscopic DA white dwarfs, SDSS J0753+2447 and SDSS J1557+0916 have very red $H - K$ colours and high proper motions. They are therefore excellent infrared excess candidates. Applying the same procedure to the photometric-only DA candidate sample, SDSS J0959−0200 is the strongest infrared excess candidate among the three photometric-only objects (see Section 5.3.4). SDSS J1440+1223 and SDSS J1509- +0539 also appear to suffer from background contamination.

Another four spectroscopic objects with quasar-like infrared colours and high proper motions are classified as three magnetic white dwarfs (DAH) and one DZ white dwarf. We would expect that the infrared spectra of all of these objects should be close to a Rayleigh-Jeans distribution, suggesting that the inferred infrared excess is probably real. In fact, one of the DAH, SDSS J1212+0136 is a well-studied DAH plus brown dwarf binary [Schmidt et al., 2005], which exhibits a genuine infrared excess [see Sect. 5.3.1.3; Debes et al., 2006]. This inspired the further investigation of the other two DAH white dwarfs [see Section 5.3.4; Breedt et al., 2012].

As discussed in Section 1.2.2.1, the metals seen in DAZ white dwarf atmospheres are from recent or ongoing accretion [e.g. Dupuis et al., 1993a; Koester & Wilken, 2006]. This accretion is often thought to be associated with a dusty debris disc originating from the tidal disruption of rocky asteroids. The DZ found here, SDSS J1342+0522 (see Figure 5.11), exhibits a very red $H - K$ colour. The excess in K over the model spectrum is slightly under 3σ and therefore is, in our classification scheme, only a marginal candidate for having an infrared excess. This DZ white dwarf warrants further investigation. *Spitzer* observations would be ideal, especially as SDSS J1342+0522 does not appear in the WISE catalogue.

Finally, eight quasars have nominally significant proper motions ($\sim 3 - 5\sigma$; see Table 5.3), which highlights the fact that the SDSS vs USNO-B proper motions have to be considered with caution: among a total of 328 quasars with SDSS spectra and UKIDSS data, we would expect only one to have a 3σ significant proper motion, and none at 4σ.

We conclude that dissecting the white dwarf sample selected with our constraint set (Table 4.1) using colour-colour diagrams and proper motions leads to mutually consistent results when compared to our primary methodology (Sect. 5.2-5.2.2), but the spectroscopic modelling provides an additional wealth of information.
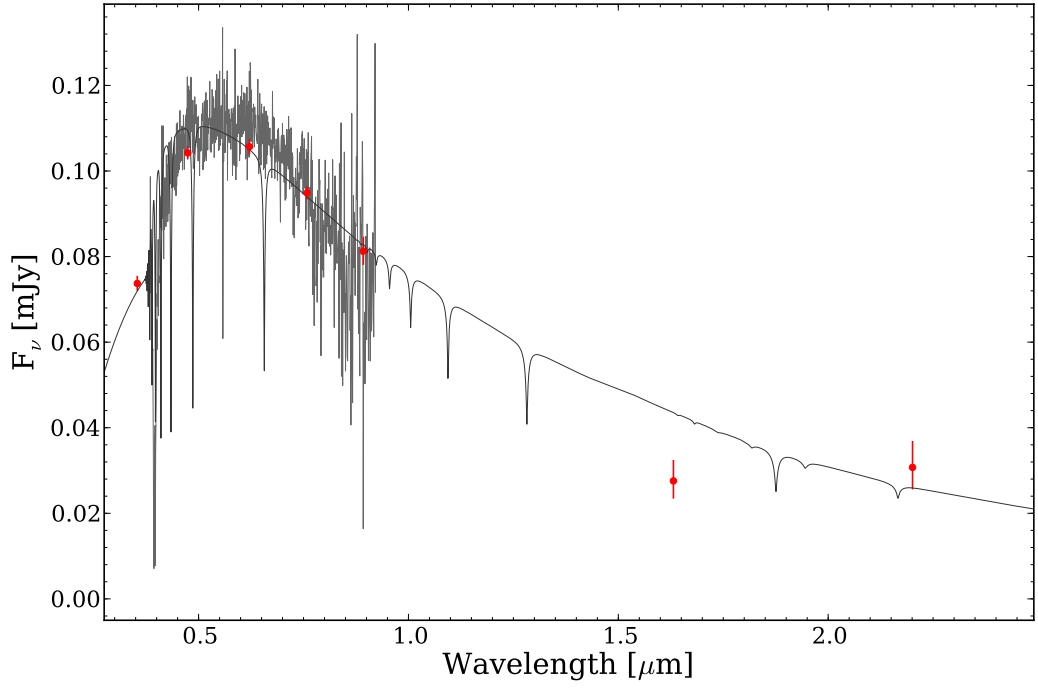
Figure 5.11: The SED of SDSS J1342+0522, a DZ white dwarf with a possible infrared excess. The best-fit to the *ugri* photometry is found for $T_{eff} = 9000K$ and $\log(g) = 7.75$ and shown as black line. The excess over the model is slightly under 3σ in the K-band and therefore is, in our classification scheme, only a marginal candidate for having an infrared excess.
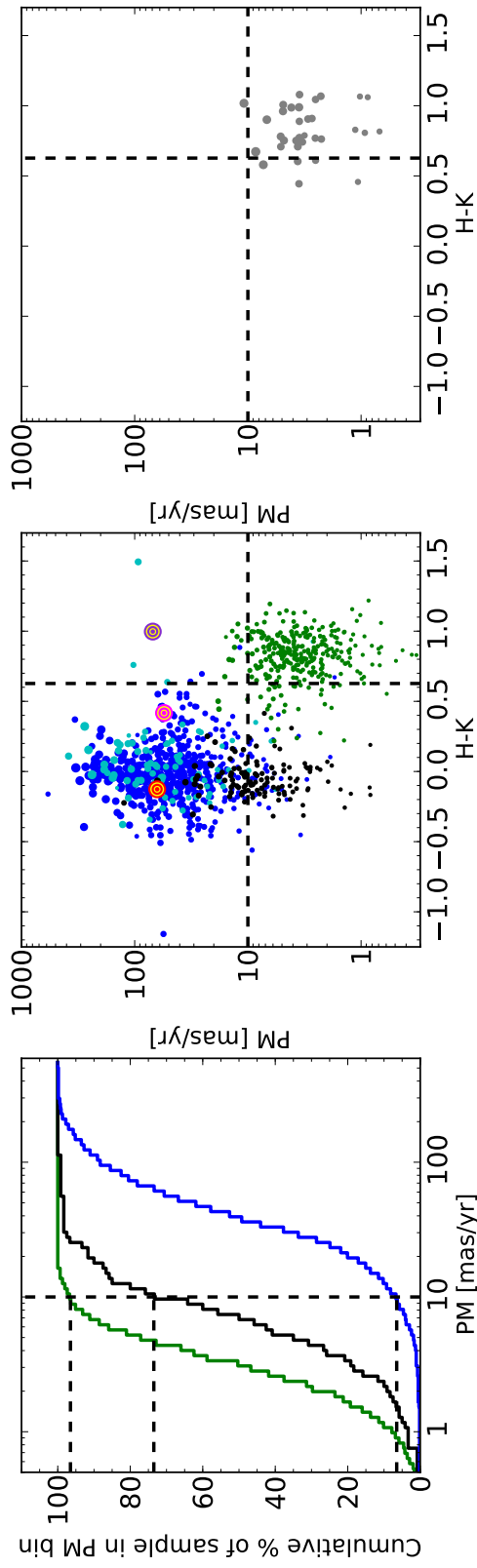
Figure 5.12: Left panel: The cumulative histogram of spectroscopically confirmed DA white dwarfs (blue), NLHS (black) and quasar (green) as a function of proper motion (PM). Black dashed lines show a proper motion of 10mas/yr and corresponding population levels. 7% of DA white dwarfs are contained within the bin of PM $\leq$ 10mas/yr. Similarly, 74% of NLHS and and 97% of quasar. Middle panel: distribution of proper motions as a function of $H - K$ colour, using the same colour-coding, and showing in addition non-DA white dwarfs in cyan. The significance of the proper motion is encoded in the size of the points, where larger points denote more significant proper motions, clipped at a maximum of 30σ. Black dashed lines show PM = 10mas/yr and $H - K = 0.627$. The position of the three benchmark objects SDSS J1228+1040, SDSS J1043+0855 and SDSS J1212+0136 (see Sect 5.3.1.1, 5.3.1.2 and 5.3.1.3) are indicated by pink, red and purple bulls-eye symbols, respectively. Right panel: same as the middle panel, but showing the (35) quasar candidates identified on the basis of their SED shape (see Table A.4) which have both H and K band data in UKIDSS and proper motions in SDSS DR7.

5.2.4 Overall numbers

A summary of the numbers of objects at each stage of the analysis is given in Table 5.4. The total numbers of white dwarfs with near-IR excess are broken down according to the spectral type of their companions in Table 5.2.

We find that 3.3% (42 of 1275) of the SDSS spectroscopically confirmed DA white dwarfs with at least one of the $YJHK$ UKIDSS magnitudes have an IR excess and are therefore candidates for having a companion or a debris disc. However, this does not take account of the fact that the sample of white dwarfs is incomplete even within UKIDSS DR8 because for many only subsets of the infrared magnitudes are available. Thus we are limited by UKIDSS coverage and the real number is higher. 2.0% of the spectroscopic DA white dwarfs are candidates for having a companion of type L0 or later, i.e. brown dwarf candidates. Similarly, 0.5% are promising disc candidates, having an excess compatible with a companion type of L7 or later. If we only discuss the objects with a detection in the K-band (required for detecting a disc), 1.2% are disc candidates, and only including objects where we are confident of the infrared excess (not "DAire:" in Table A.1; see Section 5.2.1 and 5.2.2), a lower limit of 0.8% of DA white dwarfs have a brown dwarf companion.

For the photometric-only sample, where we have fitted the SDSS and UKIDSS photometry, 5.9% are infrared excess candidates. However, this number will be affected by the efficiency of white dwarf selection (62.3%) and the efficiency of removing contaminants. Assuming that we remove all the obvious photometric-only quasar contaminants from the infrared excess objects (38, see Table A.4), the remaining 67 photometric-only infrared excess candidates will be either DA white dwarfs or NLHS. As discussed previously, we estimate that ~ 37 of these are NLHS (Section 5.2.3.3). This number is very similar to the amount of "bad fits" found in from the photometric method and so we believe the majority of "bad fits" come about from NLHS contaminants in the photometric-only sample. Therefore, we expect ~ 30 (2.7% of ~ 1103) genuine DA white dwarfs with infrared excess among the photometric-only DA white dwarf candidates. These infrared excess candidates show a similar distribution in companion type when compared to the spectroscopic sample. Considering only the objects we are confident of the excess (not "DA:ire:" in Table A.2; see Section 5.2.1 and 5.2.2), 1.8% (19) of the photometric-only DA white dwarfs candidates are likely to have a brown dwarf companion.

Table 5.3: Objects with quasar-like infrared colours ($H - K \geq 0.627$), but large (≥ 10mas/yr) and statistically significant ($> 3\sigma$) proper motions. The significance of the proper motions is listed as $\sigma_{\mathrm{p.m.}}$. Classifications are given for the objects that have SDSS spectra. The comment "BG object" refers to a second resolved source being seen in the UKIDSS images. These are most likely background galaxies which would significantly affect the $H - K$ colour. For full coordinates, refer to the online spectroscopic and photometric-only tables available via CDS.

Name	$H - K$	p.m. (mas/yr)	$\sigma_{\mathrm{p.m.}}$	Class	Comment
0043+0005	0.79 ± 0.06	13.68 ± 3.06	4.5	QSO	
0753+2447	0.64 ± 0.24	32.16 ± 3.20	10.0	DA	
0858+0938	0.88 ± 0.03	13.13 ± 3.01	4.4	QSO	
0959−0200	0.65 ± 0.15	30.25 ± 3.10	9.8	-	(1)
1031+0341	1.05 ± 0.08	12.25 ± 3.92	3.1	QSO	
1142+1347	1.02 ± 0.05	10.10 ± 2.81	3.6	QSO	
1212+0136	1.00 ± 0.06	69.19 ± 3.21	21.6	DAH	(2)
1244+0402	0.88 ± 0.17	11.80 ± 3.09	3.8	DA	BG object
1250+1549	1.49 ± 0.02	93.14 ± 3.12	29.9	DAH	(3)
1342+0522	0.64 ± 0.27	51.53 ± 3.24	15.9	DZ	
1427−0054	0.68 ± 0.04	15.99 ± 3.25	4.9	QSO	
1440+1223	1.43 ± 0.08	88.83 ± 2.65	33.5	-	BG object
1443+0910	0.96 ± 0.02	12.46 ± 2.98	4.2	QSO	
1509+0539	0.98 ± 0.25	48.29 ± 3.07	15.7	-	BG object
1514+0744	0.76 ± 0.07	102.64 ± 5.06	20.3	DAH	(3)
1553+0718	0.80 ± 0.01	14.64 ± 2.75	5.3	QSO	
1557+0916	0.70 ± 0.21	25.48 ± 2.85	8.9	DA	(1)
1557+2646	0.84 ± 0.04	10.07 ± 3.21	3.1	QSO	

(1) Farihi et al. [2012]

(2) A magnetic cataclysmic variable in a low state [Schmidt et al., 2005; Debes et al., 2006; Burleigh et al., 2006; Farihi et al., 2008a; Howell et al., 2008; Linnell et al., 2010].

(3) Breedt et al. [2012]

Table 5.4: Summary of numbers at each stage of the processing. The columns are split for the spectroscopic and photometric methods. The spectroscopic sample is also further split by the classification of the optical spectra.

Constraint	Spectroscopic Objects	Photometric-only Objects
Objects Satisfying SDSS Colour Cuts	7444	9341
Spectroscopically Confirmed		
DA white dwarfs	4636	
QSO	1280	
NLHS	840	
Other white dwarfs	661	
Other Objects	27	
Objects cross matched with UKIDSS with detection in any of Y, J, H or K	1990	1771
Spectroscopically Confirmed		
DA white dwarfs	1275	
QSO	328	
NLHS	209	
Other white dwarfs	172	
Other Objects	6	
Objects with Detections in		
H & K	1075	809
K	1108	840
Spectroscopically Confirmed		
DA white dwarfs	571	
QSO	316	
NLHS	124	
Other white dwarfs	94	
Other Objects	3	
IR Excess Objects	42	105

5.3 Notes on individual objects

Some objects of particular interest identified in the SDSS / UKIDSS cross-correlation are discussed below. We separate those into objects already known to host a disc or companion (Section 5.3.1), notable objects from the spectroscopic sample (Section 5.3.2), and the same from the photometric-only sample (Section 5.3.3).

5.3.1 Benchmark systems

Our spectroscopic sample contains two white dwarfs that were known to host debris discs and one magnetic white dwarf with a substellar companion, and hence they serve as a benchmark for our selection procedures.

5.3.1.1 SDSS J1228+1040

SDSS J1228+1040 is one of two DA white dwarfs in our SDSS/UKIDSS sample known to have a debris disc. The disc was initially identified because of the highly unusual emission lines of the Ca II 8200 Å triplet [see Figure 1.2; Gänsicke et al., 2006b], whose double-peaked shape can only be explained by metal-rich gas orbiting the white dwarf within its tidal disruption radius [Gänsicke et al., 2006b]. Near- and mid-IR observations revealed a substantial infrared excess over the white dwarf, unambiguously identifying a dusty component of the debris disc, in addition to the gaseous one [Brinkworth et al., 2009]. Our fits to the SDSS spectroscopy and photometry are shown in Fig. 5.13. The two fits differ in T_{eff} by 2000 K. However, this has very little effect on the extrapolated infrared magnitudes of the white dwarf, and the object shows a 3σ excess in H and 12σ in K, independent of the method used for fitting. At the temperature of SDSS J1228+1040, $\log(g)$ is not well constrained from fitting the *ugri* photometry alone, however, this primarily affects the widths of the hydrogen lines, and has a negligible effect on the spectral slope of the white dwarf model. This demonstrates that the detection of a genuine infrared excess is robust and independent of whether an optical spectrum is available.

Taking the infrared measurements at face value and ignoring our knowledge about this star, we have modelled the SDSS/UKIDSS spectral energy distribution as a white dwarf plus low-mass companion, which results in a most likely spectral type of $\geq$L6 for the companion. Based on the SDSS/UKIDSS data alone, it is impossible to distinguish between a low-mass companion and a dusty disc, but mid-infrared data data can break this degeneracy. We therefore classify infrared excess candidates that require a companion later than L7–8 as brown dwarf / dusty debris disc candidates

SDSS J1228+1040 exhibits a very red $H - K$ colour in the $(z - H, H - K)$ colour-colour diagram shown in Fig. 5.10, where it is clearly separated from the white dwarf model sequence. This region of the colour-colour space is therefore likely to harbour white dwarfs with a strong K-band excess. A significant number of the infrared excess candidates in Sect. 5.2.1 also lie in this region, as well as somewhat below (corresponding to a H and K-band excess). SDSS J1228+1040 is also prominent in Fig. 5.12 thanks to its relatively high proper motion and red $H - K$ colour. In summary, it is encouraging that this benchmark system indeed stands out in the various diagnostics we have considered.

5.3.1.2 SDSS J1043+0855

SDSS J1043+0855 is the second white dwarf in our sample known to have a gaseous debris disc [Gänsicke et al., 2007], though the evidence for an infrared excess in the near- and mid-IR is marginal [Melis et al., 2010; Brinkworth et al., 2012]. Based on the published results on this object, we would not expect to detect any excess in the UKIDSS photometry. In our analysis of the SDSS spectrum, we find $T_{eff} = 17912 \pm 360$ K and $\log(g) = 8.07 \pm 0.08$, consistent within the errors with the parameters in Gänsicke et al. [2007]. The corresponding model is an excellent fit to both the SDSS and UKIDSS photometry, with no detection of an infrared excess in any of the near-IR bands (Fig. 5.14). Adopting the K_s flux from Melis et al. [2010] rather than the UKIDSS measurement gives a 2σ excess above our model, which would again not be considered as an infrared excess candidate within our classification scheme (Sect. 5.2.1). This conclusion is confirmed by the fact that SDSS J1043+0855 falls very close to the model white dwarf sequence in Fig. 5.10. This system is an example where there either is no dusty disc, or where the dusty disc is too faint, e.g. edge-on, to be detected in the near-IR.
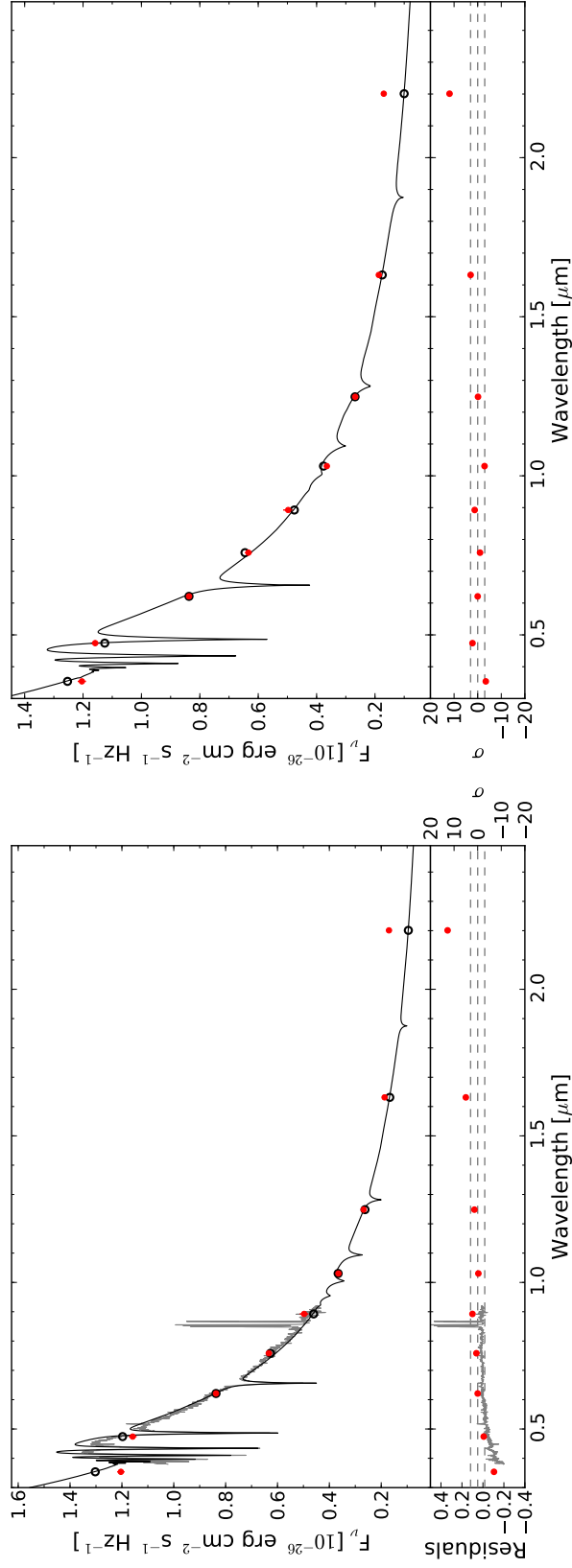
Figure 5.13: SDSS J1228+1040 is one of two DA white dwarfs in our SDSS/UKIDSS sample that are known to have a gaseous debris disc [Gänsicke et al., 2006b]. It also exhibits a substantial infrared excess in VLT/ISAAC and *Spitzer* observations [Brinkworth et al., 2009], and hence serves as a general benchmark for our method. Fitting the SDSS spectrum (left panel) results in $T_{eff} = 22037 \pm 199$K, $\log(g) = 8.19 \pm 0.04$, implying $M_{wd} = 0.74 \pm 0.02 M_\odot$, and a distance of 134 ± 3pc, consistent with the parameters derived by Gänsicke et al. [2006b]. The SDSS spectrum is shown in gray, the best-fit model in black, observed $ugrizYJHK$ fluxes in red, and model fluxes in these bands as black circles. The lower panel shows the residuals from the fit (in flux units on the left axis, and statistical significance on the right axis). The corresponding fit to the $ugri$ photometry gives a somewhat lower temperature, $T_{eff} = 20000^{+10}_{-10}$K, $\log(g) = 8.5^{+0.03}_{-0.13}$K, which has no noticeable effect on the detection of the infrared excess (right panel).
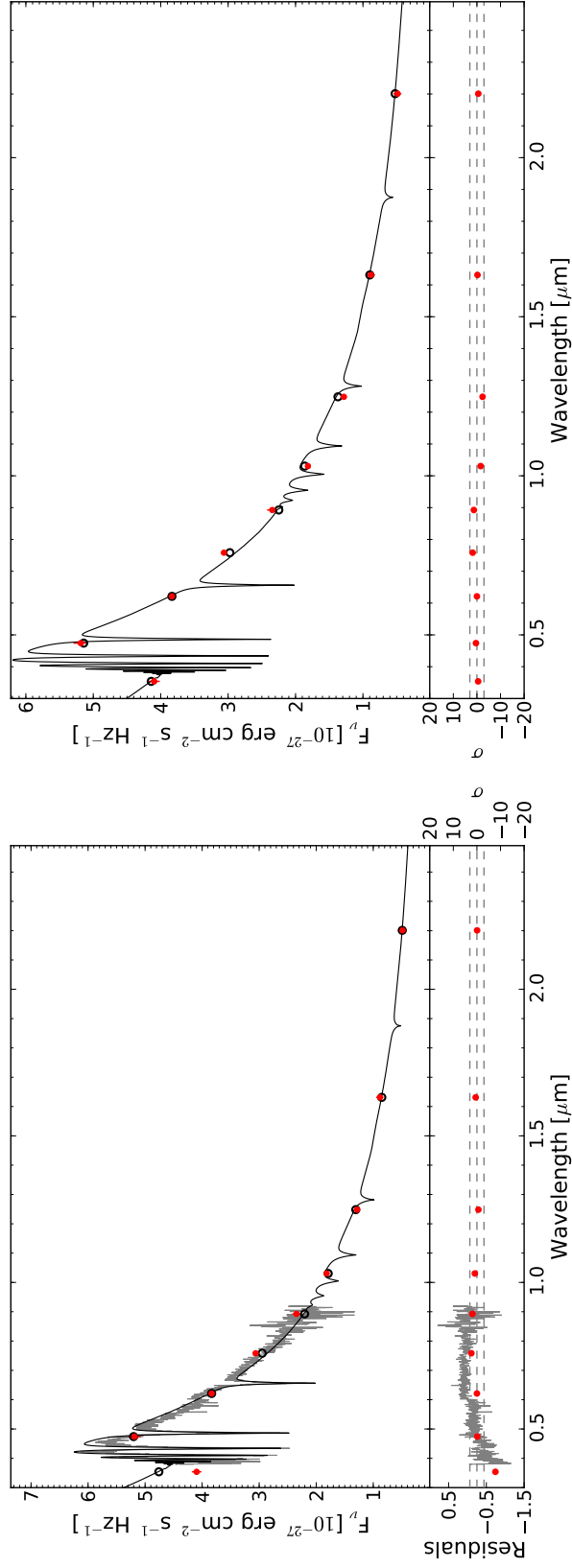
Figure 5.14: SDSS J1043+0855 is the second of only two DA white dwarfs in our SDSS/UKIDSS sample that is known to have a dusty debris disc. This object was discovered through optical Ca emission [Gänsicke et al., 2007] and has at best a marginal flux excess in the *Spitzer* mid-IR [Melis et al., 2010; Brinkworth et al., 2012]. Fitting the SDSS spectrum results in $T_{\mathrm{eff}} = 17912 \pm 360\mathrm{K}$, $\log(g) = 8.07 \pm 0.08$, the corresponding fit to the *ugriz* photometry results in $T_{\mathrm{eff}} = 16000^{+170}_{-100}\mathrm{K}$, $\log(g) = 7.5^{+0.42}_{-0.8}\mathrm{K}$ (right panel). No infrared excess is detected in the near-IR using either method, consistent with the inconspicuous location of SDSS J1043+0855 in the $(z - H, H - K)$ and proper motion *vs* $H - K$ diagrams (Figs. 5.10 and 5.12, respectively).

5.3.1.3   SDSS J1212+0136

SDSS J1212+0136 is one of three magnetic (DAH) white dwarfs that were selected by our colour cut (Table 4.1) and that, when fitting their *ugri* photometry, show a substantial infrared flux excess (Fig. 5.15, Sect. 5.2.3.3). This white dwarf was first reported to have a magnetic field of $\simeq 13\,\mathrm{MG}$ by Schmidt et al. [2003]. Schmidt et al. [2005] subsequently detected a weak Hα emission line, from which they measured an orbital period of $\sim 90\,\mathrm{min}$. Based on the J band magnitude of SDSSJ1212+0136, Schmidt et al. [2005] concluded that the companion to the white dwarf is a brown dwarf. Additional studies in the near-IR confirmed the brown dwarf to have a spectral type in the range L5–L8, and detected variable cyclotron emission, indicative of ongoing accretion onto the magnetic white dwarf [Debes et al., 2006; Farihi et al., 2008a; Howell et al., 2008]. Observations at blue and ultraviolet wavelengths show a quasi-sinusoidal flux modulation interpreted as emission from an accretion-heated polecap [Burleigh et al., 2006; Linnell et al., 2010] which is typical of strongly magnetic cataclysmic variables [Gänsicke et al., 1995; Araujo-Betancor et al., 2005a; Gänsicke et al., 2006a]. Despite the fact that no state of high accretion activity has been observed in SDSS J1212+0136, all observational evidence suggests that it is nearly a twin of the prototypical magnetic cataclysmic variable EF Eri [e.g. Beuermann et al., 2000].

Taken on its own, the very red $H - K$ colour of SDSS J1212+0136 would suggests it to be a quasar (Sect. 5.2.3.2, Fig. 5.10). However, its stellar nature is confirmed by the detection of a significant and large proper motion (Fig. 5.12). Recovering this DAH white dwarf with a brown dwarf companion shows that our methods to identify DA white dwarfs with IR-excess are sufficiently robust to also find non-DA white dwarfs with genuine infrared excess.

5.3.2   Example spectroscopic infrared excess candidates

5.3.2.1   SDSS J0135+1445

SDSS J0135+1445 is a clear candidate for being a cool white dwarf with a late-type stellar companion or brown dwarf. An excess is seen to extend over all the UKIDSS bands in Fig. 5.16. Modelling of the companion suggests that its spectral type is between L7 and L8. Spectral fitting implies a white dwarf of $\mathrm{T_{eff}} = 7467 \pm 18\mathrm{K}$ at a distance of $69\pm2\mathrm{pc}$. A $\mathrm{T_{eff}} = 8000\pm^{10}_{20}\mathrm{K}$ is calculated from fitting of the photometry, broadly similar to the recently discovered (resolved) DA plus brown dwarf binary PHL 5038 [Steele et al., 2009].
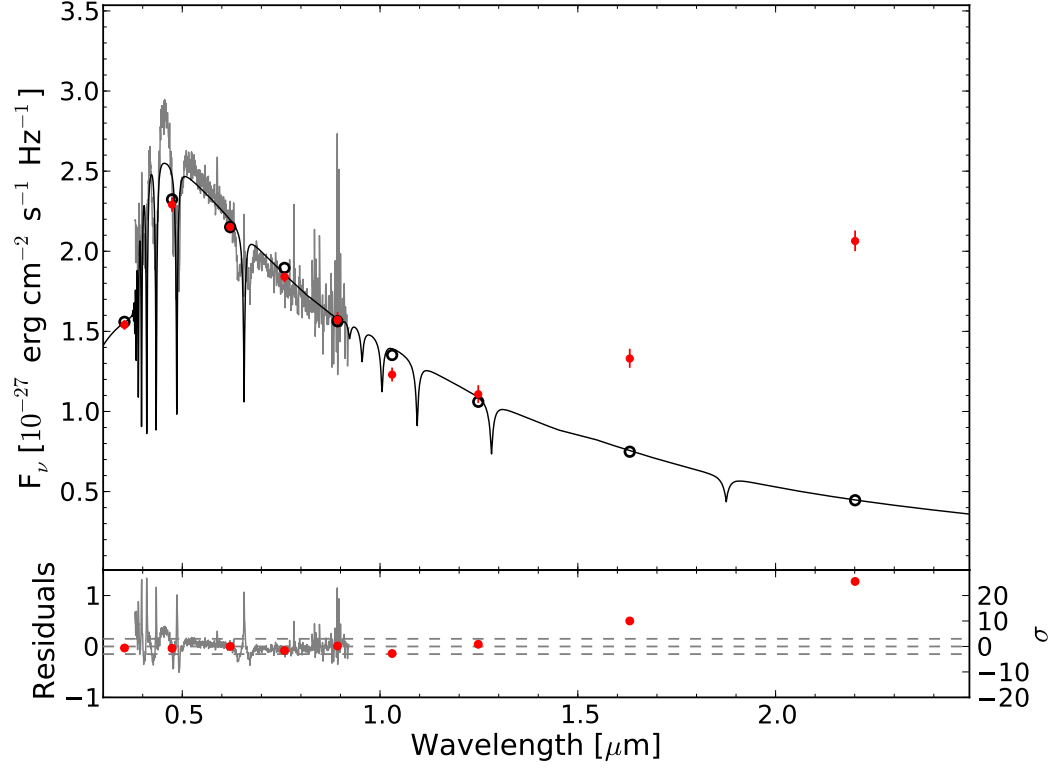
Figure 5.15: SDSS J1212+0136, a short-period binary containing a magnetic DA(H) white dwarf plus a brown dwarf companion [Schmidt et al., 2005]. The system is undergoing weak mass transfer, producing cyclotron emission that contributes to the observed near-IR excess [Debes et al., 2006; Burleigh et al., 2006; Farihi et al., 2008a]. SDSS J1212+0136 was picked up by our fit to all the photometric objects satisfying the colour cuts designed to find DA white dwarfs (Table 4.1).
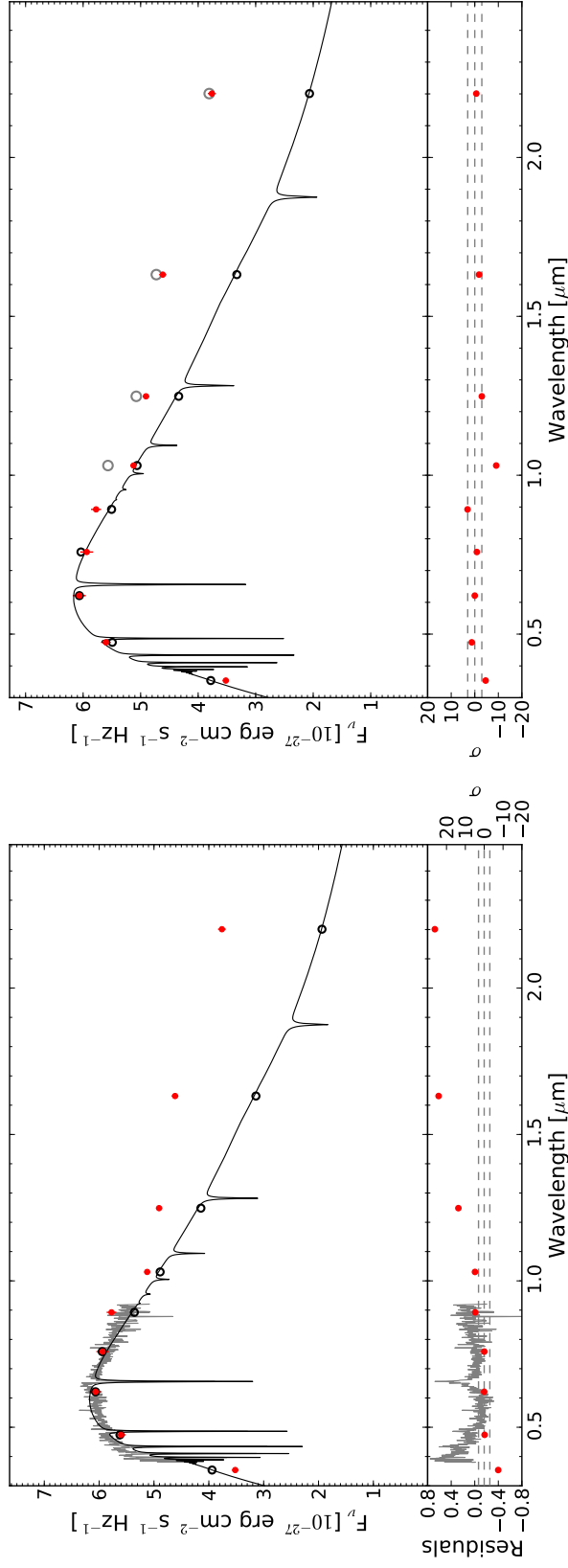
Figure 5.16: SDSS J0135+1445; a cool white dwarf with a probable low mass companion. The fit is a $T_{eff} = 7467 \pm 18$K, $\log(g) = 7.34 \pm 0.04$ spectra at a distance of 69 ± 2pc. The calculated mass is $M_{wd} = 0.29 \pm 0.01 M_\odot$. The photometry is best fit with a white dwarf of $T_{eff} = 8000^{+20}_{-10}$K, $\log(g) = 8.0$. Based upon the fit to the photometry, the addition of an L8-type companion to the white dwarf magnitudes is the best fit to the IR excess (Table A.3) and is plotted on the right hand figure as open grey circles. The model Y-band magnitude does not match the UKIDSS Y measurement, but we found that the Y-band data did relatively often disagree with SDSS z and UKIDSS J. UKIDSS J, H and K are tied to 2MASS J, H and K_s. The Y-band disagreement may be due to uncertainties in the extrapolation from J to the Y-band.

86

5.3.2.2   SDSS J0753+2447

SDSS J0753+2447 is a very strong candidate for being a DA white dwarf with a late-type brown dwarf or debris disc (Fig. 5.17). The fit to the SDSS spectrum implies $T_{\text{eff}} = 13432 \pm 710$K, $\log(g) = 7.81 \pm 0.15$, with an implied distance $d = 349 \pm 32$pc and white dwarf mass $M_{\text{wd}} = 0.50 \pm 0.08 M_{\odot}$. Fitting of the companion type was inconclusive, but the shape of the SED is similar to that of the benchmark object, SDSS J1228+1040. Therefore SDSS J0753+2447 is classified as a brown dwarf or disc candidate.

5.3.2.3   SDSS J1247+1035

SDSS J1247+1035 is a candidate for having a brown dwarf companion or dusty debris disc, however, the UKIDSS K-band is only in excess by $\sim 3\sigma$ over the white dwarf model. Far-IR photometry of the object was required to confirm the infrared excess. Using the *Spitzer Space Telescope*, Farihi et al. [2012] confirmed that SDSS J1247+1035 has a dM/L type companion (see Section 5.3.4).

5.3.2.4   SDSS J1557+0916

UKIDSS photometry of SDSS J1557+0916 shows a 4σ K band excess for both the spectroscopic and photometric fitting methods. The spectroscopic and photometric T_{eff} differ by 3800K, however, this does not significantly affect the result. This is a good example of where reddening is probably reducing the blue flux. Reddening the white dwarf model spectrum by $E(B-V) \simeq 0.05$ brings the overall SED in line with the SDSS optical spectrum. Modelling of the companion object proved inconclusive as to its spectral type (Table A.1). SDSS J1557+0916 is a good candidate for having a dusty disc or low-mass companion based on its infrared spectral shape. Farihi et al. [2012] confirmed a dust disc around SDSS J1557+0916 (see Section 5.3.4).

5.3.2.5   SDSS J2220−0041

PHL 5038 ($=$ SDSS J2220−0041) is a wide ($0.94''$) binary containing a cool ($\sim$ 8000 K) white dwarf with an $\sim$L8 companion, only the fourth white dwarf plus brown dwarf binary known [Steele et al., 2009].

5.3.3   Example photometric infrared excess candidates

As described in Sect. 4.2.2, we fitted *all* photometric objects satisfying our DA white dwarf constraint set (Table 4.1) with DA model spectra, independent on whether
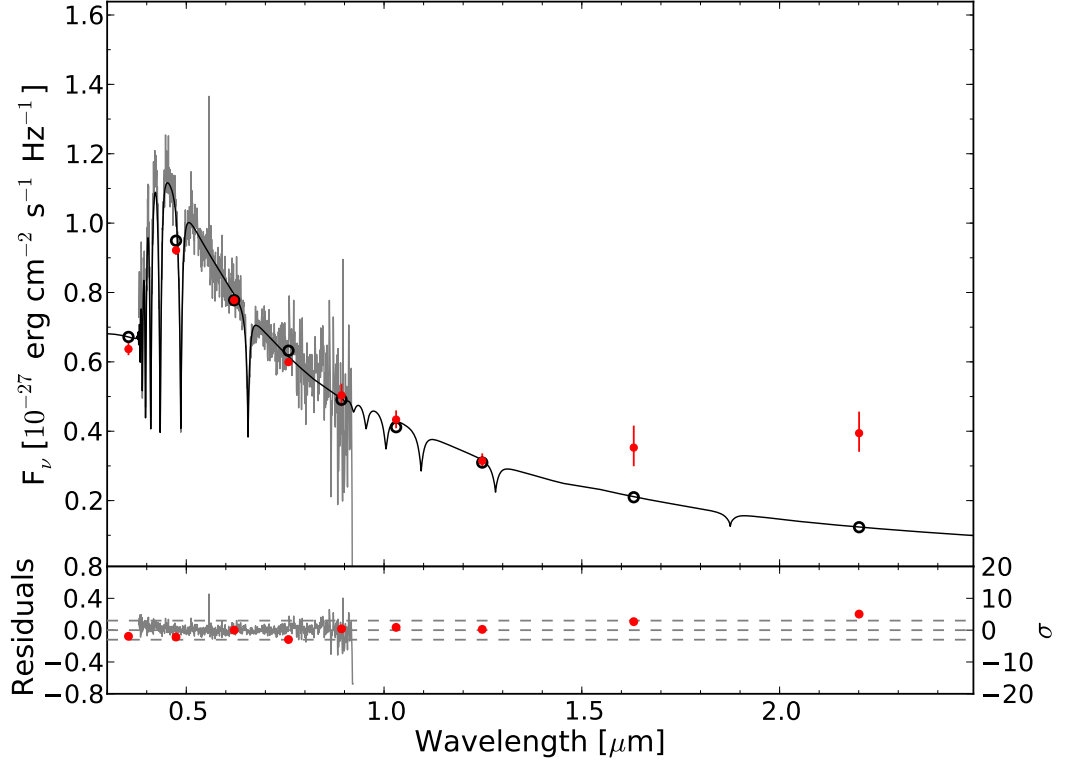
Figure 5.17: SDSS J0753+2447, a DA white dwarf plus dusty disc or low-mass companion candidate. The best-fit to the SDSS spectrum (black line) gives $T_{eff} = 13432 \pm 710$K and $\log(g) = 7.81 \pm 0.15$ at a distance of 349 ± 32pc. The implied mass of the white dwarf is $0.50 \pm 0.08 M_{\odot}$. Fitting of the 4σ K-band excess with main sequence star models proved inconclusive, however, considering the similarity to SDSS 1228+1040 (Fig. 5.13), this is an excellent candidate for having a brown dwarf companion or debris disc. Fitting the $ugri$ photometry leads to $T_{eff} = 12000 \pm_{290}^{1130}$K and $\log(g) = 7.75 \pm_{0.41}^{0.45}$ at 327_{14}^{18}pc, with no change to the conclusions as to the nature of the excess.
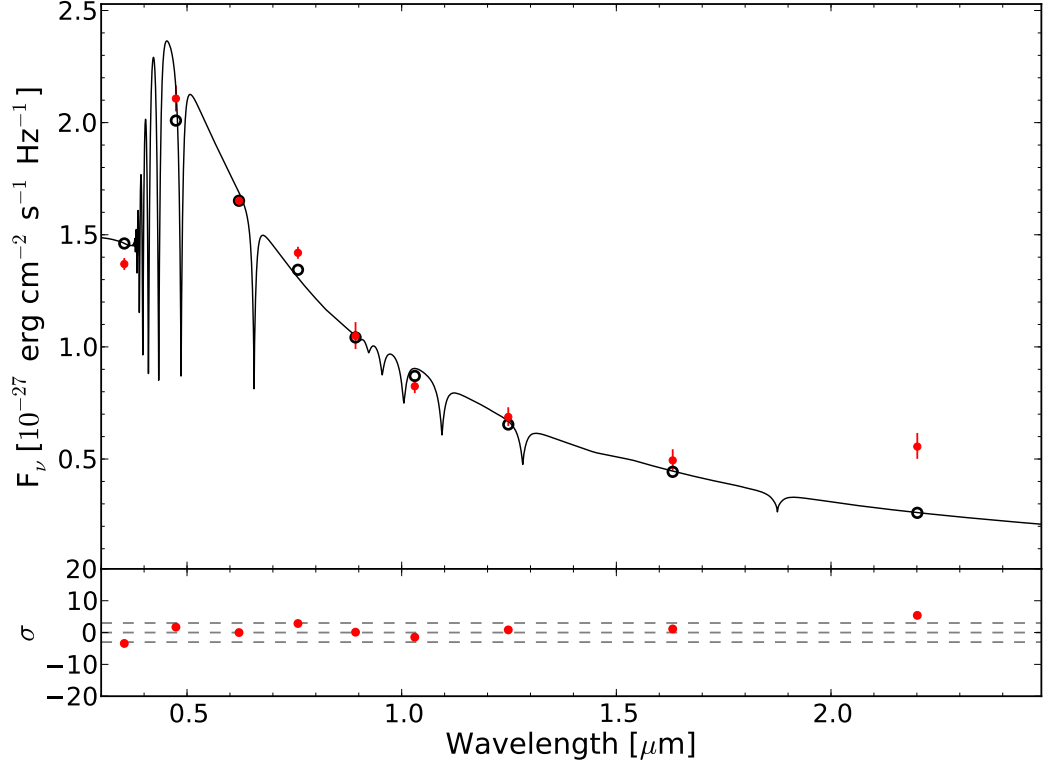
Figure 5.18: SDSS J0959−0200, a photometric-only DA white dwarf candidate (T_{eff} = 12000$\pm^{1160}_{500}$K, $\log(g)$ = 8.00$\pm^{1.20}_{0.55}$) that exhibits a strong K-band excess, making it a strong candidate for having either a late-type brown dwarf companion or a dusty debris disc. Its nature as a DA white dwarf was confirmed with ISIS on the WHT and a dust disc was found from pointed *Spitzer* observations [see Section 5.3.4; Farihi et al., 2012].

they also have an SDSS spectrum.

5.3.3.1 DA white dwarf candidates

SDSS J0959−0200   SDSS J0959−0200 is a photometric-only DA candidate with T_{eff} = 12000$\pm^{1160}_{500}$ K and $\log(g)$ = 8.00$\pm^{1.20}_{0.22}$ (Figure 5.18). The UKIDSS K-band magnitude shows a large (5σ) excess over the white dwarf model, no excess is seen at shorter wavelengths. This object is a strong candidate for having a very late type brown dwarf companion, or a dusty debris disc. Its nature as a DA white dwarf was confirmed with ISIS on the WHT and a dust disc was found from pointed *Spitzer* observations [see Section 5.3.4; Farihi et al., 2012].
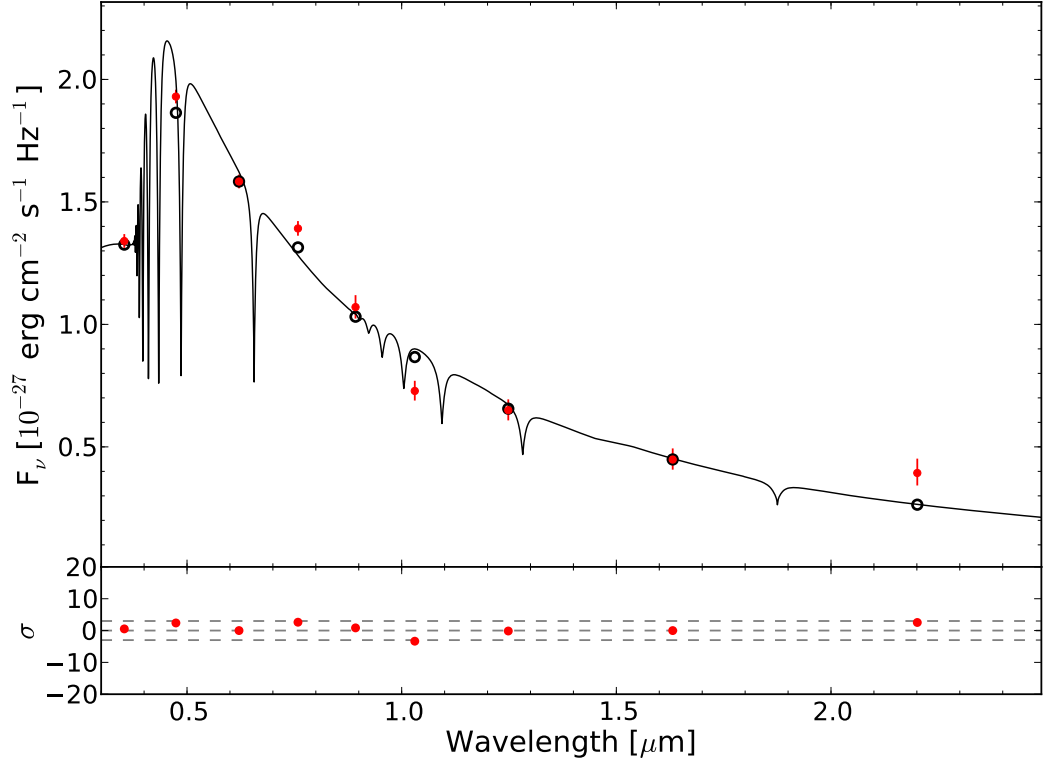
Figure 5.19: SDSS J1221+1245, a photometric-only DA white dwarf candidate (T_{eff} = 12000$\pm^{1110}_{270}$K, $\log(g)$ = 8.00$\pm^{0.51}_{0.34}$) that exhibits a borderline K-band excess. It is good candidate for having either a late-type brown dwarf companion or a dusty debris disc. Its nature as a DA white dwarf was confirmed with ISIS on the WHT and a dust disc was found from pointed *Spitzer* observations [see Section 5.3.4; Farihi et al., 2012].

SDSS J1221+1245 A second interesting photometric-only DA white dwarf candidate is SDSS J1221+1245 (Figure 5.19). The white dwarf is best fitted by a model with system parameters T_{eff} = 12000$\pm^{1110}_{270}$ K and $\log(g)$ = 8.00$\pm^{0.51}_{0.34}$. The UKIDSS K-band magnitude shows a borderline excess over the white dwarf model, but no excess is seen at shorter wavelengths. This object is again a good candidate for having a very late type brown dwarf companion, or a dusty debris disc. SDSS J1221+1245 was confirmed as a DA white dwarf by ISIS optical spectroscopy and mid-infrared *Spitzer* observations found a dust disc around the white dwarf [see Section 5.3.4; Farihi et al., 2012].

90

5.3.3.2 Other composite objects

Inspection of Simbad reveals that four of the photometric-only DA candidates with infrared excess (DA:ire and DA:ire:, Table A.2) are previously known (pre-)white dwarf binaries and one pulsating subdwarf, which provides a preview on the mixture of objects that can be expected within this sample. It also underlines that the method efficiently identifies genuine infrared-excess white dwarfs.

PG 0014+067 = SDSS J0016+0704   Brassard et al. [2001] identified PG 001-4+067 as a pulsating sdB with $T_{\mathrm{eff}} = 33550 \pm 380$K and $\log(g) = 5.77 \pm 0.10$. Fitting the *ugri* photometry with DA model atmospheres results in $T_{\mathrm{eff}} = 24000 \pm^{2100}_{600}$K with the surface gravity fixed to $\log(g) = 8$, and reveals a clear infrared excess. At such high temperatures, the slope of the optical and near-IR SED of this object is close to a Rayleigh-Jeans distribution, and while modelling the photometric data with DA models may not be perfect, we believe that PG 0014+067 does exhibit a genuine infrared excess. In their asteroseismological analysis, Brassard et al. [2001] found that the pulsation frequency spectrum of PG 0014+067 exhibits fine structure that they tentatively interpreted as a rotational period of 29.2 ± 0.9 h, revised later by [Jeffery et al., 2005] to ~ 4 d. One possibility is that PG 0014+067 has a close low-mass binary companion with an orbital period of a few days and that the sdB is tidally locked, rotating at the same period. This hypothesis can be tested by a radial velocity study of this subdwarf.

Cataclysmic variables   BK Lyn (= SDSS J0920+3356) and HS 0139+0559 (= SDSS J0141+0614) are novalike variables [Dobrzycka & Howell, 1992; Aungwerojwit et al., 2005] with optically thick accretion discs, and their optical colours are similar to that of hot white dwarfs or subdwarfs. However, their companion stars and cooler outer regions of the accretion discs start to dominate in the near-IR.

Detached binaries   Abell 31 (= SDSS J0854+0853, PN G219.1+31.2) is a planetary nebula with a nearby (0.26″) M-dwarf, both stars are most likely an associated wide binary [Ciardullo et al., 1999].

GK Vir (= SDSS J1415+0117) is an eclipsing binary containing a hot ($\simeq$ 48800 K) white dwarf plus an $\sim$M4V companion with an orbital period of 0.344 d [Green et al., 1978; Fulbright et al., 1993; Parsons et al., 2010].

5.3.4 Follow up observations

SDSS J0959−0200, SDSS J1221+1245 and SDSS J1320+0018 were confirmed to be white dwarfs with hydrogen-rich atmospheres though optical spectroscopy using ISIS on the WHT [Farihi et al., 2012]. SDSS J0959−0200 and SDSS J1221+1245 also show evidence of metal pollution in their spectra.

Farihi et al. [2012] obtained warm *Spitzer* observations for six of the infrared excess candidates discussed in this Chapter. Five of the six were confirmed to have an infrared excess. SDSS J0959−0200, SDSS J1221+1245 and SDSS J1557+0916 were all found to have an infrared excess consistent with the emission from a dust disc. SDSS J1247+1035 was found to have a dM/L-type companion and SDSS J1320+0018 was shown to have an infrared excess, however, a background galaxy is likely to be the cause. The infrared excess shown at SDSS J1506+0638 was not confirmed by the *Spitzer* observations. The study of Farihi et al. [2012] clearly shows the efficiency of the method described in this Chapter and its potential to find white dwarfs with dust discs.

SDSS J1250+1549 and SDSS J1514+0744, the two candidate magnetic white dwarfs with companions, were confirmed by Breedt et al. [2012]. Phase-resolved spectroscopy showed that the two have orbital periods of 86 and 89 minutes, respectively. They resemble the polar EF Eri in its prolonged low state and also SDSS J1212+0136 (discussed in Section 5.3.1.3). The large infrared excesses seen in both SDSS J1250+1549 and SDSS J1514+0744, as well as SDSS J1212+0136, is partially due to the brown dwarf companions, but the primary contribution will be strong cyclotron lines.

5.4 Comparison with SDSS DR6 white dwarf–main sequence binaries

Rebassa-Mansergas et al. [2010, hereafter RM10] compiled a catalogue of white dwarf–main sequence (WDMS) binaries from all spectroscopic objects within SDSS DR6. Given that their detection method was based on optical data alone, RM10 were primarily sensitive to white dwarfs with M-type companions. The distribution of their WDMS binaries as a function of effective temperature and companion star spectral type shows a clear concentration of $T_{eff} = 10,000 - 20,000\,K$ white dwarfs with ∼M4-type companions (Fig. 5.20, left panel). The large luminosity of hot white dwarfs prevents the identification of low-mass companions around them, explaining the relative dearth of late spectral types at higher temperatures. The decreasing

number of very late M-dwarfs (>M6) could also be affected to some degree by the same contrast problem, however, it is known that the companion mass distribution of WDMS binaries is dropping towards the low-mass end of the main sequence [Farihi et al., 2005].

The sample of WDMS binaries of RM10 provides a natural comparison for the work done here. We have subjected their entire sample of WDMS binaries to our DA colour cuts (Table 4.1), finding that only 93 of the 1602 systems fall within the colour cuts. This small number is not too surprising, as the red flux from the M-dwarf companions moves the majority of RM10's WDMS binaries out of our colour selection. RM10 list WD temperature *and* companion spectral type for 53 of these 93 systems. In contrast to our work here (Sect. 5.2.1), the study of RM10 included (partially) resolved systems. Consequently, we removed 21 that appeared resolved in the SDSS (or UKIDSS images where available), which leaves us with 32 objects in common. Figure 5.20 shows that the two samples only overlap for systems where the companion is relatively faint in the optical compared to the white dwarf, which is expected as our DA selection needs the white dwarf to dominate. Finally, 10 of the 32 objects are in the UKIDSS footprint.

We cross-correlated the white dwarfs with an infrared excess from our spectroscopic and photometric samples (Table A.1 and A.2), and the WDMS catalogue of RM10 and found 19 objects in common (Table A.5). This is comprised of the 10 objects above that we expect to be in the sample, along with 9 others where no spectral type is listed in RM10's catalogue. There is in general a good agreement between the white dwarf system parameters, however the underestimation of photometric temperatures is highlighted again. The spectroscopic sample and the WDMS catalogue largely find companion types within two spectral types of each other. All of these are M-type companions as expected from the sensitivity of the WDMS catalogue. Five objects are found to have an excess in the photometric method, but were rejected from the spectroscopic sample because signatures of a main sequence star companion can be seen in the optical spectra, whereas the spectroscopic sample only contains pure DA white dwarfs. Those are marked as such in Table A.5, and suffer from the same companion type biases discussed in Section 5.2.3.1.
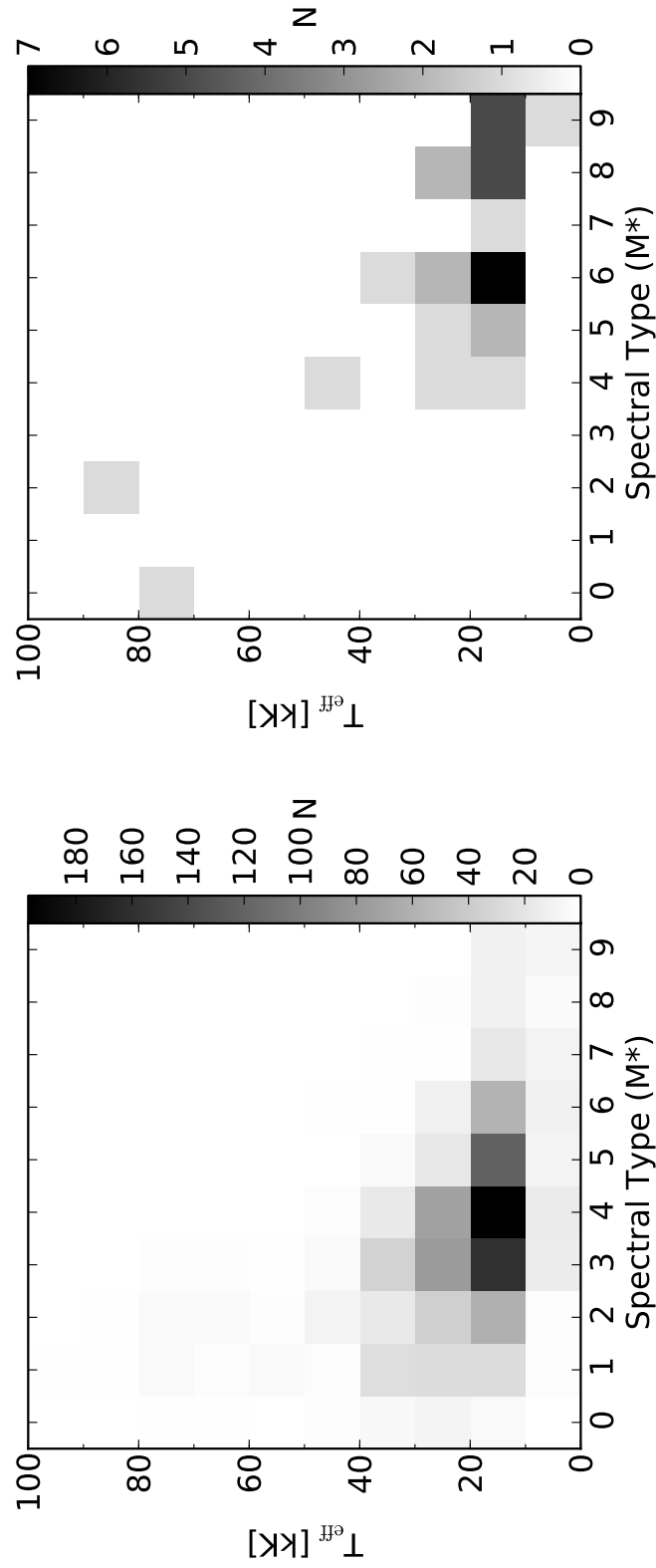
Figure 5.20: The distribution of the WDMS binaries from the catalogue of Rebassa-Mansergas et al. [2010] as a function of effective temperature of the white dwarf and spectral type of the companion star. The left hand panel shows all the 1173 objects with values for both T_{eff} and $\log(g)$. 53 of these are contained within the colour-colour region defined in Table 4.1. Excluding spatially resolved binaries leaves 32 objects satisfying all the criteria of our DA white dwarf selection, which are shown in the right hand panel.

5.5 Confirmation of infrared excess candidates in WISE

We cross-correlated all spectroscopic and photometric-only infrared excess candidates (from Table A.1 and A.2, respectively) with the preliminary data release of WISE (see Section 2.4.1) within 2.5″. The SDSS white dwarfs that are the subject of this work are largely too faint to be seen in the 12, and 22 μm bands and therefore we generally only discuss the 3.4 and 4.6 μm fluxes. Of the 42 infrared excess objects from the spectroscopic method, 3 had a detection in at least one WISE band. Similarly 14 of the 67 photometric-only objects were detected and are listed in Table 5.5.

The three spectroscopically confirmed DA white dwarfs with infrared excesses and WISE data: SDSS J0236−0103, SDSS J0847+2831 and SDSS J1448+0713, are all confirmed to have an excess in the WISE 3.4 and 4.6 μm bands. They are, however, all predicted to have late M-type companions and are not brown dwarf or debris disc candidates.

Of the 14 photometric-only infrared excess candidates with WISE data, SDSS J1524−0128 and SDSS J1549+0325 are *not* found to have an excess in the 3.4 and 4.6 μm bands. Similarly, because we do not trust the effective temperature of the white dwarf fit, we also do not believe the far-IR excess found for SDSS J0841+0501, SDSS J1441+0137, SDSS J1538+0644 and SDSS J1551−0118. This is indicated by a flat, constant excess over the white dwarf model and is continued into the far-IR WISE data in these cases (see Fig. 5.21).

The remaining 8 objects (SDSS J0207+0715, SDSS J0742+2857, SDSS J0751-+2002, SDSS J0920+3356, SDSS J1448+0812, SDSS J1456+1040, SDSS J1538+29-57, and SDSS J1635+2912) are confirmed to have an infrared excess consistent with a late type companion in the WISE far-IR data. Some interesting examples of these are shown in Fig. 5.22. SDSS J1538+2957 (Fig. 5.22) is predicted to have an M8-type companion from the photometric method. However, the spectral shape of the excess is found to be inconsistent with such an early type companion. The excess in UKIDSS, and now WISE, is more indicative of a later type brown dwarf companion or dusty debris disc. This mismatch is most likely caused by over estimating the distance to the white dwarf in the photometric method. SDSS J1635+2912 (Fig. 5.22) is one of the photometric-only debris disc candidate systems. The WISE 3.5μm flux confirms the infrared excess, but still leaves the origin of the excess, brown dwarf or disc, open.
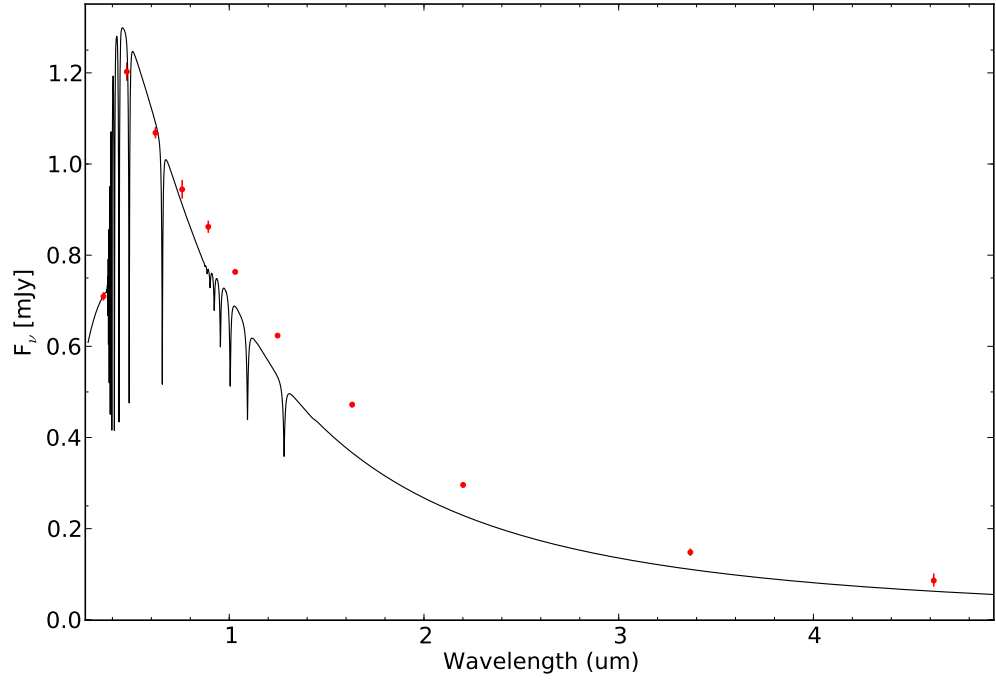
Figure 5.21: SED of SDSS J1538+0644. The SDSS, UKIDSS and WISE 3.4 and 4.6 μm fluxes are shown as red circles. The best fit white dwarf model (T_{eff} = 10,000 K, $\log(g)$ = 7.25) to the SDSS photometry is shown as a black line. The shape of the infrared excess is not consistent with any companion or disc. It is more likely that the excess is an artifact of overestimating the white dwarf effective temperature.
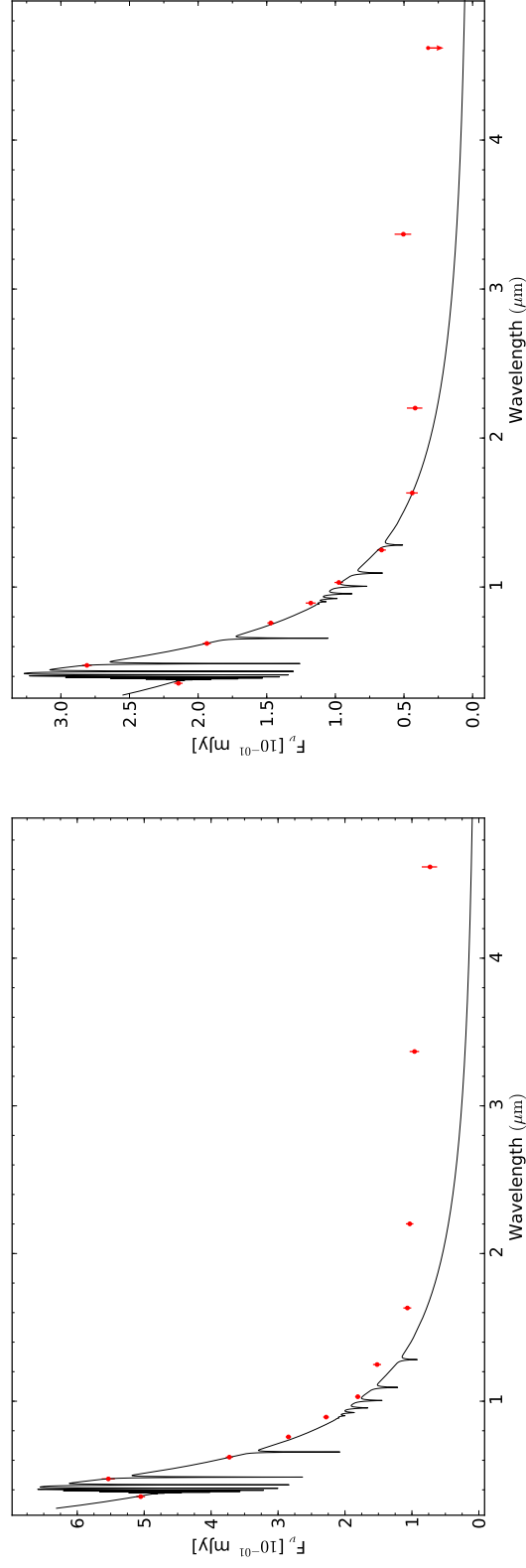
Figure 5.22: SEDs of SDSS J1538+2957 (left) and SDSS J1635+2912 (right). The plot follows the same format as Fig. 5.21. The best fit models have $T_{eff} = 20,000\,K$ and $T_{eff} = 17,000\,K$, respectively. SDSS J1538+2957 and SDSS J1635+2912 are predicted herein to have an M7: and an L6:-type companion or potential debris disc, respectively.

5.6 White dwarfs with dusty debris disc

Fitting the optical spectroscopy or photometry and probing for infrared flux excess above the best-fit white dwarf, as previously done by Tremblay & Bergeron [2007], has proven to be an efficient and robust approach. It also allows one to identify hot white dwarfs with low-level excesses which have infrared colours that are very similar to the bulk population of white dwarfs (Fig. 5.10). Our search is sensitive to companions as late as ∼L8, and to warm dusty debris discs.

Of the 1275 spectroscopically confirmed DA white dwarfs with at least one UKIDSS magnitude, 26 (2.0%) are found (or are candidates) to have an IR excess consistent with a L0-type companion or later. The exact cut-off of where the brown dwarf sequence starts is age dependent and can vary from mid-M to mid-L-type. Taking the white dwarf mass distribution and the initial-final mass relation we can calculate the white dwarf progenitor masses. This, together with the white dwarf cooling age allows us to estimate the total age of the system. The average total age of the companion is a few Gyr, and in this regime L0-type is a suitable cut-off for being a brown dwarf. Taking only the systems where we are confident of the excess (not "DAire:" in Table A.1) gives a lower limit for the number of white dwarfs with brown dwarf type companions of 0.8%. This is compatible with previous estimates. An adaptive optics imaging survey of 266 solar-like stars by Metchev & Hillenbrand [2009] found a wide (28–1590 AU) sub-stellar companion fraction of $3.2^{+3.1}_{-2.7}$%. Farihi et al. [2005] carried out an extensive near-IR imaging survey for both wide and unresolved low-mass companions to 394 known white dwarfs, finding an overall stellar companion fraction of 22%, and a brown dwarf companion fraction of < 0.5%.

When using the photometric fitting method, 105 of the 1771 photometric-only DA white dwarf candidates with UKIDSS data exhibit an IR excess, of which we eliminate 38 likely quasars (Sect. 5.2.3.2 and see Table A.4). Taking into account our estimate for the contamination by NLHS (Sect. 5.2.3.3), we find that ~ 2.7% of white dwarfs in the photometric-only sample have an infrared excess, of which 1.8% are candidates for having a brown dwarf companion. This is consistent with the frequencies found in the spectroscopic sample, though not as secure.

Taking only the objects with a detection in the K-band (required for detecting a disc), of the 571 spectroscopically confirmed DA white dwarfs, 7 (1.2%) are found to have an infrared excess compatible with a companion spectral type later or equal to L8, and are hence viable disc candidates. Similarly, 0.5% (4/840) of the photometric-only sample are disc candidates, or, scaling for the 62.3% efficiency of

Table 5.5: Table of infrared excess candidates detected in WISE. Objects confirmed to have an infrared excess from the WISE photometry are marked by a "*" in the "Excess" column.

Coord	Notes	W1	W2	Excess
0207+0715	DA:ire	15.81 ± 15.73	0.07 ± 0.20	*
0236−0103	DAire	16.85 ± 16.47	0.15 ± 0.00	*
0742+2857	DA:ire	16.52 ± 16.53	0.12 ± 0.39	*
0751+2002	DA:ire	16.50 ± 16.49	0.11 ± 0.40	*
0841+0501	DA:ire:	14.35 ± 14.31	0.03 ± 0.06	-
0847+2831	DAire	16.55 ± 16.65	0.09 ± 0.43	*
0920+3356	DA:ire:	14.33 ± 14.26	0.03 ± 0.06	*
1441+0137	DA:ire:	14.83 ± 14.80	0.04 ± 0.10	-
1448+0713	DAire	15.36 ± 15.15	0.05 ± 0.12	*
1456+1040	DA:ire	16.40 ± 15.87	0.10 ± 0.21	*
1524−0128	DA:ire:	15.48 ± 15.64	0.05 ± 0.17	-
1538+0644	DA:ire:	15.80 ± 15.75	0.06 ± 0.18	-
1538+2957	DA:ire	16.27 ± 15.93	0.08 ± 0.17	*
1549+0325	DA:ire:	14.60 ± 14.71	0.04 ± 0.08	-
1551−0118	DA:ire:	14.54 ± 14.58	0.04 ± 0.08	-
1635+2912	DA:ire:	16.97 ± 16.81	0.13 ± 0.00	*

our DA white dwarf selection, 0.8% (4/523). This is consistent with the results of Farihi et al. [2009], who estimated that the frequency of white dwarfs with dusty debris discs is at least 1%. Any search for debris discs based on K-band data is biased towards warm, bright circumstellar dust rather than faint discs or narrow rings. Of the known white dwarfs with a dusty debris disc, only about half reveal themselves shortward of $3\,\mu m$ [Kilic et al., 2006a; Farihi et al., 2009].

To confirm the infrared excess candidates we have cross matched all the spectroscopic (Table A.1) and photometric-only (Table A.2) candidates with the far-IR WISE PDR. This has provided 3.4 and 4.6μm fluxes for 7% (3/42) and 21% (14/64) of the spectroscopic and photometric-only infrared excess candidates, respectively. We find that all three of the spectroscopic infrared excess candidates also have an excess in the far-IR.

However, in the photometric-only sample, a total of six objects are found not to have a definite infrared excess at $> 3\mu$m. The remaining 8 of 14 white dwarf candidates have a real infrared excess in the WISE fluxes. We therefore find that $\sim 60\%$ of the photometric-only infrared excess candidates have real infrared excesses consistent with a MS star companion, brown dwarf companion or dust disc.

Determining the true nature of the white dwarfs with an excess in K only will

require optical spectroscopy (for the photometric-only sample; DA:ire and DA:ire:) to confirm their (DA) white dwarf nature, and far-IR data (for all) to distinguish between a late-type brown dwarf companion or a dusty debris disc. Of the three white dwarf candidates Farihi et al. [2012] observed with ISIS, one was found to be a DA white dwarf and two are DAZ white dwarfs. This is promising, but too small a sample to confirm the estimated efficiency. Farihi et al. [2012] also observed six infrared excess candidates with the *Spitzer Space Telescope*. Five were confirmed to have an excess in the infrared. Of these, three harbour dust discs, one has a dM/L-type companion and one falls on top of a background galaxy (which could not have been seen in the UKIDSS data). We discuss *Spitzer* observations of white dwarf stars in more detail in Chapter 6.

Chapter 6

Remnants of planetary systems around white dwarf stars

The previous Chapter demonstrated that through near-infrared photometry, one can identify candidate white dwarf plus dust disc systems, however, a brown dwarf or dust disc can only be confirmed through follow-up mid- and far-infrared data. The *Spitzer Space Telescope* (see Section 6.1) has been instrumental in this respect. Prior to this work, 77 white dwarfs, believed to be accreting from a disc because of their metal-polluted atmospheres (see Section 1.2.2.1), had been observed to search for dust discs. Here, we analyse *Spitzer* data for 15 new white dwarfs with metal-polluted atmospheres. This extends the sample to a point where, for the first time, we are able to make some statistical estimates of the lifetimes of dusty disc (see Section 1.2.2.5).

If Poynting-Roberson drag (the spiralling in of dust particles due to interaction with the emission from the host star) is the dominant factor in disc accretion, the theoretical lifetime of a dust disc should be of the order 10^6 yr [Rafikov, 2011a]. However, Poynting-Roberson drag is not capable of producing the observed (average) accretion rates seen in DBZ white dwarfs ($\sim 10^{10} - 10^{11}\,\mathrm{g\,s^{-1}}$). Such high accretion rates must be fuelled by the by the interaction of the dust disc with a gaseous component, resulting from sublimated dust, produced at the inner edge of the disc. This would reduce the lifetime of a $10^{22}\,\mathrm{g}$ disc to several 10^4 yr [Rafikov, 2011b]. The observational data we present here allows us to place significant constraints on these scenarios.

6.1 Observations

The *Spitzer* Space Telescope (hereafter referred to as *Spitzer*) is the final mission in NASA's Great Observatories Program, observing the Universe in infrared light. Its companions in this program are the Hubble Space Telescope (HST), the Compton Gamma-Ray Observatory (CGRO), and the Chandra X-Ray Observatory (CXO). *Spitzer* has three instruments on board, namely the Infrared Array Camera (IRAC), the Infrared Spectrograph (IRS) and the Multiband Imaging Photometer (MIPS), operated in a pointing, rather than survey, mode. Firstly, IRAC is a near- and mid-infrared imaging camera, observing simultaneously at 3.6, 4.5, 5.8 and 8.0 microns (on four detector arrays 256×256 pixels in size). IRS provides both high- and low-resolution spectroscopy at mid-infrared wavelengths (from $5 - 40$ microns), on 128×128 pixels detector arrays. The instrument also has a Peak-Up Imaging (PUI) mode for performing photometry at 16 microns. Lastly, MIPS is a second imaging camera designed to perform at far-infrared wavelengths (24, 70 and 160 microns), however it also is capable of low-resolution spectroscopy. In 24 micron mode, MIPS uses an 128×128 pixel array, however, at 70 and 160 micron a 32×32 and 2×20 pixel array are used, respectively.

Dr C. Brinkworth and Dr F. Farihi were awarded *Spitzer* time in Cycle 5 (program 50340) and Cycle 6 (program 60119), to search for infrared excesses from circumstellar dust around 16 white dwarfs published as metal-enriched (Table 6.1). These targets were chosen from the literature, and significantly increase the number of DBZ (for simplicity, we use "DBZ" to refer to all helium-rich subtypes with metals, including those with trace hydrogen) stars observed with *Spitzer* IRAC, bringing their numbers onto par with those of the DAZ stars. One of the targets, PHL 131, was subsequently found by a collaborator to be a $40,000\,$K white dwarf with interstellar calcium absorption, and thus we report its fluxes, but exclude it from the rest of the study.

Imaging observations were obtained for each of the white dwarf targets using the Infrared Array Camera [IRAC; Fazio et al., 2004]. Exposures were taken in the 4.5 and 7.9 μm channels using the medium-scale, cycling dither pattern for the Cycle 5 targets objects and in the 3.6 and 4.5 μm channels for the Cycle 6 objects. For GD 61 and NLTT 51844, images were also obtained with the blue Peak-Up Imaging array of the Infrared Spectrograph at 15.6 μm, this time using the small-scale, cycling dither pattern.

Table 6.1: *Spitzer* IRAC White Dwarf Targets.

WD	Name	SpT	V (mag)	M (M$_\odot$)	T$_{\rm eff}$ (K)	t$_{\rm cool}$ (Gyr)	[H/He]	[Ca/H(e)]	log $\langle dM_{\rm z}/dt\rangle$ (g s^{-1})	log (M$_{\rm z}$) (g)	Ref
0110−565	HE 0110−5630	DBAZ	15.9	0.71	19 200	0.12	−4.2	−7.9	8.4	20.2	1,2
0435+410	GD 61	DBAZ	14.9	0.72	17 300	0.20	−4.0	−7.5	8.9	21.5	3
0446−255	HE 0446−2531	DBAZ	16.8	0.59	12 600	0.36	−3.2	−5.7 [b]	11.5	24.9	4
0449−259	HE 0449−2554	DBAZ	16.3	0.72	12 500	0.52	−4.5	−7.2 [b]	10.0	23.5	4
0802+386	G111-54	DZ	15.5	0.78	11 000	0.85	< −6.0	−9.8	7.4	21.1	5
0838+375	CBS 78	DBZ	17.7	0.59	12 500	0.36	< −5.0	−8.0	9.2	22.7	6
0953+594	SDSS	DZA	18.4	0.58	8 200	1.12	−3.2	−7.5	9.7	23.6	5
1015+377	CBS 127	DZ	17.7	0.58	10 500	0.59	< −5.0	−8.2	9.1	22.8	6
1349−230	HE 1349−2305	DBAZ	16.5	0.67	18 200	0.14	−4.7	−8.0	8.7	22.0	1,2
1350−162	HE 1350−1612	DBAZ	17.0	0.77	15 000	0.35	−4.7	−6.7 [b]	10.4	23.4	4
1352+004	PG	DBAZ	15.8	0.59	15 300	0.20	−4.8	−9.3	7.7	20.7	1
1614+160	PG	DAZ	15.6	0.50	17 400	0.10	...	−7.2	7.8	...	1
2138−332	NLTT 51844	DZ	14.5	0.69	7 200	2.23	...	−8.6	8.5	22.5	7
2142−169 [a]	PHL 131	DO	15.8	...	...	...	...	...	...	...	2
2229+139	PG	DBAZ	16.0	0.83	15 900	0.36	−4.5	−9.0	8.0	20.9	1
2322+118	LB 1188	DZA	16.0	0.59	12 000	0.41	−5.2	−8.7	8.5	22.1	1

[a] Not metal-rich.

[b] Klein et al. [2011] find that HS 2253+8023 has a lower calcium abundance by around 1.0 dex than originally reported by Friedrich et al. [2000]. This may therefore also be true of their other stars.

Note − Objects found to have dust discs are listed in italics. The tenth column lists time-averaged metal in-fall rates. The eleventh column shows the mass of metals in the convective envelopes of the helium-rich stars. Both quantities are calculated based on the observed calcium abundances and assuming this represents 1.6 per cent of the total mass of heavy elements, as in the bulk Earth [Allègre et al., 1995].

References − (1) Koester et al. 2005a; (2) Voss et al. 2007; (3) Desharnais et al. 2008; (4) Friedrich et al. 2000; (5) Dufour et al. 2007; (6) Dupuis et al. 1993a; (7) Subasavage et al. 2007

Table 6.2: IRAC Coordinates for HE and HS White Dwarfs.

Star	α	δ
HE 0110−5630	$01^{\mathrm{h}}12^{\mathrm{m}}21.15^{\mathrm{s}}$	$-56°14'27\rlap{.}''8$
HE 0446−2531	$04^{\mathrm{h}}49^{\mathrm{m}}01.39^{\mathrm{s}}$	$-25°26'36\rlap{.}''1$
HE 0449−2554	$04^{\mathrm{h}}51^{\mathrm{m}}53.72^{\mathrm{s}}$	$-25°49'14\rlap{.}''7$
HE 1349−2305	$13^{\mathrm{h}}52^{\mathrm{m}}44.13^{\mathrm{s}}$	$-23°20'05\rlap{.}''4$
HE 1350−1612	$13^{\mathrm{h}}53^{\mathrm{m}}34.96^{\mathrm{s}}$	$-16°27'06\rlap{.}''6$

Note – Epoch 2009 positions as measured on the IRAC array from image header astrometry.

Three of the target white dwarfs were chosen from the Hamburg Schmidt [HS; Hagen et al., 1995] and the Hamburg European Southern Observatory Schmidt [HE; Wisotzki et al., 1996] quasar surveys. As discussed in Farihi et al. [2010b], the SIMBAD coordinates for these objects are often inaccurate by up to a few arc minutes, and Table 6.2 gives correct positions for these sources based on their IRAC images.

6.1.1 Data analysis

The IRAC image photometry was performed on the individual Basic Calibrated Data (BCD) frames downloaded from the *Spitzer* archive and reduced using pipeline version S18.7.0. These were corrected for array-location dependence, as described in the IRAC Data Handbook[1]. We used the point source extraction package APEX MULTIFRAME within MOPEX [Makovoz et al., 2006] to perform PSF fitting photometry on the individual BCDs. We do not apply a colour correction because we use the isophotal wavelengths in our analysis. The magnitude of the correction is therefore negligible compared to our uncertainties. The pixel phase correction for channel 1 data is also minimal in comparison to the uncertainties and therefore was not applied. A minimum 5 per cent uncertainty on the flux density was assigned to account for the systematic uncertainties in this method [Reach et al., 2005].

The Infrared Spectrometer [IRS; Houck et al., 2004] Peak-up Imaging was analyzed according to the method of Brinkworth et al. [2012]. The sky background was found to be variable over the array (see Figure 6.1), so the individual BCDs were initially median-combined to make both a flat and sky, using 3σ rejection. This was then scaled to the overall median of the Post-BCD mosaic and subtracted from each of the individual BCDs. To completely reduce the sky level to zero, the edges of the image were temporarily discarded and a median of the center of the image

---

[1]See http://ssc.spitzer.caltech.edu/irac/dh
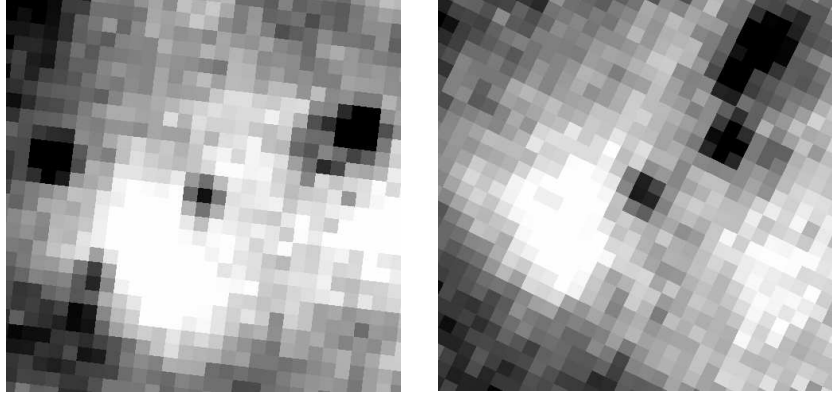
Figure 6.1: IRS Peak-Up image mosaics of GD 61 (*left*) and NLTT 51844 (*right*). The images are orientated North up and East left at $1''.8$ pixel^{-1} and $50''$ across. The background is clearly variable across the array and is therefore the primary source of error (§ 6.1.1).

was found and removed. The sky can therefore assumed to be zero and an infinite sky annulus is effectively used during photometry. The flat-fielded and median-subtracted BCDs were mosaicked using MOPEX with a dual-outlier rejection. The pixel scale for the mosaic was set to the default $1''.8$ pixel^{-1}. The photometry was performed with APPHOT within IRAF using a 3 pixel aperture radius, but no sky subtraction. The aperture correction to the calibration aperture sizes, as provided by the *Spitzer* Science Center, was performed and the fluxes were converted from MJy sr^{-1} to mJy. As an estimate of the error, a series of other apertures were placed around the target on the mosaic and the standard deviation of fluxes was taken as the uncertainty. All measured *Spitzer* fluxes are listed in Table 6.3.

6.1.2 Near-infrared observations

Supplemental near-infrared photometry for most target stars was obtained on the 23 March 2011 with the William Herschel Telescope using the Long-Slit Intermediate Resolution Infrared Spectrograph [LIRIS; Manchado et al. 1998], and on $10-12$ August 2011 with the New Technology Telescope using Son of Isaac [SOFI; Moorwood et al. 1998]. All the near-infrared observations were conducted and reduced by Dr J. Farihi. Images taken in a 9-point dither pattern were obtained the J, H, and K_s-band filters with typical total exposure times of $270\,$s in clear conditions; 3 standard star fields were observed in a similar manner for photometric zero-point calibration. These data were reduced in the standard manner, by subtracting a median sky from

Table 6.3: *Spitzer* IRAC and IRS fluxes..

WD	$F_{3.6\mu\mathrm{m}}$ (μJy)	$F_{4.5\mu\mathrm{m}}$ (μJy)	$F_{7.9\mu\mathrm{m}}$ (μJy)	$F_{15.6\mu\mathrm{m}}$ (μJy)
0110−565	135 ± 9	124 ± 8	···	···
0435+410	···	259 ± 13	153 ± 8	98 ± 10
0446−255	···	26 ± 1	15 [b]	···
0449−259	···	39 ± 2	24 ± 1	···
0802+386	···	85 ± 4	38 ± 2	···
0838+375	18 ± 1	13 ± 1	···	···
0953+594	···	9 ± 1	6 [b]	···
1015+377	20 ± 1	14 ± 1	···	···
1349−230	···	88 ± 2	66 ± 3	···
1350−162	···	23 ± 2	7 [b]	···
	32 ± 2	23 ± 1	···	···
1352+004	···	52 ± 3	15 ± 2	···
1614+160	···	63 ± 3	32 ± 2	···
2138−332	···	503 ± 25	195 ± 10	95 ± 15
2142−169 [a]	···	35 ± 2	12 ± 4	···
2229+139	···	43 ± 2	13 ± 2	···
2322+118	105 ± 5	69 ± 3	···	···

[a]Not metal-polluted.

[b]3σ upper limit.

Note – A 5 per cent uncertainty has been folded in to account for calibration errors [Reach et al., 2005]. Pipeline S18.7.0 was used to obtain BCD products for all targets.

each image in the dithered stack, flat fielding (using sky flats), then averaging and recombining frames.

LIRIS suffers from what is known as a detector reset anomaly, which appears in certain frames as a discontinuous jump (in dark current) between the upper and the lower two quadrants. To remove this unwanted signal, after flat fielding and sky subtraction, the detector rows were collapsed into a median column (with real sources rejected), and subsequently subtracted from the entire two dimensional image. The resulting fully-reduced frames exhibit smooth backgrounds, free of the anomalous gradient. Analogously, SOFI exhibits significant cross-talk between quadrants, which becomes apparent for bright sources. The IRAF script CROSSTALK was employed on each of the raw frames prior to processing as described above, effectively removing any unwanted artifacts.

Aperture photometry of standard stars and relatively bright targets was performed using $r \approx 4''$ aperture radii and sky annuli of ranging between $5''$ and $8''$. For relatively faint targets or those with neighbouring sources, smaller apertures were employed with corrections derived from several brighter stars within the same image field and filter. In a few cases, PSF-fitting photometry (i.e., DAOPHOT) was used as a second method in addition to photometry with small apertures. All data taken in the K_s-band filter were flux-calibrated using ARNICA [Hunt et al., 1998] K-band standard star photometry. The measured photometry can be found in Table 6.4.

6.2 Analysis and results

6.2.1 Removal of nearby background source flux

The IRAC mosaicked images of GD 61, CBS 127, and HE 1349−2305 all reveal nearby background objects that have the potential to contaminate aperture photometry (see Figure 6.2 and Figure 6.3 for the images of GD 61 and HE 1349−2305 respectively). The background object near GD 61 is separated by $1''\!.9$ at P.A. 25° in the images taken with LIRIS (epoch 2011.2), and is readily resolved in the H and K bands. The near-infrared brightness of this neighbour is $(J, H, K) = (17.7, 17.0, 16.7)$ mag and never approaches the apparent magnitude of the white dwarf. Based on this fact and the colours of the neighbour, it must be a background object. This source contributes weakly in the $4.5\,\mu$m image, where it is well separated by APEX, and is no longer seen at $7.9\,\mu$m. CBS 127 and HE 1349−2305 both have neighbours $2''\!.8$ distant (north and west respectively); these are satisfactorily separated by PSF fitting with APEX.
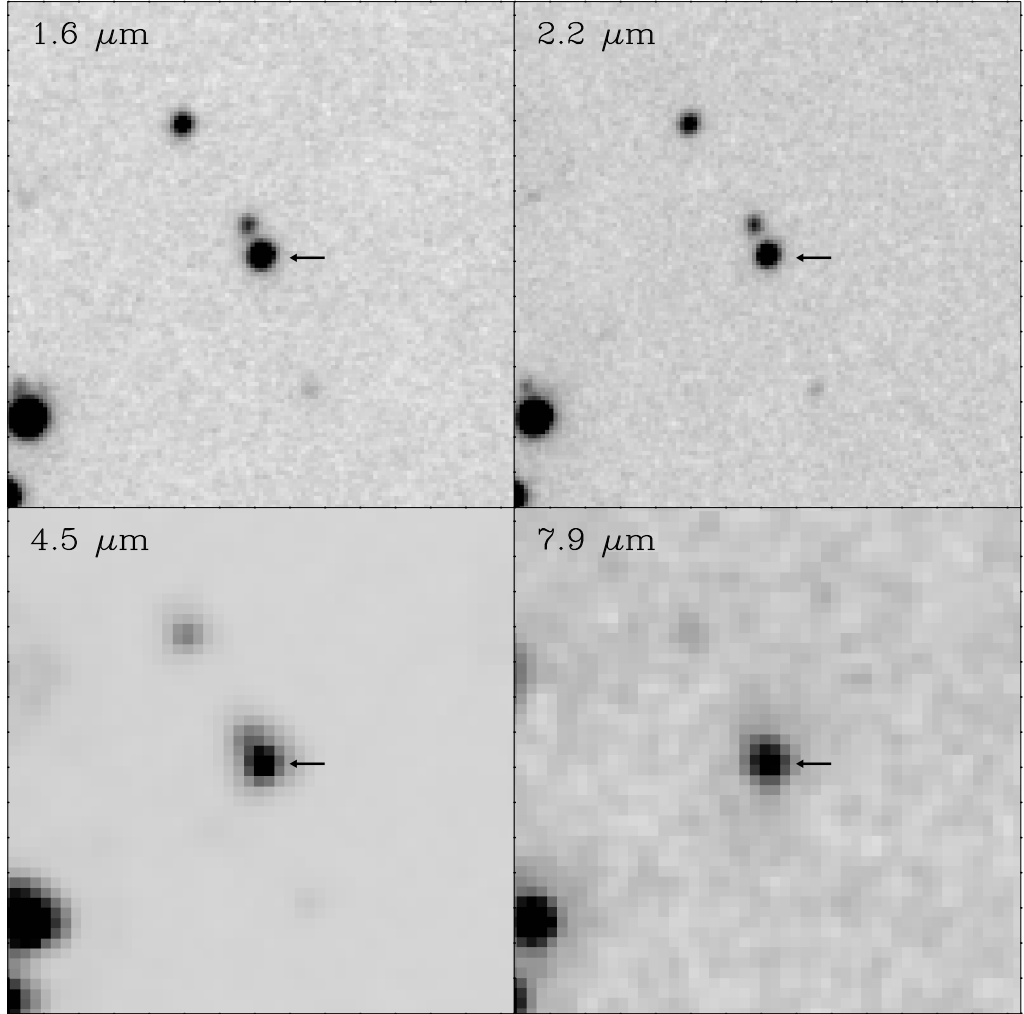
Figure 6.2: Infrared images of GD 61 taken with LIRIS at H and K_s, and *Spitzer* IRAC at 4.5 and 7.9 μm. All images are oriented North up and East left, and are $30''$ across, with $0\!''\!.25$ pixel^{-1} for LIRIS and $0\!''\!.6$ pixel^{-1} for IRAC. The white dwarf (marked by the arrow) is separated from a neighbouring source by $1\!''\!.9$. The neighbour does not influence the flux measurements presented in Table 6.3 (§ 6.2.1). The neighbouring source must be in the background based upon its brightness and colours.
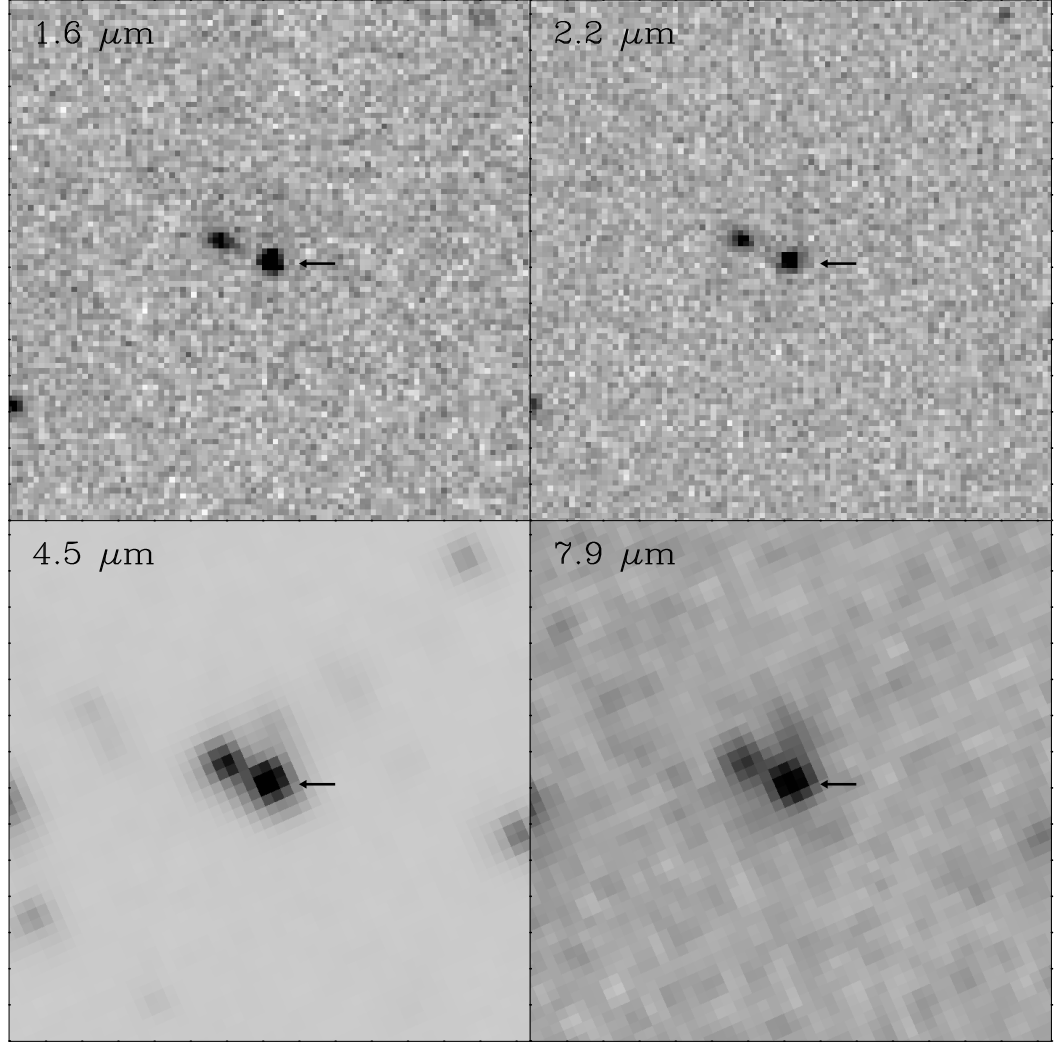
Figure 6.3: Infrared images of HE 1349−2305 taken with SOFI at H and K, and *Spitzer* IRAC at 4.5 and 7.9 μm. All images are oriented North up and East left, and are $30''$ across, with $0\!''\!\!.25$ pixel^{-1} for LIRIS and $0\!''\!\!.6$ pixel^{-1} for IRAC. The white dwarf (marked by the arrow) is separated from a neighbouring source by $2\!''\!\!.8$, but does not influence the flux measurements presented in Table 6.3 (§ 6.2.1). The neighbour is clearly extended in the H-band image and is therefore extragalactic.

Table 6.4: Near-Infrared Photometry.

WD	J	H	K	Instrument
	(mag)	(mag)	(mag)	
0110−565	16.23 ± 0.05	16.27 ± 0.05	16.24 ± 0.05	SOFI
0435+410	15.24 ± 0.05	15.16 ± 0.05	15.12 ± 0.05	LIRIS
0446−255	17.06 ± 0.05	17.09 ± 0.05	17.15 ± 0.05	SOFI
0449−259	16.52 ± 0.05	16.56 ± 0.05	16.60 ± 0.05	SOFI
0802+386	15.60 ± 0.05	15.59 ± 0.05	15.65 ± 0.05	LIRIS
0838+375	18.03 ± 0.05	18.02 ± 0.05	17.98 ± 0.05	LIRIS
0953+594	18.33 ± 0.06	18.29 ± 0.06	18.23 ± 0.06	WFCAM [a]
1015+377	17.24 ± 0.10	17.31 ± 0.12	16.78 ± 0.31	GEMINI [b]
1349−230	16.91 ± 0.05	16.94 ± 0.05	16.78 ± 0.05	SOFI
1350−162	17.13 ± 0.05	17.17 ± 0.05	17.25 ± 0.05	SOFI
1352+004	16.10 ± 0.05	16.12 ± 0.05	16.15 ± 0.05	LIRIS
1614+160	15.93 ± 0.05	15.97 ± 0.05	16.04 ± 0.05	SOFI
2229+139	16.29 ± 0.05	16.36 ± 0.05	16.53 ± 0.05	SOFI
2322+118	15.99 ± 0.05	15.98 ± 0.05	16.03 ± 0.05	SOFI

[a] Obtained by Dr Farihi at UKIRT using WFCAM (Casali et al. 2007, A&A, 467, 777).

[b] Obtained by C. Melis at Lick Observatory with the GEMINI camera (McLean et al. 1993, SPIE, 1946, 513).

6.2.2 Spectral energy distributions

Figures 6.4, 6.6 and 6.7 illustrate the SEDs of the 15 metal-rich white dwarfs listed in Table 6.1. In addition to the supplementary near-infrared photometry described above, we include shorter wavelength photometry from a variety of literature and catalog sources (e.g., *GALEX*, SDSS DR7, DENIS, and CMC). In cases where independent *JHK* observations were not taken for this program, data from 2MASS and UKIDSS were used. Where possible, a comparison of the IRAC photometry was made to data available at similar wavelengths from the *Wide-field Infrared Survey Explorer*.

For flux scaling of the spectral models in the figures, the most reliable photometry was used, which was primarily SDSS *ugriz* and the *JHK* data taken specifically for this program. The *GALEX* fluxes were not used to constrain the white dwarf atmospheric models because 1) metal lines may significantly suppress these fluxes compared with a pure helium (or hydrogen) model atmosphere and 2) the interstellar reddening to these objects is not well known.

Table 6.1 lists the best available stellar parameters from the literature for each of the science targets. We used these parameters as an initial estimate for the white

dwarf spectral models. A grid of synthetic white dwarf atmospheric spectra from Koester [2010] was interpolated to these temperature and surface gravity estimates. After comparing the fluxes from the models with the most reliable optical and near-infrared data, in some cases we found that a slightly different effective temperature provided a superior fit to the data (shown in the upper right corner of the relevant figure). These parameters thus used in the SED fits do not reflect an independent parameter determination, but rather our attempt to best constrain the infrared photospheric emission.

6.2.3   Stars with an infrared excess

We model stars with an infrared excess as a combination of the white dwarf photosphere and an optically thick, geometrically thin disc with a temperature profile $T_{disc} \propto r^{\beta}$, with $\beta = -3/4$ [Adams et al., 1988; Chiang & Goldreich, 1997; Jura, 2003]. The ratio of stellar radius to distance sets the absolute scale of the white dwarf photospheric flux, and is fixed in our modeling based on the best available parameters. The free parameters in the disc model are the inner disc radius (R_{in}), the outer disc radius (R_{out}) and the disc inclination (i). A grid of disc models was calculated with inner (T_{in}) and outer disc temperatures (T_{out}; each corresponding to a value of R_{in} and R_{out}) ranging from 100 to 1800 K in steps of 50 K, and inclination ranging from 0 to 90° in steps of 5°. T_{out} was also fixed to be cooler than T_{in}. A least χ^2 method was used to fit the H-, K- and IRAC-band infrared fluxes and provide an estimate of the uncertainties.

In Figure 6.5, the panels show a slice through the χ^2 cube at the best fit solution. The upper panel of each pair displays a slice at the best fitting T_{out}, whilst the best fit inclination defines the slice in the lower panel. Regions of high χ^2 are shown as dark areas and the least χ^2 solution is marked as a red circle and its flux is displayed in Figure 6.4. Solid black lines show the 1σ contours around the minimum, while 2 and 3σ contours are shown as dashed gray lines. The upper left of each lower panel is excluded by the condition $T_{in} > T_{out}$.

The flat disc models naturally possess a modest degree of uncertainty. The three free parameters (T_{in}, T_{out} and i) are somewhat degenerate in how they combine to determine the viewed solid angle of the disc. Even in the case when longer wavelength data (such as $24\,\mu m$ photometry) are available, this degeneracy is not broken [Jura et al., 2007a]. Broadly speaking, the inner disc edges are fairly well constrained by their 2.2 and $3.6\,\mu m$ emission. The 4.5 to $7.9\,\mu m$ flux, however, can be reproduced by a relatively wide temperature range and a higher inclination, or a narrower temperature range and a lower inclination. Importantly, the newly

detected discs mimic the emission seen at more than one dozen dusty white dwarfs observed with *Spitzer* IRAC and MIPS [e.g. Farihi et al., 2009] whose outer disc radii are consistently within the Roche limit $d \gtrsim 1\,\mathrm{km}$ solid bodies ($\sim 1\mathrm{R}_\odot$). This corresponds to an outer disc temperature near $500\,\mathrm{K}$, which is a likely lower limit for T_out when interpreting the χ^2 surfaces. All together, the infrared emissions are precisely that expected for dust particles resulting from the tidal destruction of a large planetary body, whose constituent elements now rain onto and pollute the surfaces of the host stars.

HE 0110−5630. The available photometry for HE 0110−5630 consists of *GALEX* far- and near-UV, DENIS *I*-band and *J*, *H* and *K* measurements taken with SOFI. The photospheric emission is relatively well constrained by the *J*- and *H*-band fluxes and, therefore, so is the extrapolation to longer infrared wavelengths. The measured IRAC excess for HE 0110−5630 is consistent with warm circumstellar dust and is shown in Figure 6.4. The best-fit disc model has an inner and outer temperature $1,000$ and $900\,\mathrm{K}$, respectively, at an inclination of $i = 60°$. This corresponds to a narrow ring, however, as can be seen in the χ^2 panels, the solution is degenerate with respect to inner disc temperatures above $800\,\mathrm{K}$, and inclination, and the outer temperature is not at all constrained. The χ^2 surfaces in Figure 6.5, show that a vast range in disc temperatures could provide a fit to the excess. We therefore cannot confidently estimate any of the disc parameters.

GD 61. From analysis of IRAC images and Peak-Up Imaging, this object was found to have an excess in Farihi et al. [2011a]. Here we include the *JHK* data taken with LIRIS to better constrain the stellar flux. These images resolve a nearby (background) source (Figure 6.2) that almost certainly contaminates the 2MASS photometry used in previous fits. From its spectral energy distribution and brightness, this object is not associated with the white dwarf. In the *Spitzer* IRAC images, the PSF of the white dwarf and the contaminant overlap slightly, however, the APEX PSF-fitting photometry cleanly separates the two objects. We can therefore confirm the presence of a disc from the IRAC and IRS fluxes.

When performing χ^2 fitting of the infrared excess, we exclude the $15.6\,\mu\mathrm{m}$ flux due to a possible increase owing to silicate emission, and therefore the disc continuum emission would be overestimated. Such emission has been detected in all eight dusty white dwarfs observed spectroscopically with IRS [Reach et al., 2005; Jura et al., 2009a]. A disc model with inner and outer-disc temperatures of $1,450$ and $800\,\mathrm{K}$, respectively, and an inclination $i = 85°$ is the best fit to the excess (Figure 6.4 and Figure 6.5). The disc model temperature and inclination are again degenerate, and a large range of parameters would fit the infrared fluxes. We therefore find the

values reported previously [$T_{\rm in} = 1,300\,{\rm K}$, $T_{\rm out} = 1,000\,{\rm K}$ and $i = 79°$; Farihi et al., 2011a] are not inconsistent with ours, given the uncertainties in temperature and inclination.

HE 1349−2305. After deconvolving the white dwarf and neighbouring, background source (§ 6.2.1), a significant infrared excess is still found over the stellar model (Figure 6.4). The white dwarf photosphere is well constrained by short wavelength and near-infrared photometry shown in Table 6.4. *WISE* 3.4 and 4.6 μm fluxes are also available for this object, however, the nearby source seen in Figure 6.3 is within the *WISE* beam width and therefore significantly contaminates the *WISE* fluxes. We therefore do not include these fluxes in the disc modeling. The excess is best fitted with a disc having $T_{\rm in} = 1,700\,{\rm K}$, $T_{\rm out} = 550\,{\rm K}$ and an inclination of $i = 85°$. The uncertainties are rather modest in this case.

NLTT 51844. This was one of two white dwarfs bright enough to attempt a blue Peak-Up image using IRS. The 15.6 μm flux measurement is in excess over the white dwarf model by slightly more than 3σ, similar to the MIPS 24 μm photometric excesses detected at G238-44 and G180-57 [Farihi et al., 2009]. *Spitzer* galaxy counts at these wavelengths are 6×10^{-4} galaxies per square arc second [Marleau et al., 2004] for the brightness needed to produce an apparent excess in these cases. Therefore the probability that such a source falls within a radius of two IRS Blue Peak-Up FWHM (3″.8) can be as high as 10 per cent. Thus the probability that three sources have excesses at roughly 20 μm (and not at shorter wavelengths) due to background objects, out of 30 stars surveyed at these longer wavelengths, can be as high as 65 per cent.

While we cannot yet rule out a chance alignment in these cases, the astrometric position of NLTT 51844 in the IRS image mosaic coincides within 2″ of its position in the IRAC images, based on the absolute *Spitzer* astrometry provided in the processed image files. Both NLTT 51844 and G180-57 are cool, helium-rich stars where metals can be resident for Myr timescales, and hence their accretion history is unconstrained. In any case, dust that emits only at such long wavelengths must be sufficiently far from the white dwarf that it cannot be the immediate source of the atmospheric metals. Still, if the data for NLTT 51844 (as well as G238-44 and G180-57) are not spurious, we may be seeing an important clue to the nature of numerous polluted white dwarfs without obvious infrared excesses.

6.2.4 Stars without an infrared excess

The remaining white dwarfs (Figures 6.6 and 6.7) all show no evidence for infrared excess emission. They are relatively well constrained in the optical and near-infrared
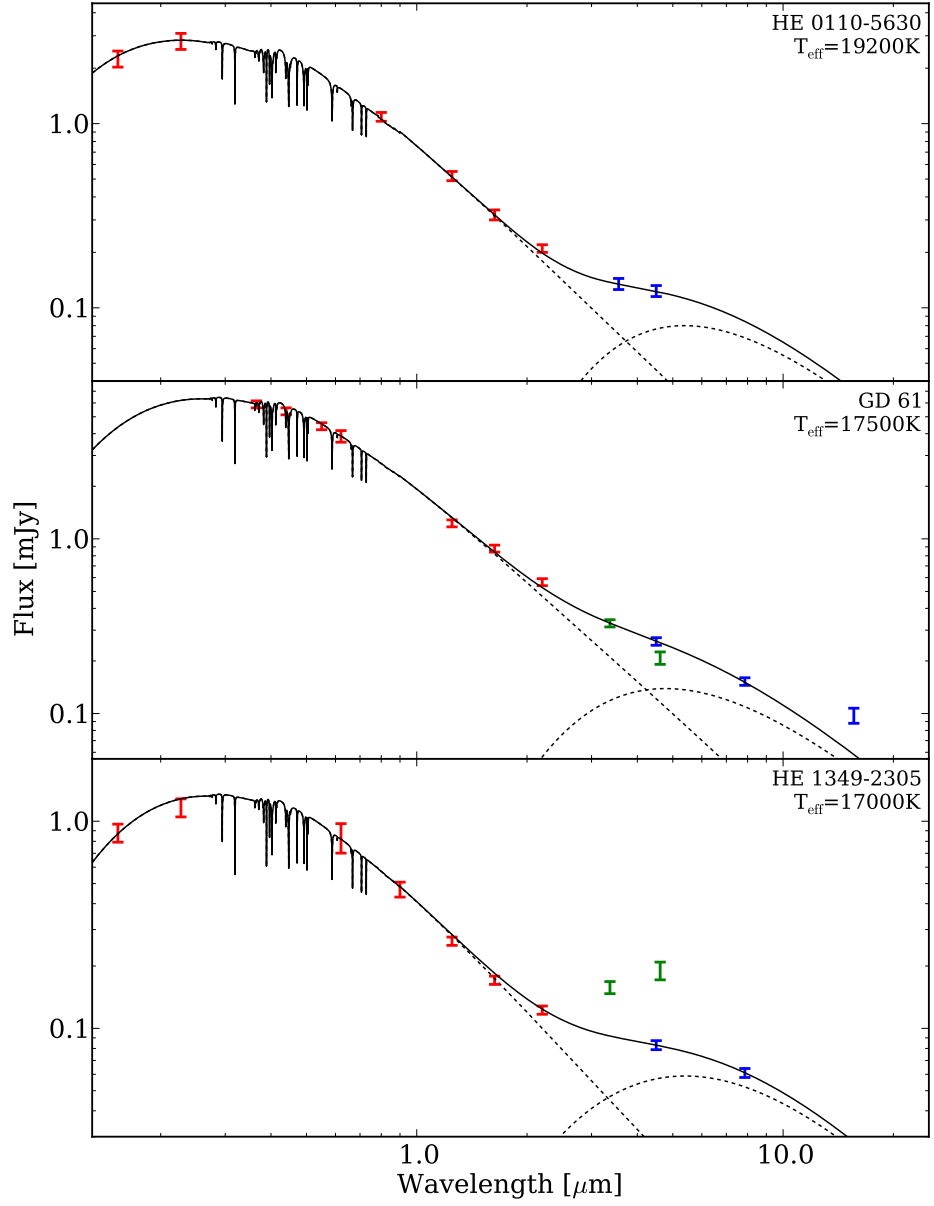
Figure 6.4: SED of HE 0110-5630, GD 61 and HE 1349−2305. The short wavelength fluxes are: HE 0110-5630: *GALEX*, DENIS *I*-band, and SOFI *JHK*, GD 61: *UBV* [Eggen, 1968] CMC *r′*, and LIRIS *JHK*, and HE 1349−2305: *GALEX*, CMC *r′*, DENIS *I*, SOFI *JHK*. These are shown in red with error bars. *WISE* data are shown in green, however, they are clearly contaminated by the neighbouring source for HE 1349−2305 (§3.1). The IRAC and IRS fluxes are shown in blue. The short wavelength photometry is fitted with a stellar model that is displayed as a black dashed line. The minimum χ^2 disc model fit, shown in Figure 6.5, is similarly displayed as a black dashed line, and the sum of the two is shown as a solid black line.
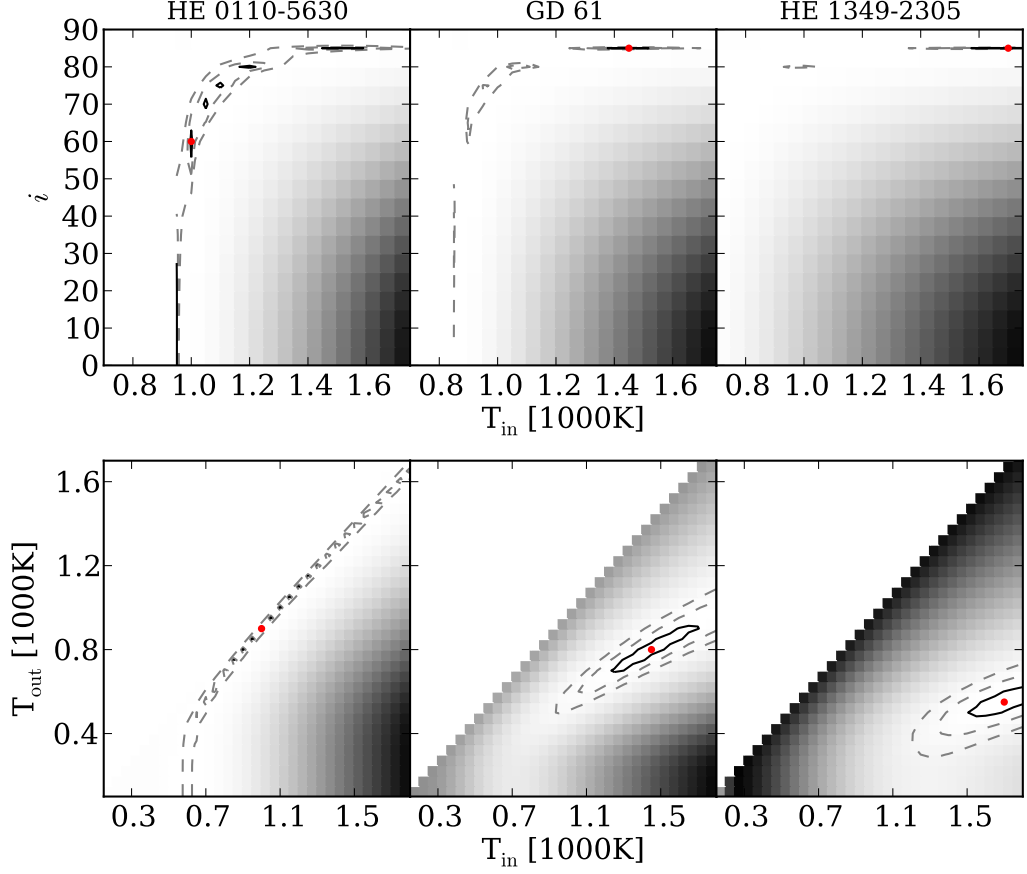
Figure 6.5: Disk modeling for HE 0110-5630, GD 61 and HE 1349−2305. The infrared excess was fitted using the method described in §6.2.3. Briefly describing the format of the panels (see §6.2.3); a slice through the χ^2 volume is displayed in each of the pairs of upper and lower panels for the minimum χ^2 fit. The upper panels show a slice at the best fitting T_{out} and the lower panels are defined by the best i. The best fitting solutions are: HE 0110-5630: $T_{in} = 1,000$ K, $T_{out} = 900$ K, $i = 60°$, GD 61: $T_{in} = 1,450$ K, $T_{out} = 800$ K, $i = 85°$ and HE 1349−2305: $T_{in} = 1,700$ K, $T_{out} = 550$ K, $i = 85°$. Regions of high χ^2 are shown as dark areas and the least χ^2 solution is marked as a red circle. Solid black lines show the 1σ contours around the minimum, while the 2 and 3σ contours are shown as dashed gray lines. Because only slices through the χ^2 cube are shown, this does not show the full extent of the χ^2 space. In the case of HE 0110-5630, i vs T_{in}, each of the regions enclosed by a solid black line represents a parameter space where χ^2 is within 1σ of the minimum. The χ^2 method does not constrain the disc parameters very well for HE 0110-5630.

and therefore we can extrapolate with some certainty to IRAC wavelengths. Below we provide notes on a few particular stars.

HE 0446−2531. This star is perhaps the most highly polluted white dwarf observed by *Spitzer* and yet does not have an infrared excess. If the analysis of Friedrich et al. [2000] is correct, this star contains 8×10^{24} g of metals in its convection zone – a mass approaching that of Pluto. The long diffusion timescale for heavy elements in this star allows for the possibility that a disc has been fully dissipated, but the very large mass involved suggests we are still within at most a few diffusion timescales of the accretion event. Two possibilities are: 1) accretion is ongoing from gaseous debris, or 2) accretion has ended but the total mass involved was at least an order of magnitude higher. It is noteworthy that this star and HS 2253+8023 are both highly polluted [Friedrich et al., 2000] yet lack infrared excess, with HE 0446−2531 having nearly ten times more metal mass in its convection zone. However, Klein et al. [2011] found that HS 2253+8023 has an order of magnitude less calcium than originally reported by Friedrich et al. [2000], and therefore the same may be true of HE 0446−2531.

HE 0449−2554. A partly-resolved extension is seen in the IRAC 7.9 μm image, and the combined source is offset slightly from the position of the white dwarf in the 4.5 μm image. While the SOFI *JHK* images of this star do not reveal any sources within a few arc seconds of the science target, the marginal, apparent excess seen in the SED (Figure 6.6) is probably caused by a background object. Better data are needed to rule out contamination in IRAC.

CBS 127. As mentioned above, a background object lies within a few arc seconds of the white dwarf, and could potentially contaminate moderate-size apertures used for IRAC photometry. We used PSF-fitting routines within APEX to ensure both stars were photometrically disentangled. There is no infrared excess observed for this white dwarf.

HE 1350−1612 was observed in both the Cycle 5 and 6 programs and images were thus taken at 3.6, 4.5 (twice), and 7.9 μm. The average 4.5 μm flux is shown in Table 6.1 and Figure 6.7. The white dwarf was not detected in the 7.9 μm image, and thus a 3σ upper limit is given. Nevertheless, all the infrared data are consistent with the predicted white dwarf photosphere.

PHL 131 is a 40,000 K white dwarf with interstellar calcium absorption, and hence not metal-rich. It was an interloper in the initial target selection for *Spitzer* observations. We do not analyze this star but its IRAC fluxes are reported in Table 6.3.
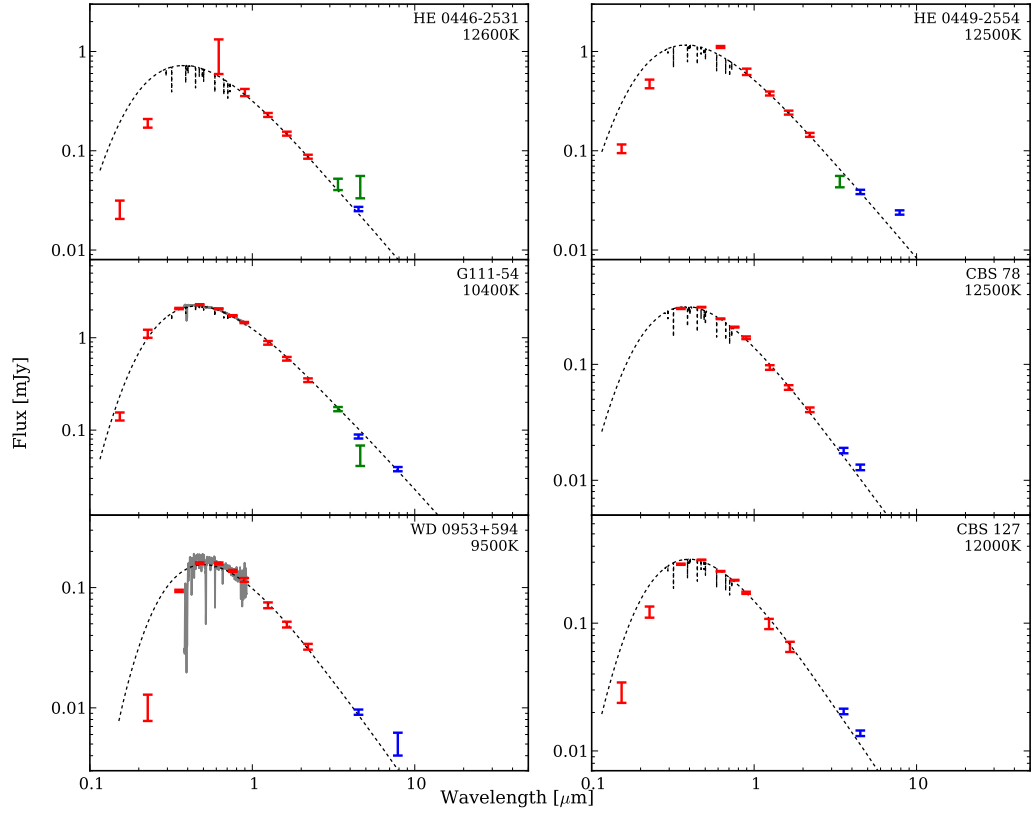
Figure 6.6: SEDs of 6 of the 12 science targets consistent with photospheric emission (§3.4). The figures follow the same general format as Figure 6.4. The SDSS optical spectrum of WD 0953+954 is shown as a gray line. The infrared excess seen in the SED of HE 0449−2554 is caused by light from a background object. The *GALEX* ultraviolet photometric is systematically low compared with the models due to a combination of interstellar reddening and metal absorption.
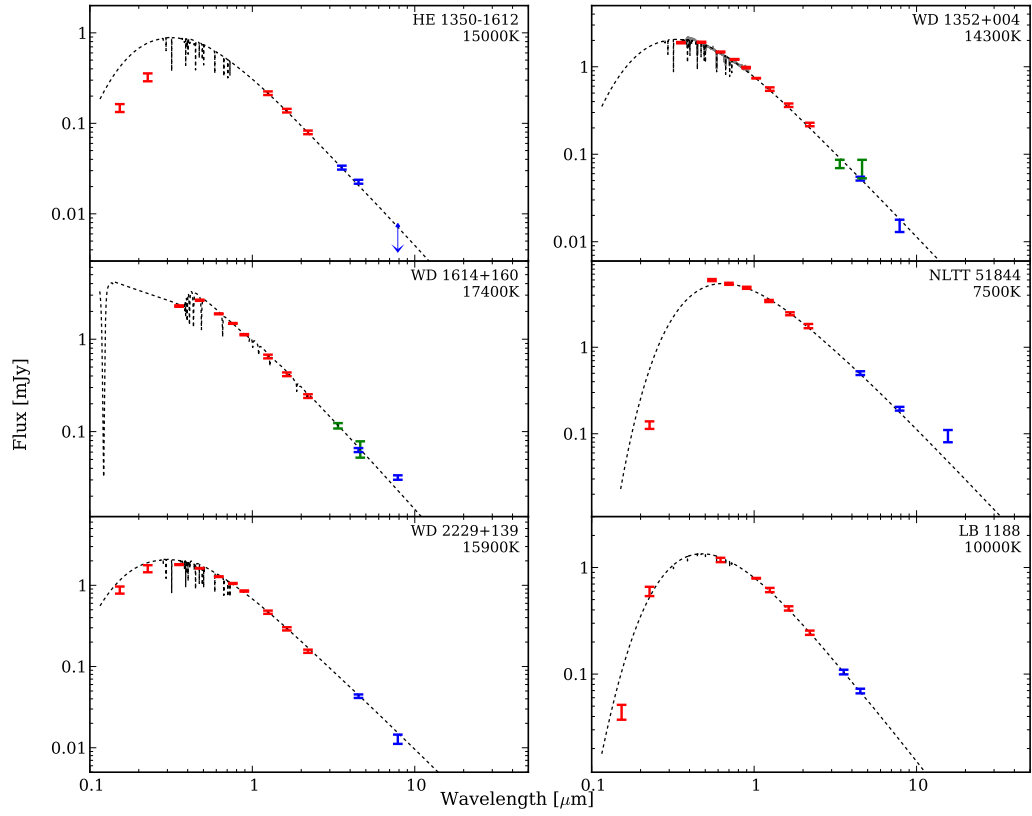
Figure 6.7: A continuation of Figure 6.6 for the remaining 6 of the 12 science targets consistent with photospheric emission (§3.4).

118

6.3 White dwarfs with planetary remnants

6.3.1 Updated statistics and accretion rates

Of the 15 metal-polluted stars surveyed, three have an infrared excess consistent with a circumstellar dust disc, indicative of a remnant planetary system. Including the objects presented here, the total number of metal-polluted white dwarfs observed with *Spitzer* in Cycle 1 through 7 is 92. This includes the 52 objects from Table 4 of Farihi et al. [2009], 8 from Table 1 of Farihi et al. [2010b], 3 white dwarfs with gas discs from Gänsicke et al. [2006b, 2007, 2008], 14 DBZ white dwarfs from Xu & Jura [2012] and the 15 objects studied here. Of these 92 objects, DAZ and DBZ-type white dwarfs are represented in proportions of 39 and 53 respectively.

Our expanded study corroborates the previous finding [Kilic et al., 2008; Farihi et al., 2009, 2010b] that the detection of infrared excess is less frequent among DBZ white dwarfs than among their DAZ counterparts. 11 of 38 (29 per cent) surveyed DAZ stars have circumstellar dust, whereas the same fraction for surveyed DBZ-type white dwarfs is only 7 of 52 (13 per cent)[2]. Because one would not expect discs to preferentially form around stars based on their atmospheric properties, the difference must be due to the longer diffusion timescales [Paquette et al., 1986; Koester & Wilken, 2006]. We will return to this point in more detail below.

Figure 6.8 illustrates the time-averaged metal accretion rate versus cooling age for the 88 metal-rich white dwarfs now observed by *Spitzer* with published abundances (four of Xu & Jura 2012 stars, including one with a detected infrared excess, do not have published abundances), updating Figure 10 from Farihi et al. [2010b]. All accretion rates were calculated by Dr J. Farihi based on the accumulated metal abundances, using Equation 2 of Koester & Wilken [2006], as performed in Farihi et al. [2009]. One difference between the method used in Farihi et al. [2009] and here is that in previous studies instantaneous and time-averaged accretion rates were calculated assuming the in-falling material either had Solar calcium abundances [1 part in 43; Koester & Wilken, 2006], or 1 per cent Solar [1 part in 109; i.e. metals only; Jura et al., 2007a; Farihi et al., 2009] by mass fraction, based on the measured calcium abundance. The additional 1/100 factor was initially introduced to "correct" the Koester & Wilken [2006] rates to reflect that only accreted heavy elements are of interest.

While the latter approach is still likely to be broadly correct, recent progress

---

[2]We exclude here the two DAZ and one DBZ that were already known to have gaseous discs [Gänsicke et al., 2008] prior to their *Spitzer* observations. The stars discussed in Farihi et al. [2012] were also not included because they were observed with *Spitzer* after they were found to have an infrared excess in Girven et al. [2011].
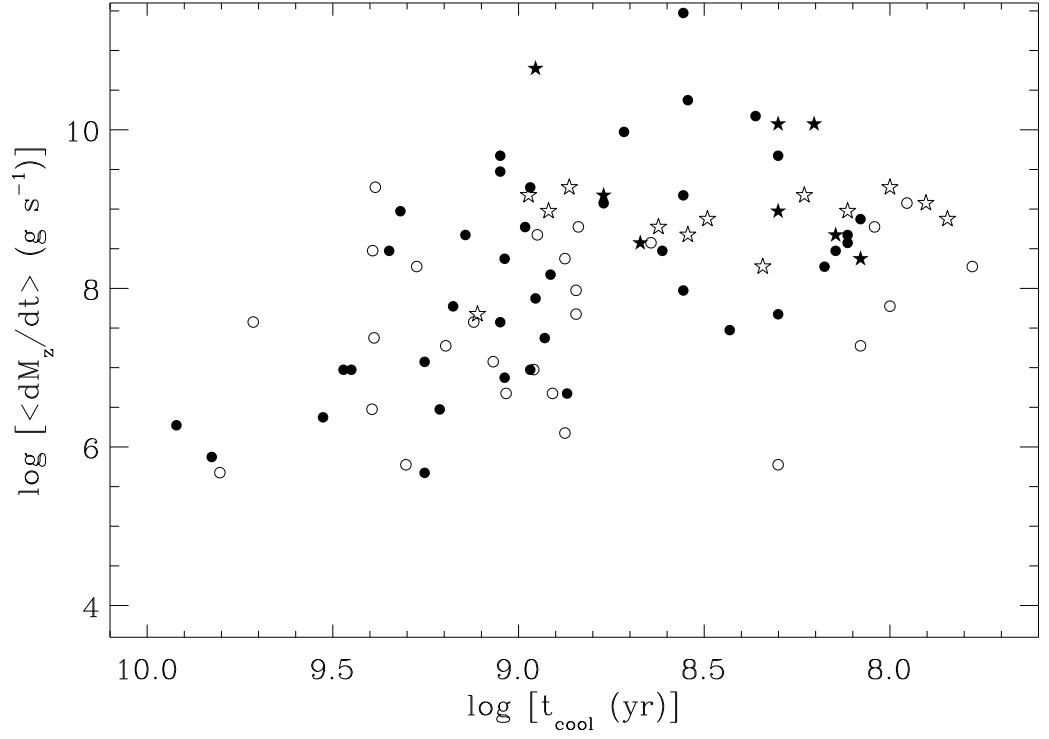
Figure 6.8: Time-averaged dust accretion rates vs. cooling age of the 88 metal-polluted white dwarfs, with published abundances, observed with *Spitzer* IRAC in Cycle 1 through 7. DAZ and DBZ-type stars are plotted as open and filled circles respectively, while objects with infrared excess are displayed as stars rather than circles.

in the field enables a more accurate estimation. There are now of order ten metal-polluted white dwarfs with measured Mg, Si, Ca, and Fe abundances [Zuckerman et al., 2003, 2007, 2010, 2011], and a handful also with O abundances [Dufour et al., 2010; Klein et al., 2010; Vennes et al., 2010; Klein et al., 2011; Melis et al., 2011; Vennes et al., 2011b]. Based on these data, it is increasingly clear that the accreted material has a composition similar to that of rocky, terrestrial material of the Solar System. Zuckerman et al. [2010] find that Ca represents, on average, close to 1 part in 60, by mass, of all the accreted heavy elements. For comparison, this ratio is 1 part in 62.5 for the Earth [Allègre et al., 1995]. Based on these facts, Figure 6.8 and Table 6.1 employ accretion rates, and convective envelope masses, assuming Ca is 1.6 per cent (1/62.5) of the total mass. To convert between the accretion rates quoted in Farihi et al. [2009, 2010b] and those shown in Figure 6.8, one must multiply by a factor of 109/62.5 for DAZ white dwarfs and 43/62.5 for DBZ white dwarfs.

Compared to the same Figures shown in previous (related) papers, the accretion rates for the DAZ white dwarfs are therefore slightly decreased, while their DBZ counterparts are slightly increased.

6.3.2 A simple estimate of the disk lifetime

The mass of metals in the convective envelope of DBZ-type white dwarfs provides a lower limit on the total mass of the destroyed parent body. From the DAZ stars, we can infer the instantaneous accretion rates because one can safely assume accretion-diffusion equilibrium (the equilibrium between mass transfer processes into and out of the visible layers of the atmosphere). There is no a priori reason that discs around hydrogen and helium-rich stars should be different [Jura et al., 2007a]. Therefore, making two assumptions: Firstly, because we do not know the form of the accretion rate over time, and whether or not there are periods of extremely high accretion, we must assume that the inferred accretion rates of DAZ stars represent an accurate cross section over disc lifetimes. Secondly, we must assume this is also true for the observed metal masses contained within DBZ stellar envelopes. Thus, we can obtain a typical disc lifetime by combining the average of these two observed quantities, i.e.,

$$t_{\mathrm{disc}} \sim \frac{\langle M_z \rangle_{\mathrm{DBZ,disc}}}{\langle dM_z/dt \rangle_{\mathrm{DAZ,disc}}}. \tag{6.1}$$

Figure 6.9 demonstrates that the mass of metals in the convective envelope of DBZ white dwarfs is not a strong function of temperature, and hence cooling age.
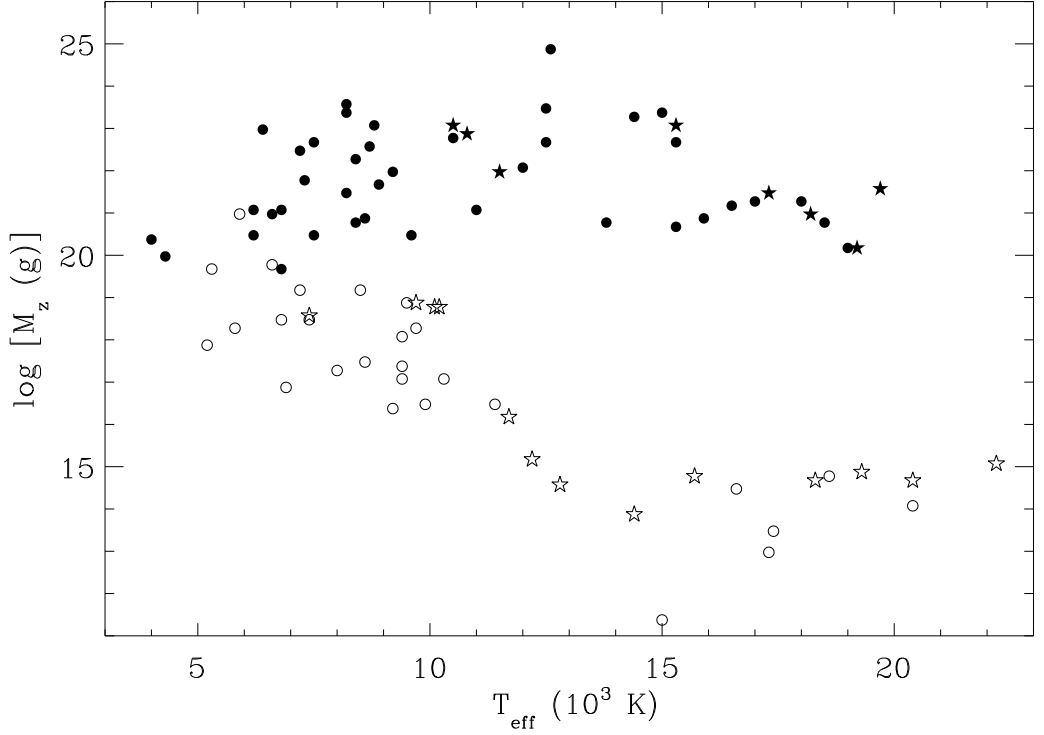
Figure 6.9: Mass of metals within the convective envelopes (or above $\tau = 5$, whichever is larger) of the 88 metal-polluted white dwarfs, with published abundances, observed with *Spitzer* IRAC in Cycle 1 through 7, plotted as a function of effective stellar temperature. DAZ and DBZ-type stars are plotted as open and filled circles respectively, while objects with infrared excess are displayed as stars rather than circles.

Therefore, calculating the average convective envelope metal mass across cooling ages should be robust. In contrast, the convective envelope depth increases substantially in this temperature range for DAZ stars [Koester, 2009], as can be seen by the large increase in convective envelope metal masses at longer cooling ages in Figure 6.9.

Among 13 DAZ white dwarfs observed to have infrared excess with *Spitzer*, the average metal accretion rate is $9.7 \times 10^8 \, \mathrm{g \, s^{-1}}$. Among 8 DBZ-type stars with dust detected by *Spitzer*[3] the average metal content of the convection zone is $4.1 \times 10^{22} \, \mathrm{g}$, and we thus estimate $t_{\mathrm{disc}} \simeq 1.3 \times 10^6 \, \mathrm{yr}$. However, Figure 6.8 shows that the accretion rates and convection zone metal content vary by orders of magnitude, and sug-

---

[3]This does not include SDSS J220934.84+122336.5, the DBZ star from Xu & Jura [2012] with an infrared excess, because no calcium abundances are published.

gests that using the logarithmic mean and standard deviation, $\langle\log[dM_z/dt\,(\mathrm{g\,s^{-1}})]\rangle =$ 8.8 ± 0.4 and $\langle\log[M_z\,(\mathrm{g})]\rangle = 21.9 \pm 1.1$, may be a more appropriate choice. The resulting estimate for the disc lifetime is $\log[t_{\mathrm{disc}}\,(\mathrm{yr})] = 5.6 \pm 1.1$. Because the metal masses in the DBZ stars are lower limits on the total parent body masses, it is reasonable to presume the same for the disc lifetimes.

At least 1 per cent of all white dwarfs with cooling ages less than $0.5\,\mathrm{Gyr}$ have dusty discs [see Chapter 5; Farihi et al., 2009; Girven et al., 2011; Steele et al., 2011]. Assuming that all white dwarfs host (remnants of) planetary systems and go through intermittent phases of debris accretion, one would expect any given star to exhibit detectable infrared excess for $0.01 \times 0.5 \times 10^9\,\mathrm{yr} = 5 \times 10^6\,\mathrm{yr}$, which is broadly consistent with our estimate above.

6.3.3   How complex is the evolution of the dust disks?

Different possible scenarios for the evolution of dust discs, and corresponding estimates for their lifetimes have been discussed in more detail by Jura [2008], Rafikov [2011a,b], and Bochkarev & Rafikov [2011].

A main motivation of the work of Jura [2008] was to explain the existence of metal-polluted white dwarfs without infrared excess detection by the continuous accretion from a gaseous disc that is replenished by the repeated tidal destruction of multiple small asteroids. In this scenario, dust discs are associated with the disruption of massive asteroids, and Jura [2008] estimated the lifetimes of the gaseous and dust discs to be $\sim 0.5 \times 10^4\,\mathrm{yr}$ and $\sim 1.5 \times 10^5\,\mathrm{yr}$, respectively, though he underlined the uncertainty of these estimates. Jura [2008] discussed his scenario in the context of a much smaller sample of metal-polluted white dwarfs, in which the majority of high dM/dt stars were displaying infrared excess identifying the presence of dusty discs. It is unlikely that the much larger accretion rates that are now known for some stars without infrared excess can be explained by multiple impacts of small asteroids.

Rafikov [2011a] showed that Poynting-Robertson drag can explain accretion rates of $\sim 10^8\,\mathrm{g/s}$, and estimated the lifetime of massive ($\sim 10^{22}\,\mathrm{g}$) dust discs to be several Myr. The higher accretion rates observed in a number of white dwarfs require the presence of gas that increases the viscosity, and Rafikov [2011b] shows that sublimation of the inner disc may be sufficient to lead to a runaway evolution which produces accretion rates of $10^{10} - 10^{11}\,\mathrm{g/s}$, exhausting the disc in $\sim 10^5\,\mathrm{yr}$. Rafikov [2011b] explicitly excluded the generation of gas by multiple impacts of additional asteroids. Extending the analysis to the global evolution of the debris discs, Bochkarev & Rafikov [2011] confirm that massive discs have expected life times

of several Myr if subject to Poynting-Robertson drag only, but that sublimation may substantially shorten these estimates.

Our disc lifetime estimate in the previous section is broadly compatible with all the estimates summarized above. However, our approach assumed that accretion rates do not change significantly as a function of disc age, and that the *Spitzer* sample is representative of the potential changes in the accretion rate. Zuckerman et al. [2010] suggested that accretion onto a white dwarf could proceed through three distinct phases; a build-up, a steady state, and a decline, where the steady state lifetime should be orders of magnitude longer than the beginning and ending episodes. If correct, and disc lifetimes are typically $\simeq 10^6$ yr, then it will be very unlikely for an arbitrary white dwarf with circumstellar dust to be observed in anything other than a steady state phase.

Inspection of Figure 6.8 shows, as already mentioned in § 6.3, that the fraction of DBZ with *Spitzer* infrared excess is substantially smaller than that of DAZ. The detection of dust seems to be associated with a minimum accretion rate, and if we only consider white dwarfs with $dM/dt \geq 10^8 \mathrm{g\,s^{-1}}$, we find that 10/21 (48 per cent) of DAZ have infrared excess, compared to only 7/30 (23 per cent) for the DBZ[4]. This difference is, however, subject to small number statistics and future observations may show that both DAZ and DBZ are equally likely to show an infrared excess. If there is a real disparity, this fact is most likely related to the one significant difference between DBZ and DAZ; their diffusion time scales, and allows some independent gauge of the disc lifetime. Assuming a typical lifetime of the discs that is similar to or greater than the diffusion time scale of the DBZ stars ($t_{\mathrm{disc}} \gtrsim t_{\mathrm{diff}} \simeq 10^5 - 10^6$ yr), we would expect a similar ratio of DAZ and DBZ stars exhibiting infrared excess. By contrast, if $t_{\mathrm{disc}} \ll t_{\mathrm{diff}}$, it would be very unlikely to detect the discs around any given DBZ. Thus, the small but non-negligible fraction of DBZ with observed infrared excess leads us to conclude that the typical disc life time is somewhat shorter than the diffusion time scales in DBZ – or that the disc lifetimes vary by substantial amounts (which is in fact consistent with the large uncertainty in our logarithmic estimate of the life time). It appears unlikely that a large fraction of the highly polluted DBZ white dwarfs without infrared excess are currently accreting from a gaseous disc, as the life times of these gaseous discs are short [Jura, 2008].

Figure 6.8 also reveals a fairly well defined upper limit in dM/dt for DAZ white dwarfs. Based on our updated calculation of the accretion rates, there are no DAZ white dwarfs observed with *Spitzer* with accretion rates above $2 \times 10^9 \mathrm{\,g s^{-1}}$. The

---

[4]Again excluding the two DAZ and one DBZ that were identified because of their gaseous discs [Gänsicke et al., 2008]

most extremely metal-polluted DAZ white dwarf star currently known, GALEX-1931+0117[5] [Vennes et al., 2010], still only accretes at a rate of $1.5 \times 10^9 \, \mathrm{g \, s^{-1}}$ [Gänsicke et al., 2012]. In contrast, there are several DBZ white dwarfs with metal accretion rates one to two orders of magnitude larger than observed in any DAZ, and substantially exceeding the rates that can be explained by Poynting-Robertson drag [Rafikov, 2011a,b]. For instance, HE 0446–2531, HE 0449–2554, and HE 1350–162 all have accreted several $10^{23} \, \mathrm{g}$ to nearly $10^{25} \, \mathrm{g}$ within the last diffusion time scale, i.e. $\simeq 10^6 \, \mathrm{yr}$ (or correspondingly larger amounts of material if the accretion ended several diffusion time scales ago). This is comparable to the extremely metal-polluted DZ white dwarf, SDSS J0956+5912, which has at least $1.5 \times 10^{23} \, \mathrm{g}$ of metals in its atmosphere[Koester et al., 2011]. Assuming the planetary bodies and physical mechanisms do not depend on the type of white dwarf, this substantial difference in the maximum accretion rates found for DAZ and DBZ white dwarfs forces us to conclude that either the calculated metal accretion rates for DBZ white dwarfs suffer from systematic errors, or the extremely high metal accretion rates found among DBZ white dwarfs simply have not been seen yet in DAZ white dwarfs.

One may speculate that both DAZ and DBZ white dwarfs can undergo a short-lived phase of very high rate accretion. Whereas the long diffusion time scales of DBZ provide an efficient "memory" to such events, the opposite is true for the DAZ, where the large amount of metals would be cleared out of the atmosphere within days to at most years – reducing the probability of witnessing such an event. A number of possible scenarios that would lead to such phases are conceivable. Secondary impacts of asteroids on an existing massive dust disc could generate sufficient amounts of gas to lead to runaway accretion [Jura, 2008]. Alternatively, a collisional cascade in the initially highly eccentric disc may generate sufficient amounts of gas to cause runaway accretion, effectively preventing the formation of a longer lived disc. In either scenario, the perturbed debris discs are expected to evolve on relatively short timescales, and Gänsicke et al. [2008] have shown that the structure of the gaseous disc in SDSS J084539.17+225728.0 changes on timescales of a few years. An initial spike in the accretion rate could also be related to the direct accretion of a substantial fraction of the disrupted asteroid, with the possible subsequent formation of a debris disc feeding the white dwarf at a lower rate. Another alternative comes from the fact that asteroid accretion events are, by definition, produced from eccentric orbits. One can therefore envisage that a fraction of discare therefore born in an unstable configuration. The disc would, similarly to the above scenario, have many disc–disc interactions, producing a significant amount of gas. Therefore the

---

[5]Not included in our Figure because it has not been observed with *Spitzer*

disc could accreted at a very high rate, leaving a heavily-polluted white dwarf without a dust disc. A larger sample of dust discs with substantially improved data are needed to test such scenarios.

Chapter 7

Hot subdwarf stars with F to K-type companions

7.1 Introduction

The Roche-lobe overflow subdwarf evolution channel is predicted to produce a large number of subdwarfs with F to K-type companions, such as that seen in the population synthesis models of Han et al. [2003] (see Section 1.3.2 for a more detailed discussion). Here we make use of large-area ultraviolet, optical and infrared photometric surveys to search for this largely unseen population. To aid our search for subdwarfs with companions, we combined the grids of synthetic sdB and main–sequence star spectra described in Section 3.4.2 and 3.4.3, respectively. We produced synthetic colours of the composite systems (using the method described in Section 3.4.4) and designed a method to select composite systems. The large wavelength range sampled by cross-matching ultraviolet, optical and near-infrared surveys allows us to separate composite subdwarf plus companion systems from single subdwarfs and single main–sequence stars in colour-colour space. The combination of a very blue and a red colour allows for a significant contribution from both the subdwarf and companion components to be seen in a colour-colour diagram.

7.2 Cross-matching

7.2.1 Sample I: GALEX, CMC and 2MASS

We cross-matched the CMC14 catalogue (Section 2.2.1) with 2MASS (Section 2.3.1) using a $2''$ matching radius (see Chapter 3.1). Because the surveys used here avoid the Galactic plane, the contamination from matching to other stars within $2''$ will

be relatively small (as discussed in Chapter 4). With these combined catalogues, we were able to calculate an $(r_{\mathrm{CMC}} - J)$ colour as a diagnostic for spectral type, as well as $(J - K)$, indicative of strong companion star contributions in composite systems (see Figure 7.1).

Based upon the $(r_{\mathrm{CMC}} - J)$ colour of the models described in Section 3.4.2 and 3.4.3, the CMC sample was cut to include only stars bluer than a G0V star (5750 K on the Castelli & Kurucz 2003 grid), i.e. $(r_{\mathrm{CMC}} - J) < 0.9$. The cut includes all possible combinations of subdwarf plus companion, but removes a significant fraction of contaminants. This does not limit our selection of subdwarfs with companions as discussed in Section 7.3. The sample was also limited to $r_{\mathrm{CMC}} < 16.0$, primarily to match the magnitude limit of 2MASS ($K_s \simeq 14.3$). This resulted in ~ 1.9 million objects.

All objects within the $(r_{\mathrm{CMC}} - J)$ colour cut were cross-matched with the GALEX AIS DR6 (Section 2.1.1), providing magnitudes in the $\mathrm{m_{FUV}}$ and $\mathrm{m_{NUV}}$ bandpasses, centered around 1500 and 2300Å, respectively. The matching was performed using the predefined cross-matching tables in GALEX CasJobs [Budavári et al., 2009] searching for all sources within $2''$. The resulting catalogue of neighbours contains approximately $560,000$ matched objects and hereafter will be referred to as the "*C2M*" sample. The mean of any multiple GALEX observations was taken where available and both bands were corrected for non-linearity according to Morrissey et al. [2007].

Finally, the objects from the match between CMC, 2MASS and GALEX were further cross-matched with the SDSS DR7 (Section 2.2.2). This sample will hereafter be referred to as the "*C2MS*" sample which is smaller and photometrically deeper. The SDSS CasJobs predefined cross-matching tables [Li & Thakar, 2008] were utilised. Objects were limited to have good quality photometric magnitudes (see Table 7.1). This resulted in a sample of $\sim 105,000$ objects for which good SDSS u, g, r, i and z magnitudes were available along with GALEX, CMC and 2MASS photometry. For ~ 1.5 per cent of objects within this sample, SDSS optical spectra are available.

7.2.2 Sample II: GALEX, SDSS and UKIDSS

The GALEX, CMC and 2MASS cross-matched sample discussed above benefits from covering a large area (limited by the GALEX footprint), but is relatively shallow with a limiting magnitude of $r = 16.0$ and $K_s = 14.3$. This restricts our ability to construct volume-limited samples.

A second, complimentary sample was selected from GALEX, SDSS and the

Table 7.1: Colour selection for finding subdwarfs with companions, for both the *C2M* and *C2MS* (with or without SDSS magnitudes) and *SU* samples. Constraints with a "Sample" flag were only applied to that sample, whereas constraints with no flag were applied to both samples. "bad_flags" is defined as saturated, bright, edge or nodeblend and "nChild" is the number of children objects detected by SDSS.

Colour	Constraint		Sample
r_{CMC}	$\leq$	16.0	*C2M*
$(r_{\text{CMC}} - J)$	$<$	0.9	
r_{CMC} Uncertainty	$\leq$	0.10	
$E(B - V)$	$\leq$	0.15	
$(m_{\text{FUV}} - r_{\text{CMC}})$	$\leq$	$3.8 * (r_{\text{CMC}} - K_s) - 0.3$	
$(m_{\text{FUV}} - r_{\text{CMC}})$	$\leq$	$-2.7 * (r_{\text{CMC}} - K_s) + 4.7$	
$(m_{\text{FUV}} - r_{\text{CMC}})$	$\geq$	-3.0	
FUV artifact flag	$\leq$	1	
m_{FUV} Uncertainty	$\leq$	0.05	*C2M*
	$\leq$	0.10	*SU*
	AND		
$(m_{\text{NUV}} - r_{\text{CMC}})$	$\leq$	$1.3 * (r_{\text{CMC}} - K_s) + 0.54$	
$(m_{\text{NUV}} - r_{\text{CMC}})$	$\leq$	$-1.45 * (r_{\text{CMC}} - K_s) + 3.3$	
$(m_{\text{NUV}} - r_{\text{CMC}})$	$\leq$	$3.5 * (r_{\text{CMC}} - K_s) + 0.12$	
$(m_{\text{NUV}} - r_{\text{CMC}})$	$\geq$	-2.0	
NUV artifact flag	$\leq$	1	
$(r_{\text{CMC}} - K_s)$	$\leq$	1.75	*C2M*
m_{NUV} Uncertainty	$\leq$	0.05	*C2M*
$(r_{\text{SDSS}} - K)$	$\leq$	1.5	*SU*
m_{NUV} Uncertainty	$\leq$	0.10	*SU*
SDSS specific:			
flags & bad_flags	$=$	0	
nChild	$=$	0	

UKIDSS LAS DR9 (Section 2.3.2). UKIDSS adds a significant increase in depth over 2MASS. SDSS and UKIDSS were cross-matched to find the closest match within $2''$ using the UKIDSS-SDSS pre-match tables. This sample was then matched to GALEX within $2''$, using the CasJobs neighbours search, returning approximately $120,000$ objects. Again, multiple GALEX neighbours were combined into a single measurement and fluxes were corrected for non-linearity [Morrissey et al., 2007]. This sample will hereafter be referred to as the "SU" sample. It is limited in area by the current size of UKIDSS, but extends several magnitudes deeper than 2MASS in K. Because the UKIDSS LAS area is entirely encompassed by the SDSS footprint, we can make use of the higher precision, deeper SDSS photometry, rather than CMC. The number of objects at each stage of the analysis is given in Table 7.2.

7.3 Selecting ultraviolet excess objects

7.3.1 Colour-colour diagrams

Figure 7.1 shows colour-colour diagrams for the objects with detections in GALEX, CMC and 2MASS. We compare $(m_{FUV} - r_{CMC})$ vs $(r_{CMC} - Ks)$ and $(m_{NUV} - r_{CMC})$ vs $(r_{CMC} - Ks)$, where the $(J - K_s)$ colour of each object is colour-encoded in the plot. For single stars, the $(J - K_s)$ range corresponds to spectral types O5 to K0. The colour indices are tailored to highlight in colour-colour space the position of composite blue plus red objects. The $(r_{CMC} - K_s)$ colour of an object is a relatively good indication of stellar spectral type and $(m_{FUV} - r_{CMC})$ will indicate objects with an excess in the ultraviolet in contrast to single main–sequence stars. The truncation at $(r_{CMC} - K_s) \sim 1.5$ is caused by our imposed cut of $(r_{CMC} - J) < 0.9$.

In Figure 7.2, the same sources are plotted but now encoding the density of sources on a grey scale to better represent relative numbers. The main sequence is found along the bottom edge of the main group of objects in the $(m_{FUV} - r_{CMC})$ vs $(r_{CMC} - Ks)$ plane, and more centrally through the main group in the $(m_{NUV} - r_{CMC})$ vs $(r_{CMC} - Ks)$ plane (Figure 7.1). Simulated colours derived from our main–sequence star model (Section 7.1) confirm that this is the expected position of the main sequence in our chosen colours. Similarly, composite sdB plus companion star models are also shown in Figure 7.2, highlighting the region of colour-colour space where we expect to find such systems.

The large scatter in $(m_{FUV} - r_{CMC})$ or $(m_{NUV} - r_{CMC})$ for a given $(r_{CMC} - K_s)$, especially at the red end, can be explained due to a few factors. First of all, even though we formally require the r_{CMC} uncertainty to be less than 0.1, there appears to be additional systematic scatter in the r_{CMC} magnitudes. Investigating the vertically

extended regions in our colour-colour diagrams (Figure 7.1) when using the much more reliable r_{SDSS} instead of r_{CMC}, we find that the spread is significantly reduced. However, the larger sky coverage of the CMC is far more important for our study especially as the subdwarf plus companion systems fall in a relatively clean part of the diagram. Another reason for the observed spread is the fact that the GALEX magnitudes have been shown to suffer from non-linearities for bright stars, amongst other problems [e.g. Morrissey et al., 2007; Wade et al., 2009]. Although we corrected for non-linearity using the method described in Morrissey et al. [2007], the equations are empirical and there may be a significant scatter in individual measurements.
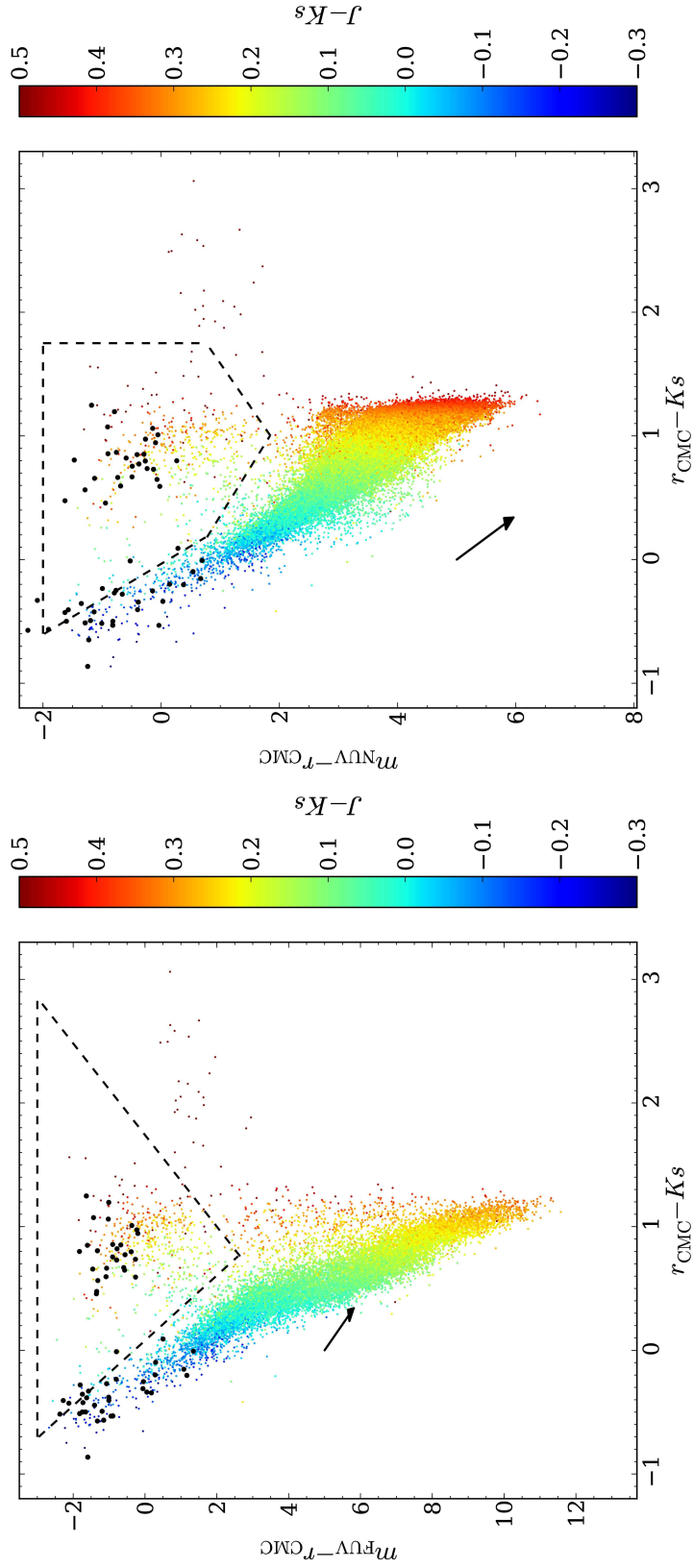
Figure 7.1: Colour–colour diagrams of ($m_{FUV} - r_{CMC}$) vs ($r_{CMC} - Ks$) (left; $\sim$ 15,000 objects) and ($m_{NUV} - r_{CMC}$) vs ($r_{CMC} - Ks$) (right; $\sim$ 105,000 objects) for objects with matches in GALEX, CMC and 2MASS catalogues (the $C2M$ sample) and satisfying the magnitude cuts in Table 7.1. The majority of objects are main-sequence stars and therefore do not have m_{FUV} magnitudes. This causes the factor of 10 difference in numbers of objects in the two diagrams. E(B − V), taken from the GALEX catalogue Schlegel et al. [1998] map value, is also limited to < 0.15 and for clarity, $m_{NUV} \leq 16.5$. The plotted colour for each point corresponds to the ($J - K_s$) value, where colours above 0.5 and below -0.3 are shown as 0.5 and -0.3, respectively. For single stars, this range corresponds to spectral types O5 to K0. The sdB/sdO star candidates from Kilkenny et al. [1988] with matches in the $C2M$ catalogue are shown as black circles (totalling 84 objects). A reddening vector corresponding to E(B − V) = 0.15 is shown as a black arrow centered on (0,5) in both diagrams. The dashed black lines show the colour-colour selections as discussed in Section 7.3.2 and Table 7.1.

132
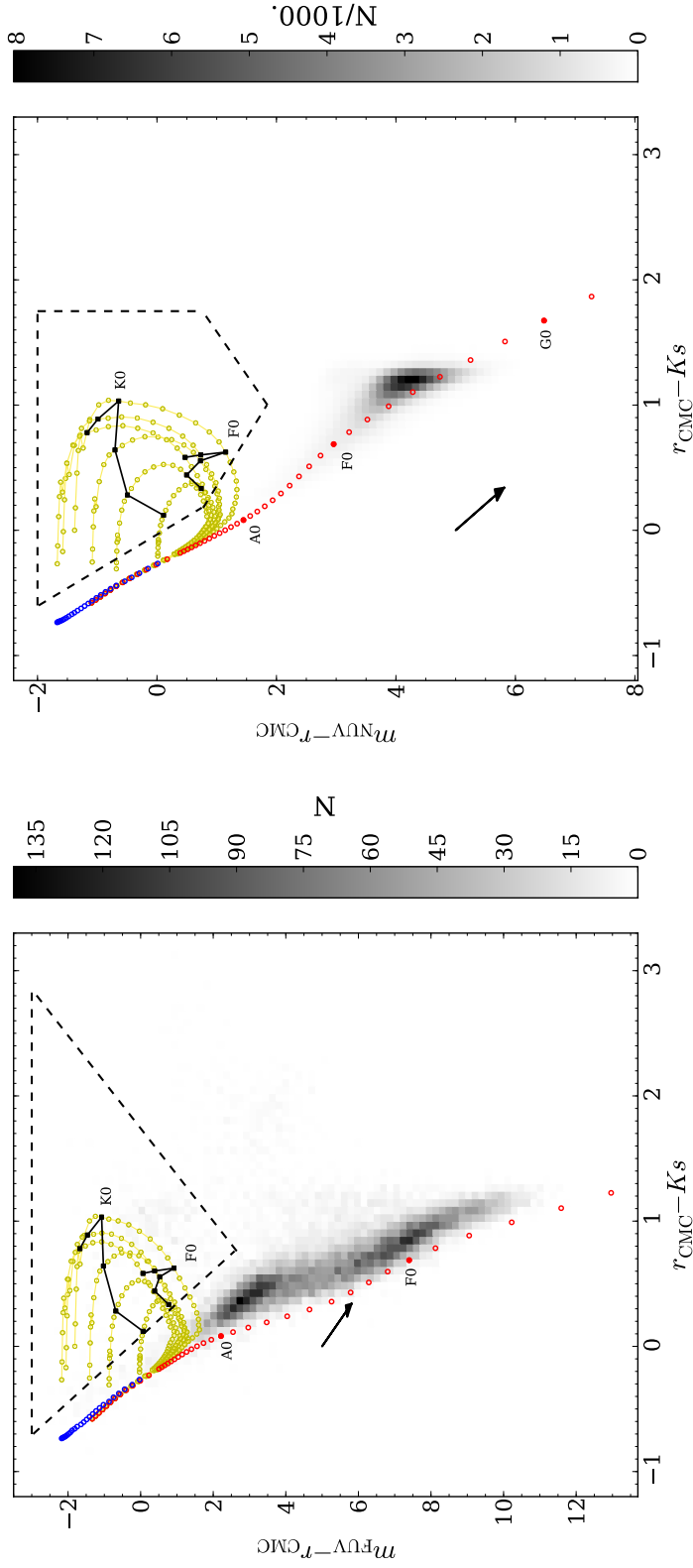
Figure 7.2: 2D density plots of the ($m_{\text{FUV}} - r_{\text{CMC}}$) vs ($r_{\text{CMC}} - Ks$) and ($m_{\text{NUV}} - r_{\text{CMC}}$) vs ($r_{\text{CMC}} - Ks$) colour-colour diagrams in Figure 7.1, however, m_{NUV} is no longer limited to 16.5. The grey scale is shown on the respective colour bars, labelled by the number of objects (N) on the left and N/1000 on the right. The reddening vector corresponds again to $E(B - V) = 0.15$ and is shown as a black arrow centered on $(0, 5)$. The dashed black lines show the colour-colour selections as discussed in Table 7.1. Additionally, subdwarf ($15,000\,\text{K} \leq T_{\text{eff}} \leq 40,000\,\text{K}$) and main-sequence star model colours (Section 7.1) are plotted as blue and red open circles, respectively. The yellow lines show a single subdwarf ($15,000\,\text{K} \leq T_{\text{eff}} \leq 40,000\,\text{K}$ in steps of $5,000\,\text{K}$) paired with the sequence of main-sequence stars described in Section 7.1. As a reference, subdwarfs (of the above temperatures) with approximately a K0 or F0-type companion are joined with a black line.

In addition, despite limiting $E(B - V) \leq 0.15$, much of the spread around the main sequence can be accounted for by considering the effects of interstellar reddening. The $E(B - V)$ magnitude for each object is taken from the GALEX catalogue, which is itself calculated from the Galactic reddening maps of Schlegel et al. [1998]. The interstellar reddening is illustrated by the reddening vectors in Figure 7.1. These are calculated by folding the mean extinction curve of Fitzpatrick & Massa [2007] through the relevant filter transmission curves. In the $(m_{FUV} - r_{CMC})$ vs $(r_{CMC} - Ks)$ plane, reddening of blue objects moves them above the main sequence in $(m_{FUV} - r_{CMC})$, a region populated by a number of objects. However, reddening in the $(m_{NUV} - r_{CMC})$ vs $(r_{CMC} - Ks)$ plane approximately moves objects along the main sequence. The components of the reddening vectors are approximately the same in both $(m_{FUV} - r_{CMC})$ and $(m_{NUV} - r_{CMC})$ because the 2200Å bump in the reddening function [Papoular & Papoular, 2009] coincides with the central wavelength of m_{NUV}. However, the intrinsic and significant variations in the reddening law along different lines of sight affect the ultraviolet magnitudes more so than the optical values. Fitzpatrick & Massa [2007] show that even when considering the standard stars that are used to calculate the adopted reddening function, a significant spread around the mean extinction curve is observed. This leads to large departures from the mean law, affecting the ultraviolet region in particular. These variations in the extinction curve, along with the variation of the true reddening to the subdwarf compared with that calculated in the Schlegel et al. [1998] maps, are thus likely responsible for the stellar sources populating a vertically extended region in the $(m_{NUV} - r_{CMC})$ vs $(r_{CMC} - Ks)$ plane. In any case, the outliers form only a small fraction of the total source population and the reddening vector does not move main–sequence stars into the colour selections we discuss below.

7.3.2 Isolating subdwarfs in binaries

In order to classify our sources and check for known objects within our sample, we resolved all positions using SIMBAD[1], and also consulted any available SDSS optical spectra. In the upper-left corner of the $(m_{FUV} - r_{CMC})$ vs $(r_{CMC} - Ks)$ colour-colour diagram, one would expect to find white dwarfs and single-star subdwarfs, which is corroborated by classifications in the SIMBAD database. Unfortunately, none of our sources with colours consistent with single subdwarfs have SDSS spectra that could conclusively confirm their classification (due to them saturating in SDSS). The objects towards the right of the diagram, with $(r_{CMC} - K) \sim 2.0$, prove to be galaxies. These are removed by use of the point source flag in SDSS.

---

[1]http://simbad.u-strasbg.fr/simbad/

Kilkenny et al. [1988] created a catalogue of subdwarf stars and candidates from previous studies, including work on the PG survey. This includes subdwarfs both with and without companions. We matched this catalogue to the *C2M* catalogue, resulting in 284 objects. The subset for which appropriate quality limits ($m_{NUV} \leq 16.5$ and the magnitude uncertainty limits defined in Table 7.1) are satisfied are plotted in Figure 7.1 (83 sources). We see that this sample splits into two distinct groups. A significant fraction falls in the region where single subdwarfs and white dwarfs are expected to lie. However, a good number of these (~ 35 per cent) lie at a much redder ($r_{CMC} - K_s$) colour, where, from the synthetic magnitudes calculated in Section 7.1, we expect subdwarfs with main–sequence star companions. The objects in this redder region (inside the black dashed lines in Figures 7.1 and 7.2), would appear to be main–sequence F or G-type stars from their ($r_{CMC} - K_s$) colour, but have an ultraviolet excess in ($m_{FUV} - r_{CMC}$) and/or ($m_{NUV} - r_{CMC}$) colour. This confirms that a significant fraction of the Kilkenny et al. [1988] sample show photometric evidence for being composite, but also that we have detected a large number of new sources within that same region of colour space.

For the new *C2MS* objects in the colour selection, where SDSS spectra are available (25 objects), they can be seen to be mostly subdwarfs with evidence of companions, along with one (single) white dwarf and two cataclysmic variable stars (CV: see Table 7.3 and Figure 7.3). SIMBAD, however, only returns four known subdwarfs in this region of colour-colour space. This may be expected as previous work has intentionally focused on single-lined sdB systems that are therefore dominated by the subdwarf. The number of objects grouped under a few broad classifications are summarised in Table 7.3. Note that close to 90 per cent of the *C2M* sources (without SDSS) within the colour selection are unknown.

Table 7.2: Summary of numbers at each stage of the sample selection. The left hand columns shows which surveys were included at that stage in the processing. The "In cuts" columns are those objects satisfying the criteria from Figure 7.1 and Table 7.1 and the "Σ" column displays the total number of objects in this catagory.

| Sample Name | Surveys | | | | Total (approx) | In cuts | | |
	Ultraviolet	Optical	Infrared			Σ	SDSS Spectra	SIMBAD
		CMC	2MASS		1,900,000	-	-	-
C2M	GALEX	CMC	2MASS		560,000	449	-	58
C2MS	GALEX	SDSS	CMC	2MASS	105,000	93	25	24
		SDSS	UKIDSS		220,000	-	-	-
SU	GALEX	SDSS	UKIDSS		120,000	134	72	47

Table 7.3: Table of classifications for the 449, 93 and 134 objects in the *C2MS*, *C2MS* and *SU* samples, respectively, and inside the colour-colour selection boxes from Figure 7.1 and Table 7.1. The SDSS spectra column is from visual inspection of the optical spectra.

Classification	*C2M* SIMBAD	*C2MS* SIMBAD	*C2MS* SDSS spectra	*SU* SIMBAD	*SU* SDSS spectra
Subdwarf	7	4	22	7	62
Composite	9	1	0	4	0
CV/Nova	21	8	2	10	4
Galaxy	2	0	0	0	2
Quasar	0	0	0	0	0
WD	19	11	1	26	4
Total with classification	58	24	25	47	72
Total without classification	391	69	68	88	63
Σ	449	93	93	134	134

In order to isolate composite subdwarfs while avoiding obvious contaminants, we devised cuts in colour-colour space (Table 7.1) guided by our simulated composite subdwarf colours and the SIMBAD and SDSS spectroscopic classifications discussed above. The right hand side of the cuts was chosen to avoid contamination from galaxies and quasars, and similarly on the lower side the main sequence was avoided. At the left hand edge, the cuts were chosen to avoid early-type stars and single subdwarfs. We require objects to be in both the $(m_{FUV} - r_{CMC})$ vs $(r_{CMC} - Ks)$ and $(m_{NUV} - r_{CMC})$ vs $(r_{CMC} - Ks)$ cuts because objects residing in just an individual box are likely to arise from spurious *GALEX* fluxes. Contamination of this region due to interstellar reddening is small because very few objects will be moved from the main sequence, along the reddening vector, into the box, as shown in Figure 7.1. Similarly, the scatter from a poor r_{CMC} magnitude does not lead to a large contamination, because the subdwarfs with companion region is sufficiently far from the main sequence.

We repeated a similar selection using the *SU* sample, again using (not shown) $(m_{FUV} - r_{SDSS})$ vs $(r_{SDSS} - K)$ and $(m_{NUV} - r_{SDSS})$ vs $(r_{SDSS} - K)$ colour-colour diagrams. All magnitudes were limited to have uncertainties less than 0.1 mag and $E(B - V) \leq 0.15$. An increase in the number of quasars was seen, which encroached on the cuts used for $(m_{NUV} - r_{CMC})$ vs $(r_{CMC} - Ks)$. The upper limit on $(r_{SDSS} - K)$ was therefore reduced to 1.5, as shown in Table 7.1, however the contamination was not completely removed. The cuts on $(m_{FUV} - r_{SDSS})$ vs $(r_{SDSS} - K)$ remained unchanged, where we ignore the small differences between UKIDSS K magnitude versus 2MASS K_s magnitudes[2]. After these adjustments, 134 objects reside within the cuts, 72 of which have SDSS spectra. This is significantly more than the *C2MS* sample because many of the *C2MS* objects are saturated in SDSS. As for the 2MASS sample, we provide broad classifications for the *SU* sample in Table 7.3. We also show the positions of the objects with SDSS spectra on a $(m_{FUV} - r_{CMC})$ vs $(r_{CMC} - Ks)$ colour-colour diagram in Figure 7.3. Comtaminants do not cluster in a particular region of colour-colour space.

With our selection cuts in place, we can use the tracks of our synthetic subdwarf-companion pairs to consider the completeness of our composite subdwarf sample. We find that our region covers only a limited range in companion type for a given subdwarf temperature, as systems that are either dominated by the companion or the subdwarf fall outside our region. This choice is required to reduce contamination from single stars. Based on our simulated colours, we find

---

[2]Assuming a $J - K_s$ colour of ~ 0.3 and using the transformations of Carpenter [2001], the difference between the K_s and K magnitude is ~ 0.003 and therefore negligible.
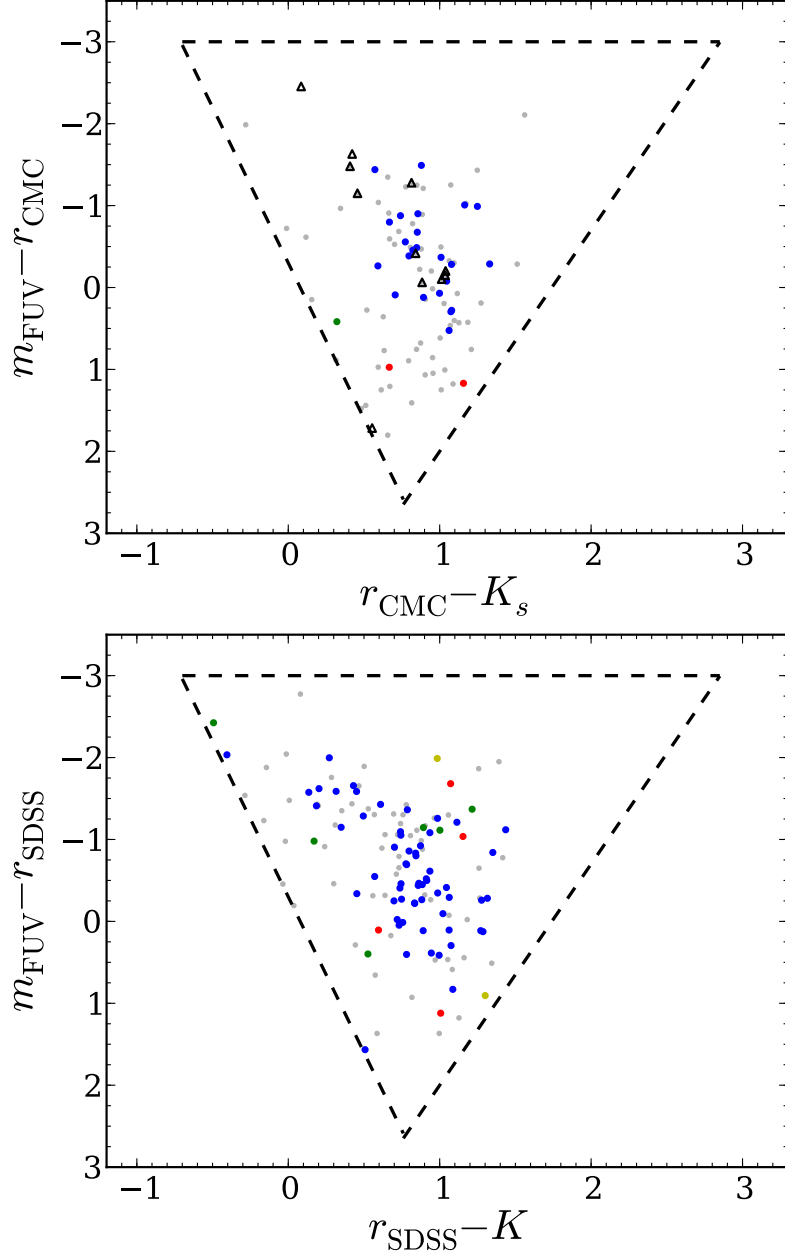
Figure 7.3: $(m_{FUV} - r_{CMC})$ vs $(r_{CMC} - Ks)$ and $(m_{FUV} - r_{SDSS})$ vs $(r_{SDSS} - K)$ colour-colour diagrams showing the locations of objects within the colour cuts described in Table 7.1, and having SDSS spectra, for the *C2MS* (left) and *SU* samples (right), respectively. Objects classified as subdwarfs, white dwarfs, CVs and Galaxies are shown in blue, green, red and yellow, respectively. Those with no classification are shown in gray. A total of 93 and 134 objects are shown in the *C2MS* and *SU* panels, respectively (see Table 7.3). The eleven objects which were targetted for follow-up spectroscopy in Section 7.4 are shown as black, open triangles in the left-hand figure.

that subdwarfs with temperatures up to $30,000\,\mathrm{K}$ would fall in the ($\mathrm{m_{FUV}} - r_{\mathrm{CMC}}$) vs ($r_{\mathrm{CMC}} - Ks$) colour cut for even the coolest main–sequence companion in our grid ($3,000\,\mathrm{K}$: $\sim$M5). $35,000\,\mathrm{K}$ and $40,000\,\mathrm{K}$ subdwarfs, however, would require $\gtrsim 3,750\,\mathrm{K}$ ($\lesssim$M0) and $\gtrsim 5,000\,\mathrm{K}$ ($\lesssim$K0) companions, respectively, to make them stand out from the main sequence populations. In the case of early-type companions, subdwarfs plus O-type and B-type stars are also lost as they merge back into the blue end of the main sequence. A $15,000\,\mathrm{K}$, $20,000\,\mathrm{K}$, $30,000\,\mathrm{K}$ or $40,000\,\mathrm{K}$ subdwarf would be identified if it had an $\lesssim 7,500\,\mathrm{K}$ ($\gtrsim$F0), $\lesssim 8,250\,\mathrm{K}$ ($\gtrsim$A5), $\lesssim 8,000\,\mathrm{K}$ ($\gtrsim$A5) or $\lesssim 8,500\,\mathrm{K}$ ($\gtrsim$A5) companion, respectively.

For the colour-colour tracks, the companions are restricted to be main–sequence stars. However, we may also expect to find a population of subdwarfs with sub-giant or giant companions similar to HD 185510 [Fekel & Simon, 1985], HD 128220 [Howarth & Heber, 1990] and BD-7°5977 [Viton et al., 1991; Heber et al., 2002]. In fact, the binary population synthesis of Han et al. [2003] predicted that the majority of K-type companions to subdwarfs should be evolved companions. We calculated the ($\mathrm{m_{FUV}} - r_{\mathrm{CMC}}$) vs ($r_{\mathrm{CMC}} - Ks$) location of G7 to K3-type giant stars (Figure 7.4: upper-right panel) by taking the solar metalicity, zero age horizontal branch stars from the Castelli & Kurucz [2003] model atmosphere library and again rescaling the fluxes to a corresponding zero age horizontal branch luminosity from the isochrones of Girardi et al. [2000]. All combinations of subdwarf plus giant star systems fall outside of the colour cuts described in Table 7.1. Systems with either overluminous subdwarfs, or companions in an intermediate state between the main-sequence and the horizontal branch may, however, fall within the colour cuts. We do not expect these to be a significant population in our sample. Since we do not expect specific formation mechanisms to become more or less prevalent as a function of distance, we can still use our sample to study the spatial distribution of subdwarfs (see Section 7.6.9.3 and 7.6.11) even if the sub-sample of subdwarfs with evolved companions is selected against.

We may also expect that some detached white dwarf plus main–sequence type companion systems are found to be contaminants of the sample, since these are composite systems with a hot component and a cooler companion. However, we simulated the colours of such systems and, with the exception of very low gravity white dwarfs, they do not fall in the colour-colour region selected in Table 7.1 (see Figure 7.4: lower two panels). In this colour space, the small radius of the white dwarf means that the flux is dominated by all but the latest of main sequence companions and so they lie closer to the main sequence in both diagrams. They are thus unlikely to constitute a significant contaminant.

140
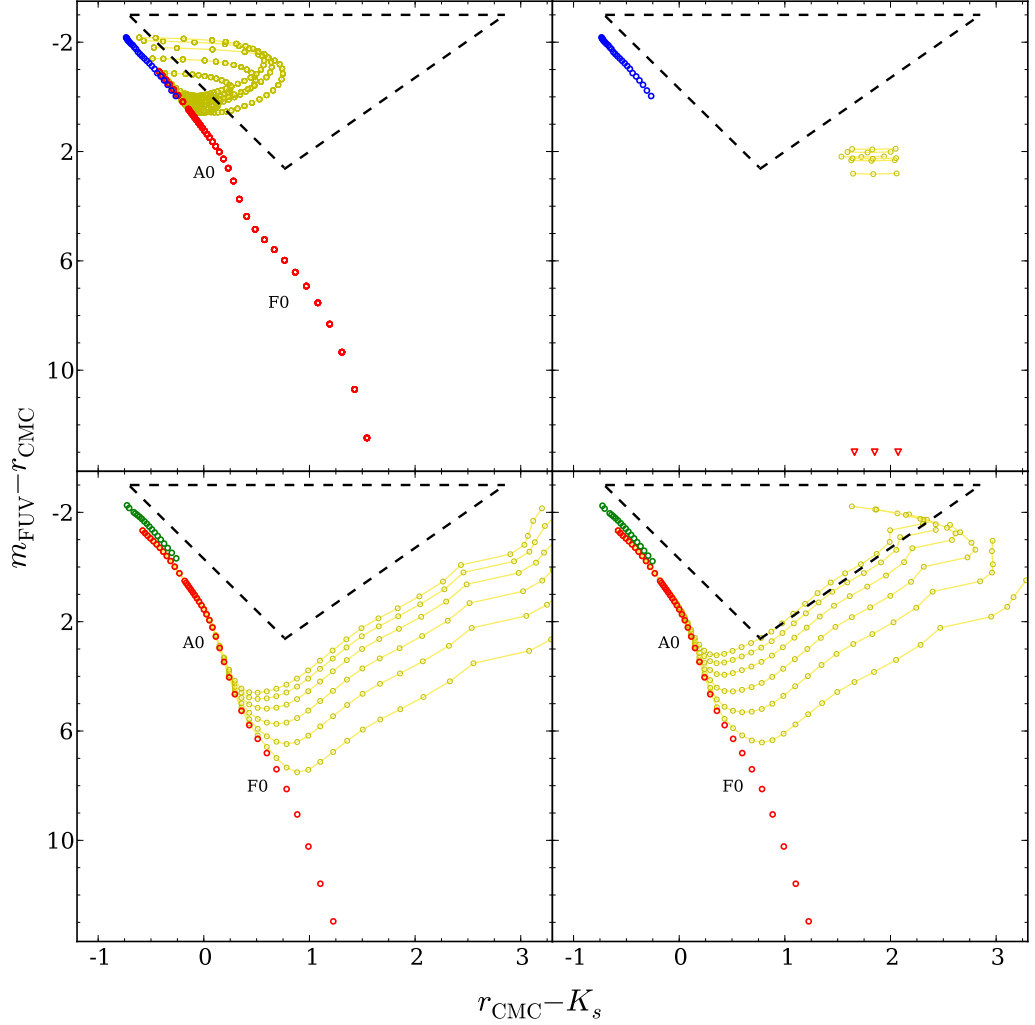
Figure 7.4: Potential contaminants of the subdwarf plus main–sequence star sample, following the same format as Figure 7.2. See Section 7.3.2 for a discussion. Top-left: Subdwarfs (blue open circles: described in Section 7.1) with metal-poor $(\log([M/H]/[M/H]_{solar}) = -1.5$: red open circles) main–sequence star companions. Composite objects are shown in yellow. Top-right: Subdwarfs with giant star companions (ranging in spectral type from approximately G7 to K3). Single G and K-type giants do not fall in the range of the Figure, and therefore we mark their $(r_{CMC} - K_s)$ position by downward pointing red triangles. Bottom-left: $\log(g) = 8$ DA white dwarfs (green open circles) with main–sequence companion stars (described in Section 7.1). The yellow lines track a white dwarf of a single temperature whilst varying the companion type. Bottom-right: $\log(g) = 7$, and therefore larger radii, DA white dwarfs with main–sequence companion stars. The DA white dwarf model grid was kindly provided by D. Koester [for a description, see Koester, 2010], and ranges from $15,000\,\mathrm{K} \leq \mathrm{T_{eff}} \leq 40,000\,\mathrm{K}$ in steps of $5,000\,\mathrm{K}$.

Looking out of the Galactic plane to distances of over $1\,\mathrm{kpc}$, we may expect to see a sizeable fraction of thick disk and halo stars. Therefore, the companions to the subdwarfs in our samples may be metal-poor. In Figure 7.4 (upper-left panel), we show that subdwarfs with metal-poor $(\log([\mathrm{M/H}]/[\mathrm{M/H}]_{\mathrm{solar}}) = -1.5$: ATLAS9: Castelli & Kurucz 2003) companions indeed still fall in our colour selection. We discuss the associated possible biases on our fitting technique in Section 7.5.

A summary of our sample sizes at various stages of the analysis can be found in Table 7.2. The full list of 449 objects inside our *C2M* sample can be found in Table B.1.

7.4   Spectroscopic observations

We discuss here some spectroscopic follow-up obtained to verify that the *C2M* sample objects likely contain a subdwarf component before turning to the modelling of their spectral energy distributions (SED) in Section 7.5. All the spectroscopic observations were conducted and reduced by Dr E. Breedt, Dr D. Steeghs and P. Longa-Peña.

7.4.1   WHT

Nine objects falling within the colour-colour cuts described in Table 7.1 were observed in July and December 2010, using the 4.2m William Herschel Telescope (WHT) at the Roque de los Muchachos Observatory, La Palma, Spain. We used the ISIS (Intermediate dispersion Spectrograph and Imaging System) dual-beam spectrograph mounted at the Cassegrain focus of the telescope, with a R600 grating on both the blue and the red arms, and a $1''$ slit. The blue arm of the spectrograph is equipped with a 2048×4096 pixel EEV12 CCD, which we binned by factors of 3 (spatial direction) and 2 (spectral direction). The 2048×4096 pixel REDPLUS CCD on the red arm was binned similarly. This setup delivers a wavelength coverage of $3772 - 5136\text{Å}$ on the blue arm, with an average dispersion of 0.88Å per binned pixel, and $5983 - 7417\text{Å}$ on the red arm, with an average dispersion of 0.98Å per binned pixel. We determined the resolution to be 1.2Å, from measurements of the full width at half maximum of night-sky lines. The setup during the December observations was identical, except that the CCDs were binned 2×2.

The spectra were debiased and flatfielded using the STARLINK[3] packages KAPPA and FIGARO and then optimally extracted using the PAMELA code [Marsh,

---

[3]Maintained and developed by the Joint Astronomy Centre and available from http://starlink.jach.hawaii.edu/starlink

Table 7.4: Follow-up spectroscopic observations and classifications.

Name	R.A.	Dec	r_{CMC} [mag]	Classification	Telescope
0018+0101	$00^h18^m43.51^s$	$+01°01'23''.6$	15.1	sdB	WHT
0051−0955	$00^h51^m20.33^s$	$−09°55'23''.2$	14.4	A-type star	WHT
1602+0725	$16^h02^m09.07^s$	$+07°25'10''.9$	14.7	sdB	WHT
1618+2141	$16^h18^m06.46^s$	$+21°41'25''.4$	14.9	sdB	WHT
1619+1453	$16^h19^m49.30^s$	$+14°53'09''.9$	14.7	sdB	WHT
2020+0704	$20^h20^m27.21^s$	$+07°04'13''.5$	14.3	sdB	WHT
2047−0542	$20^h47^m42.37^s$	$−05°42'31''.0$	14.9	sdB	WHT
2052−0457	$20^h52^m26.23^s$	$−04°57'45''.3$	14.5	sdB	WHT
2138+0442	$21^h38^m00.82^s$	$+04°42'11''.6$	14.8	sdB	WHT
2331−2515	$23^h31^m03.65^s$	$−25°15'47''.9$	14.5	sdB	MagE
2342−2750	$23^h42^m41.41^s$	$−27°50'01''.7$	15.1	sdB	MagE

1989]. We derive the wavelength calibration from Copper-Neon and Copper-Argon arc lamp exposures taken during the night, selecting the arc lamp exposure nearest in time to each science spectrum.

Finally, the raw spectra were converted to flux units and the telluric absorption lines removed. For the July run, the flux calibration was done using a model spectrum of a "flux standard" DA white dwarf, observed on the same night. The December run suffered from poor weather and no flux standard was observed. We calibrated these two spectra using an earlier observation of SP1446+259, taken with the same instrumental setup. The shape of the spectrum is therefore reliable, but the absolute flux level is not. Our analysis does not depend on the absolute flux of the targets, so our conclusions are unaffected.

We plot the resultant spectra in Figure 7.5 and find that all but one of the nine objects chosen from the colour-colour selection are sdB stars with companions (Table 7.4). We plot the $(m_{FUV} - r_{SDSS})$ vs $(r_{SDSS} - K)$ location of these nine stars in Figure 7.3.

7.4.2 MagE

In addition to the WHT spectra, two candidates were observed on 7-8 June 2010, using the MagE (Magellan Echellette) spectrograph mounted on the Magellan-Clay telescope at Las Campanas Observatory, Chile. We used the $1''$ slit with the 175 lines/mm grating to cover $\sim 3100 - 11200$ Å at a resolution of $R = 4100$. The data were unbinned and we used the slow readout mode.

The spectra were reduced with the Carnegie pipeline written by D. Kelson. This Python-driven pipeline performs typical calibrations: flat-fielding, sky back-
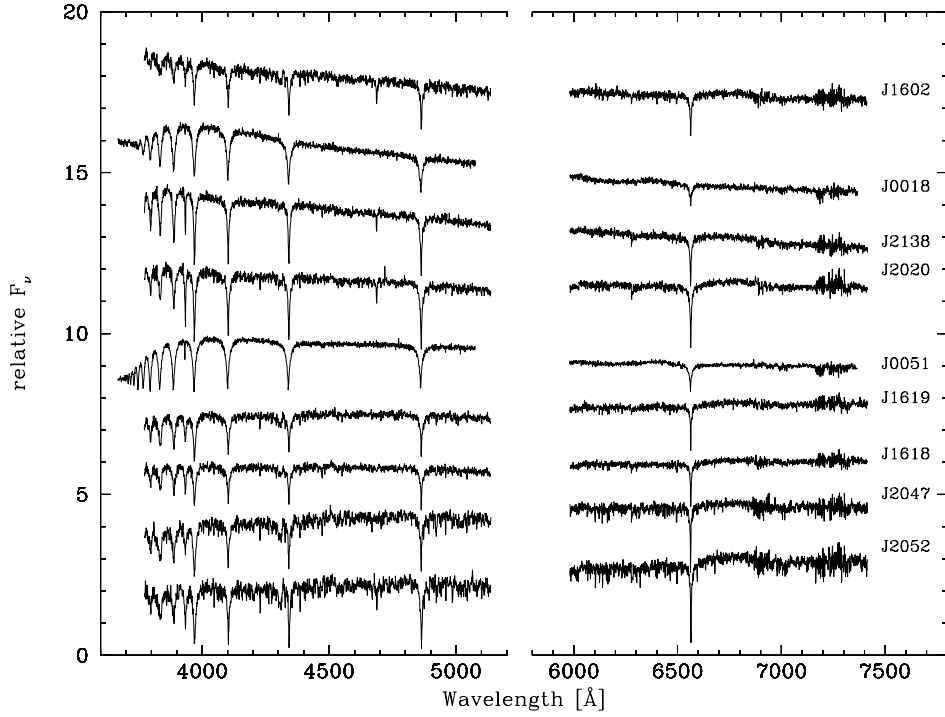
Figure 7.5: WHT optical spectra of nine candidate subdwarf plus companion stars chosen from the colour-colour selection seen in Figure 7.1. Eight of the nine targets are subdwarfs with hints of absorption lines from the companion star (see also Section 7.3). Spectra are ordered approximately by effective temperature of the subdwarf, and shifted in flux by appropriate amounts. $0051-0955$ is probably an A-type star rather than a subdwarf based upon the many orders Balmer absorption seen at $3700 - 3800\,\AA$ (and the expertise of Prof. U. Heber).

ground subtraction followed by optimal extraction and wavelength calibration. The wavelength calibrations were derived from Thorium-Argon lamp exposures taken during the night, which provided ample suitable lines over the entire wavelength range. The pipeline selects the closest lamp exposures in time to each science spectrum. Raw spectra were then flux calibrated using a spectrum of the flux standard Feige 110, observed at the end of each night. We find that both objects observed have spectra consistent with being sdB stars with some evidence for a companion. We plot the $(m_{\mathrm{FUV}} - r_{\mathrm{SDSS}})$ vs $(r_{\mathrm{SDSS}} - K)$ location of these two stars in Figure 7.3.

This initial exploration of eleven of our candidates thus offers strong evidence that we are primarily selecting composite subdwarf systems with our colour cuts, with a low contamination rate. We discuss contamination of our samples further in Sections 7.6.8 and 7.6.9.

7.5   Fitting composite systems

To quantify the likely composition of our subdwarf candidates, we pursued SED fitting exploiting the broad wavelength range of the photometric data that is available. The subdwarf star dominates the ultraviolet flux while the main–sequence companion clearly dominates in the infrared. This permits the decomposition of the SED into two components at a common distance. In this section we demonstrate that good constraints on both the subdwarf and companion star effective temperature can be derived from such fits. The observed magnitudes were fitted with the grid of subdwarf plus main–sequence star magnitudes discussed in Section 7.1, with the additional option of having a subdwarf with no companion (shown as MS $T_{\mathrm{eff}} = 0\,\mathrm{K}$ in Table 7.5 onwards). This was performed by minimising a weighted χ^2 whilst varying the distance, subdwarf and companion effective temperatures (described in Section 3.4.5.2). Uncertainties were taken from the one sigma contours in the χ^2 surface. This fitting was restricted to the sub-samples where SDSS photometry is available, since we require multi-band optical photometry in order to decompose the SED.

Reddening from interstellar dust can potentially significantly bias the subdwarf effective temperature (as described in Section 3.4.5.2). Without prior knowledge of the reddening to the system, this is not easily corrected for. To estimate an upper limit for this effect, we calculate the reddening at the position of the subdwarfs from the Schlegel et al. [1998] maps and use these values to first deredden the magnitudes. Refitting these values gives a second set of system parameters that will, in general, be overcorrected for reddening in comparison to the fits without any

reddening. The Schlegel et al. [1998] maps estimate the reddening value as would be seen for an extragalactic source. The reddening for a subdwarf star, subject to local variation, should always be less than this. Therefore, the true system parameters will lie somewhere in between the reddened and unreddened limits.

As shown in Figure 7.4, subdwarfs with metal-poor companions fall in the colour cuts defined in Table 7.1. They are not a contaminant, but fitting the metal-poor systems with solar metalicity models will lead to biased system parameters. Less absorption in the ultraviolet from metal lines means the companions will contribute a fairly significant amount of flux at short wavelengths. To test the effect of this, we fitted the *C2MS* and *SU* samples with a grid of subdwarfs plus metal-poor $(\log([M/H]/[M/H]_{solar}) = -1.5)$ companions from the Castelli & Kurucz [2003] AT-LAS9 model atmosphere library. This has the effect of reducing all subdwarf effective temperatures by a few thousand Kelvin and shifting the distribution of companion types later by a few hundred Kelvin. If anything, this accentuates the conclusions we draw in Section 7.7.

A final potential bias to our fitting method is that approximately 10 per cent of subdwarfs are evolved and therefore will have lower surface gravities and bloated radii compared with their unevolved equivalent [Heber, 2009]. Fitting a system with an evolved subdwarf using our subdwarf plus main–sequence star model grid (described in Section 7.1), we would find that the companion star is cooler and the subdwarf is hotter than the true temperature. However, this situation will most likely result in a high minimum χ^2 and therefore be flagged as a bad fit.

7.6   Fit results and individual objects

All the fit parameters for the 93 objects in our colour cut found in the *C2MS* sample (Table 7.2) are given in Table B.2. Similarly, the 134 *SU* objects are shown in Table B.3. We adopt a somewhat unusual notation for the upper and lower uncertainties, denoted by the "{" symbol, because the subdwarf and companion effective temperature uncertainties are strongly correlated. "{" indicates the upper and lower 1σ uncertainties added to the best fit value. The upper values all correspond to the same fit solution and similarly for the lower values. As an example, consider a hypothetical system where SD $T_{eff} = 15,000\{^{25,000}_{10,000}$ K, and MS $T_{eff} = 2,000\{^{1,000}_{3,000}$ K. This corresponds to three solutions: the best fit (a $15,000$ K subdwarf with a $2,000$ K companion), a 1σ uncertainty in the direction of increased subdwarf temperature (a $25,000$ K subdwarf with a $1,000$ K companion), and a 1σ uncertainty in the direction of decreased subdwarf temperature (a $10,000$ K subdwarf with a $3,000$ K compan-

ion). One cannot mix and match these combinations. For example, a 10,000 K subdwarf with a 1,000 K companion, or a 25,000 K subdwarf with a 3,000 K companion, are *not* valid solutions. A minimum uncertainty is set to one grid point and therefore is also limited by the extent of the grid: a minimum and maximum subdwarf temperature of 11,000 and 40,000 K, respectively. We examine systematic uncertainties in Section 7.6.8, leading to estimates of a few thousand Kelvin for a more realistic error. We show example SEDs and fits to a few objects that are found to have approximately G0 and A7-type companions in Figures 7.6 and 7.7, respectively.

We compared our results to published effective temperatures and/or known companions for the *C2MS* and *SU* samples, shown in Table 7.5 and 7.6, respectively. The best fit is not always satisfactory, indicated by a high χ^2. We include the "Q" (Quality) column in Tables B.2 and B.3 to show where this is the case. "Q" values correspond to; 1:Good fit, 2:Average fit, 3:Poor fit, 4:WD/WD+MS/CV and 5:Quasar/Galaxy. The classifications in this catagory between values of 1, 2 and 3 are purely qualitative, whereas 4 and 5 are drawn from the SIMBAD and SDSS spectra classifications. Values of three and above are excluded from the histograms shown in Figure 7.9, 7.10 and 7.11. SIMBAD has an entry for many more objects, but without any specific details. All objects which were previously known (in one or more of: Ferguson et al. 1984, Kilkenny et al. 1988, Allard et al. 1994, Saffer et al. 1994, Thejll et al. 1995, Ulla & Thejll 1998, Jeffery & Pollacco 1998, Aznar Cuadrado & Jeffery 2001, Maxted et al. 2001, Williams et al. 2001, Aznar Cuadrado & Jeffery 2002, Maxted et al. 2002, Edelmann et al. 2003, Morales-Rueda et al. 2003, Stark & Wade 2003, Napiwotzki et al. 2004, Reed & Stiening 2004, Lisker et al. 2005, Østensen 2006, Wade et al. 2006, Stark & Wade 2006, Stroeer et al. 2007, Wade et al. 2009, Geier et al. 2011a and Vennes et al. 2011a) to be composite subdwarf plus companion systems are highlighted in Tables B.2 and B.3.

7.6.1 Potential systematic temperature differences

When comparing the system parameters calculated herein and those from the literature, there are a number of possible causes for discrepancies: Firstly, one must consider the fact that often in the literature fitting is performed on the absorption line profiles of the subdwarf with a single star model [e.g. Saffer et al., 1994], whereas our study suggests that these systems all have a significant contribution from the companion. The single subdwarf fit would then result in biased system parameters.

Secondly, if the subdwarf's companion is a sub-giant or giant type star, our method would underestimate the subdwarf's effective temperature because we only
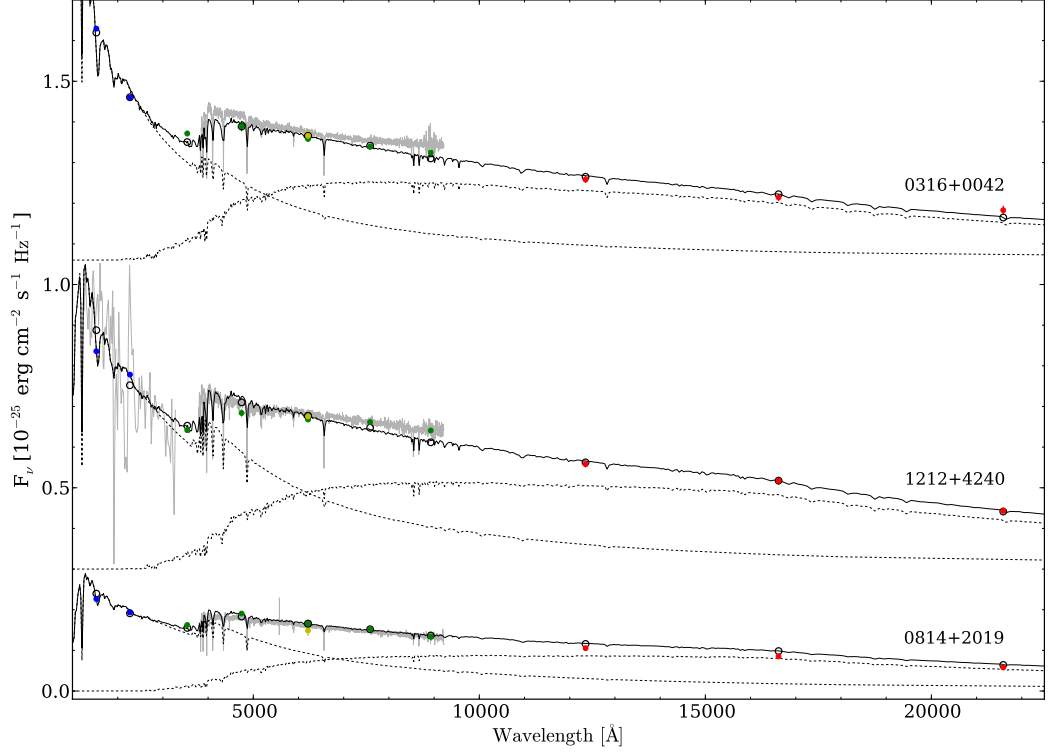
Figure 7.6: The SEDs of, and fits to, 0316+0042 (PG 0313+005), 0814+2019 and 1212+4240 (PG 1210+429), all of which having approximately G0-type companions. The optical SDSS spectra are shown in grey. The GALEX, SDSS, CMC and 2MASS magnitudes are plotted in blue, green, yellow and red, respectively with corresponding errorbars. The fit to 0316+0042 comprises a $T_{eff} = 28,000\,K$ sdB model and a $6,250\,K$ star (black dashed lines). Similarly, a $T_{eff} = 21,000\,K$ sdB model and a $5,500\,K$ star is used for 0814+2019 and a $T_{eff} = 23,000\,K$ sdB model and a $5,750\,K$ star for 1212+4240. The composite spectra and magnitudes are the solid black line and open black circles, respectively. The absolute flux level of the SDSS spectrum does not match the model well in all cases. This is most likely related to calibration issues of the SDSS spectroscopy, as it disagrees with the SDSS photometry. For 1212+4240, an archive IUE ultraviolet spectrum plotted in grey. 0316+0042 and 1212+4240 are offset in flux by 0.30 and 1.05 units, respectively, for clarity.
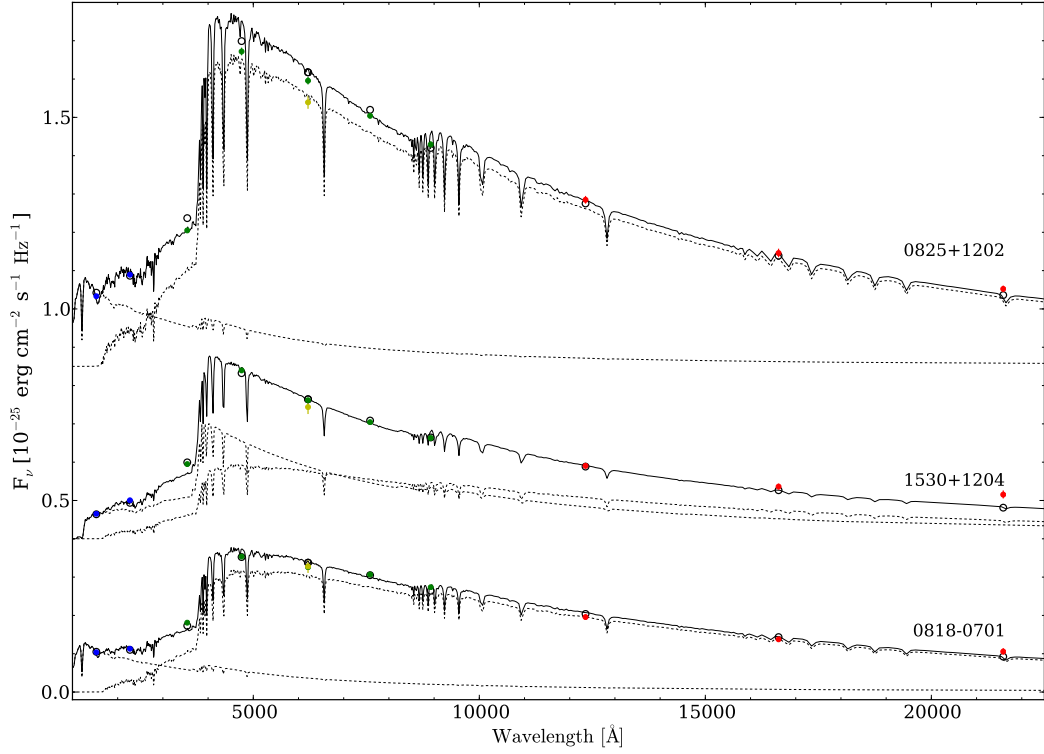
Figure 7.7: The SEDs of, and fits to, 0818−0701, 0825+1202 and 1530+1204, all of which having approximately A7-type companions, following the same format as Figure 7.6. The fit to 0818−0701 comprises a $T_{\mathrm{eff}} = 22,000\,\mathrm{K}$ sdB model and a $7,750\,\mathrm{K}$ star (black dashed lines). Similarly, a $T_{\mathrm{eff}} = 22,000\,\mathrm{K}$ sdB model and a $8,250\,\mathrm{K}$ star is used for 0825+1202 and a $T_{\mathrm{eff}} = 11,000\,\mathrm{K}$ sdB model and a $8,000\,\mathrm{K}$ star for 1530+1204. 1530+1204 and 0825+1202 are offset in flux by 0.40 and 0.85 units, respectively, for clarity.

149

use main–sequence star models for the companion. While this may affect isolated cases, we do not expect a significant population of sub-giant and giant companion stars to be present in our sample given the colour selection cuts we employed (see Section 7.3.2).

Finally, the suppression of the subdwarf's ultraviolet flux due to line blanketing could cause a biased effective temperature. Subluminous B stars show peculiar abundance patterns. Some metals (mostly the lighter ones) are found to be strongly depleted, while heavier elements can be strongly enriched [O'Toole & Heber, 2006; Blanchette et al., 2008]. The abundance patterns are caused by atomic diffusion, which depends on various parameters (see Michaud et al. 2011, for the state-of-the-art of modelling), however, metalicity may not be an important one. Because the abundance pattern differs from star to star, the ultraviolet line blocking for any individual subdwarf will deviate from that predicted from the solar metalicity models adopted here. Therefore, we cannot quantify the systematic uncertainty in the temperature determination of the subdwarf stars. O'Toole & Heber [2006] regard solar metalicity models as appropriate for sdB stars cooler than about $30000\,\mathrm{K}$, but prefer models of scaled supersolar abundances for hotter stars as a proxy for enhanced ultraviolet line blocking. Because the effective temperatures of our program stars are mostly below $30000\,\mathrm{K}$, we stay with solar metalicity model spectra.

7.6.2 0018+0101

Lisker et al. [2005] calculated an effective temperature for 0018+0101 (HE 0016+0044) of $28,264 \pm 800\,\mathrm{K}$. This compares relatively well with our SU sample estimate of $25,000 - 23,000\,\mathrm{K}$, however, a significantly higher temperature is measured when using the $C2MS$ sample ($39,000 - 40,000\,\mathrm{K}$). Either a $23,000$ or a $40,000\,\mathrm{K}$ subdwarf provide an adequate fit to the SED, and small changes in the χ^2 surface lead to the alternate solution. The flat χ^2 surface comes about from a very blue ($\mathrm{m_{FUV}} - \mathrm{m_{NUV}}$) colour ($-0.64$) that is difficult to reconcile with the rest of the SED.

7.6.3 1300+0057 and 1538+0934

The published effective temperatures for 1300+0057 [39359 K: HE 1258+0113: Stroeer et al., 2007] and 1538+0934 [35114 K: HS 1536+0944: Lisker et al., 2005], both in the SU sample, are only upper limits on the effective temperatures. Lisker et al. [2005] note the presence of a cool ($\sim$K0-type) companion in the spectrum of 1538+0934 and therefore specifically state that the estimated temperature is an upper limit. Stroeer et al. [2007] also note the presence of a cool companion based on the $B - J$

colour for 1300+0057 and therefore one may assume the temperature is also an over-estimate. In both cases, the best fit model (30,000 and 23,000 K for 1300+0057 and 1538+0934, respectively) corresponds to a bluer ($m_{\mathrm{FUV}} - m_{\mathrm{NUV}}$) colour than the *GALEX* fluxes. Therefore the higher published effective temperature model does not agree with the data.

7.6.4   1517+0310 and 1518+0410

In the cases of 1517+0310 and 1518+0410 (PG 1514+034 and PG 1515+044, respectively: *SU* sample), the companion effective temperatures measured ($6,000\{^{6,250}_{5,750}\,\mathrm{K}$ and $5,500\{^{5,750}_{5,250}\,\mathrm{K}$, respectively) are significantly different from that in the catalogue of Østensen [2006] (K2 and K4.5; corresponding to effective temperatures of $\sim 4,800$ and $4,300\,\mathrm{K}$, respectively). The whole SED of 1517+0310 is not particularly well fit by the calculated best model. The system has a very blue ($m_{\mathrm{FUV}} - m_{\mathrm{NUV}}$) colour and therefore the best fit model is forced to be a hot subdwarf, which leads to a correspondingly increased companion effective temperature.

7.6.5   1709+4054

1709+4054 (PG 1708+409: *C2MS* sample), was classified by Saffer et al. [1994] to be a subdwarf with an effective temperature of 28,500 K. We determined $25,000 - 28,000\,\mathrm{K}$ if we apply no reddening and $27,000 - 29,000\,\mathrm{K}$ when applying the full Schlegel et al. [1998] reddening. However, Saffer et al. [1994] fit the line profiles of this composite system with a single star subdwarf model, and therefore comparing the two sets of temperatures is not comparing like for like.

7.6.6   2138+0442

For the case of 2138+0442 (PG 2135+045; *C2MS* sample), we find a slightly lower effective temperature ($24,000 - 26,000\,\mathrm{K}$) compared with the published value of Aznar Cuadrado & Jeffery [$\sim 28,000\,\mathrm{K}$: 2002]. Including the full Schlegel et al. [1998] reddening ($26,000 - 28,000\,\mathrm{K}$), however, the temperatures agree. Aznar Cuadrado & Jeffery [2002] treat 2138+0442 as a composite system fitting both objects in the blue region of the spectrum, thus the above mentioned problem of fitting a single star model (Section 7.6.1) does not apply.

7.6.7   2244+0106

2244+0106 (PB 5146) was found to be a post-EHB star with a high velocity in Tillich et al. [2011]. They estimate a $\mathrm{T_{eff}} = 33580 \pm 680\,\mathrm{K}$, $\log(g) = 4.75 \pm 0.20$

and a distance of $18.29 \pm 2.45\,\mathrm{kpc}$, compared with our $22,000 - 26,000\,\mathrm{K}$ at $6.1 - 7.9\,\mathrm{kpc}$. However, the companion star is not accounted for in Tillich et al. [2011] and therefore the subdwarf's effective temperature is probably overestimated. This is also consistent with the unusually low surface gravity.

7.6.8 Overlap

Where the *C2MS* and *SU* samples overlap, a comparison of the fits is given in Table 7.7 and shown in Figure 7.8. The two sets of fits appear consistent within the uncertainties. We analysed the distribution of the difference between all the *C2MS* and *SU* parameters (distance, subdwarf and companion temperature) and find that the distributions are all approximately Gaussian, centered about zero. We do not find any evidence to suggest that the two samples effective temperatures are systematically offset. The errors on the subdwarf effective temperature from the χ^2 fit may be slightly underestimated, and a more realistic error is of order a few thousand Kelvin. The one difference is that the UKIDSS data should better constrain the companion star effective temperature due to the greater depth and higher photometric accuracy of the near-infrared data.

Overall, in individual cases, we must bear in mind that we may occasionally select the wrong solution (in cases where the χ^2 surface is relatively flat), and we cannot identify the exact amount of reddening that should be corrected for. However, this study is aimed at providing a statistical analysis of the sample rather than correct parameters for all individual systems. The uncertainties in the measured parameters should be randomly distributed and therefore not effect the distributions. It is thus not a significant issue for the analysis presented here, but these uncertainties should be considered when consulting the fitted parameters of individual systems.

We saw earlier that the key contaminants in our colour box are composite systems containing white dwarfs (Table 7.3, shown in Figure 7.3). Indeed, from the *C2MS* sample 0018+0101, 0141+0614, 0923+0652, 2117−0015 and 2117−0006 are candidates for being DA white dwarfs with infrared excesses based on their photometry [Girven et al., 2011]. However, such a classification can only be confirmed through follow-up spectroscopy. SDSS spectroscopy is available for 2117−0006, and Girven et al. [2011] classify it as a "Narrow Line Hot Star" (NLHS), which they believe to be a group primarily made up of subdwarfs. 0018+0101, a confirmed sdB star (discussed in Section 7.6.2), is also catalogued as a NLHS by Girven et al. [2011], corroborating the subdwarf label.

Table 7.5: Individual objects of interest from the *C2MS* sample. Only subdwarfs with measured system parameters are displayed, but all known CVs and white dwarfs are shown. The "{" notation is described in Section 7.6 and does not simply represent uncertainties because the uncertainties in the subdwarf and companion parameters are correlated. The fit parameters shown are not corrected for interstellar reddening. The subdwarfs and CV categories are objects confirmed in the literature. We also cross-matched the *C2MS* sample with the white dwarf plus infrared excess candidate catalogue of Girven et al. [2011] (see Chapter 5). Objects in this catalogue have not yet been confirmed to be white dwarfs and subdwarf stars are the main contaminant. The comments column for the "WD + IR excess candidates" are the classifications according to the SDSS spectra found in Girven et al. [2011]. NLHS corresponds to Narrow Line Hot Star (probable subdwarf). Objects may fall in both the subdwarfs or CV catagories as well as be a candidate white dwarf with an infrared excess in Girven et al. [2011].

Name	Identifier	This Paper sdB $T_{\rm eff}$ (1000K)	This Paper MS $T_{\rm eff}$ (1000K)	This Paper d (kpc)	Literature sdB $T_{\rm eff}$ (K)	Literature MS Type	Ref / Comments
Subdwarfs							
0018+0101	HE 0016+0044	$40{^{40}_{39}}$	$5.50{^{5.75}_{5.25}}$	$1.5{^{1.5}_{1.4}}$	28264		Lisker et al. [2005]
1212+4240	PG 1210+429	$23{^{24}_{22}}$	$5.75{^{6.00}_{5.50}}$	$1.5{^{1.7}_{1.4}}$		K2.5	Østensen [2006]
1517+0310	PG 1514+034	$40{^{40}_{39}}$	$6.00{^{6.25}_{5.75}}$	$1.1{^{1.1}_{1.0}}$		K2	Østensen [2006]
1709+4054	PG 1708+409	$26{^{28}_{25}}$	$5.50{^{5.75}_{5.25}}$	$1.7{^{1.9}_{1.6}}$	28500		Saffer et al. [1994, 1998]
2138+0442	PG 2135+045	$25{^{26}_{24}}$	$5.00{^{5.25}_{4.75}}$	$1.2{^{1.3}_{1.1}}$	$\sim$28000	$\sim$K2	Aznar Cuadrado & Jeffery [2002]
CV							
0141+0614	HS 0139+0559	$12{^{13}_{11}}$	$7.25{^{7.50}_{7.00}}$	$4.8{^{5.4}_{4.3}}$			Heber et al. [1991], Aungwerojwit et al. [2005]
0812+1911		$14{^{15}_{13}}$	$7.25{^{7.50}_{7.00}}$	$4.8{^{6.9}_{4.8}}$			Szkody et al. [2006]
1015−0308	SW Sex	$18{^{19}_{17}}$	$7.00{^{7.25}_{6.75}}$	$2.6{^{2.9}_{2.3}}$			e.g. Green et al. [1982], Penning et al. [1984]
2143+1244		$30{^{31}_{29}}$	$6.25{^{6.50}_{6.00}}$	$2.9{^{3.3}_{2.6}}$			Szkody et al. [2005]
WD + IR excess candidates							
0018+0101	HS 0016+0044	$40{^{40}_{39}}$	$5.50{^{5.75}_{5.25}}$	$1.5{^{1.5}_{1.4}}$			Girven et al. [2011]
0141+0614	HS 0139+0559	$12{^{13}_{11}}$	$7.25{^{7.50}_{7.00}}$	$4.8{^{5.4}_{4.3}}$			NLHS
0923+0652		$29{^{30}_{28}}$	$6.75{^{7.00}_{6.50}}$	$2.1{^{2.9}_{2.0}}$			
2117−0015		$13{^{14}_{12}}$	$6.75{^{7.00}_{6.50}}$	$3.5{^{3.5}_{2.3}}$			
2117−0006		$21{^{22}_{20}}$	$6.25{^{6.50}_{6.00}}$	$2.0{^{2.9}_{1.9}}$			NLHS

153

Table 7.6: Individual objects of interest from the *SU* sample, following the same format as Table 7.5. The "{" notation is described in Section 7.6 and does not simply represent uncertainties because the uncertainties in the subdwarf and companion parameters are correlated.

Name	Identifier	This Paper sdB T_{eff} (1000K)	MS T_{eff} (1000K)	d (kpc)	Literature sdB T_{eff} (K)	MS Type	Ref / Comments
Subdwarfs							
0018+0101	HE 0016+0044	24{25}{23}	4.25{4.50}{4.00}	1.2{1.3}{1.2}	28264		Lisker et al. [2005]
1300+0057	HE 1258+0113	30{31}{29}	3.50{3.75}{3.25}	1.7{1.8}{1.6}	39359[a]		Stroeer et al. [2007]
1517+0310	PG 1514+034	40{40}{39}	6.00{6.25}{5.75}	1.1{1.0}{1.0}		K2	Østensen [2006]
1518+0410	PG 1515+044	26{27}{25}	5.50{5.75}{5.25}	1.8{1.7}{1.7}		K4.5	Østensen [2006]
1538+0934	HS 1536+0944	23{24}{22}	5.00{5.25}{4.75}	1.8{2.0}{1.7}	35114[a]	K0	Lisker et al. [2005]
CV							
0141+0614	HS 0139+0559	14{15}{13}	7.25{7.50}{7.00}	3.7{4.9}{3.7}			Heber et al. [1991]
0813+2813		20{21}{19}	6.25{6.50}{6.00}	6.4{6.7}{4.6}			Szkody et al. [2005]
0920+3356	BK Lyn	20{21}{18}	6.75{7.00}{6.25}	2.3{2.3}{1.7}			Dobrzycka & Howell [1992], Ringwald [1993]
1015−0308	SW Sex	21{22}{20}	6.75{7.00}{6.50}	2.0{2.5}{1.9}			e.g. Ballouz & Sion [2009], Ritter & Kolb [2009]
2333+1522		17{18}{16}	6.75{7.00}{6.50}	12.6{17.8}{12.3}			Szkody et al. [2005]
WDMS							
0032+0739		21{22}{20}	5.25{5.50}{5.00}	4.4{6.9}{4.4}			Rebassa-Mansergas et al. [2011]
0300−0023	WD 0257−005	38{39}{34}	5.00{5.25}{4.75}	3.2{3.4}{2.8}			
0920+1057		34{35}{33}	4.75{5.00}{4.50}	3.3{3.5}{3.1}			
1016+0443		29{30}{28}	4.50{4.75}{4.25}	4.8{7.9}{4.8}			
1352+0910		29{30}{28}	4.00{4.25}{3.75}	4.0{6.5}{4.0}			

[a] Noted presence of a cool companion, therefore temperature is an upper limit, see Section 7.6.3.

Table 7.6:

Name	Identifier	This Paper				Literature	
		sdB T$_{\text{eff}}$ (1000K)	MS T$_{\text{eff}}$ (1000K)	d (kpc)	sdB T$_{\text{eff}}$ (K)	MS Type	Ref / Comments
WD + IR excess candidates							
0018+0101	HS 0016+0044	24^{25}_{23}	$4.25^{4.50}_{4.00}$	$1.2^{1.3}_{1.2}$			NLHS
0032+0739		21^{22}_{20}	$5.25^{5.50}_{5.00}$	$4.4^{6.9}_{4.4}$			DA
0141+0614	HS 0139+0559	14^{15}_{13}	$7.25^{7.50}_{7.00}$	$3.7^{4.9}_{3.7}$			
0814+2811		22^{23}_{21}	$6.00^{6.25}_{5.75}$	$3.7^{4.0}_{3.3}$			NLHS
0854+0853	PN A66 31	40^{40}_{39}	$3.00^{3.25}_{3.00}$	$1.2^{1.2}_{1.2}$			
0920+3356		20^{21}_{18}	$6.75^{7.00}_{6.25}$	$2.3^{2.3}_{1.7}$			
0925−0140	BK Lyn	17^{18}_{16}	$5.50^{5.75}_{5.25}$	$9.4^{14.9}_{9.4}$			
0951+0347		23^{24}_{22}	$4.00^{4.25}_{3.75}$	$1.9^{2.0}_{1.7}$			NLHS
0959+0330	PG 0957+037	31^{32}_{30}	$3.00^{3.25}_{3.00}$	$1.1^{1.2}_{1.1}$			
1006+0032	PG 1004+008	26^{27}_{25}	$5.00^{5.25}_{4.75}$	$3.3^{3.6}_{3.1}$			NLHS
1100+0346		34^{36}_{33}	$3.75^{4.25}_{3.50}$	$2.7^{2.9}_{2.6}$			
1116+0755		28^{29}_{27}	$5.00^{5.25}_{4.75}$	$2.3^{2.3}_{1.4}$			NLHS
1135+0731		29^{30}_{28}	$6.25^{6.50}_{6.00}$	$6.4^{8.2}_{5.7}$			NLHS
1215+1351		21^{22}_{20}	$4.50^{4.75}_{4.25}$	$3.1^{5.1}_{3.1}$			NLHS
1228+1040	WD 1226+110	21^{22}_{20}	$3.00^{3.25}_{3.00}$	$2.2^{3.8}_{2.2}$			DA: Gänsicke et al. [2006b]
1237−0151		23^{25}_{22}	$4.75^{5.00}_{4.50}$	$3.9^{4.3}_{3.6}$			
1300+0057	HE 1258+0113	30^{31}_{29}	$3.50^{3.75}_{3.25}$	$1.7^{1.8}_{1.6}$			NLHS
1315+0245		33^{34}_{32}	$3.25^{3.50}_{3.00}$	$0.9^{1.0}_{0.8}$			
1323+2615		20^{21}_{19}	$5.00^{5.25}_{4.75}$	$5.8^{5.8}_{3.6}$			
1352+0910		29^{30}_{28}	$4.00^{4.25}_{3.75}$	$4.0^{6.5}_{4.0}$			DA
1422+0920		26^{27}_{25}	$4.75^{5.00}_{4.50}$	$3.5^{3.7}_{3.2}$			NLHS
1442+0910		26^{27}_{24}	$5.00^{5.25}_{4.75}$	$6.6^{7.1}_{5.9}$			
1443+0931		28^{29}_{27}	$4.50^{4.75}_{4.25}$	$4.5^{4.5}_{2.7}$			NLHS
1500+0642		27^{28}_{26}	$4.25^{4.50}_{3.75}$	$3.9^{4.2}_{3.7}$			NLHS
1507+0724		27^{28}_{26}	$4.50^{4.75}_{4.25}$	$4.1^{4.4}_{3.8}$			
1510+0409		26^{27}_{25}	$4.00^{4.25}_{3.75}$	$3.4^{3.6}_{3.2}$			NLHS

Table 7.6:

Name	Identifier	This Paper			Literature		Ref / Comments
		sdB T$_{\text{eff}}$ (1000K)	MS T$_{\text{eff}}$ (1000K)	d (kpc)	sdB T$_{\text{eff}}$ (K)	MS Type	
Possible WD							
1525+0958		$29\{^{30}_{28}$	$3.25\{^{4.25}_{3.00}$	$2.8\{^{4.8}_{2.8}$			Girven et al. [2011]
1538+0644	HS 1536+0944	$14\{^{15}_{13}$	$7.25\{^{7.50}_{7.00}$	$6.5\{^{8.6}_{6.4}$			NLHS
1543+0012	WD 1541+003	$21\{^{22}_{20}$	$4.75\{^{5.00}_{4.50}$	$2.9\{^{4.5}_{2.8}$			NLHS
1554+0616		$29\{^{30}_{28}$	$4.75\{^{5.00}_{4.50}$	$3.8\{^{5.8}_{3.6}$			
1619+2407		$24\{^{25}_{23}$	$6.50\{^{6.75}_{6.25}$	$4.3\{^{4.8}_{3.8}$			NLHS
2049−0001		$18\{^{19}_{17}$	$5.25\{^{5.50}_{5.00}$	$6.0\{^{6.4}_{5.6}$			
2117−0006		$30\{^{31}_{29}$	$6.50\{^{6.75}_{6.25}$	$2.1\{^{2.3}_{1.8}$			NLHS
2147−0112	FBS 2145−014	$25\{^{26}_{24}$	$3.25\{^{3.50}_{3.00}$	$1.6\{^{1.7}_{1.5}$			

Table 7.7: Comparison of fits using the *C2MS* sample against that using the *SU* sample where there is overlap. The "{" notation is described in Section 7.6 and does not simply represent uncertainties. The "Q" (Quality) column values correspond to; 1:Good fit, 2:Average fit, 3:Poor fit, 4:WD/WD+MS/CV and 5:Quasar/Galaxy. 0141+0614 and 1015−0308 are CVs (see Table 7.5.)

Name	Identifier	*C2MS*				*SU*			
		sdB T_{eff} (1000K)	MS T_{eff} (1000K)	d (kpc)	Q	sdB T_{eff} (1000K)	MS T_{eff} (1000K)	d (kpc)	Q
0018+0101	HE 0016+0044	40{40{39	5.50{5.75	1.5{1.5{1.4	2	24{25	4.25{4.50	1.2{1.3	1
0054+1508		21{22{20	7.25{7.50	3.2{4.8{3.2	2	29{30	7.25{7.50	2.8{3.3	3
0141+0614	HS 0139+0559	12{13{11	7.25{7.50	4.8{5.4{4.3	4	14{15{13	7.25{7.50	3.7{4.9{3.7	4
0316+0042	PG 0313+005	28{29{27	6.25{6.50	2.2{2.2{1.4	1	26{27	6.00{6.25	2.0{2.2	1
0737+2642		25{26{24	5.50{5.75	1.6{1.8{1.5	1	25{26	5.50{5.75	1.6{1.8{1.5	1
0755+2128		17{18{16	7.25{7.50	2.3{3.5	1	21{22	7.00{7.25	2.0{2.4{1.9	1
0814+2019		21{22{20	5.50{5.75	2.0{3.2{2.0	1	20{21{19	6.25{6.50	3.5{3.7{2.7	1
0829+2246		26{27{24	6.00{6.25	2.7{3.0{2.4	1	21{22{20	5.25{5.50	1.9{2.6{1.8	1
0833−0006		29{30{28	7.25{7.50	3.1{3.6{2.9	2	29{30	6.75{7.00	2.4{2.7{2.1	2
0929+0603		21{21{20	5.75{6.00	1.6{2.5{1.5	2	29{30{28	6.00{6.25	1.6{2.0{1.4	1
0937+0813	PG 0935+084	23{24{22	6.00{6.25	2.0{2.8{1.8	1	21{22{20	5.75{6.00	1.7{2.3{1.6	1
0941+0657	PG 0939+072	21{22{20	6.25{6.50	1.7{2.5{1.6	1	29{30{28	6.50{6.75	1.7{2.0{1.5	2
1015−0308	SW Sex	18{19{17	7.00{7.25	2.6{2.9{2.3	4	21{22	6.75{7.00	2.0{2.5{1.9	4
1018+0953		28{29{27	5.75{6.00	1.6{1.6{1.0	1	35{36{34	5.50{5.75	1.3{1.5{1.2	1
1113+0413	PG 1110+045	29{30{28	4.75{5.00	0.9{1.4{0.9	1	30{31{29	4.75{5.00	0.9{1.0{0.8	1
1203+0909	PG 1200+094	27{28{25	5.75{6.00	1.5{1.6{1.3	1	27{28{26	5.75{6.00	1.5{1.6{1.3	1
1233+0834		30{31{29	6.00{6.25	1.9{2.1{1.7	2	30{31{29	6.00{6.25	1.9{2.2{1.7	1
1325+1212	PG 1323+125	26{27{25	5.75{6.00	2.1{2.3{1.9	1	26{28{25	5.75{6.00	2.1{2.4{1.9	1
1326+0357	PG 1323+042	24{25{23	5.00{5.25	1.5{1.7{1.4	2	22{23	4.75{5.00	1.4{1.5{1.2	1
1402+3215		22{23{21	6.25{6.50	1.9{2.1{1.7	1	22{23{21	6.25{6.50	1.9{2.1{1.7	1
1421+0753	KN Boo	27{28{26	5.25{5.50	1.6{1.7{1.5	1	27{28{26	5.25{5.50	1.6{1.7{1.5	1
1502−0245	PG 1459−026	24{25{22	6.25{6.50	1.8{1.9{1.5	1	30{31{29	6.00{6.25	1.4{1.6{1.3	1
1542+0056		29{30{28	6.50{6.75	1.5{2.1{1.4	1	29{30{28	6.50{6.75	1.5{1.7{1.3	1

157
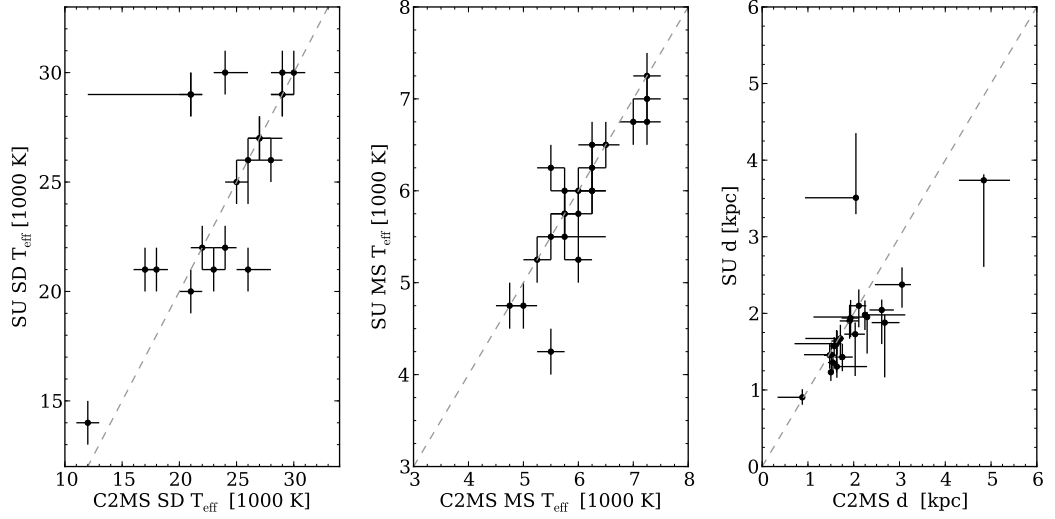
Figure 7.8: A comparison of fits using the *C2MS* sample versus that using the *SU* sample, where there is overlap. Objects with a "Q"≥ 3 in Table 7.7 are excluded. The dashed line shows a one to one relation between the parameters.

7.6.9 Distributions of fits – *C2MS* sample

The distribution of subdwarf and companion effective temperatures for the *C2MS* sample is shown in Figure 7.9 and the distribution of distances for the *C2MS* and *SU* samples in Figure 7.10. Here we compare the parameters with and without reddening corrections. Objects that are known to be contaminants, such as white dwarfs and CVs, have been removed from all three (distance, subdwarf and companion temperature) histograms. Galaxies should be flagged by SDSS and are therefore removed by the flags in Table 7.1. Using Table 7.3 to estimate the remaining fraction of contaminants, we know that 12 per cent (3/25) of the objects with SDSS spectra are contaminants. Therefore, approximately eleven (12 per cent of 93) of the whole *C2MS* sample will be contaminants. The two CVs and one white dwarf with SDSS spectra (Table 7.3) can be removed from the histograms. Thus, the contamination of the *C2MS* sample (now with and without SDSS spectra) used for calculating distributions will be 9 per cent (8/90). Since any such contaminants will be distributed right across our fit parameters, we believe they do not distort our statistical analysis to a significant degree.

7.6.9.1 Subdwarf temperature distribution

Taking the system parameters calculated without correcting for reddening, we find that the subdwarf effective temperatures (Figure 7.9) are spread from $20,000-$

30,000 K and peak around 20,000 − 24,000 K. We do see a pronounced drop in numbers below 20,000 K. Reddening is not the issue here; applying the full Schlegel et al. [1998] reddening correction to the objects before fitting does not lead to a significant shift in the distribution, though it is slightly smoothed.

Based on our theoretical tracks for composite systems, we know that we have a reduced completeness below $\sim 25,000$ K (see Section 7.3.2). For example, cool subdwarfs of $\sim 15,000$ K with an M-type companion will be missed by the colour selection. This could lead to a bias towards hotter subdwarfs, which we select over a wider range of companion types. In addition, the redder $(r_{CMC} − K_s)$ colours (Figure 7.2) means that at the K_s magnitude limit (14.3), systems will be detected down to fainter r_{CMC} magnitudes. This is, however, offset by the increasing intrinsic brightness of cooler subdwarfs (because of decreasing $\log(g)$ and increasing radius). We previously discussed a bias towards cooler subdwarfs if our assumption of a main–sequence type companion is incorrect (Section 7.6.1). However, we believe this to be a relatively small fraction given our sample selection (Section 7.3.2).

To quantify these possible biases, the limitations on distance introduced by various magnitude cuts can be seen in Table 7.8. These are derived by taking the absolute magnitudes of the composite system and calculating the distance the object would have to be moved to in order to have an apparent magnitude at the relevant limit. The primary effects in this case are caused by the saturation limit of SDSS ($r_{SDSS} > 14.1$), corresponding to a minimum distance, and the faint K_s magnitude limit of 2MASS ($K_s < 14.3$), setting a maximum distance. These significantly depend on companion spectral type (see below) and, to a lesser extent, on subdwarf effective temperature. It can be seen that the imposed r_{CMC} magnitude limit does not have an effect because the K_s limit is always more restrictive. In essence, in the *C2MS* sample, the 2MASS depth limits the volume over which we are complete.

7.6.9.2 Companion type distribution

As discussed in Section 7.3.2, the way in which we select subdwarfs with companions introduces a bias in companion type. We expect our selection to be complete for subdwarfs with $20,000$ K $\leq$ T$_{eff}$ $\leq 35,000$ K and companions in the range A5 to M5-type. Similarly, including the more extreme subdwarf temperatures ($15,000$ K $\leq$ T$_{eff}$ $\leq 40,000$ K), we are complete for F0 to K0-type companions. The companion type range is smaller in the latter case because, for example, a $40,000$ K subdwarf with a M5-type companion does not fall in our colour selection, whereas a $35,000$ K subdwarf with a M5-type companion does.

The distribution of companion effective temperature in Figure 7.9 ramps up

159

Table 7.8: Limitations on the distance of subdwarf plus main–sequence star candidates caused by the relative magnitude cuts. This is calculated for $15,000$, $20,000$, $30,000$ and $40,000\,$K subdwarfs and companions with effective temperatures of $3,250\,$K (M0), $5,000\,$K (K0), $7,250\,$K (F0). The absolute r and K-band magnitudes are listed in the "Abs" r and K columns, respectively. The important limits considered are; the saturation of r_{SDSS} at 14.1 (therefore a minimum distance), the cut made on r_{CMC} at 16.0 (therefore a maximum distance), the K_s-band magnitude limit of 2MASS at 14.3 and the K_s-band magnitude limit of UKIDSS at 17.8.

| sdB T_{eff} | MS T_{eff} | Abs | d (kpc) | | Abs | d (kpc) | |
(K)	(K)	r	r_{SDSS}=14.1	r_{CMC}=16.0	K	Ks=14.3	K=17.8
$15,000$	$7,250$	2.2	2.4	5.8	1.9	3.1	15.6
	$5,000$	2.9	1.7	4.1	2.8	2.0	9.9
	$3,250$	3.0	1.7	4.0	3.2	1.7	8.5
$20,000$	$7,250$	2.5	2.1	5.0	2.0	2.8	14.3
	$5,000$	3.6	1.3	3.0	3.4	1.5	7.7
	$3,250$	3.7	1.2	2.8	4.0	1.1	5.8
$30,000$	$7,250$	2.8	1.8	4.4	2.2	2.7	13.5
	$5,000$	5.0	0.7	1.6	3.9	1.2	6.0
	$3,250$	5.5	0.5	1.2	5.3	0.6	3.1
$40,000$	$7,250$	2.7	1.9	4.5	2.2	2.7	13.5
	$5,000$	4.6	0.8	1.9	3.9	1.2	6.2
	$3,250$	5.0	0.7	1.6	5.1	0.7	3.5

from early spectral types towards $\sim$ G0, as might be expected from the initial mass function (IMF). On the other hand, the subsequent turn over and drop towards mid-K-type may be a product of our selection biases. A $15,000\,$K subdwarf with a M0-type companion saturates in SDSS at $d \leq 1.7\,$kpc and is too faint for 2MASS at $d \geq 1.7\,$kpc (Table 7.8). Therefore we are not sensitive to all subdwarfs with M0-type companions. The best way to reduce such biases and test our completion is by probing to fainter K_s-band magnitudes. This was the key motivation behind our second sample, the SU sample, which extends several magnitudes deeper and reaches $K \sim 17.8$, though at the expense of limited sky coverage.

7.6.9.3 Distance distribution

The calculated distance distribution seen in Figure 7.10 shows a rapid increase towards $\sim$ 2kpc, followed by an extended tail. As we discussed previously, the limitations on distance due to our magnitude cuts and limits are important and are a complex function of subdwarf effective temperature and companion type (Table 7.8). There are no clean regions where all temperatures and companion types are sampled evenly to give a complete, volume-limited sample. If one assumes that all subdwarfs
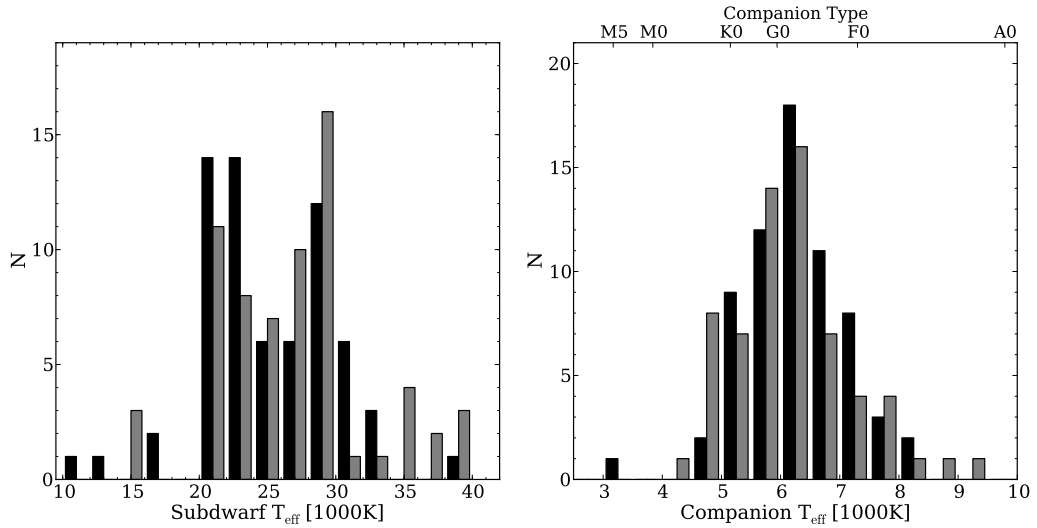
Figure 7.9: Distributions of the subdwarf (left) and companion (right) effective temperatures calculated from the fitting method described in Section 7.5 when applied to the *C2MS* sample. The grey and black histograms show the system parameters when calculated with and without the (maximum) reddening correction, respectively. Adjoining pairs of histogram show the number of objects in the same bin. Only 66 of the 93 objects in this sample (Table 7.3) are shown in the histograms. The remaining 27 are contaminants (from their SIMBAD classification or their SDSS spectra), or the subdwarf–companion model provides a bad fit ("Q" ≥ 3 in Table B.2), have been removed. The subdwarf effective temperature histogram is grouped in bins of 2,000 K and the companion star histogram uses bins of 500 K.

(independent of temperature and companion type) are drawn from same parent distance distribution, and we select each subdwarf–companion system with equal probability, the distribution shown in Figure 7.10 would represent the true distance distribution. Therefore we would be relatively confident that the peak appears at $1.5 - 2.0$kpc. However, Table 7.8 does show that for some combinations of subdwarf and companion temperature we are no longer complete at this peak distance. Here again the deeper *SU* sample can provide us with a more complete sample.

7.6.10 Distribution of fits – *SU* sample

The corresponding distributions of the subdwarf and companion effective temperature for the *SU* sample are shown in Figure 7.11 with the distribution of distances in Figure 7.10. The subdwarf effective temperature distribution is broadly consistent with that of the *C2MS* sample, with most subdwarf temperatures between $20,000 - 30,000$ K. It is also similar to that shown for uncontaminated sdBs by
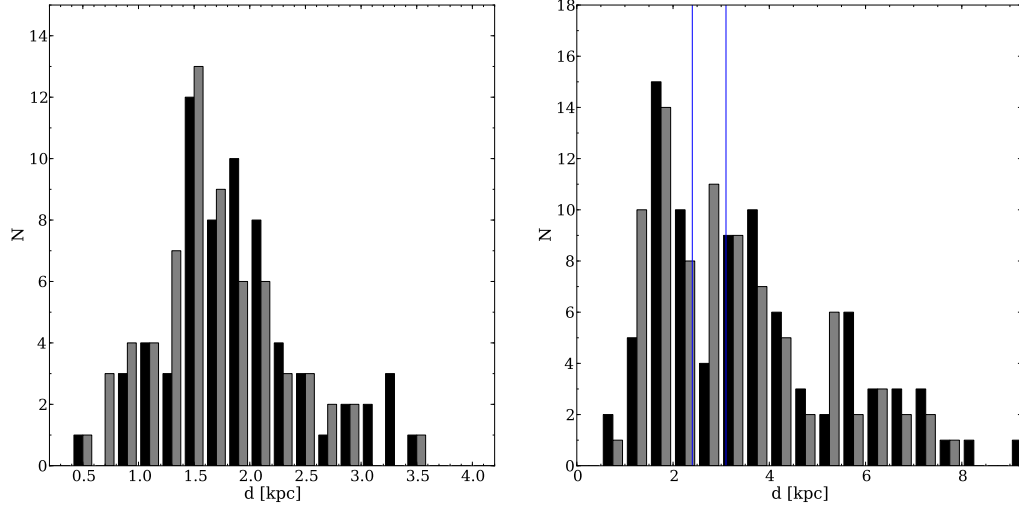
Figure 7.10: Distribution of the distance to the subdwarf-companion star systems as calculated from the fitting method described in Section 7.5 when applied to the *C2MS* (left) and *SU* samples (right). The grey and black histograms show the system parameters when calculated with and without the reddening correction, respectively. Adjoining pairs of histogram show the number of objects in the same bin. Objects that are known to be contaminants have been removed. Only 66 of the 93 objects in the *C2MS* sample are shown in the histogram (left).The remaining 27 are contaminants (from their SIMBAD classification or their SDSS spectra), or the subdwarf–companion model provides a bad fit ("Q" $\geq$ 3 in Table B.2 or B.3), have been removed. In the *SU* histogram, 84 objects are included, where 50 have been removed (= 134, see Table 7.3). The distances are given in kpc and the bin sizes are 0.2 and 0.5 kpc for the *C2MS* and *SU* samples, respectively. The vertical lines in the right hand plot show the region where the volume limited sample is defined (2.4 to 3.1 kpc).

Green et al. [2006, Figure 1]. To establish a volume–limited sample, we again refer to Table 7.8 where we contrast the impact of the 2MASS versus UKIDSS K-band limits. The distances sampled are significantly larger, though as before dependent on subdwarf and companion temperature. Overall, the SU sample should be less biased against finding lower temperature subdwarfs compared to the $C2MS$ sample (see the second example given in Section 7.6.9.2; a $15,000$ K subdwarf with a M0-type companion would now be detected to 8.5 kpc). This does not appear to have increased the numbers of low temperature subdwarfs found and thus it appears that their absence is not due to our sample biases, but represents an intrinsic deficit of cool subdwarfs within the subdwarf population. Accounting for reddening (as seen in the grey histogram) does not have a large effect, although it shifts the calculated subdwarf effective temperatures systematically higher by $1,000 - 2,000$ K.

Comparing the distribution of companion effective temperatures to the $C2MS$ sample, the SU sample has a larger number of objects with early M-type companions. Hence, the SU sample overcomes the main limitation found within the $C2MS$ sample, the shallow K_s-band data. The increased depth of UKIDSS allows us to probe significantly more systems with M-type companions, however we still see a deficit compared with K-type companions and earlier. This also seems obvious from the lack of systems populating the subdwarf plus M-type companion region of the colour-colour diagram in Figure 7.1. Selecting subdwarfs with companions later than $\sim$M5-type is still limited by the colour selection method as discussed previously (Section 7.3.2). Probing deeper in the K-band does not help for companion types later than $\sim$M5. Accounting for reddening has a complementary effect to that on effective temperature. As the subdwarfs become hotter, the required companion also shifts to higher temperatures.

We searched for a correlation between subdwarf and companion effective temperatures, but none was found at a level above the parameter uncertainties. Better statistics, from larger samples, are needed to investigate the subtleties of the population. From the population synthesis models of Han et al. [2003], one might expect to see F-type companions primarily associated with low ($T_{eff} \lesssim 20,000$ K) temperature subdwarfs (see Section 7.7).

Overall, when considering confirmed subdwarf systems, we believe that the fitting method is producing temperatures accurate to within a few thousand Kelvin and companion temperatures to within several hundred Kelvin (a few spectral types). There is some disagreement between individual fit results when compared with the literature. However, our principal goal is not to achieve superior parameters for individual systems. Indeed, more data are required to accurately establish

163
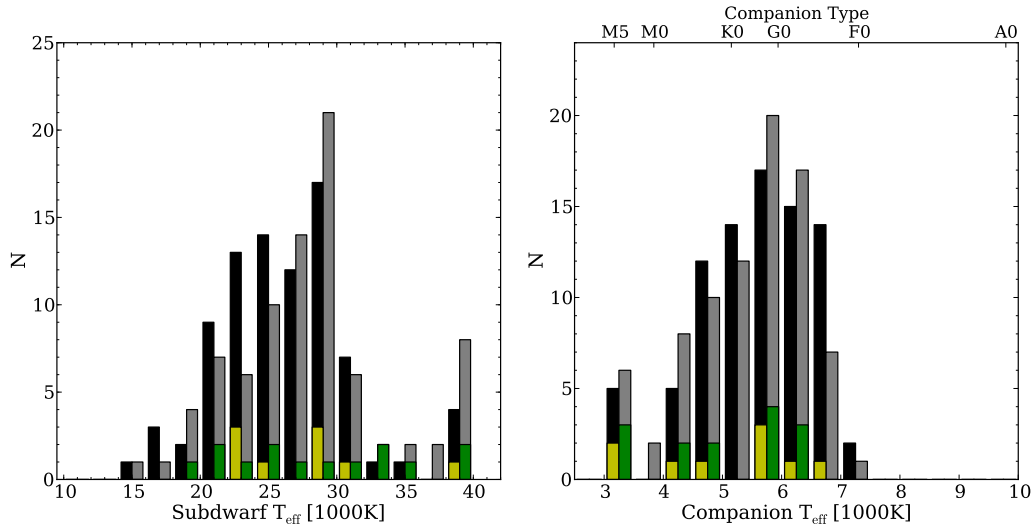
Figure 7.11: Distributions of the subdwarf (left) and companion (right) effective temperatures calculated from the fitting method described in Section 7.5 when applied to the *SU* sample. The grey and black histograms show the system parameters when calculated with and without the reddening correction, respectively. Adjoining pairs of histogram bars show the number of objects in the same bin. A total of 84 objects are included in the histograms, where 50 objects that are known to be contaminants (from their SIMBAD classification or their SDSS spectra), or the subdwarf–companion model provides a bad fit ("Q"≥ 3 in Table B.2), have been removed. Similarly, the green and yellow histograms shows distributions (with and without reddening corrections) when the distances to the objects are limited to be between 2.4 and 3.1kpc, such that the histogram is a volume limited sample. 11 and 16 objects are included in the histograms, respectively. The subdwarf effective temperature histogram is grouped in bins of $2,000 \, \mathrm{K}$ and the companion star histogram uses bins of $500 \, \mathrm{K}$.

parameters for individual systems. Our method does appear to be efficient in finding composite subdwarf binaries, while our SED fitting is accurate enough to allow us to consider the broad statistical parameter distributions within our samples. There will be some influence from contaminants. However, the fraction of contaminants is relatively small (Table 7.3), and wherever possible they have been removed from the distributions.

7.6.11   A volume-limited sample

The advantage of using the *SU* sample is that significantly larger distances are probed. Referring to Table 7.8, the sample is complete for F0 to M0-type companions over distances of 2.4 to 3.1kpc. Although we can therefore construct a volume limited

164

sample in this region, only 14 objects with good quality fits to the SED fall within this region (Figure 7.11). It is impossible to draw meaningful conclusions about parameter distributions for such a small sample.

Following the assumptions described in Section 7.6.9.3, and thus assuming the distribution seen in Figure 7.11 is representative of the true distance distribution, the peak at 2 ± 1kpc in our distance distribution may then be associated with representing the spatial distribution of the bulk of the subdwarf binaries. Then, assuming the distribution follows a simple disk population of the form $r^2 \exp(-r/H)$, where r is the distance from the center of the disk and H is the scale height, the turning point in a distance histogram should represent $2H$. Therefore, the scale height of the subdwarf population in the SU sample is 1 ± 0.5kpc.

A $1/V_{\mathrm{max}}$ technique [Schmidt, 1968] may also be employed here, similar to that used in Rowell & Hambly [2011] to constrain the white dwarf luminosity function, but here to use the entire subdwarf plus companion sample to constrain the scale height.

7.7 Discussion

Existing samples of subdwarfs have shown that a substantial fraction of them reside in binaries. Han et al. [2003] used population synthesis models to calculate that the intrinsic binary fraction should be $76 - 89$ per cent. Our samples explicitly target composite systems and thus should be dominated by subdwarfs with bound binary companions. Heber [2009] states that the vast majority of subdwarfs have a temperature between $20,000 - 40,000$ K. The temperature distribution found here appears approximately consistent with this range, however we do find a sub-sample of cooler subdwarfs with temperatures below $20,000$ K. In the SU sample, where sample biases against cooler subdwarfs are smallest, they make up $\sim 5 - 10$ per cent. This is true whether or not we account for the full Schlegel et al. [1998] reddening value, and thus cannot be an artifact due to reddening. Fitting of the ultraviolet part of the SED is especially important for calculating a reliable subdwarf effective temperature, because this is the region where the subdwarf dominates.

Utilising the SED from the ultraviolet down to the infrared, we have a large range over which both the subdwarf and the companion can dominate a region of the spectrum. We show that both samples here are sensitive to companions of spectral type A5 to M5 for $20,000$ to $35,000$ K subdwarf effective temperatures and F0 to K0-type if $15,000$ and $40,000$ K subdwarfs are included. These ranges can be seen in Figure 7.2. Many subdwarfs are found to indeed have companions in this regime.

165

In the *C2MS* sample (Figure 7.9), the distribution of companion type is seen to be a broad peak from F-type companions to $\sim$ K0. A significant turnover is then seen towards late K and M-type companions. This turnover can be explained, for the *C2MS* sample, because we are only sensitive to these systems over a very small distance range. However, the *SU* sample extends several magnitudes deeper in the K-band and therefore removes this bias, but still shows a clear deficit of early M-type companions. This is contrary to the relative abundance of late type companions found in many previous surveys. If the M-type companions were only paired with cool subdwarfs, they would not have been selected by the colour cuts, but this is not consistent with the results of the radial velocity studies. It therefore appears that subdwarfs with F, G and K-type main–sequence companions are intrinsically much more common than those with lower mass M-type main–sequence companions, for a broad range of subdwarf temperatures (subject to the colour selections described in Section 7.3.2).

The population synthesis models of Han et al. [2003] predict that a significant fraction of subdwarfs will form through a channel involving stable Roche lobe overflow. These are expected to be $\sim$ 20,000 K subdwarfs with $\sim$F0 or K0-type companions close to the main sequence [see Figure 15 & 19 of Han et al., 2003]. It is believed that these have not been found previously because of the "GK selection effect" [Han et al., 2003], where subdwarfs with F, G and K-type companions were not targeted by the PG survey because they would show composite spectra (features such as the Ca II K line and the G-band). However, Wade et al. [2006] and Wade et al. [2009] find that only $\sim$ 3 per cent of the rejected PG stars show indications of being a subdwarf with a companion. The majority are (single) metal-poor F stars. Here we are primarily selecting subdwarfs with F to K-type companions and therefore we would be sensitive to this peak. We do indeed find a significant fraction of subdwarfs with effective temperatures around 20,000 K and some objects below 20,000 K. We do not see the RLOF systems dominate quite as strongly as they do in Han et al. [2003]. However, too many cool subdwarfs are found here to be appropriate for creation solely through the first common envelope ejection channel (peaking at $\sim$ 30,000 K) and thus the RLOF channel appears to be a significant contributor.

Part of the Lisker et al. [2005] SPY survey sample looked at objects with composite spectra. They do not find a clear contribution from cool subdwarfs. The SPY survey does, however, suffer from strong pre-selection biases. The majority of targets were selected from the Hamburg/ESO survey [Friedrich et al., 2000] and required not to show evidence of a companion in the low resolution prism spec-

troscopy. The companion types that we are finding in this study also appear to broadly match the predictions of Han et al. [2003]. The first stable RLOF channel is very efficient at producing F to K-type companions. Between F and K-type companions, Han et al. [2003] predict ∼F0-type companions to be the most prevalent (by a factor of ∼ 3), followed by very few ∼G0-type companions, and then two smaller peaks of approximately equal amplitude at ∼ K0 and ∼M0-type [see Figure 15 of Han et al., 2003]. Our distribution does not show the feature at F0, but we may not be sensitive enough to F0-type companions, especially in composite systems with low temperature subdwarfs. Our colour cuts only select $15,000\,$K subdwarfs with F0 or later type companions and therefore we may not show the main peak at ∼F0-type (right hand panels of Figures 7.9 and 7.11), if it is indeed there. Equally, most of the K-type companions to subdwarfs predicted by Han et al. [2003] are evolved and luminous. Therefore they would not be selected in our colour cuts because the luminosity of the companion would dominate the subdwarf. If any of these objects are selected, they will be fitted photometrically as a much hotter companion than K-type, therefore enhancing the F0-type peak or broadening it. Thus we should not detect the peak at K0.

In a simulation, we took a theoretical sample of subdwarfs with companions that matched the distributions from Han et al. [2003] and used the surface gravities discussed in Section 7.5. We then applied the magnitude and colour cuts relevant for the *C2MS* and *SU* samples. The objects which satisfy these criteria do show a similar distribution in effective temperature and companion type to that seen in the real samples, again suggesting that our observed samples are in broad agreement with the model populations of Han et al. [2003].

More recently, Clausen et al. [2012] present independent population synthesis calculations of subdwarfs. In their Figure 13, the distribution of companion effective temperature is shown using a variety of input model parameters. Run 6 is the most comparable to the distribution from Han et al. [2003] in terms of input parameters. In this run, and the majority of others, Clausen et al. [2012] predict a vast majority of M-type or later companions to the subdwarfs. This does not agree with our samples, which show a lack of M-type companions and a significant proportion of K-types. This suggests that observational samples such as those presented here have the ability to directly constrain binary population synthesis models.

The scale height of subdwarfs is rarely discussed. We used the two samples here to estimate the scale height at 1 ± 0.5kpc from the peak in their distance distributions near 2 ± 1kpc (Figure 7.10). However, to do so we must assume that the each subdwarf plus companion system (independent of system parameters) is

drawn from the same parent distance distribution, and we pick each of these with the same frequency. If the scale height is $\sim$ 1kpc, it is therefore most consistent with the Galactic thick disk scale height [e.g. 0.75 ± 0.07kpc, de Jong et al., 2010]. If the subdwarf population was associated with the thin disk, a smaller scale height of 0.3 kpc would be expected [Jurić et al., 2008], while a rise towards 25 kpc would have indicated a halo population [de Jong et al., 2010]. More accurate modelling of individual subdwarfs together with a larger volume limited sample is required to study the distribution and reliably quantify the scale height of the subdwarf population. Our methods are well suited to offer such large samples as ongoing and near-future surveys cover an increasing part of the sky.

Chapter 8

PG 1258+593 and its common proper motion magnetic white dwarf counterpart

The formation mechanism for magnetic white dwarfs is, to this day, strongly debated. The two favoured scenarios (discussed in more detail in Section 1.2.4) are, firstly, that magnetic white dwarfs are the remnants of magnetic Ap and Bp stars [Moss, 1989], and secondly, that the magnetic fields are generated by binary interactions in the common envelope phase of evolution [Tout & Pringle, 1992]. In the latter case, the two components of the binary would either merge into a single white dwarf, or become a short period magnetic white dwarf plus low-mass star binary that would rapidly evolve into a magnetic-cataclysmic variable. A set of magnetic white dwarfs in wide common proper motion pairs would place valuable constraints on the feasibility of the hypotheses because these would not have experienced common envelope evolution, unless the system was originally a (unlikely) triple system. Here, we report the discovery of one such system; the magnetic white dwarf, SDSS J1300+5904, and the DA white dwarf, PG 1258+593.

8.1 Selection

We devised a method to select white dwarf common proper motion pairs from the SDSS DR7 (described in Section 2.2.2) using colour-colour diagrams and the SDSS proper motion tables. To select white dwarfs from the millions of objects in the SDSS, we designed some broad colour-colour cuts around the white dwarf "banana", as shown in Table 8.1 and Figure 8.1.

Table 8.1: Colour-colour cuts to select a broad region around the white dwarf "banana" in SDSS $ugriz$ colour-colour space (see Figure 8.1). Proper motion, $\mu\,! = 0$ ensures all objects have a calculated proper motion in the SDSS database. "bad_flags" is defined as saturated, bright, edge or nodeblend and "nChild" is the number of children objects detected by SDSS.

Constraint		
$(u-g)$	$\leq$	$3.917 \times (g-r) + 2.344$
$(u-g)$	$\leq$	$0.098 \times (g-r) + 0.825$
$(u-g)$	$\geq$	$1.299 \times (g-r) - 0.079$
$(g-r)$	$\leq$	0.450
$(g-r)$	$\geq$	$2.191 \times (r-i) - 0.638$
$(r-i)$	$\leq$	$-0.560 \times (i-z) + 0.282$
g	$\leq$	19
μ	$! =$	0
flags & bad_flags	$=$	0
nChild	$=$	0
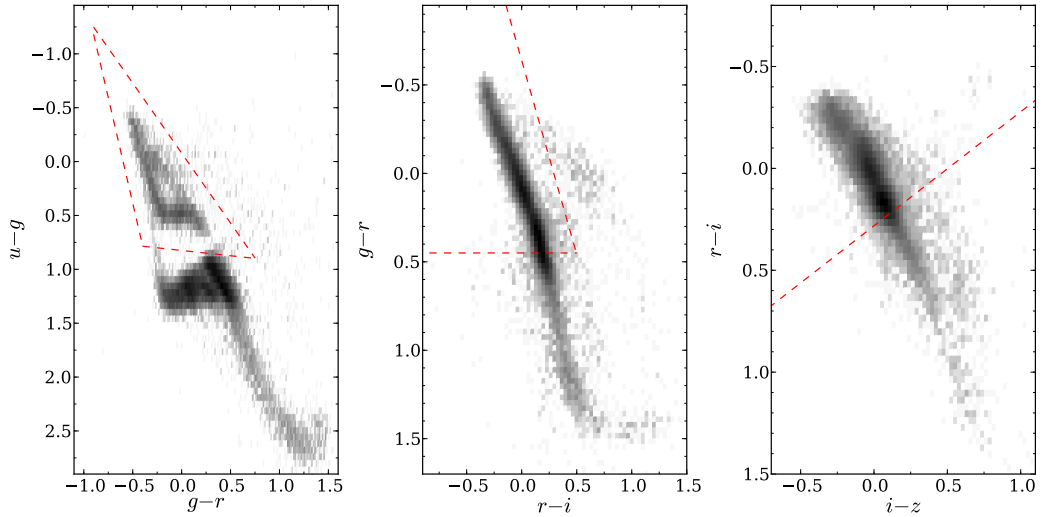
Figure 8.1: Colour-colour cuts to select a broad region around the white dwarf "banana" (red dashed line; see Table 8.1) in SDSS $ugriz$ colour-colour space. The underlying density map shows a random selection of stellar objects from SDSS DR7.

170

Applying the cuts in Table 8.1 to the SDSS DR7 "SpecPhoto" and "PhotoObj" tables [using the CasJobs SQL interface; Li & Thakar, 2008] returns 26836 spectroscopic and 59513 photometric-only objects, respectively. The broad colour-cuts select all types of ($T_{eff} \gtrsim 8,000\,K$) white dwarf, as opposed to just DA white dwarfs as in Chapter 4. The cuts will suffer a significant level of contamination from main-sequence stars and quasars, however, both will have relatively small proper motions and therefore will be excluded by our proper motion constraints.

Using the SDSS proper motion table, we carried out a search for white dwarf pairs with a separation $2'' \leq r \leq 60''$, both having the magnitude of the proper motion (μ) being at least $15\,mas/yr$ and 3σ significance. We require a minimum proper motion as well as a significance to remove any spurious matches from, for example, quasars with significant proper motions (see Section 5.2.3.4). The two sets of proper motion are also required to match within;

$$|\mu_{\alpha_1} - \mu_{\alpha_2}| \leq \kappa \times \sqrt{(\sigma_{\mu_{\alpha_1}}{}^2 + \sigma_{\mu_{\alpha_2}}{}^2)} \tag{8.1}$$

$$|\mu_{\cos\delta_1} - \mu_{\cos\delta_2}| \leq \kappa \times \sqrt{(\sigma_{\mu_{\cos\delta_1}}{}^2 + \sigma_{\mu_{\cos\delta_2}}{}^2)} \tag{8.2}$$

where the subscripts 1 and 2 refer to the primary and secondary object, respectively, α and δ refer to the right ascension and declination aspects of the μ, respectively, and $\kappa = 2.0$. This limits the two components of proper motion to match within 2σ. We used 2σ to limit the number of candidates for follow-up observations to a reasonable amount. This resulted in a total of 37 pairs (listed in Table 8.2). Follow up spectroscopy was obtained for a number of objects, and below we discuss one such pair in detail; PG 1258+593 and SDSS J1300+5904.

Table 8.2: Table of CPM white dwarf pairs.

Name	R.A._1	Dec_1	R.A._2	Dec_2	r [as]	$PM_{R.A.1}$ [mas/yr]	PM_{Dec1} [mas/yr]	$PM_{R.A.2}$ [mas/yr]	PM_{Dec2} [mas/yr]
0002 + 0733	00:02:15.34	+07:33:59.2	00:02:16.14	+07:33:49.9	15.1	−104 ± 3	−65 ± 3	−105 ± 3	−64 ± 3
0023 + 0643	00:23:35.57	+06:43:25.5	00:23:36.25	+06:43:20.6	11.3	112 ± 9	−44 ± 9	99 ± 3	−43 ± 3
0144 − 1852	01:44:40.42	−18:52:57.6	01:44:39.63	−18:52:57.3	11.1	19 ± 2	−11 ± 2	15 ± 2	−13 ± 2
0332 − 0049	03:32:36.60	−00:49:18.4	03:32:36.86	−00:49:36.9	18.9	−25 ± 5	−24 ± 5	−31 ± 4	−23 ± 4
0344 + 1509	03:44:11.49	+15:09:45.6	03:44:10.91	+15:10:22.1	37.5	24 ± 3	−42 ± 3	22 ± 3	−38 ± 3
0344 + 1510	03:44:10.91	+15:10:22.1	03:44:11.49	+15:09:45.6	37.5	22 ± 3	−38 ± 3	24 ± 3	−42 ± 3
0405 + 8147	04:05:53.42	+81:47:36.0	04:05:54.99	+81:47:51.1	15.5	10 ± 3	−31 ± 3	11 ± 3	−28 ± 3
1019 + 1216	10:19:55.91	+12:16:31.5	10:19:54.61	+12:17:18.0	50.2	−24 ± 2	−18 ± 2	−27 ± 2	−24 ± 2
1019 + 1217	10:19:54.61	+12:17:18.0	10:19:55.91	+12:16:31.5	50.2	−27 ± 2	−24 ± 2	−24 ± 2	−18 ± 2
1054 + 5307	10:54:49.09	+53:07:15.3	10:54:49.87	+53:07:59.2	44.5	−113 ± 3	−36 ± 3	−114 ± 3	−38 ± 3
1107 + 5246	11:07:49.56	+52:46:51.0	11:07:51.05	+52:46:53.1	13.7	−16 ± 3	6 ± 3	−18 ± 3	7 ± 3
1110 + 4517	11:10:16.69	+45:17:36.4	11:10:20.99	+45:18:01.7	51.9	25 ± 3	−47 ± 3	27 ± 4	−45 ± 4
1110 + 4518	11:10:20.99	+45:18:01.7	11:10:16.69	+45:17:36.4	51.9	27 ± 4	−45 ± 4	25 ± 3	−47 ± 3
1113 + 0032	11:13:06.26	+00:32:43.7	11:13:06.07	+00:32:43.2	2.9	−366 ± 3	−89 ± 3	−362 ± 2	−85 ± 2
1255 + 4101	12:55:36.76	+41:01:52.6	12:55:40.38	+41:02:06.9	43.3	−11 ± 3	−19 ± 3	−7 ± 3	−15 ± 3
1255 + 4102	12:55:40.38	+41:02:06.9	12:55:36.76	+41:01:52.6	43.3	−7 ± 3	−15 ± 3	−11 ± 3	−19 ± 3
1300 + 5904	13:00:33.46	+59:04:06.9	13:00:35.21	+59:04:15.7	16.0	42 ± 3	74 ± 3	42 ± 3	75 ± 3
1309 + 5503	13:09:54.23	+55:03:39.1	13:09:55.74	+55:03:38.4	13.0	53 ± 3	−29 ± 3	52 ± 3	−31 ± 3
1313 + 2030	13:13:32.57	+20:30:39.4	13:13:32.15	+20:30:39.6	5.9	−32 ± 5	25 ± 5	−38 ± 4	35 ± 4
1314 + 1732	13:14:26.37	+17:32:28.1	13:14:26.82	+17:32:09.2	20.0	−41 ± 3	−58 ± 3	−40 ± 2	−58 ± 2
1346 + 4900	13:46:43.33	+49:00:52.3	13:46:45.37	+49:00:13.5	43.8	−17 ± 3	−14 ± 3	−9 ± 3	−22 ± 3
1412 + 4216	14:12:07.58	+42:16:27.2	14:12:08.78	+42:16:24.7	13.6	−82 ± 3	−61 ± 3	−80 ± 3	−57 ± 3
1419 + 0326	14:19:59.79	+03:26:13.1	14:20:03.56	+03:26:05.4	56.9	−17 ± 3	8 ± 3	−17 ± 3	2 ± 3
1420 + 0326	14:20:03.56	+03:26:05.4	14:19:59.79	+03:26:13.1	56.9	−17 ± 3	2 ± 3	−17 ± 3	8 ± 3
1435 + 1440	14:35:45.88	+14:40:10.7	14:35:45.88	+14:41:02.7	53.1	−3 ± 3	−17 ± 3	1 ± 3	−18 ± 3
1435 + 1441	14:35:45.15	+14:41:02.7	14:35:45.15	+14:40:10.7	53.1	1 ± 3	−18 ± 3	−3 ± 3	−17 ± 3

Table 8.2:

Name	R.A.$_1$	Dec$_1$	R.A.$_2$	Dec$_2$	r [as]	PM$_{R.A.1}$ [mas/yr]	PM$_{Dec1}$ [mas/yr]	PM$_{R.A.2}$ [mas/yr]	PM$_{Dec2}$ [mas/yr]
1440 + 2443	14:40:11.67	+24:43:09.4	14:40:12.67	+24:43:14.1	14.4	−16 ± 3	−19 ± 3	−22 ± 2	−12 ± 2
1703 + 3304	17:03:55.91	+33:04:38.4	17:03:56.78	+33:04:35.8	11.2	−2 ± 3	−51 ± 3	0 ± 3	−51 ± 3
1729 + 2915	17:29:29.63	+29:15:54.5	17:29:29.25	+29:16:09.5	15.8	−150 ± 3	−199 ± 3	−150 ± 14	−197 ± 14
1729 + 2916	17:29:29.25	+29:16:09.5	17:29:29.63	+29:15:54.5	15.8	−150 ± 14	−197 ± 14	−150 ± 3	−199 ± 3
2047 + 0021	20:47:11.40	+00:21:27.6	20:47:13.68	+00:22:03.8	49.8	−6 ± 3	−101 ± 3	−8 ± 3	−95 ± 3
2047 + 0022	20:47:13.68	+00:22:03.8	20:47:11.40	+00:21:27.6	49.8	−8 ± 3	−95 ± 3	−6 ± 3	−101 ± 3
2115 − 0741	21:15:07.42	−07:41:34.5	21:15:07.39	−07:41:51.6	17.0	−30 ± 3	−118 ± 3	−25 ± 3	−117 ± 3
2242 + 1250	22:42:31.14	+12:50:04.9	22:42:30.33	+12:50:02.4	12.1	−33 ± 3	−76 ± 3	−34 ± 3	−73 ± 3
2259 + 1404	22:59:32.21	+14:04:39.3	22:59:32.74	+14:04:44.2	9.1	29 ± 3	−16 ± 3	28 ± 3	−14 ± 3
2302 + 2430	23:02:49.38	+24:30:27.9	23:02:50.37	+24:30:13.4	19.9	−48 ± 3	−125 ± 3	−51 ± 3	−124 ± 3

Table 8.3: Coordinates, proper motions, and PSF magnitudes of the two white dwarfs extracted from SDSS DR7.

Object	PG 1258+593	SDSS J1300+5904
R.A. (2000)	13 00 35.20	13 00 33.46
Dec (2000)	+59 04 15.6	+59 04 06.9
PM R.A. [mas yr^{-1}]	42.4 ± 2.6	41.8 ± 3.0
PM Dec [mas yr^{-1}]	75.0 ± 2.6	73.9 ± 3.0
u	15.54 ± 0.01	19.08 ± 0.03
g	15.20 ± 0.04	18.23 ± 0.04
r	15.52 ± 0.02	17.93 ± 0.02
i	15.76 ± 0.04	17.80 ± 0.04
z	16.04 ± 0.02	17.79 ± 0.03

8.2 Observations

One of the objects returned by our query was the faint blueish SDSS J1300+5904, which turned out to be a CPM companion to PG 1258+593[1]. The angular separation between the two objects is $16.1 \pm 0.1''$ (Fig. 8.2) and, at a distance of 68 ± 3 pc (see Sect. 8.3), the minimum binary separation is 1091 ± 7 AU. Coordinates, proper motions, and $ugriz$ point-spread function (PSF) magnitudes of both white dwarfs are given in Table 8.3.

SDSS J1300+5904 had already been noted as a CPM companion by Farihi et al. [2005], however it was classified as a white dwarf with a featurless (DC) spectrum, based on a relatively poor quality spectrum. Inspecting the SDSS fibre spectrum, however, unambiguously identifies it as a magnetic (DAH) white dwarf given the clear detection of a Zeeman-triplet in Hα (Fig. 8.5). SDSS J1300+5904 was targeted for SDSS spectroscopy as a white dwarf candidate; no SDSS spectrum was obtained for PG 1258+593.

All observations in this Chapter were conducted and reduced by Dr E. Breedt. We observed PG 1258+593 on February 13, 1997, using the Intermediate Dispersion Spectrograph (IDS) on the Isaac Newton Telescope (INT). Two spectra of 20 min exposure time each were obtained with the R632V grating and a 1.5″ slit, covering the wavelength range 3680–5300 Å at a spectral resolution of ~ 2.3 Å. The data were reduced and calibrated as described by Moran et al. [1999], and the normalised line profiles are shown in Fig. 8.3.

[1]Initially identified as white dwarf candidate GD 322 by Giclas et al. [1967]
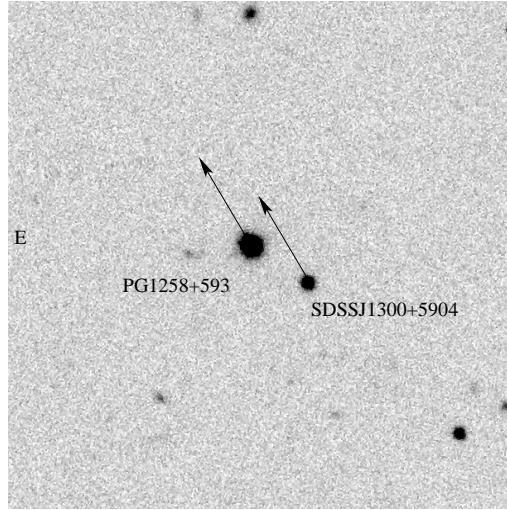
Figure 8.2: $2' \times 2'$ r band SDSS image of the white dwarf CPM pair. Proper motions are indicated over 300 years. An SDSS fibre spectrum was obtained for the fainter component of the binary.

8.3   White dwarf parameters

We analysed the INT/IDS spectrum of PG 1258+593 using the DA model spectra and the fitting routine described in Sections 3.4.1 and 3.4.5.1, respectively. The best fit is achieved for $T_{\mathrm{eff}} = 14790 \pm 77\,\mathrm{K}$ and $\log(g) = 7.87 \pm 0.02$. Adopting these atmospheric parameters, we use an updated version of Bergeron et al.'s [1995] tables[2] to calculate the corresponding white dwarf mass, $0.54 \pm 0.01\,\mathrm{M_\odot}$, radius, $(9.85 \pm 0.10) \times 10^8\,\mathrm{cm}$, and a cooling age of $(1.8 \pm 0.07) \times 10^8\,\mathrm{yr}$. Finally, we calculate $M_g = 11.03 \pm 0.1$, corresponding to a distance of $68 \pm 3\,\mathrm{pc}$ (Table 8.4). The best fit is shown in Fig. 8.3. The $u - g$ vs $g - r$ colours of PG 1258+593 are broadly consistent with the results of the spectroscopic analysis (Fig. 8.4). Our atmospheric and stellar parameters for PG 1258+593 are in excellent agreement with those published by Liebert et al. [2005a] as part of their systematic analysis of the DA white dwarfs from the Palomar Green Survey. They quote $T_{\mathrm{eff}} = 14480 \pm 229\,\mathrm{K}$, $\log(g) = 7.87 \pm 0.05$, and $M_{\mathrm{wd}} = 0.54 \pm 0.02\,\mathrm{M_\odot}$.

Given the magnetic nature of SDSS J1300+5904, establishing its atmospheric parameters is not straight-forward, and we analysed the SDSS photometry and spectroscopy with both non-magnetic and magnetic model spectra (conducted by

---

[2]http://www.astro.umontreal.ca/~bergeron/CoolingModels/

B. Külebi and Dr S. Jordan).

Figure 8.4 shows the location of SDSS J1300+5904 in the $u - g$ vs $g - r$ colour plane, which, while being somewhat displaced from the cooling tracks of non-magnetic DA white dwarfs, clearly suggest a low temperature. As a first step, we performed a least χ^2 fit to the SDSS $ugriz$ magnitudes using model DA colours from Koester et al. [2005a], which results in a temperature estimate of 6000 K. As expected from the morphology of the DA cooling tracks (Fig. 8.4), at such low temperatures, the colours provide very little information on $\log(g)$. Taking the SDSS observations at face value, the u-band flux from the SDSS imaging appears somewhat too low compared to the flux level of the SDSS fibre spectrum (Fig. 8.5). Such offsets between the SDSS spectroscopy and photometry are found in a number of objects, and are in most cases strongest in the u-band. The discrepancy seen in SDSS J1300+5904 is consistent with the location of SDSS J1300+5904 in the $u - g$ vs $g - r$ colour plane (Fig. 8.4), where the $u - g$ colour of the object is too red with respect to the DA cooling tracks. A reduced u band flux with respect to the extrapolation of the spectrum could otherwise be caused by a large Balmer jump, contrary to that expected for a ~ 6000 K DA white dwarf. In reality, magnetic splitting probably leads to a shallower Balmer jump than in the non-magnetic case. Photometric variability due to rotation, such as observed e.g. in the magnetic white dwarf GD 356 [Brinkworth et al., 2004], also cannot be ruled out, and further study is warranted.

In a second step, we made use of the known distance, $d = 68 \pm 3$ pc. For a given choice of T_{eff}, we vary $\log g$ to match the observed SDSS magnitudes, and the best-fit $\log g$ then provides M_{wd} and R_{wd} by adopting a white dwarf mass-radius relation [Fontaine et al., 2001]. In the light of the flux discrepancy in the u-band discussed above, we restrict the fit to the $griz$ magnitudes, and find $T_{\text{eff}} = 6300 \pm 300$ K, $\log g = 7.93 \pm 0.13$, corresponding to a white dwarf mass $M_{\text{wd}} = 0.54 \pm 0.06 \, M_{\odot}$, radius $R_{\text{wd}} = (9.33 \pm 0.64) \times 10^8$ cm, and cooling age of $1.7^{+0.4}_{-0.2} \times 10^9$ yr.

PG 1258+593 is detected by GALEX [Martin et al., 2005] at $m_{\text{fuv}} = 15.30 \pm 0.02$ and $m_{\text{nuv}} = 15.33 \pm 0.01$. Adopting T_{eff} and $\log(g)$ from Table 8.4, and $d = 68 \pm 3$ pc from above, we folded a DA model spectrum from [Koester et al., 2005a] through the GALEX far and near-ultraviolet response curves, obtaining $m_{\text{fuv}} = 15.37$ and $m_{\text{nuv}} = 15.30$, in excellent agreement with the GALEX measurement when taking into account the low, but non-zero amount of reddening along the line of sight and the systematic uncertainties in the GALEX calibration. In contrast, SDSS J1300+5904 is not detected by GALEX. For an assumed distance of 68 pc, the limiting magnitude of GALEX, $m_{\text{nuv}} = 20.5$, implies upper limits for T_{eff} between
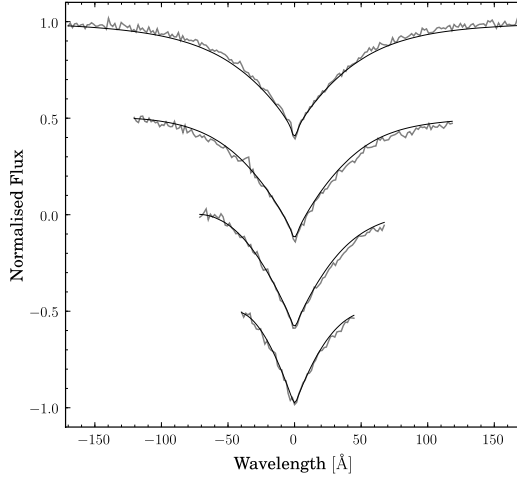
Figure 8.3: Normalised INT/IDS Hβ–Hϵ (top to bottom) line profiles of PG 1258+593 (gray line) and the best-fit model (black line) for $T_{\mathrm{eff}} = 14790\,\mathrm{K}$ and $\log g = 7.87 \pm 0.02$.

6350 and 6650 K for a mass range from 0.47 to 0.63 $M_\odot$, which is consistent with the results we obtained from fitting the *griz* magnitudes for the same distance.

We also fitted non-magnetic DA model spectra to the observed spectrum of SDSS J1300+5904. This results in $T_{\mathrm{eff}} \simeq 6500\,\mathrm{K}$, which corroborates the low temperature suggested by the photometry, but can obviously not properly account for the observed Balmer line profiles (Fig. 8.5).

Finally, fixing the distance to $68 \pm 3\,\mathrm{pc}$, and $\log g = 7.93$, we analysed the spectrum of SDSS J1300+5904 with magnetic white dwarf models, using a simplified version of the code explained in Euchner et al. [2002] and following the procedure outlined in Külebi et al. [2009] to fit for a centred magnetic dipole. Due to the lack of a consistent theory that describes Stark broadening in the presence of magnetic fields in this regime [e.g. Jordan, 1992] the computed line profiles are subject to systematic uncertainties. Hence discrepancies between the apparent strengths of the Balmer lines and the slope of the continuum are observed [see Achilleos et al., 1991]. We have used the approach of Gänsicke et al. [2002] and used two different methods to asses the effective temperature: Fitting only the Balmer lines (6000 K) and fitting the continuum slope (6800 K). In the case where only Balmer lines are fitted the slope of the model spectrum is normalized with respect to the observed one. The Zeeman splitting observed in Hα implies a magnetic field strength of $\simeq 6\,\mathrm{MG}$ and suggests an intermediate inclination between the line-of-sight and the

177

Table 8.4: Atmospheric and stellar parameters for PG 1258+593 and SDSS J1300+5904.

	PG 1258+593	SDSS J1300+5904
T_{eff}[K]	14790 ± 77	6300 ± 300
$\log(g)$	7.87 ± 0.02	7.93 ± 0.11
M_{wd}[$M_\odot$]	0.54 ± 0.01	0.54 ± 0.06
R_{wd}[10^8 cm]	9.85 ± 0.10	9.33 ± 0.64
Cooling age [10^8 yr]	1.8 ± 0.07	18.5 ± 0.5
B_{wd}[MG]	≤ 0.3	$\simeq 6$

magnetic axis. Figure 8.5 shows a magnetic model spectrum for a centered dipole with polar strength of 6 MG with an inclination of ~ 45 degrees as an example of a satisfying fit.

8.4 Stellar evolution of the CPM pair

Within the errors, both white dwarfs in this CPM pair have equal masses, similar or slightly below the mean mass of DA white dwarfs, $0.593 \pm 0.016 M_\odot$ [e.g. Koester et al., 1979; Finley et al., 1997; Liebert et al., 2005a; Kepler et al., 2007], but their different effective temperatures result in an age difference of 1.67 ± 0.05 Gyr, implying that their progenitor stars had rather different main-sequence life times.

It is long known that stars undergo different amounts of mass loss depending on their initial mass, and Weidemann [1977] pioneered the investigation of the initial-final mass relation (IFMR) for white dwarfs. The bulk of recent observational work constraining the IFMR has been carried out using white dwarfs in open clusters spanning a range of ages [e.g. Ferrario et al., 2005; Kalirai et al., 2005; Dobbie et al., 2006; Catalán et al., 2008b,a; Kalirai et al., 2008; Rubin et al., 2008; Salaris et al., 2009; Casewell et al., 2009; Dobbie et al., 2009; Williams et al., 2009]. These studies exploit the fact that the age of the cluster population can be determined from the main-sequence turn-off. The measured white dwarf cooling age can then be used to calculate the lifetime of the white dwarf progenitor and thus its initial mass can be estimated.

Clusters, however, are still relatively young, and therefore the low mass stars have not evolved into white dwarfs yet. This means the low mass end of the IFMR, below $\sim 2 M_\odot$, is very poorly constrained, and the progenitors of both PG 1258+593 and SDSS J1300+5904 most likely had initial masses in this range. The question also remains as to whether the IFMR is indeed a one-valued relation, or whether there is a spread.
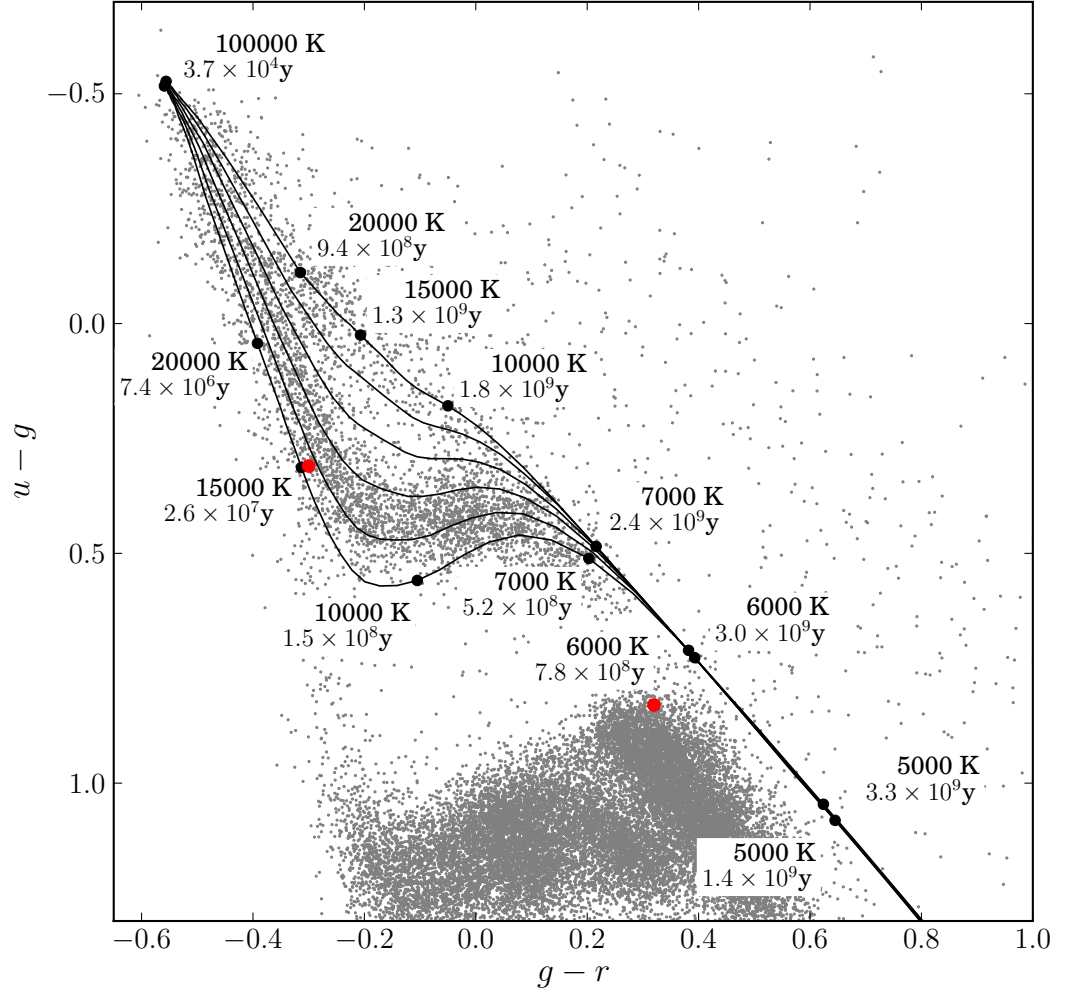
Figure 8.4: SDSS $u - g$ vs $g - r$ colour-colour diagram showing PG 1258+593 (left) and its magnetic CPM companion SDSS J1300+5904 (right) as red circles. Theoretical DA cooling tracks shown as black lines for (from left to right) $\log g = 7 - 9.5$ in steps of 0.5. The black open and black filled circles track $\log g = 9.5$ and $\log g = 7.0$ respectively, with corresponding cooling times.

179
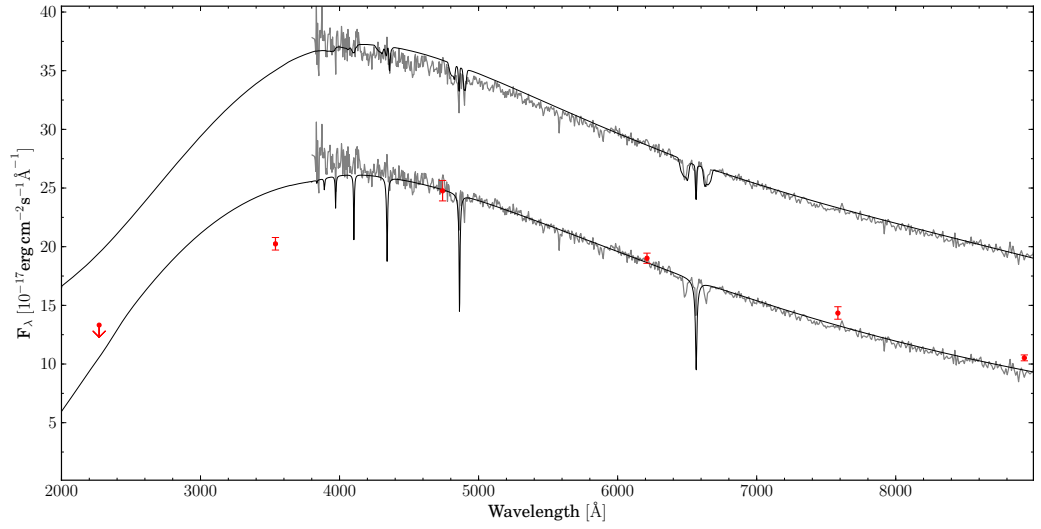
Figure 8.5: The SDSS spectrum of SDSS J1300+5904 along with non-magnetic (bottom curves, $T_{\mathrm{eff}} = 6500\,K$, $\log(g) = 7.93$) and magnetic (top curves, $T_{\mathrm{eff}} = 6000\,K$, $\log g = 7.93$) white dwarf models. The top curves are offset by 10 flux units. The magnetic white dwarf model is calculated for a centered dipole with polar strength of $6\,\mathrm{MG}$ at an inclination against the line-of-sight of 45 degrees. Shown in red are the fluxes corresponding to the SDSS *ugriz* PSF magnitudes of SDSS J1300+5905. The left-most red point indicates the upper limit on the near-ultraviolet flux of SDSS J1300+5905 implied by the non-detection with GALEX.

Wide white dwarf binaries that did not interact during their evolution can in principle provide additional semi-empirical constraints on the IFMR. The cooling ages in such binaries can be determined from standard white dwarf evolution models. The strongest constraints can be expected to come from binaries containing two white dwarfs with unequal properties, such that the cooling ages differ significantly. This method has the advantage that some of the white dwarfs will be of low mass and thus constrain the low mass end of the IFMR. To our knowledge, such an approach to the IFMR was attempted only twice. Greenstein et al. [1983] analysed the Sanduleak-Pesch white dwarf binary (WD 1704+481), but their results were invalidated by the discovery that one of the two white dwarfs is itself an unresolved close white dwarf binary that underwent a common-envelope evolution [Maxted et al., 2000]. Finley & Koester [1997] modelled both components of PG 0922+162, a CPM binary containing two relatively massive white dwarfs, and their results are consistent with the IFMR obtained from open clusters.

Here we make use of the age difference between PG 1258+593 and SDSS-J1300+5904 to provide a semi-emirical upper limit on the progenitor mass of PG-1258+593. We adopt the main-sequence life times as a function of initial mass from the stellar evolution models of Pols et al. [1998]. For any given choice of the progenitor mass of PG 1258+539 (M_i^{PG}), the age difference of $1.67 \pm 0.05 \,\mathrm{Gyr}$ then implies a progenitor mass for SDSS J1300+5904 (M_i^{SDSS}). Figure 8.6 illustrates the relation between M_i^{PG} and M_i^{SDSS} for solar and half-solar metalicity models with and without overshooting. As the main-sequence life time is a very strong function of the initial mass, M_i^{SDSS} levels off very steeply for $1.4 \lesssim M_i^{\mathrm{PG}} \lesssim 1.8 \,\mathrm{M}_\odot$, and in a most conservative interpretation, $M_i^{\mathrm{PG}} < 2.2 \,\mathrm{M}_\odot$. Being more adventurous, one may choose to adopt the most recent IFMR cluster relations [e.g. Casewell et al., 2009; Salaris et al., 2009] to turn the mass of SDSS J1300+5904 into a conservative upper limit of $M_i^{\mathrm{SDSS}} < 3 \,\mathrm{M}_\odot$, and therefore $M_i^{\mathrm{PG}} < 1.8 \,\mathrm{M}_\odot$.

Admittedly, for a single white dwarf binary this proves to be merely consistent with the current IFMR rather than improving it. It may however be in favour of a spread in the IFMR since we find two white dwarfs with similar masses, yet very different ages and thus implying different progenitor masses. If we take current IFMRs, progenitor masses in the range $1 - 1.4 \mathrm{M}_\odot$ would be expected. The mass errors in Table 8.4 represent only the statistical uncertainty in fitting the observed Balmer lines with model spectra. Systematic uncertainties in the models and/or fitting procedure are difficult to assess, but are likely to outweigh the statistical errors. We estimate that the largest current mass difference consistent with the observational data is $\simeq 0.1 \,\mathrm{M}_\odot$, which would move, following the procedure outlined
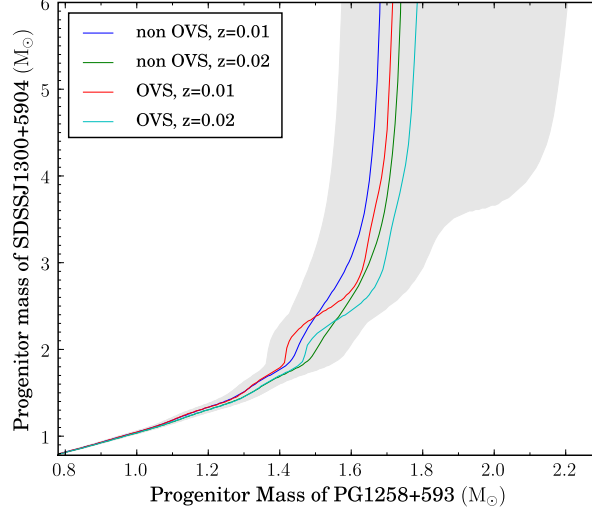
Figure 8.6: The mass of the progenitor star of SDSS J1300+5905 as a function of the mass of the progenitor star of PG 1258+593, given the difference between cooling ages indicate the difference between progenitor lifetimes. Calculations are made for over-shoot (OVS) and non over-shoot models, as well as solar ($z = 0.02$) and half solar ($z = 0.01$) metalicities. Allowing for 1σ errors on cooling times leads to a spread into the grey shaded region.

above, both progenitor stars into a range $\simeq 1 - 1.4\,M_\odot$.

Our study of PG 1258+593 and SDSS J1300+5904 outlines the potential of using white dwarf CPM binaries for constraining the IFMR, bearing in mind that SDSS contains at least a few dozen of such binaries. However, to fully exploit this method, i.e. to reduce the spread seen in the relation shown in Fig 8.6, high-quality follow-up spectroscopy plus broad-band photometry are necessary to deliver accurate T_{eff} and $\log(g)$ measurements.

A final caveat for the white dwarf CPM binary presented in this study is that the magnetic field may have affected the IFMR for SDSS J1300+5904, however, there is currently no evidence for such an effect [Wickramasinghe & Ferrario, 2005; Catalán et al., 2008b].

Table 8.5: Known spatially resolved double degenerate systems with one magnetic component.

	LB 11146	RE J0317-853	SDSS J1300+5904
MWD T_{eff} [K]	16000	33800	6300 ± 300
MWD M_{wd} [$M_\odot$]	0.9	1.32	0.54 ± 0.06
MWD B [MG]	670	340	$\simeq 6$
Companion Type	DA	DA	DA
Companion T_{eff} [K]	14500	16000	14790 ± 77
Companion M_{wd} [$M_\odot$]	0.91 ± 0.07	~ 0.93	0.54 ± 0.01
Separation [$''$]	0.015	6.7	16.1 ± 0.1
Separation AU	~ 0.6	~ 200	$\gtrsim 1091$
Ref.	1,2,3,4	5,6,7,8	9

[1] Liebert et al. [1993]; [2] Glenn et al. [1994]; [3] Schmidt et al. [1998]; [4] Nelan [2007]; [5] Barstow et al. [1995]; [6] Ferrario et al. [1997]; [7] Burleigh et al. [1999]; [8] Vennes et al. [2003]; [9] this paper.

8.5 The origin of magnetic white dwarfs

The origin of highly magnetic ($\gtrsim 1$ MG) white dwarfs is an unsettled issue. Early estimates of the fraction of magnetic white dwarfs hinted at a value of $\sim 4\%$ [e.g. Schmidt & Smith, 1995], and led to the conclusion that their masses were on average higher than those of non-magnetic white dwarfs [Liebert, 1988]. The space density of magnetic white dwarfs and their high masses were taken as being suggestive for magnetic white dwarfs descending from chemical peculiar Ap/Bp stars, with the strong fields of the magnetic white dwarfs explained by magnetic flux conservation [e.g. Angel et al., 1981; Tout et al., 2004]. However, more recent work suggests that the fraction of magnetic white dwarf may actually be as high as $10 - 15\%$ [Liebert et al., 2003; Wickramasinghe & Ferrario, 2005], casting doubt as to whether the space density of Ap/Bp stars is sufficient for producing all magnetic white dwarfs [Kawka & Vennes, 2004; Wickramasinghe & Ferrario, 2005].

Liebert et al. [2005b] spotted another oddity about magnetic white dwarfs, namely that not a single magnetic white dwarf has been found in any of the > 1600 known (wide and close) white dwarf plus M-dwarf binaries [Silvestri et al., 2007; Heller et al., 2009; Rebassa-Mansergas et al., 2010] – contrasting the large frequency of *interacting* magnetic white dwarf plus M-dwarf binaries, i.e. magnetic cataclysmic variables, which make up 25% of all known CVs [Wickramasinghe & Ferrario, 2000]. This motivated Tout et al. [2008] to outline a very different scenario for the origin of magnetic white dwarfs, in which dynamos during the common envelope evolution of close binaries generate strong magnetic fields in the core of the white dwarf progenitor. During the common envelope phase of evolution of a white dwarf plus

M-dwarf binary, the separation shrinks, leading primarily to two different possible outcomes. If the two stars avoid merging, they leave the common envelope as a short-period binary that will relatively rapidly start mass transfer as a magnetic cataclysmic variable. In fact, a number of such systems, magnetic pre-cataclysmic variables, are known [Reimers et al., 1999; Reimers & Hagen, 2000; Szkody et al., 2003; Schmidt et al., 2007; Schwope et al., 2009]. Alternatively, the two stars may coalesce, forming a single magnetic white dwarf, which will typically be more massive than non-magnetic field white dwarfs.

Given the larger number of observational constraints that are available for magnetic white dwarfs in binaries, these systems hold a strong potential in improving our understanding of the origin of magnetic white dwarfs. Until now, only two spatially resolved white dwarf binaries containing one magnetic white dwarf were known, RE J0317–853 and LB 11146, see Table 8.5. RE J0317–853 is a hot, massive white dwarf, rotating with a spin period of 725 sec, and has a very large magnetic field [Barstow et al., 1995; Burleigh et al., 1999]. Its DA companion LB 9802 is cooler and of lower mass[3] than RE J0317–853, a paradox in terms of stellar evolution which is resolved if the magnetic component is assumed to be a relatively recent merger [Ferrario et al., 1997]. LB 11146 is a relatively close binary, that might have undergone common envelope evolution [Nelan, 2007]. Hence, the properties of both RE J0317–853 and LB 11146 are consistent with a binary origin of the magnetic field. In addition to these two spatially *resolved* white dwarf plus magnetic white dwarf binaries, about half a dozen unresolved spectroscopic white dwarf binaries containing a magnetic white dwarf are known [Kawka et al., 2007, and references therein], and hence it is not known if they underwent binary interaction or not.

PG 1258+593/SDSS J1300+5904 differ from the two previously known spatially resolved binaries in that the two white dwarfs appear to have evolved without interacting, and their properties agree with standard stellar evolution theory. Taking the observational facts at face value, it seems entirely plausible that the strong magnetic field of SDSS J1300+5904 is related to the Ap phenomenon and not related to common envelope evolution, unless it is itself an unresolved binary, or unrecognised merger. The first option appears contrived, but not impossible (see the case of WD 1704+481; Maxted et al. 2000). The SDSS spectrum shows no evidence for an additional binary companion, unless it is a featureless DC white dwarf, similar to that in G62-46 [Bergeron et al., 1993], or a very late type dwarf. Using the star spectral templates of Araujo-Betancor et al. [2005b], a hypothetical unresolved late

---

[3]The physical association of RE J0317–853 is so far purely based on the small separation on the sky, no proper motions are available for the two stars. However, a preliminary analysis of HST/FGS data does appear compatible with the system being a CPM pair [Külebi et al., 2010].

type companion to SDSS J1300+5904 has to be of spectral type L5 or later to go unnoticed. White dwarf plus brown dwarf binaries are extremely rare [Farihi et al., 2005], so finding one with a CPM white dwarf companion appears rather unlikely, however infrared data could rule this out for certain. The second option, a merger, can also not be excluded. The mass of SDSS J1300+5904 is slightly below the mean mass for single white dwarfs, so any merger event would have either been the merger of two low mass white dwarfs, possibly helium core white dwarfs, or had to involve a low mass star. In the case that SDSS J1300+5904 is the product of a merger, one would expect the white dwarf to be rapidly spinning, which might be detectable via photometric variability [e.g. Brinkworth et al., 2004, 2005]. Thus SDSS J1300+5904 warrants further study.

Chapter 9

Summary and Outlook

The advent of large scale digital sky surveys has, and will continue to, revolutionise the world of astronomy. I have taken a handful of current surveys, introduced and developed methods to select interesting objects and applied those methods to the study of stellar remnants and their companions. They are, however, equally applicable to the analysis of objects on all scales of astronomy and will continue to be relevant for the multitude of upcoming photometric, spectroscopic and time-domain surveys.

9.1 Selecting stellar remnants from large scale digital sky surveys

I have developed three detailed methods to select white dwarfs and hot subdwarfs from large scale digital sky surveys using colour-colour diagrams and SED fitting:

Firstly, in Chapter 4, I demonstrated a method to select DA white dwarfs in $ugriz$ colour space, and applied this to SDSS DR7. I identified 7444 DA white dwarfs with $g \leq 19$ and SDSS spectroscopy, approximately 70% more than the corresponding number from DR4 [Eisenstein et al., 2006], and 9341 photometric-only DA candidates. Using this sample, I estimate the spectroscopic completeness of DA white dwarfs with $T_{\mathrm{eff}} \gtrsim 8000 \, \mathrm{K}$ in SDSS DR7 to be $\simeq 44 \, \mathrm{per \, cent}$.

Secondly, in Chapter 5, I cross-correlated our samples of spectroscopic and photometric DA white dwarfs with UKIDSS DR8 to carry out the currently largest and deepest untargeted search for low-mass companions to, and debris discs around, DA white dwarfs. Our search in the SDSS and UKIDSS led to the identification of a significant number of DA white dwarfs with low-mass companions, including several brown dwarf and dusty debris disc candidates.

Thirdly, in Chapter 7, I use a combination of ultraviolet, optical and infrared photometry to select hot subdwarfs stars with mid-M to early-F-type near main–sequence companions. This selects a complementary sample to those found from radial velocity surveys, which typically limit themselves to objects with no obvious evidence for a companion in the optical range. I applied this method to two samples, one selected from a match between GALEX, CMC and 2MASS (covering a large area), and the other using GALEX, SDSS and UKIDSS (probing deeper in the K_s-band and therefore further away). I also use the SDSS for fitting in the *C2MS* sample. Such samples offer direct tests of binary evolution pathways.

9.2   Remnants of planetary systems around white dwarf stars

In Chapter 6, I obtained and analysed *Spitzer* observations of 15 white dwarfs with metal-polluted atmospheres, all but one having helium-dominated atmospheres. Of these, HE 0110−5630, GD 61 and HE 1349−2305 are found to have an infrared excess consistent with closely-orbiting circumstellar dust. These discs are likely formed from the disruption of large asteroid analogues within the remnant planetary systems. A marginal excess is measured at $15.6\,\mu$m around NLTT 51844, but more data are needed to rule out contamination from extragalactic sources.

This survey nearly doubles the number of disc detections around DBZ white dwarfs. Using this substantially enlarged sample, I estimate a typical disc lifetime by comparing the accreted metal masses inferred from DBZ stars with dust to the instantaneous accretion rates for DAZ stars with dust. Accounting for the large scatter by taking the logarithmic average, I find $\log[t_{\mathrm{disc}}(\mathrm{yr})] = 5.6 \pm 1.1$, which is compatible with the relatively wide range of disc lifetimes estimated from different theoretical models of white dwarf discs.

The fraction of highly-polluted DBZ white dwarfs exhibiting an infrared excess is low (23 per cent) compared to that among DAZ white dwarfs (48 per cent). Assuming that the formation and evolution of circumstellar discs is similar for both types of stars, this difference suggests that the disc life times are typically shorter than the DBZ diffusion time scales.

I also show, in Section 6.3, that the highest time-averaged accretion rates are found among white dwarfs with helium-rich atmospheres, many of which do not exhibit infrared excess, and I suggest that these stars have experienced very high accretion rates during short-lived phases. These events should occur in hydrogen-dominated white dwarfs as well, but their short diffusion timescales substantially

lower the probability of detection.

9.3 The formation of subdwarfs in the RLOF channel

A significant number of subdwarfs with F to K-type companions were found in Chapter 7. The system parameter distributions are consistent with the systems being produced, at least in a significant part, by the very efficient Roche-lobe overflow channel [Han et al., 2003]. However, neither the predictions of Han et al. [2003] or Clausen et al. [2012] match the observed distribution completely. I find that M-type companions are far less prevalent than K-type systems.

It is clear that, at least for a large fraction of the subdwarf population, prior binary evolution plays an important role. This group has largely gone unstudied previously. With future surveys such as the Southern SkyMapper project and VISTA, the same procedure as carried out here can be applied to a large field in the southern sky. This would find many more subdwarfs with early type companions and allow for a thorough test of our understanding of the prior binary evolutionary pathways required to form the large subdwarf populations we see. Similarly, the complete and final WISE survey could be an excellent addition to this search, allowing us to probe for fainter companions and covering the whole sky.

9.4 The origin of magnetic fields in white dwarf stars

Chapter 8 shows how wide, non-interacting white dwarf pairs can be used to constrain the initial-final mass relation. In the example case, I also find that SDSS-J1300+5904, the common proper motion companion to the DA white dwarf PG-1258+593, is a magnetic white dwarf with $B \simeq 6\,\mathrm{MG}$. The masses of both white dwarfs are $\sim 0.54\,\mathrm{M_\odot}$, slightly below the average of non-magnetic white dwarfs. Nevertheless, the two white dwarfs exhibit a significant difference in their effective temperatures, implying an age difference of $\sim 1.6\,\mathrm{Gyr}$. Adopting standard stellar evolution models, I show that assuming a progenitor mass of $\sim 1.5\,\mathrm{M_\odot}$ for PG 1258+593 implies a progenitor mass of $\sim 2 - 3\,\mathrm{M_\odot}$ for SDSS J1300+5904, consistent with the mass of Ap stars. An origin of the magnetic field related to common envelope evolution is not impossible, but requires the assumption of an initial triple system.

9.5 Follow-up studies

Several follow-up studies have started (and in some cases finished) based on the work presented here: Farihi et al. [2012] obtained optical spectroscopy to confirm the nature of three candidate DA white dwarf stars from Chapter 4. Warm *Spitzer* observations were also obtained for six of the white dwarf plus infrared excess candidates discussed in Chapter 5. Five out of six were confirmed to have a mid-infrared excess, three of which being consistent with the emission from a dusty disc [Farihi et al., 2012]. This study highlights the efficiency and potential of both the method designed to photometrically select DA white dwarf stars (Chapter 4), and the method to select white dwarfs with near-infrared excess (Chapter 5).

In Section 5.2.3.4, I developed a method to find magnetic white dwarfs with low mass companions and strong cyclotron emission, similar to SDSS J1212+0136 (discussed in Section 5.3.1.3), from near-infrared colours and proper motions. Breedt et al. [2012] followed-up two of these candidates with phase resolved spectroscopy and showed that both are magnetic white dwarfs with a low mass companion and possibly polars in a low state. With continued releases of optical, near-infrared and proper motion surveys, we have the potential to discover and unlock the mysteries of these rare systems.

Copperwheat et al. [in prep.] are leading a follow-up survey of the subdwarf plus companion candidates discussed in Chapter 7 to search for radial velocity variations. This is a complementary sample to those initially found from radial velocity surveys and will provide vastly improved constraints for binary evolution models.

9.6 Outlook

All of the methods discussed in this work are variations on a similar theme and each can be tweaked and reused. Similar studies to that presented here, making use of later SDSS, UKIDSS and WISE data releases, as well as the corresponding surveys in the southern hemisphere, e.g. SkyMapper, VISTA and VST, promise to further increase the sample sizes of the white dwarf and subdwarf systems I have discussed.

9.6.1 SkyMapper, VISTA and VST

SkyMapper is a wide-field (5.7 square degrees), fully automated 1.35 m telescope in New South Wales, Australia [Keller et al., 2007]. It aims to be the southern equivalent of the SDSS. It uses six filters from the ultraviolet to the near-infrared, including a Strömgren-like u-band, SDSS-like g, r, i and z filters and a narrow

v-band filter near 4000 Å. SkyMapper improves over the SDSS by providing some temporal coverage and imaging large parts of the Galactic plane.

The VLT Survey Telescope (VST) is the latest addition to ESO's Paranal Observatory, being a 2.6 m telescope with a $1° \times 1°$ field of view, specifically designed for survey operations. The VST, like the VLT, is equipped with a number of different filters, covering a range of wavelengths from the ultraviolet to the near-infrared. The VST will be dedicated to a number of survey programs, including: the Kilo-Degree Survey (KiDS; de Jong et al. 2012), the VST ATLAS, and the VST Photometric H-alpha Survey of the Southern Galactic Plane (VPHAS+).

Firstly, the VST ATLAS will be the largest of these surveys, covering 4500 square degrees in five filters (SDSS u, g, r, i and z-bands) to a depth comparable with the SDSS. KIDS will probe approximately 2.5 magnitudes deeper than SDSS and ATLAS, but cover just 1500 square degrees in u, g, r and i. Lastly, VPHAS+ will cover 1800 square degrees of the Galactic plane in u, g, H_α, r and i. One of the primary focuses of the VPHAS+ project is to search for compact blue objects and binaries, and therefore is ideally suited to the method I have shown here.

With SkyMapper and the VST providing SDSS-like coverage in the southern hemisphere (including the Galactic plane), the Visible and Infrared Survey Telescope for Astronomy (VISTA) will provide UKIDSS-like coverage to complement. VISTA is a 4 m, wide-field (1.65 degree diameter field of view), near-infrared telescope, capable of observing the southern sky in broadband Z, Y, J, H and K_s filters.

There are six large public surveys being conducted by VISTA, including the VISTA Variables in the Via Lactea (VVV; Minniti et al. 2010) and VISTA Hemisphere Survey (VHS). On the one hand, VHS will survey the entire southern hemisphere in two near-infrared bands. It will delve approximate four magnitudes deeper than the previous 2MASS and DENIS surveys of the region. On the other hand, VVV focuses on the southern Galactic plane (520 square degrees), observing in all five broad band filters as well as performing multiple observations. VVV will be an excellent test bed of data for searching for variability and period distributions in white dwarf and subdwarf binaries (and single stars). The methods will then truly excel with the Pan-STARRS and LSST surveys discussed below.

The combination of SkyMapper, the VST surveys and the VISTA public sky surveys will allow for the methods outlined in this work to be re-applied to the southern sky relatively straight-forwardly. The increased density of sources will lead to orders of magnitude larger samples of white dwarfs and subdwarfs. This is not only outstanding for large sample statistics, but also because of the inherent rarity

of many of the objects we have studied.

9.6.2 GAIA

The Gaia mission, expected to be launched in August 2013, aims to produce a 3D map of the Galaxy, almost out to the Galactic center [Perryman et al., 2001]. It will be the successor to the Hipparcos mission, improving in accuracy by a factor of 100. The data produced from the spacecraft will include photometry in four broadband filters, course grid spectroscopy and high-resolution spectroscopy of the Calcium triplet at $8470 - 8740\,\text{Å}$ (used to calculate radial velocities). Gaia will provide positions, distances and velocities for around a billion objects. The trigonometric parallaxes are expected to have uncertainties of < 1 per cent and potentially probe out to distances of $10\,\text{kpc}$. The Gaia proper motions should meet accuracies of $20\,\mu\text{as}$ at $V = 15$ and $200\,\mu\text{as}$ at $V = 20$.

With the Gaia colours, distances and proper motions, one should be able to unambiguously separate white dwarfs from all other types stars, something not possible with the techniques used here. Gaia should find a total of $\sim 100,000$ white dwarfs, an unprecedented sample, key to furthering our studies of, for example, the white dwarf luminosity function (and thus the age of the Galaxy). Similar to the photometric fitting methods described herein, we will be able to take advantage of the Gaia low resolution spectroscopy for temperature estimates. With the addition of follow-up optical spectroscopy, to calculate accurate effective temperatures and surface gravities (making use of the parallaxes, and therefore not having distance as a free parameter), we will be able to probe the mass distribution of white dwarfs, along with constraining the (poorly understood) low mass end of the initial-final mass relation.

Such a large sample of white dwarfs will unlock a statistically significant sample of even the rarest objects, such as: the white dwarfs with oxygen-rich atmospheres discovered in Gänsicke et al. [2010], the extremely metal-polluted white dwarfs discussed in Koester et al. [2011], and the white dwarfs with gaseous and dusty discs similar to SDSS J1228+1040 (see Chapter 5). The high resolution spectroscopy of the Calcium triplet provided by Gaia will be particularly key for the latter of these.

9.6.3 LSST

The Large Synoptic Survey Telescope (LSST; Tyson 2002), based in Chile, with its $8.4\,\text{m}$ diameter primary mirror, is estimated to see first light in 2018. This revolu-

tionary telescope will perform a wide-field survey (3.5 degree field of view) covering the entire available sky (18,000 square degrees) every few nights for 10 years. The LSST will observe in 6 bands from $320 - 1050$ nm: u, g, r, i, z and y, reaching a limiting magnitude of 23.9, 25.0, 24.7, 24.0, 23.3 and 22.1 (5σ limits), respectively, for single images (~ 2.5 magnitudes deeper for co-added images). It will take a 15 second exposure every 37 seconds and produce light curves for around one billion stars. The photometry is expected to reach an accuracy of 0.01 mag in u, whilst the precision astrometry will provide proper motions to accuracies of 0.2 mas/yr at $r = 21$ and 1.0 mas/yr at $r = 24$.

The LSST will cover an area roughly double that of the SDSS, and being in the southern hemisphere, will be capable of finding orders of magnitude more white dwarfs than seen in Chapter 4. Perhaps more importantly, the multi-colour time domain data for white dwarf and subdwarf binaries will allow direct probing of variability and period distributions.

9.6.4 Pan-STARRS

The Panoramic Survey Telescope and Rapid Response System (Pan-STARRS; Hodapp et al. 2004) will be an array of four 1.8 m telescopes, the first of which (PS1) is already operational. PS2 is expected to see first light in 2013. The complete array will survey the whole sky observable from its location in Hawaii (three quarters of the sky) on a continual basis (approximately 6000 square degrees every night). All four cameras will point in the same direction, summing to have an equivalent area to a 3.6 m telescope, with a 3 degree field of view. The cameras are the largest ever built, with 1.4 billion pixels per image. A single observation will reach a 5σ depth of 24th magnitude in a broadband filter, however, similar to LSST, the co-added images will probe far deeper. Each Pan-STARRS telescope will be equipped with an identical set of five to six optical and near-infrared filters, including g, r, i, z and y.

Pan-STARRS will excel in many of the same ways as LSST for white dwarf and subdwarf research, however, Pan-STARRS should begin releasing data as soon as 2013. In the short term it will therefore be the best resource for time-domain analysis of variable systems, such as close binaries and cataclysmic variables. It will also enable vast and photometrically deep searches similar to that performed in this work.

Other notable surveys, on a similar vein, are the Optical Gravitational Lensing Experiment (OGLE; Udalski et al. 1992) and The Palomar Transient Factory (PTF; Rau et al. 2009). Both of which are already providing wide-field, time-domain

surveys, but not quite to the precision and depth of Pan-STARRS and LSST.

9.6.5 White dwarfs with early-type companions

I also envisage a slight redesign of the method to select subdwarfs with early type companions (Chapter 7) that could be used to produce a sample of white dwarfs with early type companions, complementary to the sample in Chapter 5. Selecting objects with one hot and one cool component would again benefit from the large wavelength range sampled from the ultraviolet down to the near-infrared.

9.6.6 Summary

With the huge data flow coming from all of the above discussed surveys, the potential for data mining is growing rapidly. The methods I have discussed are straight forward to reapply to future surveys and will find orders of magnitude more objects. They are also easily modified to focus on any type of binary with two objects of different temperature, such as scataclysmic variables. Many of the upcoming surveys will exploit variability information, which will become an important indicator for distinguishing targets from contaminants. The parallax distances from Gaia will also be instrumental in this. As I have shown herein, photometric surveys are excellent for selecting candidate objects, but there is a fast growing need for large-scale spectroscopic follow-up surveys. These are a must for the near future.

Appendix A

A catalogue of white dwarf stars with infrared excess in UKIDSS

Table A.1: 42 DA white dwarf infrared excess candidates from the spectroscopic method. In all columns, ':' indicates an uncertain classification. The notes column indicates the level of certainty of the IR excess. The key to the notes2 column is: bg (background contamination), disc (disc candidate), moreIR (more infrared data required), resolved (resolved or partially resolved binary). The "Eisenstein" column is the classifications according to the Eisenstein et al. [2006] catalogue. The column "JHK" firstly indicates whether the object has a UKIDSS J, H and/or K magnitude. Secondly, if the corresponding letter is bold, it means an excess was found in that band.

Coord	$T_{eff}(K)$	$\log(g)$	$M_{wd}(M_\odot)$	$R_{wd}(10^8\ cm)$	$d\ (pc)$	Companion	Notes	Notes2	Eisenstein	JHK
0032+0739	21045 ± 249	7.42 ± 0.05	0.37 ± 0.02	1.37 ± 0.05	398 ± 15	M6	DAire:	resolved,bg:	DA	**JHK**
0039−0030	12392 ± 544	7.35 ± 0.16	0.32 ± 0.05	1.37 ± 0.15	417 ± 44	M9	DAire:		DA_auto	**JHK**
0135+1445	7467 ± 18	7.34 ± 0.04	0.29 ± 0.01	1.33 ± 0.03	69 ± 2	L6	DAire		DA	**JHK**
0207+0702	10073 ± 77	8.32 ± 0.09	0.80 ± 0.06	0.72 ± 0.05	162 ± 10	L7	DAire:			**JHK**
0236−0103	20566 ± 498	7.66 ± 0.09	0.46 ± 0.04	1.15 ± 0.04	411 ± 25	M6	DAire		DA+M:	JH
0253−0027	18974 ± 286	7.71 ± 0.06	0.47 ± 0.03	1.11 ± 0.05	380 ± 15	L4	DAire	moreIR	DA_auto	**JHK**
0748+2058	86726 ± 7732	7.15 ± 0.27	0.53 ± 0.06	2.23 ± 1.37	2021 ± 469	M3	DAire	resolved:	DA+M:	**JHK**
0753+2447	13432 ± 710	7.81 ± 0.15	0.50 ± 0.08	1.02 ± 0.10	349 ± 32	L5:	DAire	disk	DA_auto	**JHK**
0847+2831	12828 ± 930	7.76 ± 0.20	0.48 ± 0.11	1.05 ± 0.14	357 ± 42	M6	DAire		DA+M:	**JHK**
0907+0536	19416 ± 458	7.78 ± 0.09	0.51 ± 0.05	1.06 ± 0.06	367 ± 21	L6	DAire:	moreIR	DA_auto	**JHK**
0933+3200	11565 ± 381	8.36 ± 0.20	0.83 ± 0.13	0.70 ± 0.11	229 ± 34	L4	DAire:	resolved:		**JHK**
0950+0115	21785 ± 365	7.89 ± 0.06	0.57 ± 0.03	0.99 ± 0.04	329 ± 14	L8	DAire:	moreIR	DA	JH
1002+0939	21785 ± 808	7.92 ± 0.14	0.58 ± 0.08	0.97 ± 0.09	515 ± 45	L0	DAire		DA_auto	**JHK**
1010+0407	13588 ± 668	7.76 ± 0.11	0.48 ± 0.05	1.05 ± 0.07	280 ± 18	L8:	DAire:	moreIR	DA_auto	JH
1015+0425	34526 ± 86	7.38 ± 0.07	0.41 ± 0.02	1.51 ± 0.08	691 ± 39	L4	DAire:	moreIR	DA_auto	**JHK**
1016+0020	21045 ± 703	8.48 ± 0.12	0.92 ± 0.07	0.64 ± 0.06	325 ± 32	L6	DAire:	moreIR	DA	**H**
1037+0139	11433 ± 208	8.38 ± 0.13	0.84 ± 0.08	0.69 ± 0.07	151 ± 14	L5:	DAire		DA	**JHK**
1120+0639	20331 ± 609	7.69 ± 0.11	0.47 ± 0.05	1.13 ± 0.09	517 ± 38	L3	DAire:	resolved,bg:	DA_auto	**J**
1141+0420	11835 ± 818	7.37 ± 0.22	0.32 ± 0.08	1.35 ± 0.21	317 ± 46	M7	DAire		DA+M:	**JHK**
1208+0610	23076 ± 1125	7.64 ± 0.17	0.46 ± 0.08	1.18 ± 0.14	725 ± 81	M7	DAire		DA_auto	JH
1218+0042	11173 ± 180	8.30 ± 0.11	0.79 ± 0.07	0.73 ± 0.06	171 ± 13	L8	DAire:	moreIR	DA	JH
1228+1040	22037 ± 199	8.19 ± 0.04	0.74 ± 0.02	0.80 ± 0.02	134 ± 3	L6:	DAire	disk	DA_auto	**JHK**
1246+0707	10793 ± 189	8.03 ± 0.16	0.62 ± 0.10	0.88 ± 0.10	200 ± 21	L2	DAire			**HK**
1247+1035	17912 ± 159	7.82 ± 0.04	0.52 ± 0.02	1.03 ± 0.03	394 ± 9	L6:	DAire:	bg:,resolved:		**JHK**
1314+0057	17707 ± 163	7.80 ± 0.04	0.51 ± 0.03	1.04 ± 0.03	312 ± 8	L6	DAire:	disk:		HK
1320+0018	19193 ± 213	8.40 ± 0.04	0.87 ± 0.03	0.68 ± 0.02	142 ± 5	L8	DAire:	disk:	DA	**JHK**
1329+1230	13432 ± 272	7.42 ± 0.05	0.34 ± 0.02	1.32 ± 0.05	209 ± 8	M7	DAire		DA_auto	**JHK**
1331+0040	15964 ± 714	7.72 ± 0.17	0.47 ± 0.08	1.09 ± 0.12	465 ± 48	?	DAire	moreIR	DA	
1341+0056	18330 ± 436	7.99 ± 0.10	0.61 ± 0.06	0.92 ± 0.06	360 ± 22	M7	DAire			**JHK**
1352+0910	36154 ± 722	7.49 ± 0.11	0.45 ± 0.04	1.39 ± 0.13	849 ± 76	M5	DAire			**JHK**
1410+0225	11565 ± 246	8.63 ± 0.13	1.00 ± 0.07	0.56 ± 0.06	152 ± 16	≥ L8	DAire:	moreIR	DA	JH
1425−0013	10670 ± 169	7.97 ± 0.17	0.58 ± 0.10	0.91 ± 0.10	242 ± 26	L8:	DAire:	moreIR	DA	**JHK**
1448+0240	14728 ± 247	7.41 ± 0.06	0.34 ± 0.02	1.34 ± 0.06	292 ± 13	L4	DAire:	moreIR	DA	JH
1448+0713	12250 ± 256	7.87 ± 0.09	0.53 ± 0.05	0.98 ± 0.06	143 ± 8	M8	DAire:			**JHK**
1450+0000	17106 ± 175	7.93 ± 0.05	0.58 ± 0.03	0.95 ± 0.03	311 ± 9	L8:	DAire	moreIR		**JHK**
1557+0916	22811 ± 734	7.75 ± 0.11	0.50 ± 0.05	1.09 ± 0.08	488 ± 35	L1:	DAire		DA_auto	**JHK**
1609+2905	8773 ± 91	8.26 ± 0.14	0.76 ± 0.09	0.75 ± 0.08	122 ± 12	≥ L8	DAire			**JHK**
1619+2533	25595 ± 1139	7.21 ± 0.15	0.33 ± 0.04	1.65 ± 0.20	879 ± 101	M5	DAire			**JHK**
1625+3026	72136 ± 4550	7.77 ± 0.19	0.64 ± 0.08	1.21 ± 0.21	739 ± 112	≥ L8	DAire		DA_auto	**JHK**
2220−0041	7467 ± 21	7.66 ± 0.12	0.41 ± 0.06	1.10 ± 0.08	69 ± 5	M5	DAire:	resolved	DA_auto	**JHK**
2225+0016	11045 ± 235	8.44 ± 0.16	0.88 ± 0.10	0.65 ± 0.08	167 ± 20	L6	DAire:	resolved:	DA_auto	**JHK**
2331+1342	11173 ± 284	8.79 ± 0.15	1.09 ± 0.08	0.49 ± 0.07	141 ± 19	L6	DAire		DA+M:	**JHK**

Table A.2: 67 photometric-only infrared excess candidates which are found to have an infrared excess in the photometric method. The columns follow the same format as that in Table A.1. The key to the "Notes2" column is: bf (visually bad fit), bg (background contamination), disc (disc candidate), hotWD (high T_{eff} white dwarf and so small changes in, e.g. flux calibration, remove the excess), moreIR (more infrared data required), resolved (resolved or partially resolved binary), qso (quasar), ? (unknown). Also, the "Simbad Name" and "Simbad Class" columns give an indication of what is already known about the objects. If the surface gravity could not be constrained, it was assigned the canonical value of 8.0 and therefore no error could be defined. We do not quote the distances to the systems because the uncertainty is so large. The two objects marked as "QSO:" are borderline cases of the objects found in the online QSO table and are therefore left as candidates for being DA white dwarfs with an infrared excess.

Coord	$T_{eff}(K)$	$\log(g)$	Companion	Notes	Notes2	JHK	Simbad Name	Simbad Class
0016+0704	24000±2100	8.00	L0	DA:ire		**JHK**	V* EK Psc	Variable Star
0104+1459	12000±90/60	7.75±0.12	L5	DA:ire	moreIR	**JH**		
0141+0614	11000±50	8.50±0.08	L8:	DA:ire:	bf	**JHK**	2MASS	Nova
0207+0715	14000±2040/1940	9.25±0.37	L6:	DA:ire	bf	**JHK**	PB6668	Star
0742+2857	9000±50	7.25±0.25	L6	DA:ire		**JHK**		
0751+2002	20000±2160/2190	8.25±3.25?	L5	DA:ire		**JHK**		
0758+2406	13000±640/660	8.00±0.25	L2:	DA:ire:		**JHK**		
0841+0501	8000±180	8.00±0.12	≥L8:	DA:ire	bf	**JHK**		
0842+0004	22000±100	8.00	M9	DA:ire		**JH**		
0854+0853	60000±6890/7210	8.00	M6	DA:ire		**JHK**	PN A66.31	PN
0906+0001	7000±10/0	8.00	≥L8:	DA:ire:		**JHK**		
0920+3356	12000±90/110	9.00±0.28/0.15	L8:	DA:ire:	bf	**JHK**	V* BK Lyn	Nova
0923+0652	7000±10/0	8.00	≥L8:	DA:ire:	bf,bg	**JHK**		
0925−0140	14000±80	7.50±0.28/0.37	M9	DA:ire		**JHK**		
0952+1205	26000±1540/1330	8.00	≥L8:	DA:ire:	bf	**HK**		
0959−0200	12000±1780/1330	8.00±1.20/0.22	L6	DA:ire	disk	**JHK**		
0959+0330	32000±500/570	8.00	L0	DA:ire		**JHK**	PG0957+037	UV
1005−0225	14000±120/50	7.75±0.45/0.93	L5:	DA:ire:	bf	**JHK**		
1006+0032	20000±140/90	9.50±0.93	L8	DA:ire	bf:	**JHK**	PG1004+008	UV
1038+1100	10000±90	7.75±0.17/0.27	L3	DA:ire		**JHK**		
1057+0628	7000±30	8.00	L8:	DA:ire:	QSO:	**JHK**		
1103+0101	7000±18/0	8.00	≥L8:	DA:ire:	bf:	**JHK**	[VV2006]J110336.3+010141	Quasar
1103+1100	34000±2040/2030	8.00	L4	DA:ire:	hotWD,moreIR	**J**	PG1101+113	SD
1116+0755	22000±110/90	8.00	M9	DA:ire		**JHK**		
1153+0048	15000±1560/1770	9.50±0.36	≥L8:	DA:ire:	bf	**JHK**	LBQS1151+0104	Star
1221+1245	12000±1770	8.00±0.51/0.34	L8:	DA:ire:	disk:	**JHK**		
1224+0907	7000±30	8.00	L7	DA:ire	bg:,resolved:,bf:	**JHK**		
1237−0151	20000±40	8.75±0.32	L4:	DA:ire:	resolved,bg:	**JHK**		
1246+1600	19000±550/530	9.50±0.46	≥L8:	DA:ire:	bf:	**JHK**		
1315+0245	28000±1580/1530	8.00	L1:	DA:ire:	resolved,bg:	**JHK**		
1319+0152	16000±1070	8.25±0.36	≥L8:	DA:ire:	bf	**HK**	WD1317+021	DA
1323+2615	17000±530/510	9.50±0.89	≥L8:	DA:ire:	bf	**HK**		
1334+0534	30000±390/330	8.00	≥L8:	DA:ire:	bf:	**HK**		
1348+1100	22000±330	8.00	L1	DA:ire	moreIR	**J**		
1355+1454	22000±2180/250	8.00	L1	DA:ire		**JHK**	PB4150	SD

196

Table A.2:

Coord	T$_{\rm eff}$(K)	log(g)	Companion	Notes	Notes2	JHK	Simbad Name	Simbad Class
1416+1352	38000±20800	8.00	M6	DA:ire		**JHK**	PK_003+66_1	Galaxy
1423−0138	16000±850/380	8.00±0.21/0.41	≥L8:	DA:ire:	moreIR	**JH**	PG1438+018	SD
1441+0137	26000±420/60	8.00	L6:	DA:ire:	bf:	**JHK**		
1442+0910	20000±140	7.75±1.13/0.59	M7	DA:ire		**JHK**	WD1446+028	DA
1448+0812	24000±2380	8.00	M7	DA:ire		**JHK**		
1455+0458	30000±2380	8.00	M8	DA:ire		**JHK**		
1456+1040	14000±240	8.75±0.91/0.75	L1:	DA:ire		**JHK**		
1507+0724	26000±2400	8.00	M7	DA:ire		**JHK**		
1523+0023	24000±2330	8.00	M8	DA:ire		**JHK**		
1524−0128	18000±20	9.25±0.02	≥L8:	DA:ire:	bf	**JHK**	BPS_CS_22890−0079	SD
1527+0802	20000±1930	9.50±0.83	≥L8:	DA:ire:		**JHK**		
1538+0644	10000±80	7.25±0.10/0.92	L6	DA:ire:	bf:	**JHK**		
1538+2957	20000±40	5.75±0.84	M7:	DA:ire		**JHK**		
1540+2908	34000±4270	8.00	M7	DA:ire:		**JH**		
1548+0006	14000±240/50	8.50±0.08	L6:	DA:ire:		**JHK**		
1549+0325	13000±770/300	7.25±0.64/0.32	L7:	DA:ire:	bf	**JHK**	PG1546+036	UV
1551−0118	13000±1040	8.25±0.28	≥L8:	DA:ire:	bf	**JHK**		
1554+0616	17000±630	7.25±1.57	M6	DA:ire:	resolved,bg:	**JHK**		
1614+2235	20000±200	8.50±0.88	L6	DA:ire		**JHK**	SDSS	SD
1635+2912	17000±1090	5.50±0.74/0.50	L6:	DA:ire:	moreIR,disk:,bg:	**JHK**		
2042+0055	28000±2160	8.00	≥L8:	DA:ire:	bf:	**HK**		
2049−0001	16000±3560	8.75±0.82	≥L8:	DA:ire:	bf:	**HK**		
2052+0018	12000±130	8.00±0.24	≥L8:	DA:ire:	bf:	**HK**		
2117−0015	12000±130	8.00±0.05	≥L8:	DA:ire:	bf:	**HK**		
2135−0031	30000±2590	8.00	M7	DA:ire		**JHK**		
2147−0112	26000±2590	8.00	L1:	DA:ire	resolved:	**JHK**	2MASS	Blue
2308+0658	28000±2280	8.00	M6	DA:ire		**JHK**		
2326+1230	18000±2040	8.75±0.58	≥L8:	DA:ire:	bf:	**JHK**	2MASS	Star
2330+1450	13000±1880	9.50±0.64	≥L8:	DA:ire:	bf:	**JHK**		
2335+1047	11000±420	7.75±0.55/0.46	L4	DA:ire:	resolved,bg:	**JHK**		
2344+0817	8000±100	8.00	L8:	DA:ire:	bf:	**JHK**	PB5517	Star
2348+0200	8000±10	8.00	L6:	DA:ire:	QSO:	**JHK**		

Table A.3: Infrared excess candidates which are found to have an excess in either the spectroscopic or photometric-only methods, but all have an SDSS spectrum for classification. The table follows the same format as Table A.1 and A.2, with addition that S and P in the titles refers to the spectroscopic and photometric methods, respectively. Fiber and fit parameters are only shown if an infrared excess was found in the corresponding method.

Coord	S T$_{\mathrm{eff}}$(K)	S log(g)	P T$_{\mathrm{eff}}$(K)	P log(g)	S Companion	P Companion	Notes	S Notes	P Notes	Classification	Simbad Name	Simbad Class
0018+0101	21045 ± 249	7.42 ± 0.05	22000±220	8.00±	M6	L1	DA:ire	resolved,bg:		NLHS		
0032+0739	12392 ± 544	7.35 ± 0.16			M9		DA:ire:			DA		
0039−0030			11000±50	7.75±0.10		L2	DA:ire			DA		
0118−0025			26000±880	8.00±		L3	DA:ire		resolved	NLHS		
0135+1445	7467 ± 18	7.34 ± 0.04	8000±20	8.00±	L6	L8	DA:ire			DA		
0207+0702	10073 ± 77	8.32 ± 0.09	15000±1090	8.75±0.89	L7	?	DA:ire:		bf	DA		
0236−0103	20566 ± 498	7.66 ± 0.09	18000±1200	8.75±0.75	M6	≥L8:	DA:ire		bf	DA		
0253−0027	18974 ± 286	7.71 ± 0.06			L4		DA:ire	moreIR		DA		
0333+0020			22000±2360	8.00±		M9	DA:ire			NLHS		
0748+2058	86726 ± 7732	7.15 ± 0.27	40000±3640	7.75±0.45	M3	M5	DA:ire	resolved:	resolved:	DA		
0753+2447	13432 ± 710	7.81 ± 0.15	12000±3120	8.50±0.43	L5:	L6:	DA:ire	disk		DA		
0814+2811			9000±550	8.25±1.04		≥L8:	DA:ire:		bf	NLHS		
0847+2831	12828 ± 930	7.76 ± 0.20	12000±2090	9.50±1.55	M6	M9	DA:ire			DA		
0851+0330			20000±2740			L6	DA:ire			WDMS		
0907+0536	19416 ± 458	7.78 ± 0.09			L6	L6	DA:ire:	moreIR		DA		
0933+3200	11565 ± 381	8.36 ± 0.20	10000±1070	7.50±0.36	L4	L2	DA:ire	resolved:	resolved:	DA		
0950+0115	21785 ± 365	7.89 ± 0.06			L8	L8	DA:ire:	moreIR		DA		
0951+0347			24000±100	8.00±0.48		≥L8:	DA:ire:		bf	NLHS		
1002+0939	21785 ± 808	7.92 ± 0.14	20000±240	8.00±0.52	L0	L0	DA:ire			DA		
1010+0407	13588 ± 668	7.76 ± 0.11			L8:		DA:ire:	moreIR		DA		
1015+0425	34526 ± 86	7.38 ± 0.07			L4		DA:ire:	moreIR		DA		
1016+0020	21045 ± 703	8.48 ± 0.12			L6		DA:ire:	moreIR		DA		
1025+1200			22000±610	8.00±		L1	DA:ire			NLHS		
1037+0139	11433 ± 208	8.38 ± 0.13	15000±360	8.50±0.34	L5:	L1	DA:ire			DA		
1100+0346			32000±6520	8.00±		M7	DA:ire			NLHS		
1106+0737			28000±3180	8.00±		M5	DA:ire			WDMS		
1120+0639	20331 ± 609	7.69 ± 0.11	8000±80	8.00±	L3		DA:ire:	resolved,bg:	bf:	DA		
1135+0731						L7:	DA:ire:			NLHS		
1141+0420	11835 ± 818	7.37 ± 0.22	12000±7230	7.50±0.48	M7	M7	DA:ire			DA		
1148+0336			28000±200	8.00±		L0	DA:ire			NLHS		
1148+0640			24000±3970	8.00±		M8	DA:ire			NLHS		
1208+0610	23076 ± 1125	7.64 ± 0.17	20000±4180	8.75±1.03	M7	L3	DA:ire			DA		
1211+1437			24000±4120	8.00±		M9	DA:ire			NLHS		
1212+0136			10000±80	7.75±0.25		?	DA:ire:		bf	MWD		
1215+1351			24000±350	8.00±		M6	DA:ire:		resolved:	NLHS		
1218+0042	11173 ± 180	8.30 ± 0.11	10000±2180	7.75±0.07	L8	L8:	DA:ire:	moreIR	moreIR	DA		
1219+1244			10000±330	7.50±0.50		L8:	DA:ire:	No−Xs	bf:	DA		
1228+1040	22037 ± 199	8.19 ± 0.04	20000±530	8.50±0.34	L6:	L6:	DA:ire	disk	disk	DA		
1246+0707	10793 ± 189	8.03 ± 0.16	20000±1010	7.00±0.35	L2	L2	DA:ire			DA		
1247+1035	17912 ± 159	7.82 ± 0.04	9000±50		L6:	L6:	DA:ire	bg;resolved:	moreIR	DA		
1249+0422			11000±10	8.00±0.03		L8:	DA:ire:	No−Xs		DA		
1250+1549			9000±90	8.50±0.72		L3:	DA:ire:		bf	MWD		

198

Table A.3:

Coord	S Teff(K)	S log(g)	P Teff(K)	P log(g)	S Companion	P Companion	Notes	S Notes	P Notes	Classification	Simbad Name	Simbad Class
1300+0057			26000±2000	8.00±		≥L8:	DA:ire:		bf:	NLHS		
1310+0233			26000±	8.00±		M8	DA:ire:			NLHS		
1314+0057	17707 ± 163	7.80 ± 0.04	17000±	8.25±1.21	L6	≥L8:	DA:ire:	disk:	bf	DA		
1320+0018	19193 ± 213	8.40 ± 0.04	19000±	8.75±0.64	L8	L8:	DA:ire:	disk:	disk:	DA		
1329+1230	13432 ± 272	7.42 ± 0.05	12000±80	7.50±0.09	M7	M8	DA:ire			DA		
1331+0040	15964 ± 714	7.72 ± 0.17			?		DA:ire:	moreIR		DA		
1334+0647			8000±20	8.00±		≥L8:	DA:ire	No−Xs	moreIR	DA		
1341+0056	18330 ± 436	7.99 ± 0.10	17000±530	7.75±1.16		M6:	DA:ire			DA		
1352+0910	36154 ± 722	7.49 ± 0.11	28000±2300	8.00±0.01	M5	M6	DA:ire			DA		
1410+0225	11565 ± 246	8.63 ± 0.13	11000±	8.00±	≥L8	L8	DA:ire:	moreIR	moreIR	DA		
1414+0212			8000±20	8.00±		≥L8:	DA:ire	No−Xs	moreIR,bf:	DA		
1415+0117			32000±3360	8.00±		M6	DA:ire			WDMS		
1422+0920			22000±	8.00±		M9:	DA:ire			NLHS		
1424+0319			30000±20	8.00±		L5	DA:ire			NLHS		
1425−0013	10670 ± 169	7.97 ± 0.17			L8:		DA:ire:	moreIR	hotWD	DA		
1436+0138			24000±590	8.00±		L4	DA:ire:		moreIR	NLHS		
1443+0931			26000±	8.00±		M9	DA:ire			NLHS		
1448+0240	14728 ± 247	7.41 ± 0.06	13000±	8.00±0.52	L4	L6	DA:ire	moreIR	moreIR	DA		
1448+0713	12250 ± 256	7.87 ± 0.09	11000±	7.75±0.55	M8	M9	DA:ire:	moreIR		DA		
1450+0000	17106 ± 175	7.93 ± 0.05			L8:		DA:ire	moreIR		DA		
1500+0642			26000±110	8.00±		L1:	DA:ire			NLHS		
1510+0409			28000±2000	8.00±		M8	DA:ire			NLHS		
1514+0744			10000±60	8.50±0.30		L5:	DA:ire:		bf	MWD		
1519+0715			26000±	8.00±		M7	DA:ire		moreIR	NLHS		
1525+0958			28000±	8.00±		M9	DA:ire			NLHS		
1539+2706			28000±	8.00±		M9	DA:ire	bf		DA		
1541+0417			24000±	9.50±0.81		L2	DA:ire:			NLHS		
1543+0012			17000±	7.75±0.83		L8:	DA:ire:		bf	NLHS		
1557+0916	22811 ± 734	7.75 ± 0.11	18000±	7.75±0.41	L1:	L5	DA:ire			DA		
1609+2905	8773 ± 91	8.26 ± 0.14	9000±	7.75±0.31	≥L8	L8	DA:ire			DA		
1614+2616			24000±150	8.00±		L5	DA:ire			NLHS		
1619+2407			9000±	8.75±1.02		≥L8:	DA:ire:		bf	NLHS		
1619+2533	25595 ± 1139	7.21 ± 0.15	18000±	9.50±1.89	M5	L6:	DA:ire		bf	DA		
1625+3026	72136 ± 4550	7.77 ± 0.19	40000±	8.00±	M5	M6	DA:ire			DA		
1637+3113			26000±400	8.00±		M9	DA:ire			NLHS		
1640+3117			26000±	8.00±		M7	DA:ire:			NLHS		
1645+3109			17000±2510	9.50±1.24		≥L8:	DA:ire:		bf:	NLHS		
2038+0109			20000±	9.00±1.23		≥L8:	DA:ire:		bf:	NLHS		
2117−0006			8000±20	8.00±		≥L8:	DA:ire:		bf:	NLHS		
2118+0028			15000±	8.25±0.21		≥L8:	DA:ire:	No−Xs	bf:,resolved,bg:	DA		
2220−0041	7467 ± 21	7.66 ± 0.12	8000±20	8.00±	≥L8	≥L8	DA:ire:	resolved	resolved,bg:	DA		
2225+0016	11045 ± 235	8.44 ± 0.16	9000±20	7.00±0.26	L6	L5	DA:ire	resolved:	resolved:,bg:	DA		
2255−0015			17000±	9.00±0.25		L4:	DA:ire:		bf:,resolved,bg:	WDMS		
2331+1342	11173 ± 284	8.79 ± 0.15	15000±1600	9.50±0.73	L6	L8	DAire			DA		

Table A.4: Table of possible QSO. The Identifier and SIMBAD columns are both taken from the SIMBAD database.

Coord	RA	Dec.	Identifier	SIMBAD
0034+0620	8.566036	6.334840		
0051+0653	12.751500	6.891517		
0102+0640	15.503270	6.673510	USNO-A2.0 0900-00239356	Possible QSO
0118+0608	19.671600	6.139908		
0149+0718	27.281910	7.308834		
0154+0742	28.568120	7.701925	USNO-A2.0 0975-00426531	Possible QSO
0221+0632	35.448270	6.546078		
0243+0513	40.796180	5.220669		
0246+0540	41.614910	5.677792		
0731+2540	112.904500	25.682380		
0735+2611	113.798400	26.195500		
0838+0206	129.593500	2.109211		
0842+0012	130.741700	0.209119		
0855−0120	133.773100	-1.339605	2MASS	Possible QSO
0914−0213	138.552900	-2.229904		
0915−0202	138.751800	-2.041268		
0929−0138	142.472600	-1.642093		
0931−0106	142.865200	-1.110524	2SLAQ J093127.66-010638.0	QSO
1015−0203	153.913300	-2.066480	LBQS 1013-0149	QSO
1114−0040	168.733400	-0.672003	[VV2006] J111456.0-004019	QSO
1136−0112	174.019400	-1.210995	[VV2006] J113604.6-011240	QSO
1152+0523	178.247700	5.397534		
1153+0353	178.429200	3.894772		
1246+0007	191.511800	0.131972	2MASS	*
1306+2545	196.644300	25.763520		
1315+0802	198.965800	8.038745		
1319+0004	199.822300	0.076544	[VV2006] J131917.4+000435	QSO
1400+0438	210.121800	4.640576		
1405−0024	211.327700	-0.415854	[VV2006] J140518.7-002457	QSO
1419+0054	214.851300	0.901002		
2218+0622	334.669200	6.379719		
2253+0743	343.489000	7.729056	USNO-A2.0 0975-21110446	Possible QSO
2324+1316	351.177300	13.271330	USNO-A2.0 0975-21272981	Possible QSO
2328+0651	352.022800	6.855294	PMN J2328+0652	Radio Source
2334+0613	353.510200	6.217346		
2342+0408	355.676900	4.135249	2MASS	Possible QSO
2345+0329	356.256300	3.494990	PB 5525	*
2349+0518	357.323300	5.312477	USNO-A2.0 0900-20499910	

Table A.5: The 19 infrared excess candidates from both the spectroscopic and photometric fitting methods that are also found to be white dwarf + main sequence binaries in Rebassa-Mansergas et al. [2010]. Objects from the spectroscopic and photometric infrared excess candidates are denoted as "S" and "P" in the "Method" column, respectively. The first set of system parameters are from the methods described herein. Where both spectroscopic and photometric infrared excesses were found, the quoted parameters are those from the spectroscopic method, the second from Rebassa-Mansergas et al.. In some cases, such as SDSS J0207+0702, the two spectroscopic fitting techniques disagree significantly, this is where a different hot/cold fit solution was chosen. Photometric temperatures may also disagree significantly from the Rebassa-Mansergas et al. [2010] temperatures as discussed in Section 4.2.2. The columns labelled with a "R-M" prefix are the best fit taken from Table 7 of Rebassa-Mansergas et al. [2010]. R-MSp=-1 indicates that no spectral type could be associated.

Name	T_{eff}	$\log(g)$	Method	Companion	Notes	R-M T_{eff}	R-M $\log(g)$	R-M Sp
0032+0739	21045 ± 249	7.42 ± 0.05	S	M6	DAire:	21045 ± 371	7.43 ± 0.07	M2
0039−0030	12392 ± 544	7.35 ± 0.16	SP	M9	DAire:	12392 ± 737	7.39 ± 0.22	−1
0207+0702	10073 ± 77	8.32 ± 0.09	SP	L7	DAire:	18756 ± 502	7.42 ± 0.10	−1
0236−0103	20566 ± 498	7.66 ± 0.09	SP	M6	DAire	21289 ± 723	7.83 ± 0.13	M8
0748+2058	86726 ± 7732	7.15 ± 0.27	SP	M3	DAire	87731 ± 10728	7.17 ± 0.38	M2
0847+2831	12828 ± 930	7.76 ± 0.20	SP	M6	DAire	13588 ± 923	7.76 ± 0.18	M6
0851+0330	20000^{+2740}_{-2090}	$9.50^{+0.00}_{-1.55}$	P	L6	DA:ire	22550 ± 520	7.40 ± 0.08	M6
1037+0139	11433 ± 208	8.38 ± 0.13	SP	L5:	DAire	16717 ± 602	7.78 ± 0.14	M5
1106+0737	28000^{+2060}_{-3800}	8.00	P	M5	DA:ire	36154 ± 540	7.74 ± 0.09	M5
1141+0420	11835 ± 818	7.37 ± 0.22	SP	M7	DAire	12110 ± 780	7.39 ± 0.26	−1
1329+1230	13432 ± 272	7.42 ± 0.05	SP	M7	DAire	12250 ± 1036	7.47 ± 0.20	−1
1341+0056	18330 ± 436	7.99 ± 0.10	SP	M7	DAire	18330 ± 608	8.01 ± 0.13	−1
1352+0910	36154 ± 722	7.49 ± 0.11	SP	M5	DAire	35331 ± 919	7.31 ± 0.16	−1
1415+0117	32000^{+2230}_{-4360}	8.00	P	M6	DA:ire	73816 ± 4981	8.43 ± 0.18	M0
1448+0713	12250 ± 256	7.87 ± 0.09	SP	M8	DAire	12110 ± 264	7.84 ± 0.13	M6
1539+2706	28000^{+670}_{-330}	8.00	P	M9	DA:ire	36572 ± 447	7.31 ± 0.07	−1
1619+2533	25595 ± 1139	7.21 ± 0.15	SP	M5	DAire	25891 ± 1447	7.30 ± 0.20	−1
2255−0015	17000^{+620}_{-170}	$9.00^{+0.37}_{-0.25}$	P	L4:	DA:ire:	22550 ± 724	7.88 ± 0.12	M6
2331+1342	11173 ± 284	8.79 ± 0.15	SP	L6	DAire	18756 ± 1020	7.96 ± 0.20	−1

Appendix B

A catalogue of hot subdwarf stars with F to K-type companion

Table B.1: Example of: Full list of objects from the *C2M* sample with magnitudes inside the cuts described in Table 7.1. Online-only Table.

Name	R.A.	Dec	m_{FUV}	m_{NUV}	r_{CMC}	J	H	K_s	SIMBAD
0004+2301	00:04:06.09	+23:01:50.3	13.62 ± 0.01	14.33 ± 0.01	15.09	14.58	14.42	14.42	
0010+4313	00:10:00.55	+43:13:18.9	16.44 ± 0.03	16.27 ± 0.02	15.14	14.71	14.66	14.54	
0016+3157	00:16:31.06	+31:57:40.8	14.92 ± 0.01	15.31 ± 0.01	15.57	15.08	14.80	14.65	sdB
0018+0101	00:18:43.50	+01:01:25.5	13.43 ± 0.01	14.23 ± 0.01	15.11	15.05	14.88	14.71	
0031−2535	00:31:03.29	−25:35:39.5	15.46 ± 0.01	15.56 ± 0.01	15.38 ± 0.05	14.78	14.54	14.52	
0032+3714	00:32:31.93	+37:14:54.3	15.49 ± 0.01	15.52 ± 0.00	15.34	14.53	14.37	14.27	
0040−0021	00:40:22.88	−00:21:28.8	15.44 ± 0.00	15.28 ± 0.00	15.03 ± 0.09	14.90	14.85	14.70	WD
0041+3726	00:41:40.77	+37:26:38.9	16.09 ± 0.01	15.96 ± 0.00	14.78	14.20	14.06	13.98	
0046+4550	00:46:59.60	+45:50:49.1	16.49 ± 0.03	16.60 ± 0.02	15.82 ± 0.07	14.95	14.73	14.67	
0048+3856	00:48:57.39	+38:56:28.0	16.93 ± 0.01	16.75 ± 0.01	15.33	14.81	14.75	14.48	
0050+4251	00:50:29.44	+42:51:53.8	13.18 ± 0.00	13.79 ± 0.00	13.23	12.50	12.28	12.24	
0051+0921	00:51:26.89	+09:21:32.6	13.73 ± 0.01	14.17 ± 0.01	14.35 ± 0.06	13.71	13.50	13.44	Var*
0053+2229	00:53:16.89	+22:29:39.3	15.27 ± 0.01	15.56 ± 0.01	15.42 ± 0.01	14.83	14.65	14.43	
0054+1508	00:54:11.12	+15:08:19.5	16.47 ± 0.01	16.51 ± 0.00	15.29 ± 0.04	14.45	14.29	14.20	
0057+3538	00:57:20.35	+35:38:59.2	14.90 ± 0.02	15.02 ± 0.01	14.76 ± 0.07	14.07	13.87	13.88	
0103+1332	01:03:41.71	+13:32:48.9	13.37 ± 0.01	13.74 ± 0.01	13.20 ± 0.03	12.51	12.31	12.36	
0107+3940	01:07:12.57	+39:40:24.6	14.44 ± 0.02	14.48 ± 0.01	13.12 ± 0.05	12.30	12.11	12.09	
0109+4203	01:09:16.13	+42:03:04.8	13.60 ± 0.01	13.72 ± 0.01	13.41 ± 0.04	12.86	12.69	12.68	
0115+1922	01:15:25.92	+19:22:49.6	12.52 ± 0.01	12.85 ± 0.00	13.18 ± 0.03	12.66	12.58	12.58	
0115−2406	01:15:47.49	−24:06:50.9	15.12 ± 0.02	15.25 ± 0.01	14.65 ± 0.01	14.16	14.00	13.97	WD
0116−1317	01:16:44.63	+13:17:42.9	14.92 ± 0.01	15.09 ± 0.01	14.22	13.63	13.51	13.42	
0121+4558	01:21:29.49	+45:58:52.2	13.95 ± 0.01	14.41 ± 0.01	14.66	13.86	13.55	13.47	
0122+2150	01:22:06.25	+21:50:18.1	15.68 ± 0.02	15.76 ± 0.01	14.60 ± 0.03	14.12	14.03	13.98	
0129+3202	01:29:52.69	+32:02:10.2	12.65 ± 0.00	13.07 ± 0.00	14.53	14.42	14.29	14.25	Comp
0138+2430	01:38:08.67	+24:30:13.8	15.05 ± 0.01	15.15 ± 0.00	15.25	14.69	14.46	14.30	
0138+0339	01:38:26.97	+03:39:37.6	12.17 ± 0.00	12.18 ± 0.01	13.40 ± 0.01	12.67	12.25	12.19	
0141+0614	01:41:39.91	+06:14:37.3	16.59 ± 0.04	16.26 ± 0.02	15.11	14.91	14.84	14.63	Nova
0143+3234	01:43:26.27	+32:34:39.5	13.93 ± 0.01	14.17 ± 0.01	15.47 ± 0.07	15.42	15.42	15.14	
0147+3032	01:47:10.65	+30:32:15.0	14.38 ± 0.01	14.28 ± 0.01	14.79	14.71	14.66	14.77	
0147−2156	01:47:21.84	−21:56:51.7	16.40 ± 0.02	15.65 ± 0.01	15.28 ± 0.01	14.92	14.45	14.34	DA
0149−2741	01:49:30.81	−27:41:59.6	16.69 ± 0.01	16.38 ± 0.01	15.01 ± 0.04	15.10	14.55	14.05	Galaxy
0151+4631	01:51:27.57	+46:31:22.0	14.19 ± 0.01	14.69 ± 0.01	14.13	13.50	13.31	13.30	
0152−1913	01:52:30.93	−19:13:02.9	11.75 ± 0.00	13.04 ± 0.00	14.22	14.02	13.89	13.96	
0204+2729	02:04:47.13	+27:29:03.6	12.65 ± 0.01	13.26 ± 0.01	14.02	13.51	13.28	13.27	
0208+4712	02:08:01.24	+47:12:59.5	15.10 ± 0.01	15.24 ± 0.01	14.40	13.67	13.46	13.46	
0209−1955	02:09:24.50	−19:55:16.3	14.73 ± 0.01	14.92 ± 0.01	14.33	13.74	13.65	13.51	
0210+0830	02:10:21.88	+08:30:59.0	13.41 ± 0.01	13.76 ± 0.01	13.49	12.83	12.68	12.65	
0211+2851	02:11:55.12	+28:51:05.3	12.38 ± 0.01	12.41 ± 0.00	11.55 ± 0.02	10.91	10.79	10.72	
0217+0906	02:17:52.30	+09:06:02.7	14.32 ± 0.01	14.87 ± 0.01	14.78 ± 0.04	14.03	13.78	13.88	Comp
0218+1831	02:18:15.64	+18:31:37.7	11.65 ± 0.01	12.93 ± 0.01	13.62	13.68	13.71	13.76	
0219+0150	02:19:02.46	+01:50:57.1	14.81 ± 0.01	14.56 ± 0.01	14.20 ± 0.04	14.04	13.91	13.84	
0220+0635	02:20:48.95	+06:35:13.0	14.74 ± 0.01	15.03 ± 0.01	14.49	13.76	13.55	13.40	
0221−0713	02:21:57.84	−07:13:11.8	14.08 ± 0.01	14.36 ± 0.01	14.51	13.88	13.73	13.71	
0224+2340	02:24:45.41	+23:40:47.4	15.70 ± 0.03	15.84 ± 0.02	14.45 ± 0.02	13.58	13.38	13.37	
0230+4209	02:30:31.41	+42:09:30.9	15.11 ± 0.02	15.08 ± 0.01	14.54 ± 0.07	13.93	13.74	13.71	
0234+2534	02:34:15.15	+25:34:45.2	14.84 ± 0.00	15.04 ± 0.00	13.79 ± 0.04	12.94	12.74	12.71	
0241+4117	02:41:24.63	+41:17:49.3	14.34 ± 0.01	14.27 ± 0.01	13.25	12.72	12.63	12.62	
0245−1242	02:45:53.34	−12:42:21.2	13.26 ± 0.01	14.00 ± 0.01	15.14	14.34	13.90	13.59	

Table B.2: Subdwarf and companion effective temperatures, and distance estimates for the 93 *C2MS* subdwarf plus companion star candidates (Table 7.3), when fitted using the method described in Section 7.5. A MS $T_{\mathrm{eff}} = 0$K corresponds to the best fit being a single subdwarf, without the addition of a companion. The "{" notation is described in Section 7.6 and does not simply represent uncertainties. In all cases, a more realistic error on the subdwarf temperatures is a few thousand Kelvin (see Section 7.6.8). The "E(B-V)" column is the reddening according to the Schlegel et al. [1998] map. The "Q" (Quality) column values correspond to; 1:Good fit, 2:Average fit, 3:Poor fit, 4:WD/WD+MS/MS/CV and 5:Quasar/Galaxy. The classifications in this catagory between values of 1, 2 and 3 are purely qualitative, whereas 4 and 5 are drawn from the SIMBAD and SDSS spectra classifications. Values of three and above are excluded from the histograms shown in Figure 7.9, 7.10 and 7.11. The "SDSS Spec" column corresponds to the visual classification of the SDSS spectrum. The "Known Comp" highlights objects which were known previously to be composite subdwarf plus companion systems (1: Ferguson et al. 1984, 2: Kilkenny et al. 1988, 3: Allard et al. 1994, 4: Aznar Cuadrado & Jeffery 2001, 5: Aznar Cuadrado & Jeffery 2002, 6: Lisker et al. 2005, 7: Østensen et al. 2007, 8: Stroeer et al. 2007). The final column shows objects also included in Table 7.5, where "pWD" stands for possible white dwarf, according to the classification of Girven et al. [2011].

Name	Identifier	R.A.	Dec	No Correction sdB T_{eff} (1000 K)	No Correction MS T_{eff} (1000 K)	No Correction d (kpc)	Reddening Corrected sdB T_{eff} (1000 K)	Reddening Corrected MS T_{eff} (1000 K)	Reddening Corrected d (kpc)	E(B-V)	SIMBAD	Q	SDSS Spec	Known Comp	Table 7.5
0018+0101	HE 0016+0044	00:18:43.50	+01:01:25.5	40{40/39	5.50{5.75	1.5{1.5/1.4	40{40	5.50{5.75	1.4{1.5	0.029	sdB	2			SD
0040−0021	PG 0037−006	00:40:22.88	−00:21:28.8	14{13/15	12.50{12.25	6.8{6.7	14{13/15	12.75{12.50	6.9{6.7	0.020	WD	4	WD		
0054+1508		00:54:11.12	+15:08:19.5	21{22/20	7.25{7.00	3.2{3.2	21{22/20	7.00{6.75	2.9{4.2	0.059		2			
0138+2430	PG 0135+242	01:38:08.67	+24:30:13.8	17{18/16	5.50{5.75	1.9{1.9	21{22/20	4.50{4.75	1.0{1.0	0.126		1			
0141+0614	HS 0139+0559	01:41:39.91	+06:14:37.3	12{13/11	7.25{7.00	4.8{4.4	12{13/11	6.75{7.00	4.5{5.9	0.048	NL	4			CV
0316+0042	PG 0313+005	03:16:20.12	+00:42:22.3	28{29/27	6.25{6.00	2.2{2.3	27{26/28	6.00{5.75	1.9{1.8	0.087	WD	1	SD		
0643+3744		06:43:03.41	+37:44:14.7	22{23/21	6.00{6.25	1.9{1.7	27{26/28	5.75{6.00	1.6{1.8	0.140		1			
0710+2938		07:10:29.29	+29:38:52.3	21{22/20	6.75{7.00	1.5{1.5	25{26	6.75{6.50	1.5{1.6	0.074		1			
0735+2012		07:35:46.24	+20:12:35.6	21{20/22	5.50{5.75	2.1{2.4	23{24/22	5.25{5.00	1.9{2.1	0.041		2			
0737+2642		07:37:12.24	+26:42:25.3	25{24/26	5.50{5.25	1.6{1.8	25{26/24	5.25{5.00	1.5{1.4	0.039	WD	1	SD		
0754+1822		07:54:04.24	+18:22:40.4	22{23/21	7.25{7.00	3.4{3.1	25{24/26	7.50{7.25	3.5{3.3	0.045		1			
0755+2128		07:55:49.51	+21:28:18.0	17{16/18	7.25{7.00	2.3{3.5	20{21/19	7.75{7.50	2.5{1.7	0.065		1			
0804+2250		08:04:20.93	+22:50:18.0	37{36	5.75{5.50	1.5{1.5	31{30/32	4.50{4.25	1.0{0.9	0.048		3			
0805−0741		08:05:16.32	−07:41:50.6	29{30/28	7.00{7.25	2.4{2.2	28{29/27	7.00{7.25	2.1{1.7	0.117		1			
0812+1911		08:12:56.86	+19:11:57.9	14{15/13	7.25{7.50	4.8{4.8	15{16/14	7.00{7.25	4.4{4.0	0.035	CV	4	CV		CV
0814+2019		08:14:06.84	+20:19:01.0	21{22	5.50{5.75	2.0{3.2	23{24/22	5.50{5.75	2.1{1.8	0.042		1	SD		
0815+4740	PG 0812+478	08:15:48.88	+47:40:40.4	40{40	5.00{4.75	1.4{1.3	40{39	4.75{4.50	1.2{1.2	0.067	WD	2			
0818−0701		08:18:06.86	−07:01:23.9	22{23/21	7.75{7.50	3.4{3.6	14{13	5.75{5.50	2.4{3.8	0.097		2			
0820−1739		08:20:03.34	+17:39:14.0	20{21/19	6.75{6.50	2.9{2.9	20{19/21	6.50{6.25	2.6{2.6	0.033		1	SD		
0824+3028	PG 0821+306	08:24:34.03	+30:28:54.6	21{22/20	5.25{5.50	1.4{1.4	21{20/22	5.00{4.75	1.3{1.2	0.044		1	SD		
0825+2006		08:25:07.22	+20:06:36.5	24{26/23	6.00{5.75	1.7{1.5	27{28/26	6.00{6.25	1.7{1.9	0.037		1			

Table B.2:

Name	Identifier	R.A.	Dec	No Correction sdB T_{eff} (1000 K)	No Correction MS T_{eff} (1000 K)	No Correction d (kpc)	Reddening Corrected sdB T_{eff} (1000 K)	Reddening Corrected MS T_{eff} (1000 K)	Reddening Corrected d (kpc)	E(B-V)	SIMBAD	Q	SDSS Spec	Known Comp	Table 7.5
0825+1202		08:25:44.73	+12:02:45.2	22^{23}_{21}	$8.25^{8.50}_{8.00}$	$2.5^{2.7}_{2.3}$	26^{27}_{25}	$8.75^{9.00}_{8.50}$	$2.7^{2.8}_{2.5}$	0.044		1			
0825+1307		08:25:56.86	+13:07:54.3	24^{25}_{23}	$5.00^{5.25}_{4.75}$	$1.0^{1.1}_{1.0}$	27^{28}_{26}	$5.00^{5.25}_{4.75}$	$1.1^{1.1}_{1.0}$	0.034		2			
0829+2246		08:29:02.64	+22:46:37.6	26^{27}_{25}	$6.00^{6.25}_{5.75}$	$2.7^{3.0}_{2.4}$	28^{29}_{26}	$6.00^{6.25}_{5.75}$	$2.7^{2.8}_{2.4}$	0.036		1	SD		
0833−0006		08:33:37.88	−00:06:21.4	$29^{28}_{...}$	$7.25^{7.50}_{7.00}$	$3.1^{2.9}_{2.6}$	29^{30}_{28}	$7.00^{7.25}_{6.75}$	$2.5^{3.0}_{2.3}$	0.041		2			
0844+3102	PG 0841+312	08:44:08.18	+31:02:09.3	22^{23}_{21}	$4.75^{5.00}_{4.50}$	$1.0^{1.1}_{0.9}$	22^{23}_{21}	$4.75^{5.00}_{4.50}$	$1.0^{1.1}_{0.9}$	0.049		1			
0849+1337		08:49:51.40	+13:37:00.4	21^{22}_{20}	$6.75^{7.00}_{6.50}$	$2.4^{3.6}_{2.4}$	21^{22}_{20}	$6.50^{6.75}_{6.25}$	$2.0^{3.1}_{2.0}$	0.040		2			
0907+2739		09:07:34.26	+27:39:03.4	21^{22}_{20}	$5.50^{5.75}_{5.25}$	$2.5^{4.5}_{2.4}$	21^{22}_{20}	$5.50^{5.75}_{5.25}$	$2.3^{3.8}_{2.3}$	0.026	WD	3			
0923+0652		09:23:58.62	+06:52:18.3	29^{30}_{28}	$6.75^{7.00}_{6.50}$	$2.1^{2.9}_{2.0}$	29^{30}_{28}	$6.25^{6.50}_{6.00}$	$1.5^{2.2}_{1.4}$	0.054		1			pWD
0924+2035	PG 0921+208	09:24:05.20	+20:35:46.8	19^{20}_{18}	$4.25^{4.50}_{3.50}$	$1.6^{1.8}_{1.5}$	19^{20}_{18}	$3.00^{3.00}_{0.00}$	$1.6^{1.7}_{1.4}$	0.041		3			
0929+0603		09:29:20.48	+06:03:47.1	$21^{30}_{...}$	$5.75^{6.00}_{5.50}$	$1.6^{2.5}_{1.5}$	29^{30}_{28}	$5.50^{5.75}_{5.50}$	$1.2^{2.0}_{1.1}$	0.052		2			
0935+1621	PG 0932+166	09:35:41.37	+16:21:11.0	30^{31}_{29}	$5.00^{4.75}_{...}$	$1.0^{1.1}_{0.9}$	29^{30}_{28}	$4.75^{5.00}_{4.50}$	$0.9^{1.0}_{0.9}$	0.033		1			
0937+0813	PG 0935+084	09:37:40.95	+08:13:20.5	23^{24}_{22}	$6.00^{6.25}_{5.75}$	$2.0^{2.3}_{1.8}$	23^{24}_{22}	$5.75^{6.00}_{5.50}$	$1.8^{2.0}_{1.6}$	0.042	sdB	1	SD		
0941+0657	PG 0939+072	09:41:59.35	+06:57:17.2	21^{22}_{20}	$6.75^{7.00}_{6.50}$	$1.7^{2.5}_{1.6}$	21^{22}_{20}	$6.00^{6.25}_{5.75}$	$1.4^{2.1}_{1.4}$	0.040	WD	1			
0958+2236		09:58:15.97	+22:36:04.2	$33^{34}_{...}$	$6.75^{6.50}_{...}$	$1.8^{2.7}_{1.7}$	34^{35}_{33}	$6.75^{7.00}_{6.50}$	$1.8^{2.7}_{1.7}$	0.033		1			
1003+3716	PG 1000+375	10:03:19.69	+37:16:35.1	$30^{31}_{...}$	$5.50^{5.75}_{5.25}$	$1.2^{1.7}_{1.1}$	29^{31}_{28}	$5.25^{5.50}_{5.00}$	$1.1^{1.7}_{1.1}$	0.016	WD	1	SD		
1005+4317		10:05:05.07	+43:17:36.5	29^{30}_{28}	$6.75^{7.00}_{...}$	$1.9^{2.5}_{1.8}$	29^{30}_{28}	$6.75^{7.00}_{6.50}$	$1.9^{2.4}_{1.7}$	0.012		1			
1015−0308	SW Sex	10:15:09.39	−03:08:32.3	$18^{17}_{...}$	$7.00^{7.25}_{6.75}$	$2.6^{2.9}_{2.3}$	$20^{21}_{...}$	$7.00^{7.25}_{6.75}$	$2.6^{2.7}_{2.6}$	0.033	NL	4	SD		CV
1018+0721		10:18:01.55	+07:21:24.4	$29^{30}_{...}$	$6.00^{6.25}_{5.75}$	$1.9^{3.0}_{1.9}$	$30^{32}_{...}$	$5.75^{6.00}_{5.50}$	$1.6^{1.8}_{1.5}$	0.027		3	SD		
1018+0953		10:18:33.15	+09:53:36.0	$28^{27}_{...}$	$5.75^{5.50}_{5.00}$	$1.6^{1.7}_{1.6}$	29^{30}_{28}	$4.50^{4.75}_{4.25}$	$0.8^{1.0}_{0.3}$	0.037	WD	1	SD		
1027+2409	PG 1025+244	10:27:51.19	+24:09:17.0	$24^{23}_{...}$	$6.00^{6.25}_{5.75}$	$1.9^{2.3}_{1.7}$	$26^{25}_{...}$	$6.25^{6.50}_{6.00}$	$2.1^{2.4}_{1.9}$	0.017		1	SD		
1049+1842	PG 1046+189	10:49:33.53	+18:42:41.5	$20^{21}_{...}$	$5.75^{5.50}_{5.50}$	$2.1^{2.3}_{1.9}$	20^{21}_{19}	$5.50^{5.75}_{5.25}$	$2.0^{2.3}_{1.8}$	0.033		1			
1100−2113	EC 10583−2057	11:00:46.69	−21:13:12.3	$30^{31}_{...}$	$6.25^{6.50}_{6.00}$	$2.1^{2.3}_{2.0}$	$35^{32}_{...}$	$5.75^{5.75}_{5.50}$	$1.4^{1.3}_{1.2}$	0.053		1			
1102+2616		11:02:11.09	+26:16:46.3	$22^{23}_{...}$	$6.25^{6.50}_{6.00}$	$2.0^{2.2}_{1.8}$	21^{22}_{20}	$6.00^{6.25}_{5.75}$	$1.7^{2.6}_{1.7}$	0.019		1	SD		
1113+0413	PG 1110+045	11:13:17.31	+04:13:14.7	$29^{30}_{...}$	$4.75^{5.00}_{4.50}$	$0.9^{1.4}_{0.4}$	$29^{30}_{...}$	$4.50^{4.75}_{4.25}$	$0.8^{1.3}_{0.3}$	0.051		1	SD	2,7	
1131+0932	PG 1128+098	11:31:14.37	+09:32:20.4	$38^{39}_{...}$	$5.75^{6.00}_{5.50}$	$1.2^{2.1}_{1.2}$	$40^{40}_{...}$	$5.75^{6.00}_{5.50}$	$1.1^{2.1}_{1.2}$	0.039		2	SD		
1149+2231	PG 1146+228	11:49:00.50	+22:31:05.9	$23^{22}_{...}$	$5.25^{5.50}_{5.00}$	$1.4^{1.5}_{1.3}$	$24^{25}_{...}$	$5.25^{5.50}_{5.00}$	$1.4^{1.5}_{1.3}$	0.022		1	SD		
1203+0909	PG 1200+094	12:03:19.46	+09:09:51.6	$27^{25}_{...}$	$5.75^{5.50}_{5.50}$	$1.5^{1.3}_{1.3}$	$28^{26}_{...}$	$5.75^{6.00}_{5.50}$	$1.5^{1.1}_{1.1}$	0.020		1			
1212+4240	PG 1210+429	12:12:38.56	+42:40:02.1	$23^{24}_{...}$	$5.75^{5.50}_{5.50}$	$1.5^{1.4}_{1.4}$	$24^{23}_{...}$	$5.75^{5.50}_{5.50}$	$1.5^{1.7}_{1.4}$	0.015		1	SD	1,2,7	SD
1233+0834		12:33:09.68	+08:34:34.1	$30^{31}_{...}$	$6.00^{6.25}_{...}$	$1.9^{2.7}_{1.7}$	29^{30}_{28}	$5.75^{5.50}_{5.50}$	$1.6^{2.5}_{1.5}$	0.019		2	SD		
1316+4359	PG 1314+442	13:16:33.00	+43:59:04.9	$28^{29}_{...}$	$5.25^{5.50}_{5.00}$	$1.7^{1.5}_{1.1}$	$28^{29}_{...}$	$5.00^{5.25}_{4.75}$	$1.6^{1.6}_{1.0}$	0.021		1			
1325+1212	PG 1323+125	13:25:57.21	+12:12:20.6	$26^{27}_{...}$	$5.75^{6.00}_{5.50}$	$2.1^{2.3}_{1.1}$	$27^{28}_{...}$	$5.75^{6.00}_{5.50}$	$2.1^{2.3}_{1.9}$	0.034		1			
1326+0357	PG 1323+042	13:26:19.95	+03:57:54.3	$24^{25}_{...}$	$5.00^{5.25}_{4.75}$	$1.5^{1.4}_{1.4}$	$26^{27}_{...}$	$5.00^{5.25}_{4.75}$	$1.6^{1.7}_{1.5}$	0.025	sdO	2	SD		
1402+3215		14:02:32.86	+32:15:21.5	$22^{21}_{...}$	$6.25^{6.50}_{6.00}$	$1.9^{2.0}_{1.7}$	$22^{21}_{...}$	$6.00^{6.25}_{5.75}$	$1.7^{1.9}_{1.5}$	0.015		1	SD		
1404+2450	PG 1402+251	14:04:29.98	+24:50:20.6	$27^{26}_{...}$	$6.25^{6.50}_{6.00}$	$1.8^{1.6}_{1.5}$	27^{28}_{26}	$6.00^{6.25}_{5.75}$	$1.6^{1.7}_{1.5}$	0.017		1			
1407+3103		14:07:47.63	+31:03:18.3	$20^{19}_{...}$	$5.25^{5.50}_{5.00}$	$1.5^{0.9}_{...}$	20^{21}_{19}	$4.75^{4.50}_{4.50}$	$1.4^{1.4}_{0.8}$	0.011		1			
1421+0753	KN Boo	14:21:38.21	+07:53:20.9	$27^{28}_{...}$	$5.25^{5.50}_{5.00}$	$1.6^{1.7}_{1.5}$	$29^{28}_{...}$	$4.50^{4.75}_{...}$	$0.9^{1.5}_{0.9}$	0.028	sdB	1	SD		
1502−0245	PG 1459−026	15:02:12.13	−02:45:56.7	$24^{25}_{...}$	$6.25^{6.50}_{6.00}$	$1.8^{1.5}_{1.5}$	24^{26}_{23}	$6.00^{6.25}_{5.75}$	$1.5^{1.7}_{1.4}$	0.124		1	SD		
1517+0310	PG 1514+034	15:17:14.30	+03:10:27.6	$40^{40}_{...}$	$6.00^{6.25}_{5.75}$	$1.1^{1.1}_{1.0}$	39^{40}_{38}	$5.75^{6.50}_{5.50}$	$0.9^{1.0}_{0.9}$	0.039	WD	1	SD	1,7	SD
1518+2019	PG 1516+205	15:18:38.81	+20:19:47.0	$24^{26}_{...}$	$6.00^{6.50}_{6.25}$	$1.5^{1.4}_{1.4}$	$26^{27}_{...}$	$6.00^{6.25}_{5.75}$	$1.5^{1.4}_{1.1}$	0.051		1			
1524+0134		15:24:03.04	+01:34:21.3	$27^{26}_{...}$	$6.25^{6.50}_{6.00}$	$1.3^{1.4}_{1.2}$	28^{29}_{27}	$6.00^{6.25}_{5.75}$	$1.1^{1.1}_{0.7}$	0.065		1			

Table B.2:

Name	Identifier	R.A.	Dec	No Correction			Reddening Corrected								
				sdB T_{eff} (1000 K)	MS T_{eff} (1000 K)	d (kpc)	sdB T_{eff} (1000 K)	MS T_{eff} (1000 K)	d (kpc)	E(B-V)	SIMBAD	Q	SDSS Spec	Known Comp	Table 7.5
1528+1300		15:28:33.90	+13:00:57.2	40{40/39}	6.00{6.25}	1.3{1.3}	40{40/40}	5.75{5.50}	1.1{1.1}	0.040		3			
1530+1204		15:30:05.00	+12:04:02.0	11{11/32}	8.00{8.50}	4.8{4.5}	14{14/21}	9.25{8.75}	4.8{3.7}	0.038		2			
1542+0056		15:42:18.31	+00:56:12.6	29{30/11}	6.50{6.75}	1.5{2.1}	21{21/22}	6.25{6.50}	1.3{2.0}	0.098		1			
1602+0725	PG 1559+076	16:02:08.96	+07:25:10.8	32{35/30}	5.25{5.50}	0.9{1.1}	37{37/38}	5.25{5.00}	1.0{1.0/0.9}	0.047		1			
1603+0954		16:03:24.51	+09:54:42.9	29{30/28}	5.75{6.00}	2.0{3.0/2.0}	32{32/33}	5.75{6.50}	2.0{2.1}	0.059		3	SD		
1610+3450		16:10:40.72	+34:50:44.1	29{30/28}	7.50{7.75}	2.0{2.0/2.5}	31{31/30}	7.50{7.75}	2.0{2.1}	0.018		1			
1618+2141		16:18:06.46	+21:41:25.0	22{22/23}	6.00{6.25}	1.3{1.3/1.7}	24{24/21}	6.00{6.25}	1.1{1.7}	0.069		1			
1619+1453	PG 1617+150	16:19:49.35	+14:53:09.5	29{30/28}	6.00{5.75}	1.3{1.3/1.4}	29{29/30}	5.75{5.50}	1.1{1.1}	0.051		1			
1629+0026		16:29:06.76	+00:26:19.9	29{30/28}	7.25{7.50}	2.5{3.0/2.4}	32{32/33}	7.25{7.00}	2.4{2.3/2.6}	0.095		1			
1640+3842	PN G061.9+41.3	16:40:18.20	+38:42:20.6	15{16/14}	3.00{4.25}	1.8{1.8/1.6}	16{16/17}	3.00{3.25}	1.8{1.8/1.1}	0.012	PN	3			
1709+4054	PG 1708+409	17:09:59.23	+40:54:49.5	26{28/25}	5.50{5.75}	1.7{1.9}	28{28/29}	5.50{5.75}	1.8{1.8/1.5}	0.029	WD	1			SD
1710+2238		17:10:36.45	+22:38:07.4	31{32/30}	7.25{7.50}	1.4{1.5/1.3}	34{34/35}	7.50{7.25}	1.4{1.5}	0.058		1			
1734+3213		17:34:49.30	+32:13:43.5	23{23/22}	6.00{5.75}	1.7{1.6}	25{25/24}	6.00{6.25}	1.7{1.5}	0.054		1			
1822+4320		18:22:42.87	+43:20:37.4	31{32/30}	3.00{3.25}	0.5{0.5}	40{40/39}	0.00{25.00}	0.6{10.7/0.6}	0.050		1			
1834+4237		18:34:14.46	+42:37:27.3	22{23/21}	6.25{6.00}	2.7{3.2/2.4}	23{23/22}	6.00{6.25}	2.3{2.6}	0.055		3			
2020+0704		20:20:27.24	+07:04:14.5	23{24/21}	5.75{6.00}	1.1{1.1/1.2}	38{38/37}	4.50{4.25}	0.6{0.6/0.5}	0.143		1			
2023+1230		20:23:14.11	+12:30:56.9	21{22/20}	6.00{6.25}	1.7{1.7/2.6}	35{35/34}	4.75{5.00}	0.8{0.8/0.7}	0.123		2			
2047−0542		20:47:42.36	−05:42:32.0	22{23/21}	6.00{6.25}	1.6{1.6/1.8}	24{24/25}	5.75{6.00}	1.4{1.5}	0.050		1			
2052−0457		20:52:26.19	−04:57:46.0	29{30/28}	6.00{6.25}	1.2{1.2/1.7}	37{37/36}	6.25{6.50}	1.3{1.3/1.2}	0.104		1			
2056+0425		20:56:19.33	+04:25:23.6	22{22/21}	6.50{6.25}	3.0{3.0/2.7}	21{21/20}	6.00{5.75}	2.2{2.3}	0.092		1			
2105+1635		21:05:15.38	+16:35:18.3	21{22/20}	6.00{5.75}	1.8{1.8/2.0}	30{30/31}	4.75{4.50}	0.8{0.9/0.8}	0.075		3			
2117−0015		21:17:15.90	−00:15:47.7	13{14/12}	6.75{6.50}	3.5{3.2/3.5}	14{14/13}	12.75{13.00/12.50}	5.4{6.0/4.9}	0.055		1	SD		pWD
2117−0006		21:17:42.22	−00:06:19.9	21{21/22}	6.25{6.50}	2.0{2.2/2.3}	22{22/23}	6.00{6.25}	1.6{1.6/1.5}	0.074		1	SD		pWD
2129+0045		21:29:06.05	+00:45:09.6	25{25/24}	5.50{5.75}	2.0{2.1/2.9}	29{29/30}	4.75{5.00}	1.2{1.2/1.2}	0.044	WD	1	SD		
2129+1039		21:29:29.11	+10:39:09.9	21{21/23}	5.50{5.75}	1.5{1.5/2.4}	25{25/26}	5.50{5.75}	1.5{1.6/1.4}	0.064		1			
2135+2026		21:35:51.03	+20:26:45.3	21{21/22}	5.75{6.00}	1.8{1.8/2.8}	22{22/23}	5.00{5.25}	1.4{1.4/1.3}	0.124		1			
2138+0442	PG 2135+045	21:38:00.77	+04:42:11.5	25{25/26}	5.00{4.25}	1.2{1.2/1.3}	27{27/26}	4.00{4.75/3.75}	1.0{1.0}	0.056		1		3,4,5	SD
2143+1244		21:43:54.65	+12:44:58.3	30{30/31}	6.25{6.00}	2.9{3.3}	29{29/28}	5.75{5.50}	2.1{3.1/2.0}	0.095	CV	4	CV		CV
2147−0837		21:47:08.07	−08:37:47.5	29{30/28}	6.50{6.25}	2.3{3.1}	29{29/30}	6.25{6.00}	1.9{2.2/1.8}	0.044		1	SD		
2223+3850		22:23:26.78	+38:50:16.7	32{33/31}	7.75{8.00}	2.9{3.1/2.6}	28{28/29}	8.00{8.25}	2.8{2.9/2.2}	0.108		1			
2346+3657		23:46:21.39	+36:57:27.6	29{29/28}	7.25{7.50}	2.5{2.4}	22{22/23}	6.75{6.50}	2.0{2.1/1.8}	0.142		2			
2346+0344		23:46:55.71	+03:44:29.4	30{31/29}	6.75{7.00/6.50}	1.7{1.5}	29{29/30}	6.50{6.75/6.25}	1.5{1.5/1.4}	0.054		1			

Table B.3: Subdwarf and companion effective temperatures, and distance estimates for the *SU* sample of subdwarf plus companion star systems when fitted using the method described in Section 7.5, following the same format as Table B.2. A MS $T_{\rm eff}$ = 0K corresponds to the best fit being a single subdwarf, without the addition of a companion. The "{" notation is described in Section 7.6 and does not simply represent uncertainties. In all cases, a more realistic error on the subdwarf temperatures is a few thousand Kelvin (see Section 7.6.8). The final column shows objects also included in Table 7.6.

				No Correction			Reddening Corrected									
Name	Identifier	R.A.	Dec	sdB $T_{\rm eff}$ (1000 K)	MS $T_{\rm eff}$ (1000 K)	d (kpc)	sdB $T_{\rm eff}$ (1000 K)	MS $T_{\rm eff}$ (1000 K)	d (kpc)	E(B−V)	SIMBAD	Q	SDSS Spec	Known Comp	Table 7.6
0018+0101	HE 0016+0044	00:18:43.52	+01:01:23.6	24{25,23	4.25{4.50,4.00	1.2{1.3,1.2	28{29,27	4.75{5.00,4.50	1.5{1.6,1.0	0.029	sdB	1			SD
0032+0739	PB 6015	00:32:21.87	+00:39:34.4	21{22,20	5.25{5.50,5.00	4.4{4.6,4.4	21{22,20	5.00{5.25,4.50	4.1{4.6,5.5	0.040	Comp	3			WDMS
0051+0059		00:51:49.65	+00:59:50.7	27{28,26	5.00{5.25,4.75	4.5{4.8,4.2	28{29,27	5.00{5.25,4.75	4.6{4.8,4.1	0.028	WD	5			
0054+1508		00:54:11.11	+15:08:19.3	29{30,28	7.25{7.50,7.00	2.8{3.2,2.3	29{30,28	7.25{7.50,7.00	2.7{3.2,2.6	0.059		3			
0141+0614	HS 0139+0559	01:41:39.92	+06:14:37.6	14{15,13	7.25{7.50,7.00	3.7{4.9,...	14{15,13	7.00{7.25,6.75	3.6{4.7,3.5	0.048	NL	4			CV
0205+0712	PB 6645	02:05:59.87	+07:12:39.9	25{26,23	5.75{6.00,5.55	7.3{8.1,...	26{28,24	5.75{6.00,5.50	7.3{8.3,6.5	0.056		1			
0300−0023	WD 0257−005	03:00:24.57	−00:23:42.1	38{34	5.00{4.75	3.2{2.8	39{40,38	4.50{4.75,4.25	2.6{2.7,2.6	0.120	Comp	1			WDMS
0316+0042	PG 0313+005	03:16:20.13	+00:42:22.8	26{27,25	6.00{6.25,5.75	2.0{1.8,...	27{28,26	6.00{6.25,5.75	2.0{2.2,1.8	0.087	WD	1	SD		
0737+2642		07:37:12.27	+26:42:24.7	25{26,24	5.50{5.75,5.25	1.6{1.8,1.5	26{27,25	5.00{4.75,...	1.4{1.5,1.3	0.039	WD	1	SD		
0744+2103		07:44:41.80	+21:03:52.6	40{40,39	4.75{5.00,4.50	2.8{3.0,2.7	39{40,38	4.00{4.25,3.75	2.3{3.2,2.3	0.053		1			
0752+2535		07:52:39.82	+25:35:50.0	17{18,16	4.25{4.50,4.00	4.8{4.8,...	11{15,11	18.00{17.00,17.00	36.9{41.9,32.2	0.061	WD	2			
0755+2128		07:55:49.49	+21:28:18.5	21{22,20	7.00{7.25,6.75	2.0{2.4,...	17{18,16	6.50{6.75,6.25	1.7{2.4,1.7	0.065		1	SD		
0758+2818		07:58:13.60	+28:18:16.0	23{24,22	6.50{6.75,6.25	3.6{3.9,...	18{19,17	6.25{6.50,6.00	3.5{3.9,3.1	0.039		1	SD		
0809+1924		08:09:21.89	+19:24:00.1	40{40,39	0.00{25.00	2.3{36.6,...	40{40,39	0.00{25.00	2.0{31.4,1.9	0.038		3	WD		
0813+2813		08:13:52.02	+28:13:17.3	20{21,19	6.25{6.50,6.00	6.4{4.6,...	20{21,19	6.00{6.25,5.75	5.8{6.0,4.1	0.032	CV	4	CV		CV
0814+2019		08:14:06.80	+20:19:01.7	20{21,19	6.25{6.50,6.00	3.5{3.7,...	20{21,19	5.75{6.00,5.50	2.9{3.1,2.1	0.042		1	SD		
0814+2811		08:14:53.92	+28:11:22.5	22{23,21	6.00{6.25,5.55	3.7{4.3,...	22{23,21	5.75{6.00,5.50	3.2{3.9,2.9	0.030		1	SD		pWD
0829+2246		08:29:02.62	+22:46:36.8	21{22,20	5.25{5.50,5.00	1.9{1.6,...	22{23,21	5.25{5.50,5.00	1.9{1.7,1.7	0.036		1	SD		
0833−0006		08:33:37.87	−00:06:21.4	29{30,28	6.75{7.00,6.50	2.4{2.7,...	29{30,28	6.75{7.00,6.50	2.3{2.6,2.1	0.041		2			
0843−0048		08:43:51.07	−00:48:24.6	24{27,22	6.50{7.00,6.25	3.0{3.6,...	19{20,18	6.00{6.25,5.75	2.7{3.0,2.4	0.033		1			
0846+0142		08:46:28.66	+01:42:17.0	24{25,23	4.50{4.75,4.25	4.6{4.4,...	28{29,27	4.00{4.25,3.75	4.5{4.5,2.7	0.042		1			
0854+0853	PN A66 31	08:54:13.16	+08:53:52.9	40{40,39	3.00{3.00	1.2{1.2,...	40{40,39	0.00{25.00	1.1{1.6,1.1	0.065	PN	3			pWD
0856+0518		08:56:33.17	+05:18:39.6	29{30,28	3.25{3.00	2.6{2.6,...	40{40,38	3.50{3.75,3.25	3.1{3.1,3.0	0.050		1			
0859+0759		08:59:26.08	+07:59:13.3	22{23,21	5.75{5.50	2.9{3.2,...	23{24,22	3.50{5.25,3.25	2.5{2.8,2.5	0.080		1			
0902+0734		09:02:25.06	+07:34:04.0	21{22,20	6.50{6.25	3.5{3.3,...	22{23,21	6.25{6.50,6.00	3.1{3.8,2.3	0.072		1	SD		
0906+0251		09:06:40.00	+02:51:46.4	39{40,38	6.75{7.00,6.50	5.7{6.1,...	28{29,27	6.50{6.75,6.50	5.2{6.0,4.6	0.034		1	SD		
0906+0437		09:06:00.86	+04:37:45.1	21{22,20	5.75{6.00,5.50	2.4{3.4,...	27{28,26	6.25{6.50,6.00	3.0{3.7,3.3	0.037		1	SD		
0920+1057		09:20:48.04	+10:57:34.5	34{35,33	4.75{5.00,4.50	3.3{3.5,...	40{40,40	4.75{5.00,4.50	3.3{3.4,3.2	0.036	Comp	1			WDMS
0920+3356	BK Lyn	09:20:11.21	+33:56:42.4	20{18	5.50{6.25,5.25	2.3{1.7,...	20{19	6.50{6.75,6.25	2.1{1.6,2.2	0.017	NL	4	WD		CV
0925−0140		09:25:35.00	−01:40:46.8	17{16	5.50{5.25	9.4{14.9,9.4	20{19	5.50{5.75,5.25	9.3{5.8,...	0.031		2			
0929+0603		09:29:20.43	+06:03:46.2	29{28	6.00{5.75	1.6{1.4,...	29{28	5.50{5.75,5.50	1.2{1.1,...	0.052		1	SD		
0937+0813	PG 0935+084	09:37:40.93	+08:13:20.9	21{22	5.75{6.00,5.50	1.7{1.6,...	23{24,22	5.75{6.00,5.25	1.7{1.9,1.5	0.042	sdB	1	SD		
0939+3038		09:39:14.38	+30:38:17.3	39{40	6.25{6.50,6.00	5.0{4.1,...	37{38	6.00{6.25,5.75	4.4{4.0,...	0.017		1	SD		
0941+0657	PG 0939+072	09:41:59.32	+06:57:17.2	29{30,28	6.50{6.75,6.25	1.7{1.5,...	30{31	6.25{6.50,6.00	1.5{1.6,1.3	0.040		2	SD		

Table B.3:

Name	Identifier	R.A.	Dec	sdB T$_{eff}$ (1000 K)	MS T$_{eff}$ (1000 K)	d (kpc)	sdB T$_{eff}$ (1000 K)	MS T$_{eff}$ (1000 K)	d (kpc)	E(B-V)	SIMBAD	Q	SDSS Spec	Known Comp	Table 7.6
0951+0347		09:51:01.29	+03:47:57.0	23$^{24}_{22}$	4.00$^{4.25}_{3.75}$	1.9$^{2.7}_{1.7}$	28$^{29}_{27}$	4.00$^{4.25}_{3.75}$	2.0$^{2.0}_{2.0}$	0.039	WD	1	SD		
0959+0330	PG 0957+037	09:59:52.01	+03:30:32.8	31$^{32}_{30}$	3.00$^{3.25}_{}$	1.1$^{1.2}_{1.1}$	40$^{40}_{39}$	3.00$^{3.25}_{3.00}$	1.3$^{1.3}_{}$	0.025		2			pWD
1006+0032	PG 1004+008	10:06:45.75	+00:32:04.5	26$^{27}_{25}$	5.00$^{5.25}_{4.75}$	3.3$^{3.6}_{3.1}$	29$^{30}_{28}$	4.25$^{4.50}_{}$	1.9$^{3.1}_{}$	0.036		1			pWD
1011−0212		10:11:36.23	−02:12:14.6	25$^{26}_{24}$	4.75$^{5.00}_{4.50}$	4.0$^{4.4}_{}$	28$^{29}_{27}$	4.75$^{5.00}_{4.50}$	4.2$^{4.2}_{}$	0.040		1			
1012+0044		10:12:18.95	+00:44:13.4	26$^{27}_{25}$	4.75$^{4.50}_{}$	5.0$^{4.7}_{}$	29$^{30}_{28}$	3.75$^{3.50}_{}$	2.9$^{2.8}_{}$	0.033	WD	1	SD		
1015+0308	SW Sex	10:15:09.38	−03:08:32.8	21$^{20}_{}$	6.75$^{6.50}_{}$	2.0$^{1.9}_{}$	23$^{22}_{}$	6.50$^{6.25}_{}$	1.8$^{1.6}_{}$	0.033	NL	4			CV
1016+0443		10:16:42.94	+04:43:17.7	29$^{30}_{28}$	4.50$^{4.25}_{}$	4.8$^{4.9}_{4.8}$	29$^{30}_{28}$	4.00$^{3.75}_{}$	4.3$^{4.3}_{4.3}$	0.024	Comp	4	WD		
1018+0953		10:18:33.11	+09:53:36.1	35$^{36}_{34}$	5.50$^{5.25}_{}$	1.3$^{1.3}_{1.3}$	38$^{39}_{37}$	5.25$^{5.25}_{}$	1.2$^{1.3}_{}$	0.037	WD	1	WD		
1034+0327	HS 1031+0343	10:34:30.16	+03:27:36.4	18$^{19}_{17}$	4.25$^{4.50}_{}$	4.7$^{5.3}_{}$	20$^{21}_{19}$	4.50$^{19.00}_{4.25}$	5.0$^{37.9}_{3.8}$	0.038	WD	3	WD		
1040+0217		10:40:32.74	+02:17:29.7	30$^{33}_{}$	4.25$^{4.50}_{}$	2.4$^{2.8}_{}$	39$^{40}_{38}$	4.50$^{4.75}_{}$	3.0$^{3.1}_{}$	0.035		1	SD		
1055+0930		10:55:25.88	+09:30:56.3	28$^{29}_{}$	6.50$^{6.75}_{}$	7.0$^{7.1}_{}$	27$^{28}_{26}$	6.00$^{5.75}_{}$	5.5$^{5.9}_{}$	0.030		1	SD		
1057−0230		10:57:59.29	−02:30:02.1	27$^{28}_{25}$	5.50$^{5.25}_{}$	5.6$^{6.0}_{}$	27$^{26}_{25}$	5.25$^{5.00}_{}$	5.1$^{4.7}_{}$	0.042		2	SD		
1100+0346		11:00:53.55	+03:46:22.8	34$^{36}_{33}$	3.75$^{3.50}_{}$	2.7$^{2.6}_{}$	40$^{40}_{39}$	3.75$^{3.50}_{}$	2.9$^{3.0}_{}$	0.044	WD	1	SD		pWD
1113+0413	PG 1110+045	11:13:17.32	+04:13:14.5	30$^{31}_{}$	4.75$^{4.50}_{}$	0.9$^{0.8}_{}$	34$^{35}_{}$	5.00$^{4.75}_{}$	1.0$^{1.1}_{}$	0.051		1		2,7	
1116+0755		11:16:16.37	+07:55:32.5	28$^{29}_{}$	5.00$^{5.25}_{}$	2.3$^{2.4}_{}$	29$^{30}_{}$	3.75$^{3.50}_{}$	1.2$^{1.2}_{}$	0.042		1	SD		pWD
1131+0932	PG 1128+098	11:31:14.32	+09:32:19.0	40$^{40}_{}$	5.75$^{6.00}_{}$	1.2$^{1.1}_{}$	39$^{38}_{}$	5.50$^{5.25}_{}$	1.1$^{1.1}_{}$	0.039		1			
1134+0153		11:34:18.00	+01:53:22.1	38$^{39}_{}$	6.50$^{6.75}_{}$	7.0$^{7.8}_{}$	24$^{23}_{}$	6.00$^{6.25}_{}$	5.8$^{6.5}_{}$	0.031	WD	1	SD		pWD
1135+0731		11:35:36.86	+07:31:28.3	29$^{30}_{}$	6.25$^{6.50}_{}$	6.4$^{8.2}_{}$	29$^{30}_{}$	6.00$^{6.25}_{}$	5.5$^{7.3}_{}$	0.041		1	SD		
1203+0909	PG 1200+094	12:03:19.38	+09:09:51.6	27$^{26}_{}$	5.75$^{5.50}_{}$	1.5$^{1.6}_{}$	28$^{27}_{}$	5.75$^{5.50}_{}$	1.5$^{1.6}_{}$	0.020		1	SD		pWD
1215+1351		12:15:23.73	+13:51:02.3	21$^{22}_{20}$	4.50$^{4.25}_{}$	3.1$^{3.1}_{}$	21$^{22}_{20}$	4.00$^{4.25}_{}$	2.9$^{2.8}_{}$	0.032		2	SD		pWD
1228+5993	WD 1226+110	12:28:59.93	+10:40:33.0	21$^{22}_{}$	3.00$^{3.00}_{}$	2.2$^{2.2}_{}$	23$^{24}_{}$	3.00$^{3.00}_{}$	2.3$^{2.4}_{}$	0.028	WD	4	WD		pWD
1233+0834		12:33:09.62	+08:34:34.5	30$^{31}_{}$	6.00$^{6.25}_{}$	1.9$^{2.2}_{}$	30$^{31}_{}$	5.75$^{6.00}_{}$	1.7$^{1.5}_{}$	0.019		1	SD		
1235+1029		12:35:13.03	+10:29:59.5	23$^{24}_{}$	5.75$^{5.50}_{}$	3.0$^{3.4}_{}$	24$^{23}_{}$	5.75$^{5.50}_{}$	3.0$^{3.7}_{}$	0.026		1	SD		
1237−0151		12:37:04.70	−01:51:23.0	23$^{25}_{}$	4.75$^{5.00}_{}$	3.9$^{4.3}_{}$	25$^{24}_{}$	4.75$^{5.00}_{}$	3.9$^{3.6}_{}$	0.028		1			pWD
1247−0039	PG 1244−004	12:47:06.79	−00:39:25.8	33$^{34}_{}$	0.00$^{0.00}_{}$	1.8$^{43.0}_{1.8}$	39$^{40}_{37}$	0.00$^{25.00}_{0.00}$	2.1$^{41.0}_{2.0}$	0.033	WD	3	SD		pWD
1300+0045	PG 1257+010	13:00:25.52	+00:45:30.1	29$^{30}_{}$	4.75$^{5.00}_{}$	1.4$^{2.0}_{}$	29$^{30}_{}$	4.50$^{4.75}_{}$	1.2$^{2.9}_{}$	0.026		1	SD		pWD
1300+0057	HE 1258+0113	13:00:59.21	+00:57:11.8	30$^{31}_{}$	3.50$^{3.75}_{}$	1.7$^{1.6}_{}$	32$^{31}_{}$	3.50$^{3.25}_{}$	1.8$^{1.7}_{}$	0.025	WD	1	SD	8	SD
1312+2245		13:12:42.62	+22:45:04.2	26$^{25}_{}$	3.00$^{3.00}_{}$	3.7$^{3.8}_{}$	29$^{30}_{}$	0.00$^{25.00}_{0.00}$	2.1$^{59.1}_{2.1}$	0.013		3			
1315+0245		13:15:12.39	+02:45:31.7	33$^{32}_{}$	3.25$^{3.50}_{}$	0.9$^{1.0}_{}$	36$^{35}_{}$	3.25$^{3.00}_{}$	0.9$^{1.0}_{}$	0.023		1			
1316+0348	PG 1314+041	13:16:38.48	+03:48:18.5	29$^{30}_{}$	4.75$^{4.50}_{}$	1.5$^{1.4}_{}$	29$^{30}_{}$	4.50$^{4.25}_{}$	1.3$^{1.2}_{}$	0.030		1	SD		pWD
1316+0739		13:16:33.59	+07:39:41.3	29$^{30}_{}$	6.75$^{7.00}_{}$	6.0$^{5.4}_{}$	29$^{30}_{}$	6.50$^{6.75}_{}$	5.2$^{4.7}_{}$	0.026		1	SD		
1319−0141		13:19:32.20	−01:41:31.2	30$^{31}_{}$	6.25$^{6.50}_{}$	7.8$^{6.8}_{}$	29$^{32}_{}$	6.00$^{6.25}_{}$	6.6$^{8.9}_{}$	0.024		1	SD		
1323+2615		13:23:57.28	+26:15:02.5	20$^{21}_{}$	5.00$^{4.75}_{}$	5.8$^{5.6}_{}$	21$^{22}_{}$	4.25$^{4.50}_{}$	3.3$^{5.4}_{}$	0.018		1			pWD
1325+1212	PG 1323+125	13:25:57.24	+12:12:21.3	26$^{25}_{}$	5.75$^{5.50}_{}$	2.1$^{2.9}_{}$	27$^{26}_{}$	5.75$^{5.50}_{}$	2.1$^{2.3}_{}$	0.034		1	SD		
1326+0357	PG 1323+042	13:26:19.95	+03:57:54.4	22$^{21}_{}$	4.75$^{4.50}_{}$	1.4$^{1.5}_{}$	25$^{24}_{}$	5.00$^{4.75}_{}$	1.5$^{1.4}_{}$	0.025	sdO	1	SD		
1328+3108		13:28:56.72	+31:08:46.0	40$^{40}_{}$	4.75$^{4.50}_{}$	4.2$^{3.9}_{}$	38$^{39}_{}$	4.50$^{4.75}_{}$	3.8$^{3.5}_{}$	0.011	Galaxy	5	Galaxy		
1336+1126	PG 1334+117	13:36:53.99	+11:26:05.4	29$^{30}_{}$	4.25$^{4.50}_{}$	1.6$^{1.5}_{}$	30$^{31}_{}$	4.25$^{4.50}_{}$	1.6$^{1.6}_{}$	0.031		1	SD		
1341+0317		13:41:22.97	+03:17:51.6	28$^{24}_{}$	6.50$^{6.00}_{}$	8.9$^{6.0}_{}$	27$^{25}_{}$	6.25$^{6.00}_{}$	7.8$^{6.9}_{}$	0.024	WD	1	SD		
1351+0234		13:51:40.69	+02:34:29.2	29$^{30}_{}$	4.25$^{4.50}_{}$	2.5$^{2.5}_{}$	30$^{31}_{}$	3.75$^{3.50}_{}$	2.4$^{2.5}_{}$	0.027	WD	1	SD		
1352+0910		13:52:28.14	+09:10:39.1	29$^{30}_{}$	4.00$^{4.25}_{}$	4.0$^{4.0}_{}$	29$^{30}_{}$	4.00$^{4.25}_{}$	3.9$^{3.9}_{}$	0.028	DA+M	4	CV		WDMS
1402+0725	PG 1359+077	14:02:03.86	+07:25:39.1	26$^{25}_{}$	5.00$^{4.75}_{}$	2.3$^{2.4}_{}$	27$^{28}_{}$	5.00$^{5.25}_{}$	2.3$^{2.1}_{}$	0.024		1	SD		

Table B.3:

Name	Identifier	R.A.	Dec	sdB T_{eff} (1000 K)	MS T_{eff} (1000 K)	d (kpc)	sdB T_{eff} (1000 K)	MS T_{eff} (1000 K)	d (kpc)	E(B-V)	SIMBAD	Q	SDSS Spec	Known Comp	Table 7.6
1402+3215		14:02:32.83	+32:15:22.2	22^{23}_{21}	$6.25^{6.50}_{6.50}$	$1.9^{2.1}_{1.7}$	23^{24}_{22}	$6.25^{6.50}_{6.00}$	$1.9^{2.1}_{1.7}$	0.015		1	SD		
1421−0753	KN Boo	14:21:38.17	+07:53:19.6	27^{28}_{26}	$5.25^{5.00}_{5.00}$	$1.6^{1.7}_{1.5}$	27^{28}_{28}	$5.00^{5.25}_{5.25}$	$1.5^{1.6}_{1.3}$	0.028	sdB	1	SD		
1422+0920		14:22:11.11	+09:20:43.6	26^{25}_{25}	$4.75^{4.50}_{4.50}$	$3.5^{3.2}_{3.7}$	28^{29}_{27}	$4.75^{4.50}_{4.50}$	$3.5^{3.6}_{3.2}$	0.024		1	SD		pWD
1425−0302		14:25:26.81	+03:02:00.8	17^{18}_{16}	$6.25^{6.00}_{6.00}$	$7.0^{7.0}_{10.4}$	17^{18}_{16}	$6.00^{5.75}_{5.75}$	$6.2^{9.4}_{6.2}$	0.035		3			
1429−0643		14:29:47.00	+06:43:35.0	22^{21}_{21}	$6.50^{6.75}_{6.25}$	$9.3^{10.3}_{8.3}$	21^{22}_{20}	$6.25^{6.00}_{6.00}$	$7.9^{11.3}_{7.5}$	0.025	HII	4	Galaxy		
1440−1223		14:42:10.10	+12:23:34.3	21^{22}_{20}	$5.00^{4.75}_{4.75}$	$5.3^{5.3}_{}$	21^{22}_{20}	$5.00^{4.75}_{4.75}$	$5.2^{5.1}_{}$	0.029		3			
1442+0910		14:42:10.30	+09:10:07.6	26^{27}_{24}	$5.00^{4.75}_{5.25}$	$6.6^{6.7}_{}$	26^{27}_{25}	$4.75^{5.00}_{5.00}$	$6.2^{6.6}_{}$	0.023		1	SD		pWD
1443−0931		14:43:07.70	+09:31:34.0	28^{27}_{27}	$4.50^{4.75}_{4.75}$	$4.5^{4.5}_{}$	30^{31}_{25}	$3.25^{3.50}_{3.50}$	$2.6^{2.7}_{}$	0.031		1	SD		pWD
1445−0002	V594 Vir	14:45:14.93	+00:02:48.9	25^{26}_{25}	$5.50^{5.75}_{5.75}$	$4.6^{4.5}_{}$	27^{28}_{28}	$5.50^{5.75}_{5.75}$	$4.6^{5.0}_{}$	0.041	Var*	1	SD		pWD
1456−0330		14:56:01.20	+03:30:28.8	18^{17}_{17}	$4.50^{4.50}_{4.50}$	$5.6^{5.5}_{}$	19^{20}_{18}	$4.50^{4.25}_{4.25}$	$5.6^{6.1}_{}$	0.041		3			
1500+0642		15:00:11.77	+06:42:11.5	27^{26}_{26}	$6.50^{6.75}_{6.25}$	$3.9^{4.2}_{}$	34^{35}_{33}	$3.25^{3.00}_{3.00}$	$2.5^{2.4}_{}$	0.034		1	SD		pWD
1501−0537		15:01:15.02	+05:37:39.4	30^{31}_{29}	$6.00^{6.25}_{6.05}$	$5.1^{5.4}_{}$	28^{27}_{27}	$5.75^{6.00}_{6.00}$	$4.4^{4.8}_{}$	0.038		1	SD		
1502−0245	PG 1459−026	15:02:12.12	−02:45:57.8	27^{26}_{26}	$4.50^{4.75}_{4.75}$	$1.4^{1.5}_{}$	22^{23}_{21}	$5.75^{5.50}_{5.50}$	$1.3^{1.5}_{}$	0.124		1	SD		pWD
1507+0724		15:07:37.71	+07:24:16.5	29^{30}_{28}	$6.50^{6.75}_{6.25}$	$4.1^{4.4}_{}$	28^{29}_{27}	$4.00^{4.25}_{4.25}$	$3.8^{3.8}_{}$	0.030		1	SD		
1509−0143		15:09:02.07	−01:43:54.4	26^{27}_{26}	$4.00^{3.75}_{3.75}$	$3.7^{4.8}_{}$	30^{31}_{29}	$6.50^{6.75}_{6.25}$	$3.6^{4.0}_{}$	0.072	WD	1	SD		
1510+0409		15:10:42.06	+04:09:55.6	28^{29}_{27}	$5.25^{5.00}_{5.00}$	$3.4^{3.3}_{}$	30^{31}_{29}	$3.00^{3.25}_{3.25}$	$2.0^{2.1}_{}$	0.039		1	SD		pWD
1516−0926		15:16:46.27	+09:26:31.7	28^{27}_{27}	$5.25^{5.00}_{5.00}$	$4.4^{4.3}_{}$	32^{33}_{31}	$4.25^{4.00}_{4.00}$	$2.4^{2.3}_{}$	0.039		1			
1517+0310	PG 1514+034	15:17:14.27	+03:10:28.0	40^{40}_{39}	$6.00^{5.75}_{6.25}$	$1.1^{1.0}_{}$	28^{29}_{27}	$5.75^{5.50}_{5.50}$	$1.0^{0.8}_{}$	0.039	WD	1		1,7	SD
1518+0410	PG 1515+044	15:18:08.48	+04:10:43.8	26^{25}_{25}	$5.50^{5.75}_{5.25}$	$1.8^{1.7}_{}$	28^{27}_{27}	$5.25^{5.00}_{5.00}$	$1.7^{1.8}_{}$	0.047	sdO	1	SD	1,7	SD
1520−0009		15:20:20.40	−00:09:48.3	17^{18}_{16}	$5.75^{6.00}_{6.05}$	$4.2^{6.8}_{}$	18^{19}_{17}	$5.50^{5.75}_{5.75}$	$3.8^{4.2}_{}$	0.062		1			
1520+0713		15:20:00.81	+07:13:48.8	24^{23}_{23}	$5.00^{4.75}_{4.25}$	$2.4^{2.2}_{}$	27^{28}_{26}	$4.75^{4.50}_{4.50}$	$2.2^{2.4}_{}$	0.037		1			
1522+0803		15:22:12.20	+08:03:40.9	21^{29}_{14}	$22.00^{23.00}_{21.00}$	$78.3^{86.9}_{69.8}$	21^{33}_{17}	$24.00^{25.00}_{23.00}$	$80.0^{86.5}_{73.1}$	0.034		4	CV		
1524+1020		15:24:28.45	+10:20:51.6	25^{23}_{23}	$6.25^{6.50}_{6.50}$	$8.0^{9.1}_{}$	28^{29}_{26}	$6.25^{6.50}_{6.50}$	$7.9^{8.5}_{}$	0.034		1	SD		
1525+0958		15:25:34.15	+09:58:51.0	29^{30}_{30}	$3.25^{4.25}_{4.00}$	$2.8^{4.8}_{}$	33^{34}_{33}	$3.25^{3.50}_{3.50}$	$3.0^{3.1}_{}$	0.036		1	SD		pWD
1527+1016		15:27:07.20	+10:16:12.5	23^{22}_{22}	$5.50^{5.75}_{5.75}$	$2.5^{2.3}_{}$	24^{25}_{23}	$5.25^{5.00}_{5.00}$	$2.2^{2.1}_{}$	0.039		1	SD		
1536+0218		15:36:13.08	+02:18:09.4	24^{28}_{22}	$5.75^{6.05}_{5.50}$	$3.9^{5.0}_{}$	25^{24}_{24}	$5.75^{5.50}_{5.50}$	$3.9^{3.5}_{}$	0.059		1			
1538+0644	HS 1536+0944	15:38:18.87	+06:44:38.7	14^{15}_{13}	$7.25^{7.00}_{7.50}$	$6.5^{8.6}_{}$	14^{15}_{13}	$7.00^{7.25}_{6.50}$	$6.0^{8.2}_{}$	0.052		2	SD	6	pWD
1538+0934		15:38:42.85	+09:34:42.3	23^{22}_{22}	$5.00^{4.75}_{4.75}$	$1.8^{2.0}_{}$	39^{38}_{30}	$5.25^{5.50}_{5.50}$	$1.8^{2.0}_{}$	0.038		1	SD		SD
1539+0933		15:39:24.44	+09:33:28.3	19^{20}_{18}	$5.75^{5.50}_{5.50}$	$1.8^{1.7}_{}$	20^{21}_{19}	$5.50^{5.75}_{5.75}$	$1.7^{1.8}_{}$	0.035		1			
1540+0005	PG 1538+002	15:40:50.58	+00:05:17.8	26^{25}_{25}	$4.25^{4.50}_{4.00}$	$1.8^{2.0}_{}$	30^{31}_{29}	$3.25^{3.50}_{3.50}$	$1.1^{1.2}_{}$	0.087		1			
1542+0056		15:42:18.25	+00:56:11.8	29^{30}_{28}	$6.50^{6.75}_{6.05}$	$1.5^{1.3}_{}$	21^{22}_{20}	$6.25^{6.00}_{6.00}$	$1.3^{1.6}_{}$	0.098		1	SD		
1542+0155		15:42:10.89	+01:55:57.2	21^{20}_{20}	$5.75^{5.50}_{5.50}$	$2.2^{2.1}_{}$	25^{26}_{24}	$6.00^{5.75}_{5.75}$	$2.5^{2.2}_{}$	0.069		1	SD		
1543+0012	WD 1541+003	15:43:38.69	+00:12:02.1	21^{20}_{20}	$4.75^{4.50}_{4.50}$	$2.9^{4.5}_{}$	25^{24}_{24}	$5.00^{4.75}_{4.75}$	$3.2^{3.0}_{}$	0.086	WD	1	SD		pWD
1545+0132		15:45:45.57	+01:32:29.3	29^{30}_{28}	$6.00^{6.75}_{6.05}$	$3.0^{3.8}_{}$	29^{30}_{28}	$5.75^{6.00}_{6.00}$	$2.6^{3.0}_{}$	0.093		1	SD		
1546+0625		15:46:41.89	+06:25:39.3	29^{30}_{28}	$4.75^{5.00}_{5.00}$	$3.5^{5.4}_{}$	30^{31}_{29}	$4.50^{4.25}_{4.25}$	$3.1^{3.9}_{}$	0.050	WD	4	WD		
1548+0334		15:48:52.88	+03:34:29.4	23^{24}_{22}	$4.75^{5.00}_{4.00}$	$3.6^{3.8}_{}$	25^{26}_{24}	$4.75^{5.00}_{4.00}$	$3.6^{3.9}_{}$	0.107		1			
1550−0104		15:50:21.35	−01:04:53.5	24^{25}_{23}	$5.25^{5.50}_{5.50}$	$4.0^{4.4}_{}$	28^{29}_{27}	$5.25^{5.50}_{5.50}$	$4.1^{4.2}_{}$	0.120		1			
1551+0029	PG 1549+006	15:51:44.88	+00:29:48.8	23^{24}_{22}	$3.00^{3.25}_{3.00}$	$1.3^{1.4}_{}$	27^{26}_{26}	$3.00^{3.25}_{3.25}$	$1.4^{1.5}_{}$	0.074		3			pWD
1554+0616		15:54:32.27	+06:16:17.8	29^{28}_{28}	$4.75^{4.50}_{4.50}$	$3.8^{3.6}_{}$	29^{30}_{28}	$4.50^{4.25}_{4.25}$	$3.3^{3.1}_{}$	0.041		3			pWD
1619+2407		16:19:42.83	+24:07:15.7	24^{23}_{23}	$6.50^{6.75}_{6.25}$	$4.3^{4.8}_{3.8}$	27^{28}_{26}	$6.75^{6.50}_{6.50}$	$4.7^{5.1}_{4.3}$	0.067		1	SD		pWD

Table B.3:

Name	Identifier	R.A.	Dec	sdB T_{eff} (1000 K)	MS T_{eff} (1000 K)	d (kpc)	sdB T_{eff} (1000 K)	MS T_{eff} (1000 K)	d (kpc)	E(B–V)	SIMBAD	Q	SDSS Spec	Known Comp	Table 7.6
1635+2952		16:35:18.31	+29:52:03.3	25^{27}_{24}	$5.25^{5.50}_{5.00}$	$3.4^{3.7}_{3.1}$	27^{28}_{26}	$5.25^{5.50}_{5.00}$	$3.4^{3.7}_{3.2}$	0.021		1	SD		
1644+3123		16:44:44.95	+31:23:45.3	26^{27}_{25}	$5.75^{6.00}_{5.50}$	$3.1^{3.4}_{3.1}$	27^{28}_{26}	$5.50^{5.75}_{5.25}$	$2.8^{3.0}_{2.6}$	0.028	WD	1	SD		
1650+3127	PG 1648+315	16:50:22.05	+31:27:49.7	29^{30}_{28}	$5.25^{5.50}_{5.00}$	$1.6^{2.1}_{1.5}$	29^{30}_{28}	$5.00^{5.25}_{4.75}$	$1.5^{1.9}_{1.4}$	0.030	WD	1	SD		
2045+0024		20:45:37.81	+00:24:40.5	29^{30}_{28}	$6.00^{6.25}_{5.75}$	$5.7^{7.9}_{5.2}$	29^{30}_{28}	$5.50^{5.75}_{5.25}$	$4.0^{6.0}_{3.9}$	0.096	WD	2	SD		
2046−0006		20:46:43.28	−00:06:30.2	17^{18}_{16}	$6.00^{6.25}_{5.75}$	$7.4^{11.2}_{7.2}$	18^{19}_{17}	$5.75^{6.00}_{5.50}$	$6.5^{7.1}_{5.9}$	0.079		2	SD		
2049−0001		20:49:22.58	−00:01:34.7	18^{19}_{17}	$5.25^{5.50}_{5.00}$	$6.0^{6.4}_{5.6}$	20^{21}_{19}	$5.00^{5.25}_{4.50}$	$5.8^{5.8}_{3.6}$	0.093		1			pWD
2050+0057		20:50:51.37	+00:57:12.2	22^{23}_{21}	$6.00^{6.75}_{5.75}$	$6.8^{7.6}_{6.0}$	26^{28}_{24}	$6.25^{6.50}_{4.50}$	$7.4^{8.4}_{6.5}$	0.107		1	SD		
2051+0112		20:51:01.72	+01:12:59.7	23^{24}_{21}	$6.00^{6.25}_{5.75}$	$5.9^{6.5}_{5.1}$	24^{26}_{23}	$5.75^{6.00}_{5.50}$	$5.1^{5.8}_{4.7}$	0.111		1			
2052−0050		20:52:54.69	−00:50:31.8	23^{24}_{22}	$5.75^{6.00}_{5.50}$	$6.2^{6.8}_{5.7}$	24^{25}_{23}	$5.50^{5.75}_{5.25}$	$5.6^{6.2}_{5.2}$	0.093	WD	1	SD		
2057+0108		20:57:58.45	+01:08:17.7	22^{23}_{21}	$5.75^{6.00}_{5.50}$	$3.6^{3.9}_{3.3}$	23^{24}_{21}	$5.50^{5.75}_{5.25}$	$3.3^{3.5}_{2.9}$	0.083	WD	1	SD		
2059+0105		20:59:54.78	+01:05:57.0	23^{24}_{22}	$6.00^{6.25}_{5.75}$	$3.5^{3.9}_{3.1}$	25^{26}_{24}	$6.00^{6.25}_{5.75}$	$3.5^{3.9}_{3.1}$	0.075		1	SD		
2117−0006		21:17:42.22	−00:06:19.9	30^{31}_{29}	$6.50^{6.75}_{6.25}$	$2.1^{2.3}_{1.8}$	24^{25}_{23}	$6.25^{6.50}_{6.00}$	$1.9^{2.1}_{1.7}$	0.074		1	SD		pWD
2120+0037		21:20:14.38	+00:37:56.4	22^{23}_{21}	$3.00^{3.25}_{3.00}$	$2.9^{2.7}_{1.8}$	28^{29}_{23}	$3.00^{3.25}_{3.00}$	$3.1^{3.1}_{1.9}$	0.086		3	SD		
2147−0112	FBS 2145−014	21:47:43.59	−01:12:02.9	25^{26}_{24}	$3.25^{3.50}_{3.00}$	$1.6^{2.1}_{1.5}$	28^{29}_{27}	$0.00^{0.00}_{25.00}$	$1.5^{22.7}_{0.9}$	0.047		2			pWD
2236+0640	PG 2234+064	22:36:41.97	+06:40:17.5	28^{40}_{11}	$19.00^{20.00}_{18.00}$	$26.0^{29.2}_{23.4}$	27^{28}_{26}	$0.00^{0.00}_{25.00}$	$2.1^{34.8}_{2.0}$	0.132		3			pWD
2244+0106	PB 5146	22:44:51.81	+01:06:31.0	24^{26}_{22}	$5.75^{6.00}_{5.50}$	$6.9^{7.3}_{6.1}$	26^{28}_{24}	$5.75^{6.00}_{5.50}$	$6.9^{7.8}_{6.1}$	0.079	sdB	1	SD		
2245+0611		22:45:11.78	+06:11:43.7	30^{31}_{29}	$6.00^{6.25}_{5.75}$	$6.4^{7.3}_{5.6}$	39^{40}_{38}	$5.75^{6.00}_{5.50}$	$5.3^{5.8}_{4.8}$	0.095		1			
2333+1522		23:33:25.92	+15:22:22.2	17^{18}_{16}	$6.75^{7.00}_{6.25}$	$12.6^{17.8}_{12.3}$	17^{18}_{16}	$6.50^{6.75}_{6.00}$	$10.9^{15.9}_{10.7}$	0.068	CV	4	CV		CV
2346+0344		23:46:55.70	+03:44:28.5	29^{30}_{28}	$6.75^{7.00}_{6.50}$	$1.6^{1.9}_{1.5}$	29^{30}_{28}	$6.50^{6.75}_{6.25}$	$1.5^{1.7}_{1.3}$	0.054		1			

Bibliography

Aannestad, P. A., Kenyon, S. J., Hammond, G. L., Sion, E. M., 1993, AJ, 105, 1033

Abazajian, K., et al., 2003, AJ, 126, 2081

Abazajian, K., et al., 2004, AJ, 128, 502

Abazajian, K., et al., 2005, AJ, 129, 1755

Abazajian, K. N., et al., 2009, ApJS, 182, 543

Achilleos, N., Remillard, R. A., Wickramasinghe, D. T., 1991, MNRAS, 253, 522

Adams, F. C., Shu, F. H., Lada, C. J., 1988, ApJ, 326, 865

Adelman-McCarthy, J. K., et al., 2006, ApJS, 162, 38

Adelman-McCarthy, J. K., et al., 2007, ApJS, 172, 634

Adelman-McCarthy, J. K., et al., 2008, ApJS, 175, 297

Alcock, C., Fristrom, C. C., Siegelman, R., 1986, ApJ, 302, 462

Allard, F., Wesemael, F., Fontaine, G., Bergeron, P., Lamontagne, R., 1994, AJ, 107, 1565

Allègre, C. J., Poirier, J., Humler, E., Hofmann, A. W., 1995, Earth and Planetary Science Letters, 134, 515

Angel, J. R. P., Borra, E. F., Landstreet, J. D., 1981, ApJS, 45, 457

Araujo-Betancor, S., Gänsicke, B. T., Long, K. S., Beuermann, K., de Martino, D., Sion, E. M., Szkody, P., 2005a, ApJ, 622, 589

Araujo-Betancor, S., et al., 2005b, A&A, 430, 629

Aungwerojwit, A., et al., 2005, A&A, 443, 995

Aznar Cuadrado, R., Jeffery, C. S., 2001, A&A, 368, 994

Aznar Cuadrado, R., Jeffery, C. S., 2002, A&A, 385, 131

Ballouz, R., Sion, E. M., 2009, ApJ, 697, 1717

Barstow, M. A., Jordan, S., O'Donoghue, D., Burleigh, M. R., Napiwotzki, R., Harrop-Allin, M. K., 1995, MNRAS, 277, 971

Becklin, E. E., Zuckerman, B., 1988, Nat, 336, 656

Becklin, E. E., Farihi, J., Jura, M., Song, I., Weinberger, A. J., Zuckerman, B., 2005, ApJ Lett., 632, L119

Bergeron, P., Saffer, R. A., Liebert, J., 1992, ApJ, 394, 228

Bergeron, P., Ruiz, M.-T., Leggett, S. K., 1993, ApJ, 407, 733

Bergeron, P., Wesemael, F., Beauchamp, A., 1995, PASP, 107, 1047

Bergeron, P., et al., 2011, ApJ, 737, 28

Bertone, E., Buzzoni, A., Chávez, M., Rodríguez-Merino, L. H., 2004, AJ, 128, 829

Beuermann, K., Wheatley, P., Ramsay, G., Euchner, F., Gänsicke, B. T., 2000, A&A, 354, L49

Blanchette, J.-P., Chayer, P., Wesemael, F., Fontaine, G., Fontaine, M., Dupuis, J., Kruk, J. W., Green, E. M., 2008, ApJ, 678, 1329

Bochkarev, K. V., Rafikov, R. R., 2011, ApJ, 741, 36

Bond, J. C., O'Brien, D. P., Lauretta, D. S., 2010, ApJ, 715, 1050

Bonsor, A., Wyatt, M., 2010, MNRAS, 409, 1631

Bonsor, A., Mustill, A. J., Wyatt, M. C., 2011, MNRAS, 414, 930

Bradt, H., Padmanabhan, T., 2005, Physics Today, 58, 050000

Brassard, P., Fontaine, G., Billères, M., Charpinet, S., Liebert, J., Saffer, R. A., 2001, ApJ, 563, 1013

Breedt, E., Gänsicke, B. T., Girven, J., Drake, A. J., Copperwheat, C. M., Parsons, S. G., Marsh, T. R., 2012, MNRAS, 423, 1437

Brinkworth, C. S., Burleigh, M. R., Wynn, G. A., Marsh, T. R., 2004, MNRAS, 348, L33

Brinkworth, C. S., Marsh, T. R., Morales-Rueda, L., Maxted, P. F. L., Burleigh, M. R., Good, S. A., 2005, MNRAS, 357, 333

Brinkworth, C. S., Gänsicke, B. T., Marsh, T. R., Hoard, D. W., Tappert, C., 2009, ApJ, 696, 1402

Brinkworth, C. S., Gänsicke, B. T., Girven, J. M., Hoard, D. W., Marsh, T. R., Parsons, S. G., Koester, D., 2012, ApJ, 750, 86

Brown, T. M., Ferguson, H. C., Davidsen, A. F., Dorman, B., 1997, ApJ, 482, 685

Budavári, T., et al., 2009, ApJ, 694, 1281

Burleigh, M. R., Jordan, S., Schweizer, W., 1999, ApJ Lett., 510, L37

Burleigh, M. R., et al., 2006, MNRAS, 373, 1416

Carpenter, J. M., 2001, AJ, 121, 2851

Casewell, S. L., Dobbie, P. D., Napiwotzki, R., Burleigh, M. R., Barstow, M. A., Jameson, R. F., 2009, MNRAS, 395, 1795

Castellani, M., Castellani, V., 1993, ApJ, 407, 649

Castelli, F., Kurucz, R. L., 2003, in N. Piskunov, W. W. Weiss, & D. F. Gray, ed., Modelling of Stellar Atmospheres, vol. 210 of *IAU Symposium*, p. 20P

Catalán, S., Isern, J., García-Berro, E., Ribas, I., 2008a, MNRAS, 387, 1693

Catalán, S., Isern, J., García-Berro, E., Ribas, I., Allende Prieto, C., Bonanos, A. Z., 2008b, A&A, 477, 213

Chabrier, G., Brassard, P., Fontaine, G., Saumon, D., 2000, ApJ, 543, 216

Chandrasekhar, S., 1931, ApJ, 74, 81

Chayer, P., Fontaine, G., Wesemael, F., 1995, ApJS, 99, 189

Chiang, E. I., Goldreich, P., 1997, ApJ, 490, 368

Chu, Y.-H., et al., 2011, AJ, 142, 75

Ciardullo, R., Bond, H. E., Sipior, M. S., Fullton, L. K., Zhang, C., Schaefer, K. G., 1999, AJ, 118, 488

Clausen, D., Wade, R. A., Kopparapu, R. K., O'Shaughnessy, R., 2012, ApJ, 746, 186

Copenhagen University Obs., Institute of Astronomy, Cambridge, U., Real Instituto y Observatorio de la Armada en San Fernando, 2006, Carlsberg Meridian Catalog Number 14

Copperwheat, C. M., Morales-Rueda, L., Marsh, T. R., Maxted, P. F. L., Heber, U., 2011, MNRAS, 415, 1381

Covey, K. R., et al., 2007, AJ, 134, 2398

D'Antona, F., Mazzitelli, I., 1990, ARA&A, 28, 139

Davidsson, B. J. R., 1999, Icarus, 142, 525

D'Cruz, N. L., Dorman, B., Rood, R. T., O'Connell, R. W., 1996, ApJ, 466, 359

De Gennaro, S., von Hippel, T., Winget, D. E., Kepler, S. O., Nitta, A., Koester, D., Althaus, L., 2008, AJ, 135, 1

de Jong, J. T. A., Yanny, B., Rix, H., Dolphin, A. E., Martin, N. F., Beers, T. C., 2010, ApJ, 714, 663

de Jong, J. T. A., Verdoes Kleijn, G. A., Kuijken, K. H., Valentijn, E. A., 2012, Experimental Astronomy, 34

Debes, J. H., Sigurdsson, S., 2002a, ApJ, 572, 556

Debes, J. H., Sigurdsson, S., 2002b, ApJ, 572, 556

Debes, J. H., López-Morales, M., Bonanos, A. Z., Weinberger, A. J., 2006, ApJ Lett., 647, L147

Debes, J. H., Hoard, D. W., Kilic, M., Wachter, S., Leisawitz, D. T., Cohen, M., Kirkpatrick, J. D., Griffith, R. L., 2011, ApJ, 729, 4

Desharnais, S., Wesemael, F., Chayer, P., Kruk, J. W., Saffer, R. A., 2008, ApJ, 672, 540

Dobbie, P. D., Napiwotzki, R., Burleigh, M. R., Williams, K. A., Sharp, R., Barstow, M. A., Casewell, S. L., Hubeny, I., 2009, MNRAS, 395, 2248

Dobbie, P. D., et al., 2006, MNRAS, 369, 383

Dobrzycka, D., Howell, S. B., 1992, ApJ, 388, 614

Dong, R., Wang, Y., Lin, D. N. C., Liu, X.-W., 2010, ApJ, 715, 1036

Dorman, B., Rood, R. T., O'Connell, R. W., 1993, ApJ, 419, 596

Dufour, P., Kilic, M., Fontaine, G., Bergeron, P., Lachapelle, F., Kleinman, S. J.,
Leggett, S. K., 2010, ApJ, 719, 803

Dufour, P., Kilic, M., Fontaine, G., Bergeron, P., Melis, C., Bochanski, J., 2012,
ApJ, 749, 6

Dufour, P., et al., 2007, ApJ, 663, 1291

Dupuis, J., Fontaine, G., Pelletier, C., Wesemael, F., 1992, ApJS, 82, 505

Dupuis, J., Fontaine, G., Pelletier, C., Wesemael, F., 1993a, ApJS, 84, 73

Dupuis, J., Fontaine, G., Wesemael, F., 1993b, ApJS, 87, 345

Dupuis, J., Chayer, P., Hénault-Brunet, V., Vennes, S., Kruk, J. W., 2009a, in
M. E. van Steenberg, G. Sonneborn, H. W. Moos, & W. P. Blair , ed., American
Institute of Physics Conference Series, vol. 1135 of *American Institute of Physics
Conference Series*, p. 329

Dupuis, J., Hénault-Brunet, V., Chayer, P., Vennes, S., Kruk, J. W., 2009b, Journal
of Physics Conference Series, 172, 012050

Dye, S., et al., 2006, MNRAS, 372, 1227

Edelmann, H., Heber, U., Hagen, H.-J., Lemke, M., Dreizler, S., Napiwotzki, R.,
Engels, D., 2003, A&A, 400, 939

Eggen, O. J., 1968, ApJS, 16, 97

Eggen, O. J., Greenstein, J. L., 1965, ApJ, 141, 83

Eisenstein, D. J., et al., 2006, ApJS, 167, 40

Encrenaz, T., 2008, ARA&A, 46, 57

Euchner, F., Jordan, S., Beuermann, K., Gänsicke, B. T., Hessman, F. V., 2002,
A&A, 390, 633

Evans, D. W., 2001, Astronomische Nachrichten, 322, 347

Farihi, J., Christopher, M., 2004, AJ, 128, 1868

Farihi, J., Becklin, E. E., Zuckerman, B., 2005, ApJS, 161, 394

Farihi, J., Zuckerman, B., Becklin, E. E., Jura, M., 2007, in R. Napiwotzki &
M. R. Burleigh, ed., 15th European Workshop on White Dwarfs, vol. 372 of
Astronomical Society of the Pacific Conference Series, p. 315

Farihi, J., Burleigh, M. R., Hoard, D. W., 2008a, ApJ, 674, 421

Farihi, J., Zuckerman, B., Becklin, E. E., 2008b, ApJ, 674, 431

Farihi, J., Jura, M., Zuckerman, B., 2009, ApJ, 694, 805

Farihi, J., Barstow, M. A., Redfield, S., Dufour, P., Hambly, N. C., 2010a, MNRAS,
404, 2123

Farihi, J., Jura, M., Lee, J., Zuckerman, B., 2010b, ApJ, 714, 1386

Farihi, J., Brinkworth, C. S., Gänsicke, B. T., Marsh, T. R., Girven, J., Hoard,
D. W., Klein, B., Koester, D., 2011a, ApJ Lett., 728, L8

Farihi, J., Dufour, P., Napiwotzki, R., Koester, D., 2011b, MNRAS, 413, 2559

Farihi, J., Gänsicke, B. T., Steele, P. R., Girven, J., Burleigh, M. R., Breedt, E.,
Koester, D., 2012, MNRAS, 421, 1635

Fazio, G. G., et al., 2004, ApJS, 154, 10

Fekel, F. X., Simon, T., 1985, AJ, 90, 812

Ferguson, D. H., Green, R. F., Liebert, J., 1984, ApJ, 287, 320

Ferrario, L., Vennes, S., Wickramasinghe, D. T., Bailey, J. A., Christian, D. J.,
1997, MNRAS, 292, 205

Ferrario, L., Wickramasinghe, D., Liebert, J., Williams, K. A., 2005, MNRAS, 361,
1131

Finley, D. S., Koester, D., 1997, ApJ Lett., 489, L79

Finley, D. S., Koester, D., Basri, G., 1997, ApJ, 488, 375

Fitzpatrick, E. L., Massa, D., 2007, ApJ, 663, 320

Fontaine, G., Michaud, G., 1979, ApJ, 231, 826

Fontaine, G., Villeneuve, B., Wesemael, F., Wegner, G., 1984, ApJ Lett., 277, L61

Fontaine, G., Brassard, P., Bergeron, P., 2001, PASP, 113, 409

Friedrich, S., Koester, D., Christlieb, N., Reimers, D., Wisotzki, L., 2000, A&A, 363, 1040

Fulbright, M. S., Liebert, J., Bergeron, P., Green, R., 1993, ApJ, 406, 240

Gänsicke, B. T., Beuermann, K., de Martino, D., 1995, A&A, 303, 127

Gänsicke, B. T., Euchner, F., Jordan, S., 2002, A&A, 394, 957

Gänsicke, B. T., Long, K. S., Barstow, M. A., Hubeny, I., 2006a, ApJ, 639, 1039

Gänsicke, B. T., Marsh, T. R., Southworth, J., Rebassa-Mansergas, A., 2006b, Science, 314, 1908

Gänsicke, B. T., Marsh, T. R., Southworth, J., 2007, MNRAS, 380, L35

Gänsicke, B. T., Koester, D., Marsh, T. R., Rebassa-Mansergas, A., Southworth, J., 2008, MNRAS, 391, L103

Gänsicke, B. T., Koester, D., Girven, J., Marsh, T. R., Steeghs, D., 2010, Science, 327, 188

Gänsicke, B. T., Koester, D., Farihi, J., Girven, J., Parsons, S. G., Breedt, E., 2012, MNRAS, 3130

Geier, S., et al., 2011a, A&A, 526, A39

Geier, S., et al., 2011b, A&A, 530, A28

Gianninas, A., Dufour, P., Bergeron, P., 2004, ApJ Lett., 617, L57

Giclas, H. L., Burnham, R., Thomas, N. G., 1967, Lowell Observatory Bulletin, 7, 49

Girardi, L., Bressan, A., Bertelli, G., Chiosi, C., 2000, Astronomy and Astrophysics Supplement, 141, 371

Girven, J., Gänsicke, B. T., Külebi, B., Steeghs, D., Jordan, S., Marsh, T. R., Koester, D., 2010, MNRAS, 404, 159

Girven, J., Gänsicke, B. T., Steeghs, D., Koester, D., 2011, MNRAS, 417, 1210

Girven, J., Brinkworth, C. S., Farihi, J., Gänsicke, B. T., Hoard, D. W., Marsh, T. R., Koester, D., 2012a, ApJ, 749, 154

Girven, J., et al., 2012b, ArXiv e-prints

Glenn, J., Liebert, J., Schmidt, G. D., 1994, PASP, 106, 722

Graham, J. R., Matthews, K., Neugebauer, G., Soifer, B. T., 1990a, ApJ, 357, 216

Graham, J. R., Reid, I. N., McCarthy, J. K., Rich, R. M., 1990b, ApJ Lett., 357, L21

Green, E. M., Fontaine, G., Hyde, E. A., Charpinet, S., Chayer, P., 2006, Baltic Astronomy, 15, 167

Green, R. F., Richstone, D. O., Schmidt, M., 1978, ApJ, 224, 892

Green, R. F., Ferguson, D. H., Liebert, J., Schmidt, M., 1982, PASP, 94, 560

Green, R. F., Schmidt, M., Liebert, J., 1986, ApJS, 61, 305

Greenstein, J. L., 1956, Vistas in Astronomy, 2, 1299

Greenstein, J. L., Dolez, N., Vauclair, G., 1983, A&A, 127, 25

Grether, D., Lineweaver, C. H., 2006, ApJ, 640, 1051

Grillmair, C. J., et al., 2008, Nat, 456, 767

Hagen, H.-J., Groote, D., Engels, D., Reimers, D., 1995, A&AS, 111, 195

Hambly, N. C., et al., 2008, MNRAS, 384, 637

Han, Z., Podsiadlowski, P., Maxted, P. F. L., Marsh, T. R., 2003, MNRAS, 341, 669

Hansen, B., 2004, Phys. Rep., 399, 1

Hansen, B. M. S., 1999, ApJ, 520, 680

Hansen, B. M. S., et al., 2007, ApJ, 671, 380

Heber, U., 1986, A&A, 155, 33

Heber, U., 2009, ARA&A, 47, 211

Heber, U., Hunger, K., Jonas, G., Kudritzki, R. P., 1984, A&A, 130, 119

Heber, U., Jordan, S., Weidemann, V., 1991, in NATO ASIC Proc. 336: White Dwarfs, p. 109

Heber, U., Reid, I. N., Werner, K., 2000, A&A, 363, 198

Heber, U., Moehler, S., Napiwotzki, R., Thejll, P., Green, E. M., 2002, A&A, 383, 938

Heller, R., Homeier, D., Dreizler, S., Østensen, R., 2009, A&A, 496, 191

Hewett, P. C., Warren, S. J., Leggett, S. K., Hodgkin, S. T., 2006, MNRAS, 367, 454

Hoard, D. W., Wachter, S., Sturch, L. K., Widhalm, A. M., Weiler, K. P., Pretorius, M. L., Wellhouse, J. W., Gibiansky, M., 2007, AJ, 134, 26

Hoard, D. W., ed., 2011, White Dwarf Atmospheres and Circumstellar Environments, Wiley

Hodapp, K. W., et al., 2004, Astronomische Nachrichten, 325, 636

Holberg, J. B., Bergeron, P., 2006, AJ, 132, 1221

Holberg, J. B., Bergeron, P., Gianninas, A., 2008, AJ, 135, 1239

Horne, K., Marsh, T. R., 1986, MNRAS, 218, 761

Houck, J. R., et al., 2004, in J. C. Mather, ed., Society of Photo-Optical Instrumentation Engineers (SPIE) Conference Series, vol. 5487 of *Society of Photo-Optical Instrumentation Engineers (SPIE) Conference Series*, p. 62

Howarth, I. D., Heber, U., 1990, PASP, 102, 912

Howell, S. B., Harrison, T. E., Huber, M. E., Szkody, P., Walter, F. M., Harbeck, D., 2008, AJ, 136, 2541

Humason, M. L., Zwicky, F., 1947, ApJ, 105, 85

Hunt, L. K., Mannucci, F., Testi, L., Migliorini, S., Stanga, R. M., Baffa, C., Lisi, F., Vanzi, L., 1998, AJ, 115, 2594

Iben, Jr., I., 1990, ApJ, 353, 215

Jeffery, C. S., Pollacco, D. L., 1998, MNRAS, 298, 179

Jeffery, C. S., Aerts, C., Dhillon, V. S., Marsh, T. R., Gänsicke, B. T., 2005, MN-RAS, 362, 66

Jewitt, D., Chizmadia, L., Grimm, R., Prialnik, D., 2007, Protostars and Planets V, 863

Jordan, S., 1992, A&A, 265, 570

Jura, M., 2003, ApJ Lett., 584, L91

Jura, M., 2006, ApJ, 653, 613

Jura, M., 2008, AJ, 135, 1785

Jura, M., Xu, S., 2012, AJ, 143, 6

Jura, M., Farihi, J., Zuckerman, B., 2007a, ApJ, 663, 1285

Jura, M., Farihi, J., Zuckerman, B., Becklin, E. E., 2007b, AJ, 133, 1927

Jura, M., Farihi, J., Zuckerman, B., 2009a, AJ, 137, 3191

Jura, M., Muno, M. P., Farihi, J., Zuckerman, B., 2009b, ApJ, 699, 1473

Jurić, M., et al., 2008, ApJ, 673, 864

Kalirai, J. S., Richer, H. B., Reitzel, D., Hansen, B. M. S., Rich, R. M., Fahlman, G. G., Gibson, B. K., von Hippel, T., 2005, ApJ Lett., 618, L123

Kalirai, J. S., Hansen, B. M. S., Kelson, D. D., Reitzel, D. B., Rich, R. M., Richer, H. B., 2008, ApJ, 676, 594

Kawka, A., Vennes, S., 2004, in Zverko, J., Ziznovsky, J., Adelman, S. J., Weiss, W. W., eds., The A-Star Puzzle, vol. 224 of *IAU Symposium*, p. 879

Kawka, A., Vennes, S., 2006, ApJ, 643, 402

Kawka, A., Vennes, S., Schmidt, G. D., Wickramasinghe, D. T., Koch, R., 2007, ApJ, 654, 499

Kawka, A., Vennes, S., Dinnbier, F., Cibulková, H., Németh, P., 2011, in S. Schuh, H. Drechsel, & U. Heber, ed., American Institute of Physics Conference Series, vol. 1331 of *American Institute of Physics Conference Series*, p. 238

Keller, S. C., et al., 2007, Publications of the Astronomical Society of Australia, 24, 1

Kepler, S. O., Kleinman, S. J., Nitta, A., Koester, D., Castanheira, B. G., Giovannini, O., Costa, A. F. M., Althaus, L., 2007, MNRAS, 375, 1315

Kilic, M., Redfield, S., 2007, ApJ, 660, 641

Kilic, M., von Hippel, T., Leggett, S. K., Winget, D. E., 2005, ApJ Lett., 632, L115

Kilic, M., von Hippel, T., Leggett, S. K., Winget, D. E., 2006a, ApJ, 646, 474

Kilic, M., von Hippel, T., Mullally, F., Reach, W. T., Kuchner, M. J., Winget, D. E., Burrows, A., 2006b, ApJ, 642, 1051

Kilic, M., Brown, W. R., Allende Prieto, C., Pinsonneault, M. H., Kenyon, S. J., 2007a, ApJ, 664, 1088

Kilic, M., Stanek, K. Z., Pinsonneault, M. H., 2007b, ApJ, 671, 761

Kilic, M., Farihi, J., Nitta, A., Leggett, S. K., 2008, AJ, 136, 111

Kilkenny, D., Heber, U., Drilling, J. S., 1988, South African Astronomical Observatory Circular, 12, 1

Klein, B., Jura, M., Koester, D., Zuckerman, B., Melis, C., 2010, ApJ, 709, 950

Klein, B., Jura, M., Koester, D., Zuckerman, B., 2011, ApJ, 741, 64

Kleinman, S. J., et al., 1994, ApJ, 436, 875

Koester, D., 1976, A&A, 52, 415

Koester, D., 2002, A&AR, 11, 33

Koester, D., 2009, A&A, 498, 517

Koester, D., 2010, Memorie della Societa Astronomica Italiana,, 81, 921

Koester, D., Chanmugam, G., 1990, Reports on Progress in Physics, 53, 837

Koester, D., Wilken, D., 2006, A&A, 453, 1051

Koester, D., Schulz, H., Weidemann, V., 1979, A&A, 76, 262

Koester, D., Weidemann, V., Zeidler, E.-M., 1982, A&A, 116, 147

Koester, D., Provencal, J., Shipman, H. L., 1997, A&A, 320, L57

Koester, D., Napiwotzki, R., Voss, B., Homeier, D., Reimers, D., 2005a, A&A, 439, 317

Koester, D., Rollenhagen, K., Napiwotzki, R., Voss, B., Christlieb, N., Homeier, D., Reimers, D., 2005b, A&A, 432, 1025

Koester, D., Girven, J., Gänsicke, B. T., Dufour, P., 2011, A&A, 530, A114+

Koester, D., et al., 2001, A&A, 378, 556

Kuchner, M. J., Koresko, C. D., Brown, M. E., 1998, ApJ Lett., 508, L81

Kuiper, G. P., 1941, PASP, 53, 248

Külebi, B., Jordan, S., Euchner, F., Gänsicke, B. T., Hirsch, H., 2009, A&A, 506, 1341

Külebi, B., Jordan, S., Nelan, E., Bastian, U., Altmann, M., 2010, A&A, 524, A36

Lawrence, A., et al., 2007, MNRAS, 379, 1599

Li, N., Thakar, A. R., 2008, Computing in Science and Engineering, 10, 18

Liebert, J., 1988, PASP, 100, 1302

Liebert, J., Bergeron, P., Schmidt, G. D., Saffer, R. A., 1993, ApJ, 418, 426

Liebert, J., Bergeron, P., Holberg, J. B., 2003, AJ, 125, 348

Liebert, J., Bergeron, P., Eisenstein, D., Harris, H. C., Kleinman, S. J., Nitta, A., Krzesinski, J., 2004, ApJ Lett., 606, L147

Liebert, J., Bergeron, P., Holberg, J. B., 2005a, ApJS, 156, 47

Liebert, J., et al., 2005b, AJ, 129, 2376

Linnell, A. P., Szkody, P., Plotkin, R. M., Holtzman, J., Seibert, M., Harrison, T. E., Howell, S. B., 2010, ApJ, 713, 1183

Lisker, T., Heber, U., Napiwotzki, R., Christlieb, N., Han, Z., Homeier, D., Reimers, D., 2005, A&A, 430, 223

Lodders, K., 2003, ApJ, 591, 1220

Luhman, K. L., Burgasser, A. J., Bochanski, J. J., 2011, ApJ Lett., 730, L9+

Makovoz, D., Roby, T., Khan, I., Booth, H., 2006, in Society of Photo-Optical Instrumentation Engineers (SPIE) Conference Series, vol. 6274 of *Society of Photo-Optical Instrumentation Engineers (SPIE) Conference Series*, p. 10

Manchado, A., et al., 1998, in A. M. Fowler, ed., Society of Photo-Optical Instrumentation Engineers (SPIE) Conference Series, vol. 3354 of *Society of Photo-Optical Instrumentation Engineers (SPIE) Conference Series*, p. 448

Marcy, G. W., Butler, R. P., 2000, PASP, 112, 137

Marleau, F. R., et al., 2004, ApJS, 154, 66

Marsh, T. R., 1989, PASP, 101, 1032

Marsh, T. R., Gänsicke, B. T., Steeghs, D., Southworth, J., Koester, D., Harris, V., Merry, L., 2011, ApJ, 736, 95

Martin, D. C., et al., 2005, ApJ Lett., 619, L1

Maxted, P. F. L., Marsh, T. R., Moran, C. K. J., Han, Z., 2000, MNRAS, 314, 334

Maxted, P. f. L., Heber, U., Marsh, T. R., North, R. C., 2001, MNRAS, 326, 1391

Maxted, P. F. L., Marsh, T. R., Heber, U., Morales-Rueda, L., North, R. C., Lawson, W. A., 2002, MNRAS, 333, 231

Maxted, P. F. L., Napiwotzki, R., Dobbie, P. D., Burleigh, M. R., 2006, Nat, 442, 543

McCook, G. P., Sion, E. M., 1999, ApJS, 121, 1

Melis, C., Jura, M., Albert, L., Klein, B., Zuckerman, B., 2010, ApJ, 722, 1078

Melis, C., Farihi, J., Dufour, P., Zuckerman, B., Burgasser, A. J., Bergeron, P., Bochanski, J., Simcoe, R., 2011, ApJ, 732, 90

Mengel, J. G., Norris, J., Gross, P. G., 1976, ApJ, 204, 488

Mestel, L., 1952, MNRAS, 112, 583

Metchev, S. A., Hillenbrand, L. A., 2009, ApJS, 181, 62

Metzger, B. D., Rafikov, R. R., Bochkarev, K. V., 2012, MNRAS, 423, 505

Michaud, G., Richer, J., Richard, O., 2011, A&A, 529, A60

Minniti, D., et al., 2010, New Astronomy, 15, 433

Monet, D. G., et al., 2003, AJ, 125, 984

Moni Bidin, C., Piotto, G., 2010, Ap&SS, 329, 19

Moorwood, A., Cuby, J.-G., Lidman, C., 1998, The Messenger, 91, 9

Morales-Rueda, L., Maxted, P. F. L., Marsh, T. R., North, R. C., Heber, U., 2003, MNRAS, 338, 752

Moran, C., Maxted, P., Marsh, T. R., Saffer, R. A., Livio, M., 1999, MNRAS, 304, 535

Morrissey, P., et al., 2007, ApJS, 173, 682

Moss, D., 1989, MNRAS, 236, 629

Murdin, P., 2001, Encyclopedia of astronomy and astrophysics, CRC Press Inc.

Napiwotzki, R., Karl, C. A., Lisker, T., Heber, U., Christlieb, N., Reimers, D., Nelemans, G., Homeier, D., 2004, Ap&SS, 291, 321

Napiwotzki, R., et al., 2001, Astronomische Nachrichten, 322, 411

Nelan, E. P., 2007, AJ, 134, 1934

Østensen, R. H., 2006, Baltic Astronomy, 15, 85

Oswalt, T. D., Smith, J. A., Wood, M. A., Hintzen, P., 1996, Nat, 382, 692

O'Toole, S. J., Heber, U., 2006, A&A, 452, 579

Papoular, R. J., Papoular, R., 2009, MNRAS, 394, 2175

Paquette, C., Pelletier, C., Fontaine, G., Michaud, G., 1986, ApJS, 61, 177

Parsons, S. G., et al., 2010, MNRAS, 407, 2362

Penning, W. R., Ferguson, D. H., McGraw, J. T., Liebert, J., Green, R. F., 1984, ApJ, 276, 233

Perryman, M. A. C., et al., 2001, A&A, 369, 339

Pickles, A. J., 1998, PASP, 110, 863

Politano, M., Taam, R. E., van der Sluys, M., Willems, B., 2008, ApJ Lett., 687, L99

Pols, O. R., Schroder, K.-P., Hurley, J. R., Tout, C. A., Eggleton, P. P., 1998, MNRAS, 298, 525

Probst, R. G., O' Connell, R. W., 1982, ApJ Lett., 252, L69

Rafikov, R. R., 2011a, ApJ Lett., 732, L3+

Rafikov, R. R., 2011b, MNRAS, 416, L55

Rau, A., et al., 2009, PASP, 121, 1334

Reach, W. T., Kuchner, M. J., von Hippel, T., Burrows, A., Mullally, F., Kilic, M., Winget, D. E., 2005, ApJ Lett., 635, L161

Reach, W. T., Lisse, C., von Hippel, T., Mullally, F., 2009, ApJ, 693, 697

Rebassa-Mansergas, A., Gänsicke, B. T., Rodríguez-Gil, P., Schreiber, M. R., Koester, D., 2007, MNRAS, 382, 1377

Rebassa-Mansergas, A., Gänsicke, B. T., Schreiber, M. R., Koester, D., Rodríguez-Gil, P., 2010, MNRAS, 402, 620

Rebassa-Mansergas, A., Nebot Gómez-Morán, A., Schreiber, M. R., Girven, J., Gänsicke, B. T., 2011, MNRAS, 413, 1121

Reed, M. D., Stiening, R., 2004, PASP, 116, 506

Reimers, D., Hagen, H. J., 2000, A&A, 358, L45

Reimers, D., Hagen, H. J., Hopp, U., 1999, A&A, 343, 157

Richards, G. T., et al., 2002, AJ, 123, 2945

Ringwald, F., 1993, PASP, 105, 805

Ritter, H., Kolb, U., 2009, VizieR Online Data Catalog, 1, 2018

Rowan-Robinson, M., 1985, The cosmological distance ladder: Distance and time in the universe, W. H. Freeman and Co

Rowell, N., Hambly, N. C., 2011, MNRAS, 417, 93

Rubin, K. H. R., Williams, K. A., Bolte, M., Koester, D., 2008, AJ, 135, 2163

Saffer, R. A., Bergeron, P., Koester, D., Liebert, J., 1994, ApJ, 432, 351

Saffer, R. A., Livio, M., Yungelson, L. R., 1998, ApJ, 502, 394

Saio, H., Jeffery, C. S., 2000, MNRAS, 313, 671

Salaris, M., Serenelli, A., Weiss, A., Miller Bertolami, M., 2009, ApJ, 692, 1013

Schlegel, D. J., Finkbeiner, D. P., Davis, M., 1998, ApJ, 500, 525

Schmidt, G. D., Smith, P. S., 1995, ApJ, 448, 305

Schmidt, G. D., Liebert, J., Smith, P. S., 1998, AJ, 116, 451

Schmidt, G. D., Szkody, P., Silvestri, N. M., Cushing, M. C., Liebert, J., Smith, P. S., 2005, ApJ Lett., 630, L173

Schmidt, G. D., Szkody, P., Henden, A., Anderson, S. F., Lamb, D. Q., Margon, B., Schneider, D. P., 2007, ApJ, 654, 521

Schmidt, G. D., et al., 2003, ApJ, 595, 1101

Schmidt, M., 1968, ApJ, 151, 393

Schwope, A. D., Nebot Gomez-Moran, A., Schreiber, M. R., Gänsicke, B. T., 2009, A&A, 500, 867

Silvestri, N. M., et al., 2007, AJ, 134, 741

Sion, E. M., Leckenby, H. J., Szkody, P., 1990, ApJ Lett., 364, L41

Skrutskie, M. F., et al., 2006, AJ, 131, 1163

Stark, M. A., Wade, R. A., 2003, AJ, 126, 1455

Stark, M. A., Wade, R. A., 2006, Baltic Astronomy, 15, 175

Steele, P. R., Burleigh, M. R., Farihi, J., Gänsicke, B. T., Jameson, R. F., Dobbie, P. D., Barstow, M. A., 2009, A&A, 500, 1207

Steele, P. R., Burleigh, M. R., Dobbie, P. D., Jameson, R. F., Barstow, M. A., Satterthwaite, R. P., 2011, MNRAS, 416, 2768

Stoughton, C., et al., 2002, AJ, 123, 485

Strauss, M. A., et al., 2002, AJ, 124, 1810

Stroeer, A., Heber, U., Lisker, T., Napiwotzki, R., Dreizler, S., Christlieb, N., Reimers, D., 2007, A&A, 462, 269

Subasavage, J. P., Henry, T. J., Bergeron, P., Dufour, P., Hambly, N. C., Beaulieu, T. D., 2007, AJ, 134, 252

Szkody, P., et al., 2003, ApJ, 583, 902

Szkody, P., et al., 2005, AJ, 129, 2386

Szkody, P., et al., 2006, AJ, 131, 973

Taylor, M. B., 2005, in Shopbell, P., Britton, M., Ebert, R., eds., Astronomical Data Analysis Software and Systems XIV, vol. 347 of *Astronomical Society of the Pacific Conference Series*, p. 29

Telesco, C. M., Joy, M., Sisk, C., 1990, ApJ Lett., 358, L17

Thejll, P., Ulla, A., MacDonald, J., 1995, A&A, 303, 773

Tillich, A., et al., 2011, A&A, 527, A137

Tokunaga, A. T., Becklin, E. E., Zuckerman, B., 1990, ApJ Lett., 358, L21

Tout, C. A., Pringle, J. E., 1992, MNRAS, 259, 604

Tout, C. A., Wickramasinghe, D. T., Ferrario, L., 2004, MNRAS, 355, L13

Tout, C. A., Wickramasinghe, D. T., Liebert, J., Ferrario, L., Pringle, J. E., 2008, MNRAS, 387, 897

Tremblay, P.-E., Bergeron, P., 2007, ApJ, 657, 1013

Tremblay, P.-E., Bergeron, P., 2009, ApJ, 696, 1755

Tutukov, A. V., Yungelson, L. R., 1990, Soviet Astronomy, 34, 57

Tyson, J. A., 2002, in Tyson, J. A., Wolff, S., eds., Society of Photo-Optical Instrumentation Engineers (SPIE) Conference Series, vol. 4836 of *Society of Photo-Optical Instrumentation Engineers (SPIE) Conference Series*, p. 10

Udalski, A., Szymanski, M., Kaluzny, J., Kubiak, M., Mateo, M., 1992, Acta Astron., 42, 253

Ulla, A., Thejll, P., 1998, A&AS, 132, 1

Valencia, D., Ikoma, M., Guillot, T., Nettelmann, N., 2010, A&A, 516, A20

van Maanen, A., 1917, PASP, 29, 258

Vanlandingham, K. M., et al., 2005, AJ, 130, 734

Vennes, S., Schmidt, G. D., Ferrario, L., Christian, D. J., Wickramasinghe, D. T., Kawka, A., 2003, ApJ, 593, 1040

Vennes, S., Kawka, A., Németh, P., 2010, MNRAS, 404, L40

Vennes, S., Kawka, A., Németh, P., 2011a, MNRAS, 410, 2095

Vennes, S., Kawka, A., Németh, P., 2011b, MNRAS, 413, 2545

Viton, M., Deleuil, M., Tobin, W., Prevot, L., Bouchet, P., 1991, A&A, 242, 175

von Hippel, T., Kuchner, M. J., Kilic, M., Mullally, F., Reach, W. T., 2007, ApJ, 662, 544

Voss, B., Koester, D., Napiwotzki, R., Christlieb, N., Reimers, D., 2007, A&A, 470, 1079

Wachter, S., Hoard, D. W., Hansen, K. H., Wilcox, R. E., Taylor, H. M., Finkelstein, S. L., 2003, ApJ, 586, 1356

Wade, R. A., Stark, M. A., Green, R. F., Durrell, P. R., 2006, Baltic Astronomy, 15, 81

Wade, R. A., Stark, M. A., Green, R. F., Durrell, P. R., 2009, AJ, 138, 606

Warren, S. J., et al., 2007a, ArXiv Astrophysics e-prints

Warren, S. J., et al., 2007b, MNRAS, 375, 213

Webbink, R. F., 1984, ApJ, 277, 355

Weidemann, V., 1960, ApJ, 131, 638

Weidemann, V., 1977, A&A, 59, 411

Werner, M. W., et al., 2004, ApJS, 154, 1

Wesemael, F., 1979, A&A, 72, 104

Wickramasinghe, D. T., Ferrario, L., 2000, PASP, 112, 873

Wickramasinghe, D. T., Ferrario, L., 2005, MNRAS, 356, 1576

Williams, K. A., Bolte, M., Koester, D., 2009, ApJ, 693, 355

Williams, T., McGraw, J. T., Grashuis, R., 2001, PASP, 113, 490

Winget, D. E., Hansen, C. J., Liebert, J., van Horn, H. M., Fontaine, G., Nather, R. E., Kepler, S. O., Lamb, D. Q., 1987, ApJ Lett., 315, L77

Wisotzki, L., Koehler, T., Groote, D., Reimers, D., 1996, A&AS, 115, 227

Wright, E. L., et al., 2010, AJ, 140, 1868

Xu, S., Jura, M., 2012, ApJ, 745, 88

Yanny, B., et al., 2009, AJ, 137, 4377

York, D. G., et al., 2000, AJ, 120, 1579

Young, P., Schneider, D. P., Shectman, S. A., 1981, ApJ, 245, 1035

Zacharias, N., Urban, S. E., Zacharias, M. I., Wycoff, G. L., Hall, D. M., Monet, D. G., Rafferty, T. J., 2004, AJ, 127, 3043

Zuckerman, B., Becklin, E. E., 1987, Nat, 330, 138

Zuckerman, B., Koester, D., Reid, I. N., Hünsch, M., 2003, ApJ, 596, 477

Zuckerman, B., Koester, D., Melis, C., Hansen, B. M., Jura, M., 2007, ApJ, 671, 872

Zuckerman, B., Melis, C., Klein, B., Koester, D., Jura, M., 2010, ApJ, 722, 725

Zuckerman, B., Koester, D., Dufour, P., Melis, C., Klein, B., Jura, M., 2011, ApJ, 739, 101